The Hamlyn Symposium on Medical Robotics

Proceedings

23rd - 26th June 2019

Fani Deligianni, Giulio Dagnino and Guang-Zhong Yang (Eds.)

Proceedings of the 12th

Hamlyn Symposium on Medical Robotics 2019

Imperial College London and
the Royal Geographic Society, London
London, United Kingdom
23rd-26th June, 2019

Published by:
The Hamlyn Centre
Imperial College London
https://www.imperial.ac.uk/hamlyn-centre/
E-Print, London, United Kingdom — June 2019

ISSN: 2516-5029

Preface

This year celebrates the 12th anniversary of the Hamlyn Symposium on Medical Robotics. In many cultures, the number 12 symbolises faith and completeness, the one that also triggers a new cycle of changes. We are indeed living in an era of constant advances of technologies, which are shaping the future of surgery. Surgical robotics has evolved from a niche research field to common clinical practice and the commercial success of the current-generation clinical robotic systems has inspired an ever-increasing number of platforms from both commercial and research organisations. This has resulted in smaller, safer, and smarter platforms that extend the perception and dexterity of human operators.

This year's symposium was held at the Royal Geographical Society on the 23rd to 26th June 2019 and the theme of the meeting was "Clinical Challenges and Levels of Autonomy", with a fantastic line-up of scientists, engineers and clinicians in medical robotics and allied technologies. Out of the 115 papers submitted from authors in 24 countries, 58 of them were selected either as oral or poster presentations. The topics covered this year included:

- Soft and bioinspired robots
- Wearable robotics
- Virtual and augmented reality in surgical training
- Imaging and emerging integrated surgical systems
- Smart handheld devices
- Clinical translation and challenges.

We were honoured to have distinguished keynote speakers from the UK, USA, Germany, and Israel. Professor Paolo Dario from the Scuola Superiore Sant' Anna in Pisa, Italy, who is also the Editor-in-Chief of the new IEEE Transactions on Medical Robotics and Bionics, gave his insight into the role of bioinspired design for the development of surgical robots. Professor Alexander Meining from the University of Wurzburg, Germany, provided his vision on the future trends in interventional gastrointestinal endoscopy. Professor Conor Walsh, a distinguished roboticist and the founder of the Harvard Bio-design Lab demonstrated his new design of soft-exoskeleton robots that are suitable for everyday wear. Finally, Professor John Rogers, a world authority on soft electronics highlighted the importance and convergence of new concepts in materials science, mechanical engineering, electrical engineering and advanced manufacturing that has led to the emergence of diverse, novel classes of "biocompatible" electronic and microfluidic systems with skin-like physical properties.

Professor Moshe Shoham, an internationally acclaimed authority in robotics and the co-founder of Mazor Robotics, provided his view on new generations of medical and surgical robots. He was then joined by Drs Manish Chand, Qingquan Luo, Naeem Soomro, and Jim Khan for The Leaders' Forum, focussing on the role of new technologies for the future of surgery and precision medicine. The Forum involved lively debate and discussions among the panel members as well as the audience. The panel also provided unique insights into the unmet clinical demand, the challenge of bringing new products to market, and the importance of integrating engineering, clinical and business innovation. This year's Storz-Hopkins lecture was delivered by Dr Dinesh Nathwani, a distinguished

orthopaedic surgeon, about his research on navigation and robotics, and how they have changed his clinical practice.

I was delighted to see that the affiliated workshops to the Symposium have continued to grow and flourish, with most of them organised by early career researchers. A total of 11 workshops were organised and they covered from advanced bionics, micro-nano robotics, to advanced materials and emerging machine learning techniques. A detailed programme of the workshops is listed on http://hamlyn-robotics.org and these workshops have truly helped to seed new ideas and new collaborations among the attendees.

One of the highlights of the Symposium was the Surgical Robot Challenge. This year we shortlisted 11 entries, with 10 attending the challenge and 1 submitted as a video demonstration, from teams in Italy, Portugal, Thailand, Japan, Germany, UK,Netherlands and Singapore. The teams brought their robots to London to compete over a 3-day competition, starting in the lab, followed by presentations to an esteemed judging panel and then presented to the Hamlyn Symposium's audience. It was remarkable to see the TRLs (technology readiness levels) of these systems. I am sure some of them would go all the way to commercial success and clinical adoption in future.

Organising an international meeting of this scale involves a huge amount of effort and requires a dedicated team. I would like to thank the International and Local Programme Committees, the Workshop Organising Committees for dedicating their valuable time to ensure timely review of the submitted papers and to put together an excellent symposium programme. I am grateful to all the sponsors, particularly the Engineering and Physical Sciences Research Council (EPSRC) through its EPSRC/NIHR-HTC Network and the Wellcome Trust through its iTPA (Institutional Translational Partnership Award) in supporting the Symposium and affiliated Workshops. Special thanks go to the Royal College of Surgeons of England for arranging CPD accreditation of the Symposium workshops.

I would like to take this opportunity to express my gratitude to the team who have worked so hard behind the scenes and to their effort in managing all aspects of the Symposium organisation from programme preparation and publicity to registration and logistics. In particular, I would like to thank Fani Deligianni, Giulio Dagnino, Erh-Ya Tsui, Marianne Knight, Ulrika Wernmark, Florent Seichepine, Robert Merrifield, Jason Keane and Alia Talaat Ahmed, as well as all of the Hamlyn teams who have helped to make the Symposium a great success.

Lastly, special thanks go to Lady Hamlyn. This would not be possible without the generous philanthropic support from both the Helen Hamlyn Trust and Lady Hamlyn herself. For me, it has been a great honour and privilege to have had the opportunity to establish, develop and lead the Hamlyn Centre to its current internationally leading status, supported by so many talented researchers. After 12 years of success, it is time for me to hand over the baton and it is with regret, that this is the last Hamlyn Symposium that I have organised. I hope that the legacy created will be long-lasting within the community and among those who truly believe in the venture we have embarked on.

June 2019,
London, United Kingdom
Guang-Zhong Yang, CBE, FREng

Organisation

General and Programme Chair
Guang-Zhong Yang

Conference Organisers

Fani Deligianni	Review Process, Proceedings, Conference Program
Giulio Dagnino	Review Process, Conference Program
Erh-Ya Tsui	PC Coordination, Sponshorship, Social Media, Publicity
Marianne Knight	UK-RAS coordination, Sponsorship, Web
Ulrika Wernmark	Venue and Logistics
Florent Seichepine	Exhibition and Logistics
Robert Merrifield	Surgical Robot Challenge
Alia Talaat Ahmed	Website, Publicity
Jason Keane	Finance, Logistics

International Programme Committee

Andreas Melzer	University of Leipzig, Germany
Arianna Menciassi	Scuola Superiore Sant'Anna, Italy
Ashutosh Tewari	Mount Sinai School of Medicine, USA
Blake Hannaford	University of Washington, USA
Bob Webster	Vanderbilt University, USA
Bradley Nelson	ETH Zurich, Switzerland
Cameron Riviere	Carnegie Mellon University, USA
Chris Thompson	Harvard Medical School, USA
Christopher Payne	Harvard University, USA
Darwin Caldwell	IIT, Italy
Dennis Fowler	Columbia University, USA
Gabor Fichtinger	Queen's University, Canada
Giancarlo Ferrigno	Politecnico Milan, Italy
Howie Choset	Carnegie Mellon University, USA
Ichiro Sakuma	University of Tokyo, Japan
Jacques Marescaux	University Hospital Strasbourg, France
Jaesung Hong	DGIST, South Korea
Jessica Burgner-Kahrsi	University of Toronto, Canada
Joe Wang	UCSD, USA
Kevin Cleary	The Sheikh Zayed Institute, Washington, USA
Koji Ikuta	University of Tokyo, Japan
Lee Swanstrom	University of Oregon, USA
Leo Joskowicz	The Hebrew University of Jerusalem

Leonardo Mattos	IIT, Italy
Mark Talamini	Stony Brook University, USA
Paolo Dario	Scuola Superiore Sant'Anna, Italy
Paolo Fiorini	University of Verona, Italy
Peer Fischer	Max Planck Institute, Germany
Peter Kazanzides	Johns Hopkins University, USA
Philip Chiu	The Chinese University of Hong Kong, China
Pierre DuPont	Children's Hospital Boston, USA
Pierre Jannin	INSERM, France
Rajni Patel	Western University, Canada
Rick Satava	University of Washington, USA
Russ Taylor	Johns Hopkins University, USA
Simon DiMaio	Intuitive Surgical Inc, USA
Stefen Weber	University of Bern, Switzerland
Steve Wexner	Cleveland Clinic Florida, USA
Thomas Looi	Sick Kids Toronto, Canada
Toshio Fukuda	Beijing Institute of Technology, China/Meijo University, Japan
Vipul Patel	Global Robotics Institute, USA

Local Programme Committee

Andrew Schache	Liverpool University and Aintree University Hospital, UK
Brian Davies	Imperial College London, UK
Celia Theodoreli Riga	St Mary's Hospital, UK
Christos Bergeles	King's College London, UK
Colin Bicknell	St Mary's Hospital, UK
Daniel Elson	Imperial College London, UK
Daniel Leff	Imperial College London, UK
Dinesh Nathwani	Charing Cross Hospital, UK
Erik Mayer	Royal Marsden Hospital, UK
Ferdinando Rodriguez Y Baena	Imperial College London, UK
George Mylonas	Imperial College London, UK
Helge Wurdemann	University College London, UK
Jag Dhanda	Queen Victoria Hospital, UK
Jian Dai	King's College London, UK
Julian Teare	St Mary's Hospital, UK
Justin Vale	St Mary's Hospital, UK
Kamal Deep	Glasgow University and Golden Jubilee National Hospital, UK
Kaspar Althoefer	Queen Mary University of London, UK
Kawal Rhode	King's College London, UK
Len Fass	GE Healthcare, Imperial College London, UK
Neil Tolley	St Mary's Hospital, UK
Nick Cheshire	Royal Brompton Hospital, UK
Pallav Shah	Royal Brompton Hospital, Imperial College London, UK
Pietro Valdastri	University of Leeds, UK
Salzitsa Anastasova	Imperial College London, UK
Sanja Dogramadzi	Bristol Robotics Laboratory, UK

Shane Xie	University of Leeds, UK
Stamatia Giannarou	Imperial College London, UK
Thanos Athanasiou	Hammersmith and St Mary's Hospitals, UK
Zoltan Takats	Imperial College London, UK

CONFERENCE PROGRAM

Day 1: Monday 24th June 2019

Oral Session 1: Soft and Bionspired Robots

Poster Session 1

Day 2: Tuesday 25th June 2019

Oral Session 2: Clinical Translation and Challenges

Oral Session 3: Wearable Robotics and VR in Surgical Training

Oral Session 4: Imaging and Emerging Surgical Systems

Oral Session 5: Smart Handheld Devices

Variable Contraction Timing for a Soft Robotic Cardiac Assist Device

C.J. Payne[1,2], D. Van Story[1,2], D. Bautista-Salinas[2], M. Saeed[2], T. Thalhofer[1], P.J. del Nido[2], C.J. Walsh[1], N.V. Vasilyev[2]

[1]*Wyss Institute for Biologically Inspired Engineering, Harvard University USA*

[2]*Department of Cardiac Surgery, Boston Children's Hospital, USA*

nikolay.vasilyev@childrens.harvard.edu (DOI10.31256/HSMR2019.1)

INTRODUCTION

Ventricular Assist Devices (VADs) are medical implants designed to augment cardiac output for patients with heart failure. We recently proposed a soft robotic VAD (SRVAD) that adopts pneumatic soft actuators to rhythmically massage the heart left ventricle (LV) via septal bracing [1]. The performance of SRVADs is highly dependent on effective temporal synchronization between the device and the native heart contraction [1, 2]. In our previous work, we used discrete on/off valves to control airflow into the SRVAD actuators, which places inherent limitations on the dynamic response of the soft actuators. Here, we use a proportional electromechanical valve with a variable aperture for controlling the working fluid flow rate to enable arbitary actuator contraction profiles. We experimentally derived valve actuator parameters to obtain a range of actuator contraction profiles and tested these profiles *in vivo*.

MATERIALS AND METHODS

Our device and control system are thoroughly described in [1]. McKibben-based soft actuators are attached to the extracardiac bracing frame that is positioned around the LV. The frame is braced against the LV via an intracardiac bar that passes through the LV wall and is attached to the ventricular septum via an anchoring system (Fig. 1).

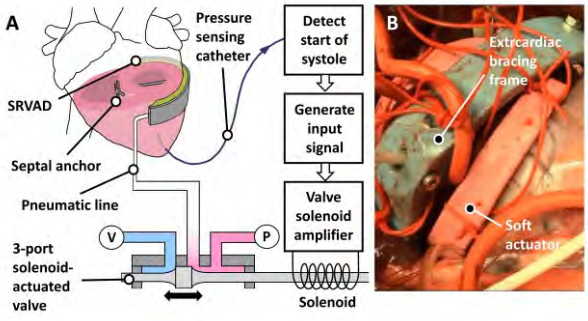

Fig. 1. (a) SRVAD, control system and (b) *in vivo* use

When cyclically pressurized, the actuators contract which causes rhythmic loading of the LV to aid blood ejection. We adopt the same control system as previously described in [1], which uses a pressure-sensing catheter to detect the beginning of the LV systole and trigger device actuation. However, instead of using a discrete on/off valve to control valve pressurization, we adopt a 3-port proportional valve (VEF3121-2-02N, SMC) that can provide a pneumatic output of abritary forward and reverse flow rate, when connected to a regulated pressure source and a vacuum source (Fig. 1, 2). A position-controlled solenoid adjusts the valve aperture to control the output flow rate. The solenoid drive electronics (VEA250, SMC) sets the valve aperture according to an input signal (0-5V); a 5V signal corresponded to the valve being fully open to the pressure source and 0V corresponds to full vacuum. The valve is fully shut in a 2-3V deadband range, and the valve aperture is proportionally open to the intermediary voltages (Fig. 2). The McKibben-based soft actuators used in our device have a non-linear pressure-contraction relationship [2]. To account for this, our actuation strategy was to provide a high initial flow rate in to the actuator and then immediately reduce the valve aperture to retard actuator contraction. The valve input voltage (V) with respect to time (t) was governed by equation 1:

$$V = 5 - \left((5 - R_V)\left(\frac{t}{T_s}\right)^K\right) \quad \text{for } (t \le T_s) \qquad (1)$$

Where T_s is the systolic actuation period, K is a constant which determines the rate of valve closure and R_V sets the valve aperture at the end of systole. V is then set to 0V (valve set to full vacuum) for the entirety of diastole to relax the actuator. The regulated pressure source can be adjusted to provide an input pressure, P.

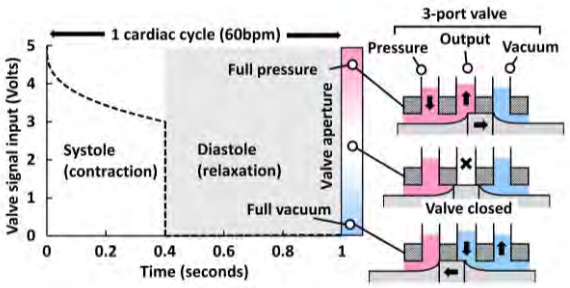

Fig. 2. 3-port proportional valve control paradigm

In a benchtop study, we empirically derived the actuation parameters (K, R_V, P) to obtain 4 distinct temporal contraction profiles within a 0.4 second time window (representing 60bpm, 40% systolic phase). Linear actuation contraction distance was measured using a potentiometer and data acquistion system, as described in [2]. We used a regulated pressure source and connected 2 McKibben actuators to the system (since two actuators are used in the SRVAD for LV support, although contraction measurements were only made on a single actuator). We used a 2m length of ¼" tubing from the valve output to the actuators. The McKibben actuators (140mm in total length) were based on a ½" mesh, with

a thermoplastic bladder and nitrile oversheath to aid device recoil, as described in [2]. The actuation parameters for the actuation profiles are listed in Table 1. We tested these 4 actuation profiles in an IACUC-approved *in vivo* porcine study (n=1) to assess the influence of actuator contraction profile on cardiac output. The device was deployed as described in [1] and the actuators were sutured to LV free wall. After SRVAD implantation, heart failure was created by injecting polystyrene microbeads of a nominal diameter of 50 to 100 µm (Megabead NIST, Polysciences Inc.) in to the coronary arteries to induce LV ischemia. During heart failure, the device was actuated for each contraction profile and the aortic blood flow was measured using a flow probe (20PS, Transonics Corp). The control system regulated T_s to be 40% of the cardiac cycle. Data analysis was based on n=7 consecutive cardiac cycles.

RESULTS

Temporal actuator contraction profiles and contraction velocity profiles are presented in Fig. 3. Key hemodynamic data is presented in Table 1. The animal heart rate was 61-67bpm during actuation periods. In vivo aortic flow data is presented in Fig. 4.

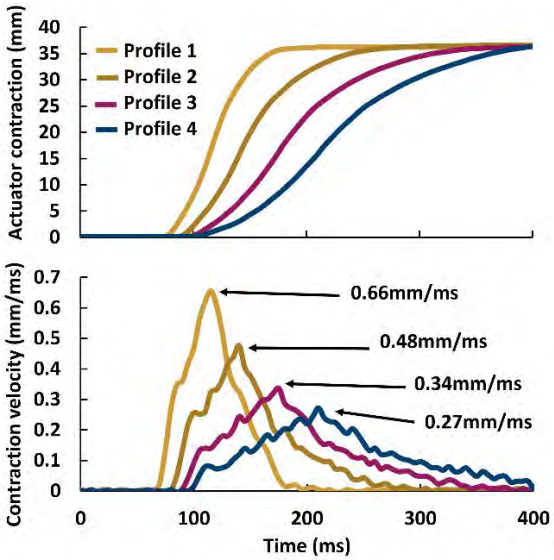

Fig. 3. 140mm McKibben soft actuator contraction profiles and corresponding contraction rates (profiles 1-4).

Profile	K	Rv	P (psi)	Mean flow rate (L/min)	Peak LV pressure (mmHg)
1	0.150	3.00	21	0.97	46.8
2	0.010	5.00	15	1.06	43.7
3	0.010	3.90	15	1.03	47.3
4	0.005	3.62	17	1.25	52.0

Table. 1. Actuation parameters and hemodynamic data for each contraction profile tested

DISCUSSION

Fluidic-based soft robotic systems commonly use on/off valve switching and static-pressure based control paradigms for device actuation. Such an approach is sufficient for many soft robotic applications, but in cardiac assist applications the dynamic response of the actuator is critical to device efficacy. The proposed control methodology has demonstrated the ability to tune the actuator response time to aid SRVAD-heart synchronization.

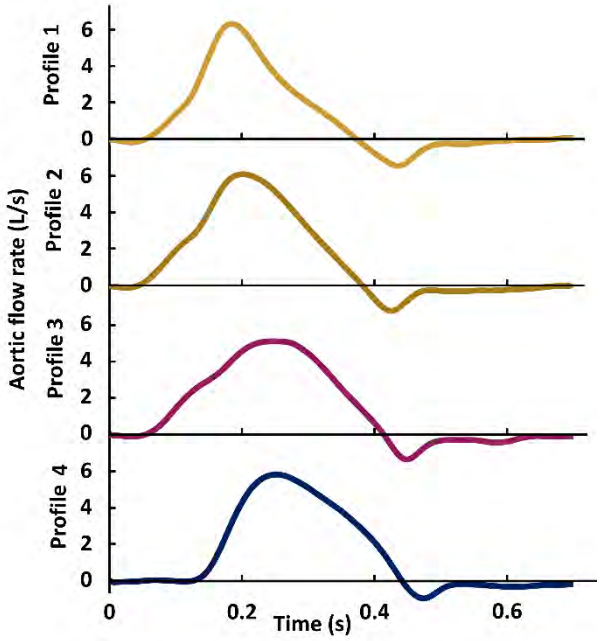

Fig. 4. Systolic phase of aortic flow traces during actuation of the SRVAD for the 4 actuator contraction profiles (average aortic flow profile is based on n=7 consecutive cardiac cycles).

Bench testing of the control system demonstrated the ability to achieve a broad range of contraction profiles. There was a 2-fold increase in full contraction response time between the extreme profiles (1 and 4) and a ×2.4 reduction in peak contraction velocity. *In vivo* testing demonstrated that the different actuator contraction profiles distinctly alter the aortic blood flow rate trace (Fig. 4). Nonetheless, cardiac output was comparable between actuator contraction profiles. Profile 4 (the slowest actuation profile) facilitated greater cardiac output and higher peak LV pressures. This agrees with prior work with direct cardiac compression devices that demonstrated that slower actuator contraction is preferable to faster contraction in maximizing cardiac output [2], but further investigation is needed to draw definitive conclusions. Future work will consider modeling of the soft actuator dynamic system to allow prediction of the optimal actuation parameters. This work will need to consider the transfer function of the electromechanical valve and fluid flow conditions. It will also be desirable to model the dynamic response of the actuator when coupled to the heart.

REFERENCES

[1] Payne C.J. et al. Soft robotic ventricular assist device with septal bracing for therapy of heart failure. Science Robotics. 2017; Nov(2) eaan6736.

[2] Payne C.J. et al. An implantable extracardiac soft robotic device for the failing heart: mechanical coupling and synchronization. Soft Robotics. 2017; Sep(3) soro.2016.0076.

Evaluation of a Soft Helical Actuator Performance with Hard and Soft Attachments for Tissue Regeneration

Eduardo Perez-Guagnelli, Joanna Jones, Dana D. Damian

Sheffield Biomedical Robotics Lab, Automatic Control and Systems Engineering Department, University of Sheffield; UK

erperezguagnelli1@sheffield.ac.uk, d.damian@sheffield.ac.uk (DOI10.31256/HSMR2019.2)

INTRODUCTION

Soft robots have the potential to interact safely within dynamic and delicate environments. As such, they can be safe to use inside the human body [1], and conform to soft tissues and organs, making them well suited to be used as implants. These robots may reside inside the human body to provide sustained therapy, for example, to regenerate tissue via mechanotherapy [2][3].

In our previous work, we introduced a rigid robotic implant and demonstrated it grows a significant length of tubular tissue by stretching it [3]. Based on literature suggesting that soft implants reduce the fibrotic response of the body [4], we advance this technology through the development of a soft pneumatic actuator that can potentially elongate tubular tissue [2].

An important factor that has not received sufficient attention is the physical interface of an implant to the tissue and how this interface affects the performance of the implant and ultimately the state of the tissue. Some findings suggest that smooth and soft surfaces are likely to improve in vivo biocompatibility [3][5][6] and reduce inflammation [4], though these studies overlooked the functional interplay between the tissue and the mechanical function of the implant.

In this study, we investigate two attachment methods of a Soft Helical-Interlayered Actuator (SoPHIA) [2] to a cadaveric oesophageal tissue and their effect on the performance of this actuator as an implant required to stretch tissue in order to induce growth. For more detailed information about SoPHIA's design, function and control, please refer to [2].

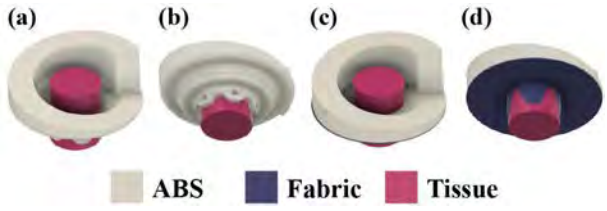

Fig. 1 Attachment systems used in this study. (a-b) Views of the Hard Connector-Hard Sleeve (HCHS). (c-d) Views of the Hard Connector-Soft Sleeve (HCSS).

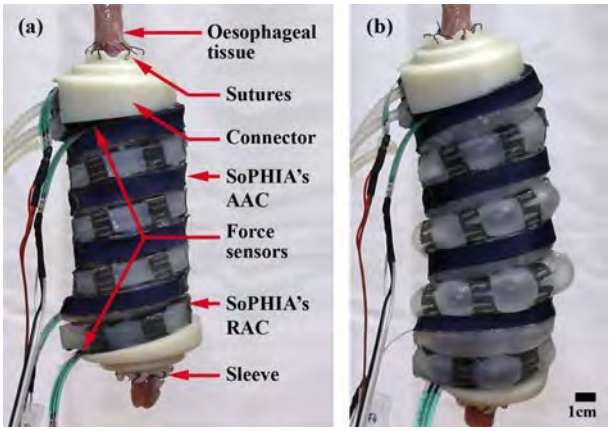

Fig. 2 Experimental setup, attachment and mechatronic components. (a) SoPHIA in relaxed and (b) pressurised state at 15 kPa for the Radial Actuation Chamber (RAC) and 20 kPa for the Axial Actuation Chamber (AAC), using HCHS.

MATERIALS AND METHODS

Design and Fabrication: *2* types of attachments were tested as interfaces between SoPHIA and the oesophagus: an entirely plastic connector with integrated hard suturing sleeve (HCHS) (Fig. 1 a-b) and a plastic connector with a soft polyester sleeve (HCSS) that were sutured to the tissue (Fig. 1 c-d). The connectors did not contact the esophageal tissue. Both sleeves were designed to minimise the amount of tissue surface that is covered by the fixation methods. The connectors were 3D printed (Mojo Stratasys) out of ABS material. The soft sleeves were fabricated out of laser cut (Denford-VLS) polyester fabric. For the HCSS, the soft sleeve was attached to the connector using cyanoacrylate adhesive. All of the designs were fixed to the oesophagus by subcuticular continuous sutures using surgical thread (Mersil Ethicon-W577) (Fig. 2).

Experimental Setup: The sleeves were fixed to a swine oesophageal tissue. Four force sensors (I.E.E. Strain Gauge, RS Components) were placed between SoPHIA and the ABS connectors (Fig. 2a) to record the amount of force that can be exerted with regards to the resistance of the ex vivo tissue. Expansion of the soft actuator is controlled by a pressure based pneumatic system [2].

Experimental Procedure: We supplied 25 and 20 kPa of pressure to the axial (AAC) and radial actuation

chambers (RAC) (Fig. 2b) respectively, in sequence, as that is the maximum pressure they can stand before failure. Combined pressurisation of the chambers caused the actuator to expand up to 25% its original size. We performed 3 trials per sleeve design.

RESULTS

Characterisation of Traction Forces

The HCHS exerted a maximum force of 0.15N on the tissue, with forces first noticeable at an axial pressure of 10 kPa and a radial pressure of around 7 kPa (Fig. 3). The HCSS exerted similar maximum forces of 0.15N in all trials by applying a total (axial and radial) pressure of 35 kPa. The forces were linearly related to both axial and radial pressure, with forces recorded from 0 kPa for both pressures (Fig. 3). The similar maximum forces for both sleeve designs confirm that the material selection has no impact on the traction force capacity that SoPHIA can exert on the tissue.

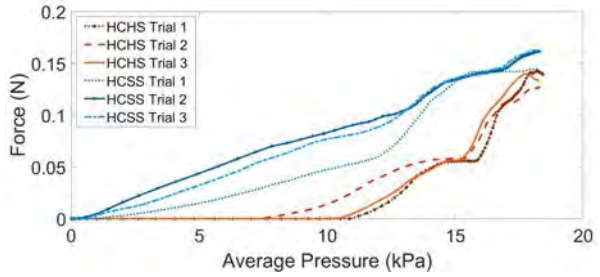

Fig.3 Force behaviour vs applied pressure among attachments.

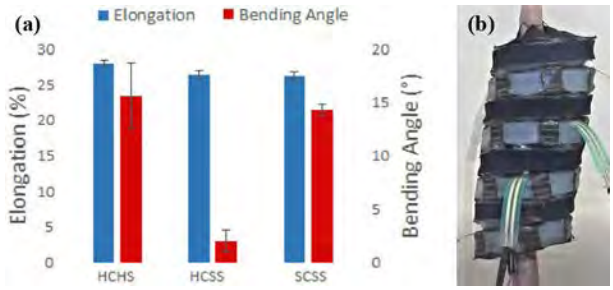

Fig. 4 (a) Bar chart of average elongations and bending angles per attachment method. We obtained 28% (± 0.4) of elongation using the HCHS, 26% (± 0.6) using the HCSS and 26% (± 0.7) using the (b) Soft Connector-Soft Sleeve (SCSS). Both, the HCHS and the SCSS showed bending angles of 15.7° (± 3.1°) and 14.3° (± 1°) respectively, compared to the HCSS which bent on average 2° (± 0.6°).

Elongation and Bending Angle

We measured the elongation and bending angle of SoPHIA, as an indication of its capability to stretch the tissue on which it is fixed. With the two designs, SoPHIA achieved a similar level of elongation around 27% (± 1) at the maximum pressurization. In contrast, the bending angles varied between the two designs (Fig. 4). Based on the overall performance metrics, we concluded that a soft attachment is most suitable for SoPHIA, and fabricated a Soft Connector- Soft Sleeve (SCSS), shown in Fig. 4b. The elongation and bending angle for the SCSS are also shown in Fig. 4a. While SoPHIA's elongation with HCHS and SCSS were consistent, the bending angles differed.

DISCUSSION

In this study, we investigated the feasibility of two attachment methods and their effect on the tissue elongation using a soft helical actuator. We demonstrated that a soft sleeve is capable of elongating axially (SCSS) and exerting similar traction forces (HCSS) as a hard sleeve (HCHS). Moreover, the soft sleeve applied forces more gradually which is better suited to clinical applications, compared to the sharper increase in forces with the hard sleeve, which could result in tissue damage. The forces applied by SoPHIA on the tissue, regardless of the attachment type, were low because of the initial fixation on a relaxed tissue. Thus, SoPHIA reached it maximum extension on a relatively not tensed tissue. In our experiments, the oesophageal tissue works as axial support for the entire system. While Fig. 4 indicates that the design of HCSS is the most effective for SoPHIA due to the low bending angle value, the extent of bending should not affect the tissue, but rather the elongation performance of SoPHIA. We hypothesise that higher bending angles are caused in general, by the manual, and thus less precise, fixation of attachments to the oesophageal tissue. However, in the in-vivo scenario, we conceive that the bending of the actuator will be naturally suppressed by the tight arrangement of the organs. We envisage the use of SoPHIA with soft tissue attachments to perform tissue elongation on tubular tissue via mechanotherapy. Next steps include standardisation of the soft attachments, advancing the mathematical model of SoPHIA and conducting in-vivo evaluation.

REFERENCES

[1] K.Sangbae, C. Laschi and B. Trimmer "Soft robotics: a bioinspired evolution in robotics,"Trends in Biotechnology, Vol. 31, no. 5, pp. 287-294, 2013.

[2] E. R. Perez-Guagnelli, S. Nejus, J. Yu, S. Miyashita, Y. Liu, and D. D. Damian, "Axially and radially expandable modular helical soft actuator for robotic implantables," in Proceedings of IEEE International Conference on Robotics and Automation. IEEE, 2018.

[3] D. D. Damian, K. Price, S. Arabagi, I. Berra, Z. Machaidze, S. Manjila, S. Shimada, A. Fabozzo, G. Arnal, D. Van Story et al. , "In vivo tissue regeneration with robotic implants," Science Robotics, vol. 3, no. 14, p. eaaq0018, 2018.

[4] P. Moshayedi, G. Ng, J. C. F. Kwok, G. S. H. Yeo, C. E. Bryant, J. W. Fawcett, K. Franze, and J. Guck, "The relationship between glial cell mechanosensitivity and foreign body reactions in the central nervous system," Biomaterials, vol. 35, no. 13, pp. 3919–3925, 2014.

[5] Matlaga BF, Yasenchak LP, Salthouse TN."Tissue response to implanted polymers: the significance of sample shape," in Journal of Biomedical Materials Research, 1976 May;10(3):391-7

[6] Omid Veiseh, Joshua C. Doloff, Minglin Ma et al. "Size- and shape-dependent foreign body immune response to materials implanted in rodents and non-human primates," in Nat Mater, 2015 Jun, 14(6):643-51

SoftSwitch: A soft implantable device for on/off drug release

Keegan Mendez[1,2], William Whyte[2,3], Garry P. Duffy[3,4], Ellen T. Roche[1,2,5]

[1]Health Sciences and Technology, Massachusetts Institute of Technology, [2]Institute for Medical Engineering and Science, Massachusetts Institute of Technology, [3]Advanced Materials and BioEngineering Research Centre, Trinity College Dublin, [4]School of Medicine, National University of Ireland Galway, [5]Department of Mechanical Engineering, Massachusetts Institute of Technology

etr@mit.edu (DOI10.31256/HSMR2019.3)

INTRODUCTION

Biological systems in the human body are elegantly perceptive to the timing and location of physiological cues and drug release (*1*). Despite this sensitivity, contemporary pharmacological strategies typically release the active biological agent in a sustained, predefined manner, lacking the precision needed to finely modulate physiological and pathological processes, and often causing undesired side effects (*2*). Implantable microelectromechanical devices show great promise in this regard, providing a means to regulate spatiotemporal drug release in response to a pre-programmed schedule, a physiological stimulus, or wireless communication from a clinician or patient (*3*, *4*). However, these rigid devices have inherent limitations in terms of tissue placement, and are currently intended for use as subcutaneous implants (*3*). Soft compliant materials have distinct advantages over rigid components; they can be designed for minimally invasive catheter delivery and moulded or shaped to the curvature of the targeted area, enabling greater spatial control following device placement. Here, we present *SoftSwitch*, a soft implantable device that allows for switchable on/off drug delivery in response to a precise actuation stimulus.

MATERIALS AND METHODS

Manufacturing: A single-pour lost wax casting technique was used. The actuation element was composed of high stiffness (Smooth-Sil 950) and low stiffness (Ecoflex 00-20) silicone to enable unidirectional actuation expansion. The self-sealing membrane (Ecoflex 00-20) was pre-stretched to varying strains (0/75%) using a custom rig and a pore was created using a hypodermic needle (0.24/ 1.65 mm). The membrane was then relaxed and bonded to the drug reservoir with a silicone adhesive (Sil-Poxy).
Device Activation Pressure: Devices were actuated using a syringe pump (PhD Ultra, Harvard Apparatus) at a slow infusion rate (100 µl/min) while pressure was measured (ArgoTrans Model 2). A sudden drop in pressure (>2% in 1sec) indicated pore opening. This was confirmed by visual inspection.
Release Studies: Acid red 1 (10mg/mL, Sigma 210633), HCl (1M), or NaOH (1M) were loaded into the device. Devices were submerged in water and actuated above their activation pressure (133mmHg). Release was quantified by measuring absorbance at 506nm (SpectraMax M3), or a pH probe (224 Conductivity TDS Meter) and universal indicator (Innovating Science IS30003).

RESULTS

Design and realization of a milli-scale soft drug delivery system. Here, we show the realization of a milli-scale soft drug delivery system (Fig 1a). The device is composed of an actuation layer, and a sealed drug reservoir. Application of a pneumatic stimulus above a predefined pressure threshold opens a self-sealing pore, causing localised drug release into the surrounding environment. Subsequent pressure evacuation allows the pore to close and re-seal (Fig 1b,c).

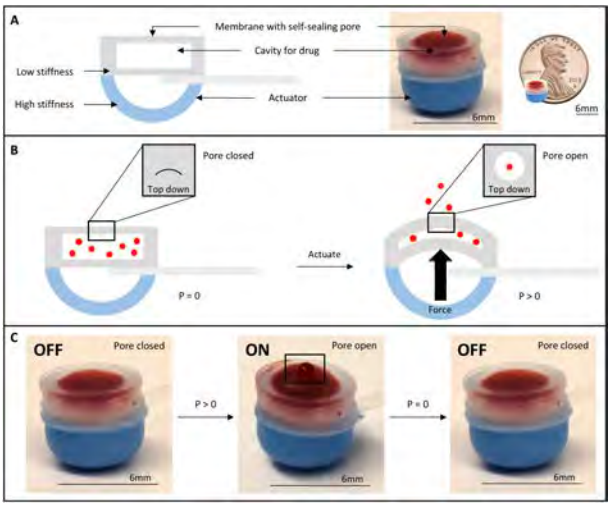

Fig. 1 Design and realization of a milli-scale soft drug delivery device. (a) The design schematic (left) and realization (right) of a milli-scale soft drug delivery device with switchable on/off control. **(b)** An overview of the device mechanism of action. The self-sealing pore remains closed when the device is at rest. The pore opens when the device is actuated. **(c)** Demonstration of on/off drug release. The pore opens, and drug is released when the device is actuated at pressures above a pre-defined threshold.

On/off drug release utilising a self-sealing silicone membrane. First, we characterized the pressure upon which the device will switch to its "on" configuration (opening of its self-sealing pore). A Huber needle of a defined size was used to create a resealable pore or drug exit point in the silicone membrane. Using a pressure gauge, we established an inverse relationship between the pore size and required opening pressure (Fig 2a).

Opening pressure could be further modulated by pre-straining the silicone membrane before needle insertion (Fig 2b). Next, we tested drug release using optimised pore size parameters (0.24mm, 75% pre-strain). Devices loaded with a model small molecule drug (acid red 1) exhibited negligible baseline release over 5 days ("off" configuration). Activation of the device on day 5 caused rapid drug release (~60% of loaded cargo). Following activation, the device switched back to its "off" configuration, and again demonstrated negligible release (Fig 2c).

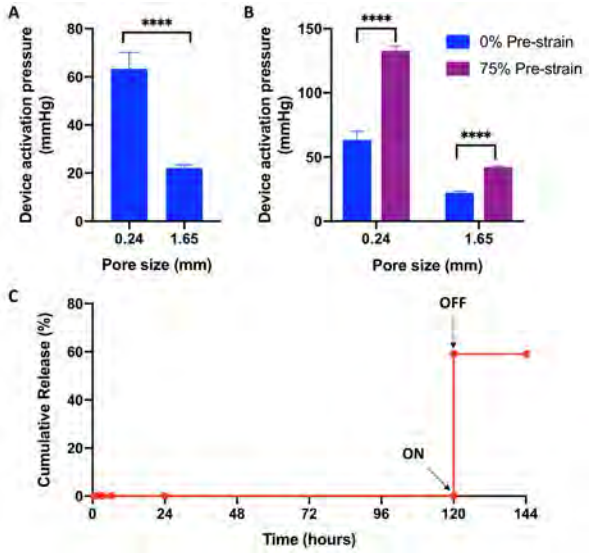

Fig. 2 On/off drug release utilizing a self-sealing silicone membrane. (a) The effect of pore size on device activation pressure (n=6), mean ± SD. **** P<0.0001, unpaired, two-tailed t-test between groups. **(b)** The effect of pre-strain on pressure to open (n=6), mean ± SD. **** P<0.0001, unpaired, two-tailed t-test between groups. **(c)** Demonstration of on/off release (n=3).

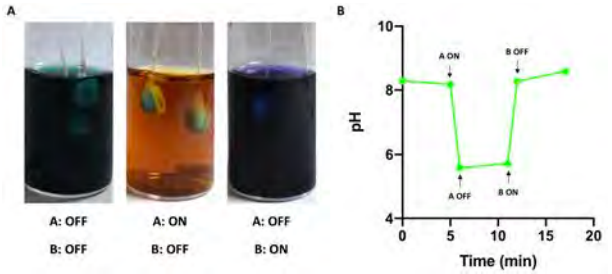

Fig. 3 Modulation of physiological pH. (a,b) Controlled modulation of pH after sequential activation and deactivation of Reservoir A (Acid) and Reservoir B (Base).

Modulation of physiological parameters. Finally, we tested the ability of the device to modulate physiological parameters using on/off delivery of drug. Two devices loaded with an acid (HCl) and base (NaOH) were submerged in water, and the pH was monitored in the surrounding fluid. The pH remained constant while the devices were in an "off" configuration. Colorimetric change of a pH buffer was monitored for visual confirmation of pH change (Fig 3a). Activation of Reservoir A containing an acid caused a drop in pH, and activation of Reservoir B containing a base restored the solution to near its starting pH (Fig 3b).

DISCUSSION

Simple drug delivery formulations often exhibit a pre-determined passive release profile, which only matches the ideal pharmacokinetic profile of certain drugs (*2*). Furthermore, these preordained formulations do not account for disease, patient or anatomical site variability. Our device, *SoftSwitch,* can tailor the treatment course accordingly via switchable on/off drug release. It can be accurately switched "on" with a precise pneumatic stimulus and exhibits negligible drug leakage in the "off" configuration even with molecules of low molecular weight (506Da). This has been difficult to achieve using other externally controlled soft material systems (*2*), and is an essential requirement for drugs with a narrow therapeutic index (*5*). The activation pressure for the "on" configuration can be tightly controlled by the initial pore size and degree of pre-stretch. Discrete opening pressure is important for device reliability and patient safety. Spatial control of drug release could be achieved by incorporating multiple reservoirs with different switches into the same device, or by designing multiple reservoirs in a distinctive geometric pattern. An array of reservoirs, each containing the same or separate drugs, could be used to finely modulate biological processes. Here we demonstrate this capability simply, using pH, which may have clinical value in the treatment of cancer where pH has been shown to impact tumour gene expression (*6*). This soft platform system could be utilised for numerous indications in difficult anatomical positions, such as rhythm control for the heart. Indeed, device placement in deeper anatomical positions may be more suitable so the reservoir is not subjected to excess musculoskeletal movement and unintentional opening of the drug reservoir. In the future, activation control could be achieved by wireless communication to an implantable actuation system i.e. an implantable, fully integrated, soft device.

In summary, *SoftSwitch* demonstrates precise, switchable on/off drug delivery to a localized site. This exquisite control of drug release shows considerable promise for enhancing the therapeutic effects of molecular therapies by enabling delivery of a precise dose of the correct cargo at the optimal time.

REFERENCES

1. A. Le Bras, Chronotherapy for atherosclerosis. *Nat. Rev. Cardiol. 2018 158*. **15**, 440 (2018).
2. J. Li, D. J. Mooney, Designing hydrogels for controlled drug delivery. *Nat. Rev. Mater.* **1**, 16071 (2016).
3. J. T. S. Jr, M. J. Cima, R. Langer, A controlled-release microchip, 335–338 (1999).
4. R. Farra *et al.*, *Sci. Transl. Med.*, in press, doi:10.1126/scitranslmed.3003276.
5. N. Huebsch *et al.*, Ultrasound-triggered disruption and self-healing of reversibly cross-linked hydrogels for drug delivery and enhanced chemotherapy. *Proc. Natl. Acad. Sci.* **111**, 9762–9767 (2014).
6. N. Rohani *et al.*, *Cancer Res.*, in press, doi:10.1158/0008-5472.CAN-18-1604.

Eversion-type soft overtube for endoscopic surgery

F. Putzu, T. Abrar, J. Konstantinova, K. Althoefer

Centre for Advanced Robotics @ Queen Mary,
(f.putzu; t.abrar; j.konstantinova; k.althoefer)@qmul.ac.uk (DOI10.31256/HSMR2019.4)

INTRODUCTION

Overtubes are commonly used to protect patients from trauma due to sharp and harmful objects during insertion and retrieval of surgical instruments as part of endoscopic procedures. Typically, overtubes are made from semi-rigid plastic. Their inner diameter usually matches the outer diameter of the surgical tool to be used. The dimensions of existing overtubes are between 540 – 650 mm (length) and 14.4 – 21 mm (outer diameter), depending on the entry point and the application area. For example, overtubes for oesophageal or gastric surgeries require longer overtubes than those used for the cricopharyngeal area or the airway, which are usually 25 cm in length. When the surgical area is far away from the point of entry i.e. stomach, a longer overtube is required [1].The most reported complications associated with the use of overtubes are damages to the mucosa such as abrasion and tears caused by friction between the overtube and the biological environment, especially during repeated insertion [2]. Other problems reported are tissue perforations and pancreatitis during endoscopic procedures [1].

Research on so-called overtubes has proven promising [3]. The work described here reports on recent advancements in the new area of eversion-type robots for endoscopic surgery. To the best knowledge of the authors, this is the first time an eversion-type inflatable overtube is being proposed as an alternative endoscopic method, capable of guiding flexible instruments to the point of interest inside a patient's abdominal cavity or for the treatment of illnesses of the oesophageal tract.

We propose an eversion-based, inflatable overtube made of a fabric sleeve structure that continuously lengthens from the tip significantly extending into the cavities. The main advantages of our proposed overtube are the increase of the depth of insertion compared to previous systems, the compliance to the surroundings and the protection of the mucosa from trauma also during insertion thanks to the frictionless movement of the device [4], [5]. It can also be used in situation where multiple flexible tools need to be inserted along a long and narrow pathway, i.e., for the treatment of oesophageal food impaction.

MATERIALS AND METHODS

The proposed overtube prototype is constructed from airtight fabric with an outer diameter of 18 mm and an inner diameter of 17 mm; the tube can extend up to 1 m. When using current overtubes, the outer surface needs to be lubricated before the procedure to lower the friction and resistance between the overtube and tissue [6].

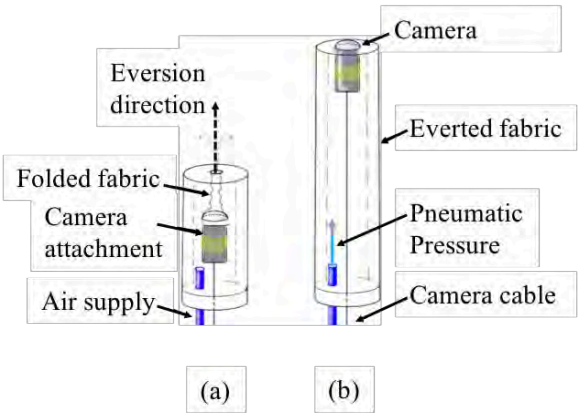

Figure 1 Schematic of the proposed eversion overtube with embedded camera: (a) actuation of overtube until fully elongated.

Similar to work by Okamura and Hawkes the proposed design is based on eversion or growing at the tip [7], [8]. When compared to existing overtubes, we note that our overtube does not need lubricating. The airtight fabric sleeve of the proposed overtube folds inside-out at the tip when pressurised by air pushing the tip forward and outwards, (Fig. 1 (a)) and, hence, no friction occurs between our overtube and the tissue. The adaptability of the device to the biological environment is enhanced, thanks to compliance of the soft material used. This can help to seal the area where the overtube is employed and avoid any gas leakage. Also, the length of the device can be tuned controlling the inner pressure of the fabric structure, even though, the position of the camera is fixed at the very end of the device.

Another advantage of the proposed device is its cost. Low cost materials are used, and, hence, an overtube based on the eversion principle is disposable.

RESULTS

In our study, we performed experiments to explore the feasibility of our overtube prototype. Firstly, we studied its capability to pass through a trocar port (standard 12 mm trocar port), see Fig. 2. Although our overtube reaches a diameter of 18mm diameter, when fully inflated, it was capable of squeezing through the narrow trocar port and continuing to elongate further.

Figure 2 Eversion overtube passing through a standard 12 mm trocar port.

We show that an eversion-type overtube can pass through narrow openings and that one overtube (even with a large outer diameter) can traverse through trocar ports with smaller diameters. Our second experiment aimed at investigating the overtube's compliance and bending capability. In these experiments, we blocked the straight-line path with obstacles, requiring the overtube to change direction. Also, we investigated the ability of our eversion overtube with regards to elongation (Fig. 3).

Figure 3 Bending of the overtube; (a) when the straight path is blocked the overtube bends, (b) an artist's impression of the overtube bending when used in the oesophagus.

From these experiments we learn that our overtube diverts from its straight path, if an obstacle is encountered. Furthermore, the tested obstruction scenarios did not influence the elongation capabilities of the overtube. Thus, the overtube can bend and carry on extending until fully extended or reaching another obstacle. The natural bending of the overtube excludes the need for other actuation means such as tendons, which are used to control the bending movement of overtubes in other work [1]. Once deployed, the hollow inside of the eversion-type overtube can be employed to guide surgical tools to the operating site. The results presented here are promising and show the feasibility of the proposed eversion-type overtube.

DISCUSSION

Our overtube is made from soft material. This combined with the principle of an inflatable cylindrical structure that the eversion robot evolves into during employment, allows us to create a system that is capable of adapting its shape to the patient's inside without imparting undue forces on the tissue and organs. Our overtube also shows superior performance when compared to other approaches with regards to punctures and perforations. The new device proves to be highly compliant and capable of adapting naturally to a given path. Our experiments also show that the length of our overtube sleeve can be adjusted by regulating the air that is pumped inside. We note that low cost materials are being employed making the system disposable, further underlining the suitability of the proposed eversion overtube for surgical applications.

One of the main advantages of our overtube concept is its compliance; this avoids unnecessary tissue trauma and simplifies the insertion process, since the device adapts naturally to a given path. The experiments reported here showed the feasibility of the chosen approach to pass a camera in to a human's abdominal cavity. We foresee that also other tools such as grasping devices can be transferred in a similar way. Although the experiments described here are initial, the concept is promising. Future work will focus on the internal friction caused by the instruments during their insertion through the overtube, and the integration of our device with existing surgical tools. We also aim to use this overtube in a preclinical study to evaluate its suitability in a more realistic setting.

ACKNOWLEDGEMENTS

This work was supported in part by the EPSRC in the framework of NCNR (National Centre for Nuclear Robotics) project (EP/R02572X/1) and the WormBot project conducted jointly with q-bot (IUK 2308/104059).

REFERENCES

[1] W. M. Tierney et al., "Overtube use in gastrointestinal endoscopy," Gastrointest. Endosc., vol. 70, no. 5, pp. 828–834, Nov. 2009.
[2] F. Y. Hondo et al., "Transgastric access By balloon overtube for intraperitoneal surgery," Surg. Endosc., vol. 21, no. 10, pp. 1867–1869, Sep. 2007.
[3] J. H. Lee, W. H. Shin and D. Kwon, "A modularized wire-driven overtube using tube type bending mechanism for robotic NOTES system," 2013 13th Int. Conf. on Control, Automation and Systems (ICCAS 2013), pp. 631-634.
[4] Putzu, F., Abrar, T., Konstantinova, J. and Althoefer, K. "Minimally Invasive Surgery Eversion Overtube". CRAS: Joint Workshop on New Technologies for Computer/Robot Assisted Surgery. (2019).
[5] M. Goldschmiedt, G. Haber, G. Kandel, P. Kortan, and N. Marcon, "A safety maneuver for placing overtubes during endoscopic variceal ligation," Gastrointest. Endosc., vol. 38, no. 3, pp. 399–400, May 1992..
[6] "Technology Status Evaluation Report: Endoscopic Retrieval Devices," Gastrointest. Endosc., vol. 50, no. 6, pp. 932–934, Dec. 1999.
[7] F. Putzu, T. Abrar, and K. Althoefer, "Plant-Inspired Soft Pneumatic Eversion Robot," in 2018 7th IEEE International Conference on Biomedical Robotics and Biomechatronics (Biorob), Enschede, Netherlands, 2018, pp. 1327–1332.
[8] J. Greer, T. Morimoto, A. Okamura and E. Hawkes, "A Soft, Steerable Continuum Robot That Grows via Tip Extension", Soft Robotics, vol. 6, no. 1, pp. 95-108, 2019. Available: 10.1089/soro.2018.0034.

Design of a Robotic Balloon-catheter Endoscope for Sinus Procedures

Yingtian Li[1], Reza Rahbar[2], Pierre E. Dupont[1, a]
[1]Cardiovascular Surgery, Boston Children's Hospital, Harvard Medical School,
[2]Department of Otolaryngology, Boston Children's Hospital, Harvard Medical School
[a]Pierre.Dupont@childrens.harvard.edu (DOI10.31256/HSMR2019.5)

INTRODUCTION

Over 30 million cases of Chronic RhinoSinusitis (CRS) occur annually in the U.S. [1, 2]. This condition involves blockage of the sinuses resulting in accumulation of mucus, pain and susceptibility to infection. Diagnosis often involves transnasal endoscopic examination of the sinuses. Subsequent treatment can also involve endoscopically-guided balloon dilation of the sinus ostia. This procedure, balloon catheter sinuplasty (BCS), has proven to be feasible, safe and effective [3], and the trend to perform this technique in treating CRS has largely increased in recent years [4].

The procedure can be challenging to perform, however, since endoscopic inspection of the airways (seeing around corners) as well as endoscopically-guided balloon positioning remain awkward (Fig. 1a). To address these challenges, transcutaneous illumination is often used to confirm the balloon catheter is properly placed before inflating the balloon [5]. And although there are flexible endoscopes on the market, poor imaging quality has limited their adoption.

Toward addressing this need, this paper introduces a concept for a multi-segment endoscopic balloon catheter that is able to crawl through the sinuses. The scalable robot design is described along with experiments that demonstrate that it can crawl through flexible lubricated tubes and navigate through a simplified model of the nasal passages while providing an endoscopic view of its path.

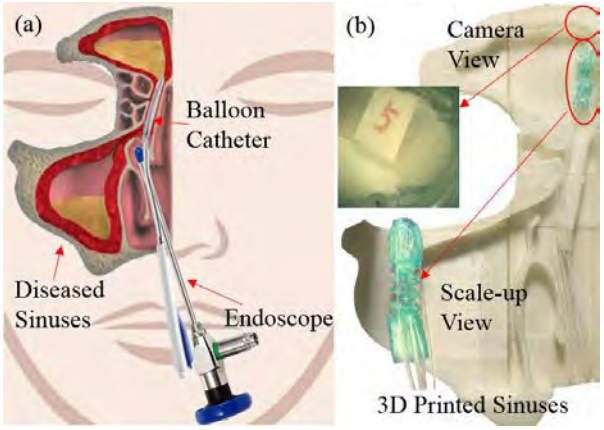

Fig. 1. Balloon catheter Sinuplasty (BCS) used to open blocked sinus ostia. (a) Current procedure – rigid endoscope is used to guide balloon catheter into ostia. (b) Robotic endoscope navigating through model of sinuses to reach frontal sinus. Chip camera mounted on balloon-catheter robot provides tip view during navigation.

MATERIALS AND METHODS

The proposed design, different from the other crawling medical robots [6 - 8], is comprised of two buckling balloons as anchor units connected by a linearly-expanding balloon as the actuator unit to control the movement. The distal buckling balloon can also be used for dilation of the sinus ostia. The prototype and the design parameters are shown in Fig. 2. This prototype was built at 2X scale to facilitate fabrication and testing.

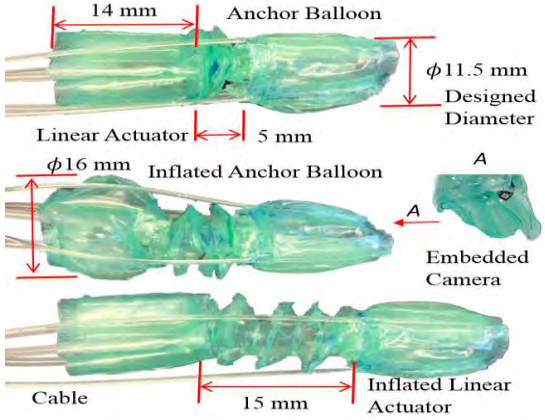

Fig. 2. Robotic balloon-catheter endoscope. Locomotion is achieved by first expanding the linear-actuator balloon when the proximal anchor balloon is inflated and the distal anchor balloon is deflated. Next, the distal balloon is inflated, the proximal balloon is deflated and then the linear actuator is deflated.

The three balloon units, fabricated as shown in Fig. 3, are made of a soft polyethylene membrane (Pregis Corp.) with a camera embedded in the distal anchor balloon. The robot has a tether comprised of three 2mm OD silicone tubes for inflating and deflating the balloons and wiring for the camera. In the current prototype, the tether also includes nylon tendons for steering the distal anchor balloon. Future versions will employ differential inflation of balloon chambers to produce steering.

One full cycle of forward locomotion is comprised of the six steps. The steps consist of sequentially inflating the proximal anchor, linear actuator and the distal anchor and then sequentially deflating the proximal anchor, the linear actuator and the distal anchor. To execute turning of the distal section for visualization of the workspace or for navigating around a corner, the proximal anchor is inflated and the distal anchor is

deflated. Differential tension is applied to the tendons to achieve the desired bending. To lock in the tip direction, the distal anchor is then inflated.

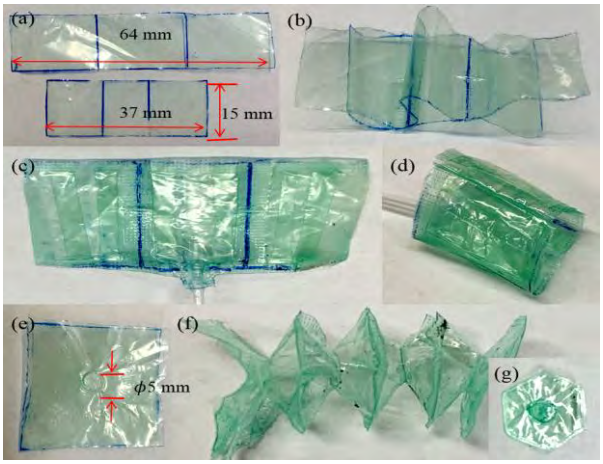

Fig. 3. Balloon fabrication. (a) Anchor balloon is made from two pieces of membrane. (b) Heat sealing on marker lines creates three chambers. (c) Chambers are sealed on proximal and distal edges. (d) Chambers are sealed longitudinally to create cylindrical balloon. (e) Linear actuator is fabricated from 8 chambers sealed to each other around circular 5mm diameter port. (f) Connected chambers. (g) Final chamber shape is hexagonal.

To evaluate the prototype, we tested its ability to locomote through three environments. The first experiment consisted of crawling through a rigid tube. Since tissues are soft, we next tested the system inside a thin flexible silicone tube. In both cases, we lubricated the interior of the tubes to mimic the slipperiness of mucus-lined passages. Finally, we tested the ability of the system to navigate inside the curved passages of a phantom model of the sinuses.

RESULTS

Robot control was performed via sequential inflation and deflation of the balloons via control tubes attached to syringes. Inflation / deflation times for all balloons is less than one second and there was no observable delay time between syringe motion and balloon response.

Fig. 4 presents the three experiments conducted for evaluating the robot. Syringe operation was performed manually and was the limiting factor with respect to robot speed, which averaged 1.5mm/sec. We are currently implementing microprocessor control of motorized syringe actuation. We demonstrated navigation to the frontal sinus in our phantom model, which required the robot to make turns. The current prototype can produce follow curves with a 35mm radius of curvature.

DISCUSSION

This paper provides proof of concept results for the design of an endoscopic balloon catheter for navigating in the sinuses. We demonstrated the ability to crawl inside lubricated soft tubes and in a model of the sinus passages.

The use of a soft robotic balloon with integrated sensing can provide a number of advantages over the current approach in which a rigid endoscope is inserted in parallel with a standard balloon catheter. The robotic balloon endoscope can traverse the sinuses with minimal trauma while providing the ability to both visualize and navigate around corners. Furthermore, the robot can also be used to perform balloon dilation inside the sinuses with the embedded camera providing accurate localization of the dilation.

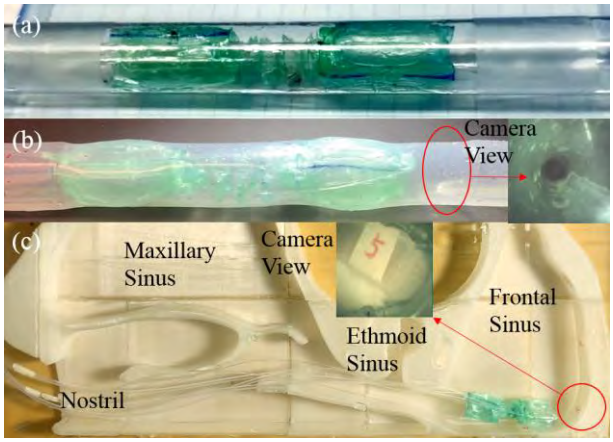

Fig. 4. Experimental results. (a) Crawling through a lubricated, but rigid tube. (b) Crawling through a lubricated soft silicone tube. (c) Balloon catheter navigating to the frontal sinus in a 3D-printed planar model of the sinuses.

ACKNOWLEDGEMENTS

This work was supported by the National Institutes of Health under grant R21HD089136.

REFERENCES

[1] Makary CA, Ramadan HH. Sinus and Upper Airway Surgery in Children. Current allergy and asthma reports. 2018 18:1-5.

[2] https://www.energiasmarketresearch.com/global-sinusitis-treatment-market-outlook

[3] Ramadan HH. Safety and feasibility of balloon sinuplasty for treatment of chronic rhinosinusitis in children. Annals of Otology, Rhinology & Laryngology. 2009 118(3):161-165.

[4] Svider PF. Evolving trends in sinus surgery: what is the impact of balloon sinus dilation? The Laryngoscope. 2018 128(6):1299-1303.

[5] Makary CA, Ramadan HH. Balloon catheter sinuplasty in pediatric chronic rhinosinusitis. Operative Techniques in Otolaryngology-Head and Neck Surgery. 2018 29(2):94-98.

[6] Dario P et al. A microrobotic system for colonoscopy. Proc Int Conf Robot Auto. 1997 2:1567-1572.

[7] Patronik NA et al. Crawling on the heart: A mobile robotic device for minimally invasive cardiac interventions. Int Conf Med Image Comput Comput Assist Interv. 2004: 9-16.

[8] Gilbertson MD et al. Soft passive valves for serial actuation in a soft hydraulic robotic catheter. J. Med Devices. 2016 10(3):030931.

Robotic intravascular suturing for endovascular repair

Estevan H. Murai[1], Daniel Martins[1], Pierre G. Silveira[2], Jian S. Dai[3], Shervanthi Homer-Vanniasinkam[4], Helge A. Wurdemann[4]

[1]*Mechanical Engineering, Federal University of Santa Catarina, Florianópolis, Brazil,*

[2]*Surgery Department, Federal University of Santa Catarina, Florianópolis, Brazil,*

[3]*Department of Informatics, King's College London, United Kingdom,*

[4]*Department of Mechanical Engineering, University College London, United Kingdom*
h.wurdemann@ucl.ac.uk (DOI10.31256/HSMR2019.6)

INTRODUCTION

Abdominal aortic aneurysm (AAA) is a disease of the human's main blood vessel causing the artery to bulge and eventually burst, causing life-threatening bleeding. The aorta can be repaired either through open surgery or Minimally Invasive Surgery (MIS) with the use of an endovascular stent graft [1]. Endovascular Aneurysm Repair (EVAR) has become the preferred minimally invasive AAA treatment due to advantages over open surgery including less blood loss, shorter surgery time and reduced mortality within the first 30 days [2]. However, patients that undergo an EVAR procedure are subject to long-term complications, such as stent-graft migration [3]. A stent graft migration can lead to loss of fixation and Type I endoleaks. The number of affected patients has decreased from 3-28% [1] to about 8.6% in recent years due to aortic stent-grafts with proximal fixation [4]. However, studies show that reinterventions are required for ca. 24% of patients [5] and hand-sewn anastomosis (conducted in open surgery) outperforms any stent design with proximal fixation [6].

In this work, we propose a novel design of a collaborative suturing catheter for EVAR allowing single-sided suturing during a minimally invasive intervention. The device has great potential to deliver a continuous suturing pattern around the artery circumference inside the aortic root (see Figure 1). Here, we describe the robotic mechanism of a large-scale suturing catheter module to demonstrate its feasibility.

MATERIALS AND METHODS

Our suturing device consists of two modules/parts as shown in Figure 1: a suturing and positioning catheter module. Each module is mounted onto a catheter tip and inserted through the femoral arteries on each side of the groin into the abdominal aorta. The large-scale prototype of the positioning module has a length of 95 mm serving two purposes: (i) The tip acts as an anchor to the aortic wall and has a partly hollow, cylindrical structure (diameter: 85 mm) allowing blood flow during the suturing procedure; (ii) The shaft of the positioning module (diameter: 30 mm) is equipped with an embedded actuated rotary joint with a platform made of ferromagnetic material on one side.

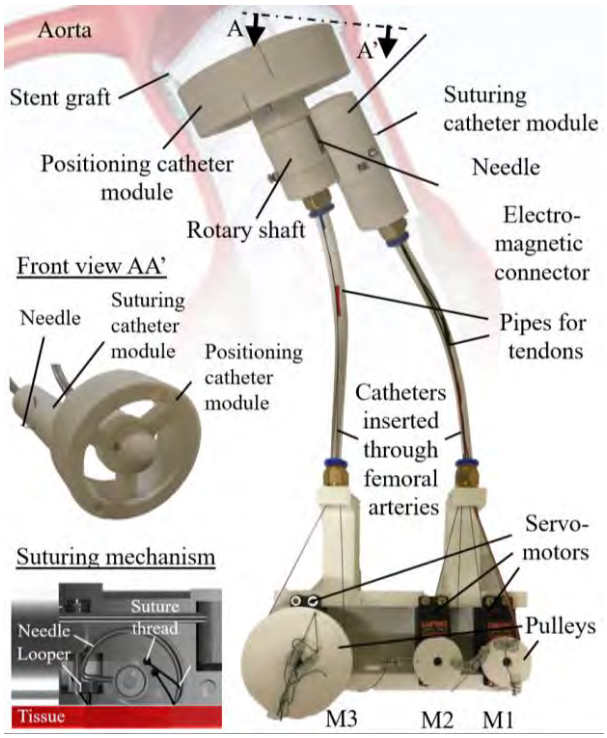

Fig. 1 Modular suturing system composed of a positioning and suturing catheter module. Each module can be inserted through the femoral arteries into the abdominal aorta where the device assembles. The top and front (small figure) view of the large-scale prototype of the modular suturing catheter shows the rotary shaft and suturing mechanism which are tendon-driven and integrated in a robotic pulley system.

The suturing catheter module connects to this platform via an electromagnetic component integrated inside the suturing module. During the suturing process, the positioning catheter provides a stable location for the suturing catheter module allowing a full rotation around the shaft of the positioning module. This prototype is made of Polylactic Acid (PLA) using an Ultimaker 2. Hence, the tip (anchor) of the positioning module is entirely rigid. It is envisaged to replace this part with a soft inflatable robot to allow size reductions to the diameter of the module's shaft when inserting and retrieving this catheter module.

The suturing catheter module builds on our previous work in [7] creating new kinematic structures for a single, one-sided stitching device. Here, our prototype

has a length of 90 mm and diameter of 30 mm. An embedded electromagnet (Uxcell XRN-XP DC 12 V 2.5 kgf) is integrated into the tip connecting the suturing module to the ferromagnetic platform of the positioning module. The needle has a semi-circular shape rotating via its center point. The eye of the needle is located at the tip of the needle feeding the suture thread into the looper. The looper has an arc shape rotating around an axis passing through the arc center point. Protrusions on the looper arc secure the suture thread and keep the loop open so the needle passes inside the loop. The suturing module is made of Selective Laser Sintering (SLS) fabricated by a FORMIGA P 110, EOS.

The suturing module follows a four-step process to perform one stitch: The default set-up of the module is shown in Figure 1 (bottom left), where the needle is inside the device and a suture thread is fed through the eye and forms an initial loop through the looper. The needle then rotates through the tissue until a reaches the looper where a new loop is created. During the final step, the needle returns to the default position.

RESULTS

The large-scale suturing catheter shown in Figure 1 is experimentally validated inside a large-scale aorta phantom environment which has a cylindrical shape with a diameter of 80 mm, length of 150 mm and thickness of 2.2 mm (see Figure 2(a)). The phantom was made of Ecoflex 00-30 silicone (Smooth-On, Inc., Easton, PA). The suturing device is inserted into the phantom vessel. All experiments are performed with a 5/0 monofilament polypropylene suture thread using a sample of a Uni-Graft KDV by B. Braun.

After the suturing catheter performed a number of stitches, the phantom vessel was cut along the longitudinal axis to assess the suture pattern. Figures 2(b)-(c) show the experimental results. The catheter performed five stitches along 30 mm of the vessel circumference. Each stitch has been successfully executed creating a sequence of intersecting loops. Using an electronic scale, the strength of the suture was measured. The suture was able to withstand forces of 17.45 N before the suture ruptured.

The experiments showed that the large-scale suturing catheter is able to successfully perform a suture pattern inside a phantom vessel. The positioning module provides stability for the suturing module. Even with a few stitches along a short length, the suture strength performs better than a number of self-fixed stent-grafts.

DISCUSSION

This paper has presented the novel design, development and testing of a new suturing catheter for EVAR allowing single-sided suturing in a minimally invasive way. Future work will aim to reduce this large-scale prototype so that the final diameter of the catheter is within 7 mm. This includes the creation of a soft robotic mechanism/structure for the positioning module that can be crimped or folded when introducing the catheter into the femoral artery and, then, inflated inside the aorta.

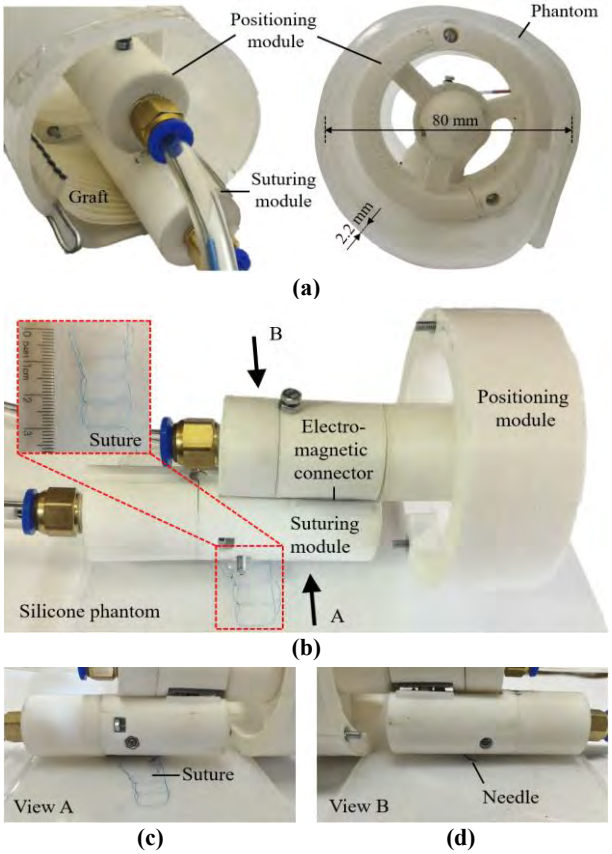

Fig. 2 (a) Experimental setup with the suturing catheter inside a phantom vessel made of Ecoflex 00-30 silicone. (b) Side view of the suturing catheter with the open phantom vessel. Close-up side views show (c) the successful suture and (d) the insertion of the needle into the phantom..

ACKNOWLEDGEMENT

This work is supported by the Engineering and Physical Sciences Research Council (EP/S014039/1) and by the Springboard Award of the Academy of Medical Sciences (SBF003-1109).

REFERENCES

[1] E.J. Waasdorp et al., The association between iliac fixation and proximal stent-graft migration during EVAR follow-up: Mid-term results of 154 talent devices, Eur. J. Vasc. Endovasc. Surg., vol. 37(6), pp. 681-687, 2009.

[2] F.A. Lederle et al., Open Versus Endovascular Repair (OVER) Veterans Affairs Cooperative Study Group FT. Outcomes following endovascular vs open repair of Abdominal Aortic Aneurysm: A Randomized Trial, J. Am. Med. Assoc., vol. 302(14), pp.1535-1542, 2009.

[3] The UK EVAR Trial Investigators, Endovascular versus open repair of Abdominal Aortic Aneurysm, N. Engl. J. Med., vol. 362(20), pp. 1863-1871, 2010.

[4] K. Spanos et al., Systematic review and meta-analysis of migration after endovascular Abdominal Aortic Aneurysm repair, Vascular, vol. 24(3), pp.323-336, 2016.

[5] A. Kaladji, et al., Long-Term Results of Large stent grafts to treat Abdominal Aortic Aneurysms, Ann. Vasc. Surg., vol. 29(7), pp. 1416-1425, 2015.

[6] T. Resch, et al., The impact of stent design on proximal stent-graft fixation in the abdominal aorta: an experimental study, Eur. J. Vasc. Endovasc. Surg., vol.20(2), pp. 190-195, 2000.

[7] E.H. Murai, H. Simas, D. Martins, New kinematic structures for one-side stitching devices, ABCM Int. Congress of Mechanical Engineering, 2015.

Automatic Bone Extraction from Depth Images in Robotic Assisted Knee Replacement

He Liu, Ferdinando Rodriguez y Baena

Mechatronics in Medicine Laboratory, Imperial College London
he.liu15@imperial.ac.uk (DOI10.31256/HSMR2019.7)

INTRODUCTION

The geometry of the bone surface plays an important role in registration for robotic assisted knee replacement. In order to map out the bone surface, an optically tracked probe is often used to collect points on the bone surface. Since this procedure is done manually by the surgeon, the surface points cannot be updated in real time. To solve this problem, most of the commercial orthopaedic robot systems, such as Mako (Stryker Corp.) and Navio (Smith & Nephew PLC), require optical markers inserted into the target bones so that the registration result is projected into the marker frame to enable real-time updates. However, the insertion of markers into the bone inevitably increases the operating time and may result in complications such as infection and fracture [1][2].

Depth sensing, with the ability of real-time spatial mapping, can free surgeons from having to manually scan the bone surface using a digitising probe. The high mapping frequency also makes it possible to track the target bone in real time without the need for markers. However, depth sensing captures the whole geometry of the environment it can see, so correctly extracting the part that needs to be tracked represents the key to adoption for depth sensing in orthopaedic registration.

In this paper, we aim to realise automatic segmentation of depth images of the surgical site in order to extract the bone surface geometry for registration. In recent years, deep learning has achieved state-of-the-art performances in image processing tasks such as image classification, segmentation, and object detection [3][4][5]. Our segmentation method is thus based on deep learning. We collected and labelled depth images from a cadaveric knee for network training.

MATERIALS AND METHODS

A depth image is a map describing the spatial geometry of the environment. Like RGB images, a depth image is also a matrix of pixels, or points, each of which contains three values. But the values of a pixel are the x, y and z coordinates of that point relative to the depth camera rather than RGB channels. As depth images and RGB images share the same data structure, the deep learning network for depth image segmentation can adopt the architectures that perform well on RGB images. However, as a relatively new imaging modality, depth sensing does not have many labelled datasets, and those for medical purposes are even fewer. Thus, a suitable depth image dataset for network training is first required.

To obtain the reference structure for the knee joint, we used a depth camera (Intel RealSense D415) to collect depth images from a cadaveric knee. Our application for access to human tissue samples was approved by the tissue bank of Imperial College. A normal incision was made over the front of the knee and the patella was pushed aside to expose the distal femur. We changed the position and angle of the knee several times during image collection and took depth images from different positions to increase the diversity of the data. These depth images were labelled by adding a fourth value to each pixel, with 1 representing the pixel is on the femur and 0 otherwise, and data augmentation by flipping and rotation was applied. The dataset contains more than 2,000 labelled depth images and is randomly divided into three groups for network training, validation and testing.

The deep learning network we built for depth image segmentation adopts the architecture called “U-Net” [6], which is a fully convolutional network that has a symmetric U shape, as shown in Fig. 1. On the left side are typical convolutional and pooling layers that increase features and contract resolution, while the right side contains deconvolutional layers to increase resolution, which are then concatenated with high resolution features from the left side to assemble a more precise output. The last layer is a 1×1 convolutional layer with a sigmoid activation which maps all the features of a pixel to a value between 0 and 1, which represents the probability of that pixel belonging to the femur. The loss function is defined as the mean of the squared pixel errors. The network is implemented using TensorFlow [7], and the Adam optimiser [8] is used for training.

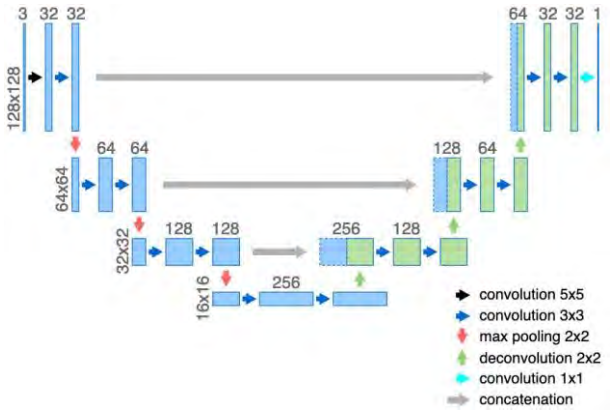

Fig. 1 Network architecture for depth image segmentation. The horizontal numbers are the channel numbers of the feature maps, and the vertical numbers are their resolutions. The input is a 128×128 depth image, and the output is the prediction mask with the same resolution.

RESULTS

After training the segmentation network for 250 epochs, the validation error stopped decreasing. The last part of the labelled dataset was used to test the segmentation performance. A mean loss of 0.0082 was achieved, and to calculate the segmentation accuracy, the output masks were converted to binary by using a pixel threshold of 0.5. The average dice similarity coefficient (DSC) between the output masks and the labels is 92.8%. Fig. 2 shows the segmentation results of some depth images chosen from the testing dataset.

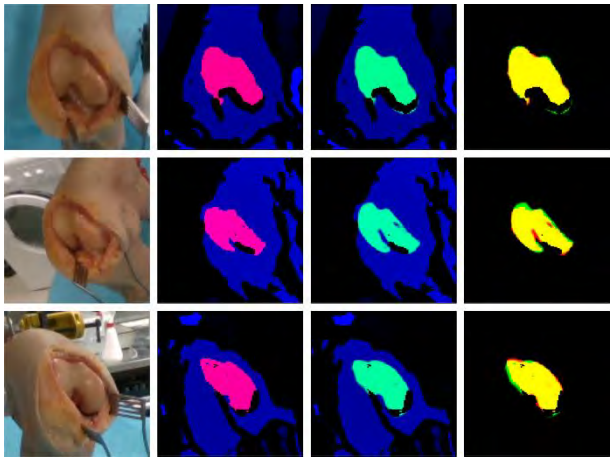

Fig. 2 Segmentation results of the depth images. Three rows are three group of results from different viewing positions. First column: RGB images of the knee joint. Second column: the depth images (blue) with labelled points (ground truths, magenta). Third column: the depth images (blue) with predicted femur points (cyan). Fourth column: the ground truths (red), the predictions (green) and their overlays (yellow).

DISCUSSION

In this paper, we proposed a deep learning based segmentation method for depth images of the knee anatomy. A fully convolutional network was built for end-to-end segmentation, and the training dataset was collected from a cadaveric knee. After training, the segmentation network performed well on testing data, with an average DSC of 92.8%.

Segmentation is important for medical image analysis as it identifies the target anatomical structure for further diagnosis or treatment plan. Studies on deep-learning based segmentation of medical images such as MRI and CT scans have achieved promising accuracy. For example, Roth et al. [9] achieved an overall accuracy of 89.3% (DSC) on CT segmentation using a fully convolutional network. Bao et al. [10] used a multi-scale patch-wise convolutional network for brain MRI segmentation and achieved an overall DSC of 85%. Using a similar 'V-Net' architecture, Milletari et al. [11] achieved an average DSC of 86.9% on segmentation of prostate MRI scans. Although our result cannot be compared with the results of other studies directly due to different imaging modalities and different datasets, the segmentation accuracy looks promising. As the purpose of our depth image segmentation is for intra-operative orthopaedic registration, the final assessment of the segmentation can be obtained in further registration experiments.

The main limitation of this study is the lack of labelled data. As a new imaging modality, depth imaging is still rarely applied in medicine, despite its potential to reconstruct anatomical structures in real time. To our knowledge, this is the first study on segmentation of depth images of the surgical scene, which means a training dataset had to be generated specifically for this study. Although real human specimens were used and data augmentation was conducted, the data may still be somewhat artificial and not sufficiently diverse. Given more data from real surgical scenarios, the segmentation results could be more reliable and convincing.

REFERENCES

[1] Kamara E, Berliner ZP, Hepinstall MS, Cooper HJ. Pin site complications associated with computer-assisted navigation in hip and knee arthroplasty. The Journal of arthroplasty. 2017 Sep 1;32(9):2842-6.

[2] Wysocki RW, Sheinkop MB, Virkus WW, Della Valle CJ. Femoral fracture through a previous pin site after computer-assisted total knee arthroplasty. The Journal of arthroplasty. 2008 Apr 1;23(3):462-5.

[3] He K, Zhang X, Ren S, Sun J. Deep residual learning for image recognition. In Proceedings of the IEEE conference on computer vision and pattern recognition 2016 (pp. 770-778).

[4] Long J, Shelhamer E, Darrell T. Fully convolutional networks for semantic segmentation. In Proceedings of the IEEE conference on computer vision and pattern recognition 2015 (pp. 3431-3440).

[5] Ren S, He K, Girshick R, Sun J. Faster r-cnn: Towards real-time object detection with region proposal networks. In Advances in neural information processing systems 2015 (pp. 91-99).

[6] Ronneberger O, Fischer P, Brox T. U-net: Convolutional networks for biomedical image segmentation. In International Conference on Medical image computing and computer-assisted intervention 2015 Oct 5 (pp. 234-241).

[7] Abadi M, Barham P, Chen J, Chen Z, Davis A, Dean J, Devin M, Ghemawat S, Irving G, Isard M, Kudlur M. Tensorflow: A system for large-scale machine learning. In 12th {USENIX} Symposium on Operating Systems Design and Implementation 2016 (pp. 265-283).

[8] Kingma DP, Ba J. Adam: A method for stochastic optimization. arXiv preprint arXiv:1412.6980. 2014 Dec 22.

[9] Roth HR, Shen C, Oda H, Oda M, Hayashi Y, Misawa K, Mori K. Deep learning and its application to medical image segmentation. Medical Imaging Technology. 2018;36(2):63-71.

[10] Bao S, Chung AC. Multi-scale structured CNN with label consistency for brain MR image segmentation. Computer Methods in Biomechanics and Biomedical Engineering: Imaging & Visualization. 2018 Jan 2;6(1):113-7.

[11] Milletari F, Navab N, Ahmadi SA. V-net: Fully convolutional neural networks for volumetric medical image segmentation. In 2016 Fourth International Conference on 3D Vision (3DV) 2016 Oct 25 (pp. 565-571). IEEE.

From Benchtop to Operating Room: The Evolution of the Galen Platform

Y. Sevimli[1], D. Levi[1], A. Bhat[1], O. Puleo[1], R.H. Taylor[2], D. Saunders[1]

[1]Galen Robotics, Inc., [2]Laboratory for Computational Sensing and Robotics, Johns Hopkins University

[yunus.sevimli, david.levi, ashwin.bhat, olivia.puleo, dave.saunders]@galenrobotics.com, rht@jhu.edu

(DOI10.31256/HSMR2019.8)

INTRODUCTION

The Galen is a cooperatively-controlled robotic platform designed for precise microsurgery [1]. With the aid of hand tremor cancellation and adaptable geometric constraints the system has the potential of enabling the wider use of minimally invasive surgery (MIS) with inherent benefits for the patient and surgeon. Intuitive operation, small footprint and ability to work with standard surgical instruments lead to minimal disturbance to the established workflows [1]. These benefits make the Galen a versatile robotic platform for multiple disciplines, including otolaryngology, neurosurgery and similar fields where high-precision and accuracy are crucial.

Conceptualized at Johns Hopkins University (JHU) and licensed for commercial development by Galen Robotics, Inc. in 2016, the system has undergone a series of design improvements on the path to commercialization. This paper explores this transition of the Galen Platform from the lab bench to the OR as well as the technical, market and user-driven factors that guided the design process.

Disclaimer: *The Galen platform is under development by Galen Robotics, Inc. and is not for commercial sale.*

DESIGN PROCESS

1- Robotic ENT Microsurgery System (REMS)

a) Needs identification

The REMS was designed to address the challenges in minimally invasive otolaryngology procedures. Delicate and millimeter-scale anatomy is often accessed through natural orifices or by drilling through bone concealing highly-sensitive anatomy. Manipulation of these delicate structures requires extreme caution as hand tremor and accidental contact with other anatomies can create adverse complications. These risks, amplified by difficult ergonomics and prolonged procedures, may overweigh the potential benefits of certain interventions.

b) Implementation

Developed at the JHU LCSR, the REMS is the initial surgical robot prototype for ENT in the Galen family. While the core technology of cooperatively controlled "steady-hand" robots is well established, the REMS is the first application of this technology in otolaryngology, to our knowledge [1]. The REMS incorporates five degrees-of-freedom (DOF) for manipulation of standard surgical instruments: two one-DOF rotational stages are connected to a delta parallel system for three-DOF Cartesian positioning. The overall size of the REMS was determined by its work volume which is roughly the size of a human skull. In order to demonstrate different surgical setups, the REMS was integrated onto the Preoperative Positioning System (PPS) that allowed the work volume of the REMS to be aligned with the surgical site using a motorized frame [2].

Fig. 1, 2 Standalone REMS (left) and REMS + PPS (right)

c) Evaluation

The REMS has been tested through several cadaver and phantom-based studies that simulated microlaryngeal surgery, sinus surgery and vessel anastomosis. A few prior publications have addressed the resolution, accuracy, stiffness and disruption to existing surgical workflows [1-3]. The robot achieved 0.140 mm translational and 0.0011 rad mean error after calibration [1]. It has also been shown that the REMS improved the peer-reviewed performance of novice surgeons during an anastomosis task by more than threefold [1]. The results of these studies, along with the personal reviews by around 100 surgeons have led to the following conclusions:

- The assumed needs have been verified: Certain otolaryngology interventions are error-prone, require difficult ergonomics and are too time consuming.
- The REMS serves as a valid test-bed to demonstrate the benefits of robotic assistance in otolaryngology surgeries, including decreased error rates, improved ergonomics and time savings.

2- Galen Mk. 1

a) Needs identification

Following commercialization, a new market research effort, backed by surgeon reviews outside otolaryngology revealed that the underlying technology of the REMS could also be useful in other disciplines, including spine and neurosurgery. These procedures often deal with larger anatomies and may require heavier instruments than those used in ENT. These findings, along with the identified improvements to user interface, mobility and cosmetics drove the design of the next prototype: *Galen Mk. 1*.

b) Implementation

In order to meet the larger spatial and force requirements of spine and neurosurgery, the design of Galen Mk.1 included sturdier structural elements, higher performance actuators, as well as a 250% larger work volume over the REMS. Furthermore, the following design changes were

implemented to improve the user experience and workflow:

- Non-motorized, weight-balanced PPS for more intuitive coarse positioning
- All electronics self-contained within the robot body
- Adjustable touch screen for user interface
- Skins for easy cleaning

Fig. 3, 4 Galen Mk. 1 concept and implementation

c) Evaluation

The Galen Mk. 1 was demonstrated to more than 80 international surgeons at the 2017 American Academy of Otolaryngology (AAO) Annual Meeting in Chicago, IL. The reception was positive particularly in reference to the robot's feel and performance. The main criticisms were the large footprint and the compliance of the PPS.

The robot has been shown to reduce unwanted tool-to-tissue forces that cause complications in microsurgery. In a study that measured lateral forces applied to the incus during placement and crimping of a stapes prosthesis, a decrease from 469.3 to 272.2 mN during crimping was reported when using the robot versus freehand [4].

3- Galen Mk. 2

a) Needs identification

Having the market needs and the potential benefits of the system reverified by a larger and more diverse sample of users, the next step towards a commercial medical device involved the determination of the requirements and a Failure Mode and Effects Analysis (FMEA) in compliance with the FDA regulations. In addition to design improvements to comply with these regulations, the next prototype also needed an overhaul of the PPS to alleviate the user criticism relating to the large footprint, insufficient stiffness and the time-consuming coarse position adjustment process.

Fig. 5, 6 Galen Mk. 2 concept and implementation

b) Implementation

The third-generation prototype of the robotic platform, the Galen Mk. 2 has completely eliminated the PPS for coarse positioning. Instead, the active delta stage was enlarged accordingly to make up for it. The resulting system is simpler, stiffer and has a smaller footprint.

In order to mitigate the identified hazards and satisfy regulatory requirements the new design includes safety circuits, joint brakes and redundant encoders on all axes. Finally, a new force sensor accommodates larger loads, allowing for a broader set of applications.

c) Evaluation

Several studies are in progress using the Mk. 2 to evaluate its utility in otolaryngology as well as in neurosurgery and orthopedics. Verification tests and early cadaveric studies have shown improved utility over its predecessors due to increased work volume, repeatability and stiffness.

Fig. 7 Cadaveric transoral thyroidectomy study with Mk. 2

DISCUSSION

Through the translational research efforts and the consequent commercial development, the Galen's potential in overcoming the challenges of minimally invasive otolaryngology surgeries has been demonstrated. To hit the next milestone of human trials, the development will be focused on regulatory compliance and integration into established hospital workflows. The team has identified design improvements in sterility, usability and maintainability, accordingly.

Close coordination between engineers and surgeons has been instrumental in navigating Galen's path from the lab bench to the OR. The authors believe that the many discoveries and setbacks along the way will be well justified in helping real patients.

REFERENCES

[1] Olds KC. Robotic Assistant Systems for Otolaryngology-Head and Neck Surgery. Ph.D Thesis, The Johns Hopkins University, 2008

[2] Sevimli Y, Wilkening P, Feng L, Balicki M, Olds KC, Keady T, Taylor RH. Surgical Workflow Integration of the Robotic ENT Microsurgical System. Hamlyn Symposium in Medical Robotics, London, June 2016.

[3] Feng L, Wilkening P, Sevimli Y, Balicki M, Olds K C, Taylor RH. Accuracy Assessment and Kinematic Calibration of the Robotic Endoscopic Microsurgical System. 38th Annual International Conference of the IEEE Engineering in Medicine and Biology Society (EMBC), Orlando, FL, August 2016.

[4] Razavi CR, Wilkening PR, Yin R, Lamaison N, Taylor RH, Carey JP, Creighton FX. Applied Force during Piston Prosthesis Placement in a 3D-Printed Model: Freehand vs Robot-Assisted Techniques. Otolaryngology Head and Neck Surgery, 2019 160(2), 320-325.

How to enhance learning of robotic surgery gestures? A tactile cue saliency investigation for 3D hand guidance

Gustavo D. Gil[1], Julie M. Walker[2], Nabil Zemiti[1], Allison M. Okamura[2], Philippe Poignet[1]

[1] *LIRMM, University of Montpellier, CNRS, Montpellier, France*

[2] *Department of Mechanical Engineering, Stanford University, Stanford, CA 94305, USA*

gustavo.gil@lirmm.fr (DOI10.31256/HSMR2019.9)

INTRODUCTION

The current generation of surgeons requires extensive training in teleoperation to develop specific dexterous skills, which are independent of medical knowledge. Training curricula progress from manipulation tasks to simulated surgical tasks [1]–[3] but are limited in time due to the need for proper mentoring for each trainee.

We propose to integrate surgical robotic training together with Haptic Feedback (HF), as is illustrated in Fig. 1. The reason is that a good use of HF during training can improve skill acquisition [4]–[7].

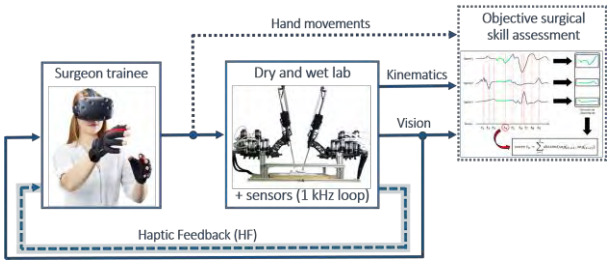

Figure 1. Full dry and wet lab approach (non-clinical setup) of our complete robotic surgery training system. During the execution of the surgical gestures the highlighted haptic feedback loop transmit to the surgeon trainee timely information about his/her performance.

In this paper we introduce an exploratory work on a portable haptic device designed to offer hand guidance in 3D space. The idea is that the HF can be felt by the trainee "as if" a force was directing his/her entire hand through of the surgical gesture execution.

Mainly, we create HF signals by stretching the skin of a pair of fingers (e.g., Thumb-Index). Our haptic device acts on the *finger pads* of the *fingertips* (see Fig. 2), in order to stimulate the cutaneous mechanoreceptors.

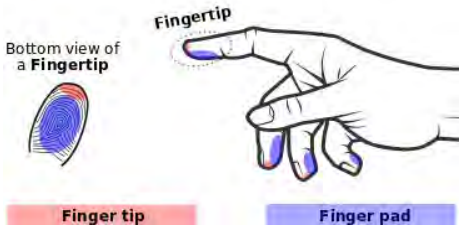

Figure 2. The colored areas indicate the jargon for different zones of the human fingertips (i.e., finger tip and finger pad).

MATERIALS AND METHODS

The device consists of a pair of servomotors mounted in a 3D printed handle, as shown in Fig. 3. Each motor rotates a lever arm to stimulate the trainee's finger pads of the thumb and index distal phalanges, while the trainee holds it in his/her hand.

The stimulations, called *haptic signals*, consist of to stretch the skin on the finger pads by rotating through a semicircular arc (see schema in Fig. 3). Thus, different movements of the arms give to the user the sensation that their hand is being pulled in certain directions. We called these senstations *haptic cues*.

Figure 3. Scheme for one actuator of the haptic device (working principle) and views of the entire device.

The experiment presented here aims to identify two key aspects: (1) cue saliencies or cue clarity; and (2) if there is a common perception of tactile cues between users. The first aspect is related to stimulus-cue repeatability by the users, while the second one is related to the identification of a common stimulus-cue set among different users.

We investigate the feasibility to induce three types of hand movements, or 3 Degrees of Freedom (DoF). Namely: right/left wrist twisting; hand moving forward/backward; and hand tilting up/down.

The experiment involved 8 right-handed engineers. 24 different stimuli were applied in a pseudorandom sequence of 240 stimuli per trial (each stimulus 10 times). Trials included two time breaks in order to release the device, relax the hand, and continue the experiment.

For each *haptic signal* (i.e., stimulation induced), users reported the cue felt from six empirically predetermined options: (1-2) hand moving Forward/Backward; (3-4) Tilt Up/Down; and (5-6) Twist Left/Right.

During the trial, the users trigger each haptic stimulus by using a key of a computer keyboard. Then, the cue felt was reported by a "number key" assigned.
Sumarizing the test method, we executed a system identification procedure to investigate the responses of the tactile sense of each user. Our aim was to identify stimuli-cues that can be used as commands to guide the user's hand in 6 different directions (i.e., in 3 DoF).

RESULTS

Each trial took about 45 minutes plus extra time for the familiarization with the procedure. People were constrained to select between 6 possible directions. It was noticeable that most of the time participants chose a direction after triggering each stimulus just 1 or 2 times.
The multidimensional nature of the results is expressed by colored marks in a two-dimensional map (Fig. 4). The meaning of the features of this map are:

- the colors encode the type of cue most often selected by the users (e.g., hand pulled Forward/Backward, hand Tilt Up/Down, and hand Twist Left/ Right).
- the x-y location of each mark corresponds to a combination of angular displacement for each servomotor (stimulus related).
- the mark size represents the cue saliency or cue clarity. The bigger diamonds correspond to the most salient cues.

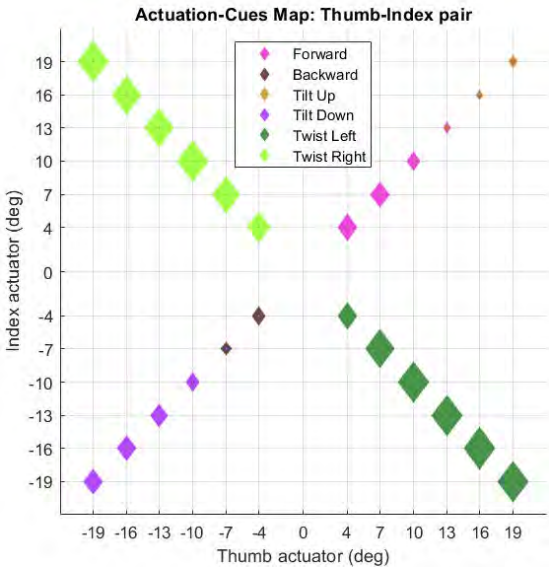

Figure 4. Cues identified by 8 users in the exploratory experiment. The mark size relates to cue saliency, the color to cue type, and the location to stimulus direction and magnitude (servomotor actuation).

From the data obtained in this exploratory study, we can agree that the device is able to induce at least two clear tactile cues, called hand Twist Left and hand Twist Right. These two cues are very salient for several combinations of servomotor values (see the 2nd and 4th quadrants of the Actuation-Cues Map), identified more than 85% of the time.

Conversely, the cues labeled as hand Tilt Up and hand moves Backward, are not as salient but are present. For the remaining cues, hand moves Forward and hand Tilt Down, it seems that a trend appears, then this haptic device deserves more research.

DISCUSSION

Interestingly, our haptic device is able to induce a directional cue (i.e., a feeling of direction) without prior training. Thus, the principle of skin stretch [8], [9] explored here allows us to envisage ungrounded and low-cost haptic devices for hand guidance.
In the experiment some people had problems with the thumb, which occasionally slipped out from the haptic device. This issue can be related to the symmetrical arrangement of the device. A modified device with a better ergonomics is foreseen for future test campaigns. A good alternative is proposed in [10] using 4 motors.
To conclude, we see the Haptic Feedback (HF) as a key ingredient of our recipe for surgical robotic training. There is potential for HF to speed training times for surgeon residents, while increasing development of relevant visual-motor skills. Our ongoing work is related to integrate the HF in the RAVEN II platform.

REFERENCES

[1] A. Volpe *et al*., "Pilot Validation Study of the European Association of Urology Robotic Training Curriculum," *Eur. Urol*., vol. 68, no. 2, pp. 292–299, Aug. 2015.
[2] S. V. Whitehurst *et al*., "Comparison of Two Simulation Systems to Support Robotic-Assisted Surgical Training: A Pilot Study (Swine Model)," *J. Minim. Invasive Gynecol*., vol. 22, no. 3, pp. 483–488, Mar. 2015.
[3] G. Whittaker *et al*., "Validation of the RobotiX Mentor Robotic Surgery Simulator," *J. Endourol*., vol. 30, no. 3, pp. 338–346, Mar. 2016.
[4] L. M. Crespo and D. J. Reinkensmeyer, "Haptic Guidance Can Enhance Motor Learning of a Steering Task," *J. Mot. Behav*., vol. 40, no. 6, pp. 545–557, Nov. 2008.
[5] M. Mulder, D. A. Abbink, and E. R. Boer, "The effect of haptic guidance on curve negotiation behavior of young, experienced drivers," in *2008 IEEE International Conference on Systems, Man and Cybernetics*, Singapore, Singapore, 2008, pp. 804–809.
[6] J. Bluteau, S. Coquillart, Y. Payan, and E. Gentaz, "Haptic Guidance Improves the Visuo-Manual Tracking of Trajectories," *PLoS ONE*, vol. 3, no. 3, p. e1775, Mar. 2008.
[7] A. Teranishi, G. Korres, W. Park, and M. Eid, "Combining Full and Partial Haptic Guidance Improves Handwriting Skills Development," *IEEE Trans. Haptics*, vol. 11, no. 4, pp. 509–517, Oct. 2018.
[8] H. Olausson, I. Hamadeh, P. Pakdel, and U. Norrsell, "Remarkable capacity for perception of the direction of skin pull in man," *Brain Res*., vol. 808, no. 1, pp. 120–123, Oct. 1998.
[9] B. T. Gleeson, S. K. Horschel, and W. R. Provancher, "Perception of Direction for Applied Tangential Skin Displacement: Effects of Speed, Displacement, and Repetition," *IEEE Trans. Haptics*, vol. 3, no. 3, pp. 177–188, Jul. 2010.
[10] J. M. Walker et al., "Holdable Haptic Device for 4-DOF Motion Guidance, " ArXiv [cs], 2019.

Autonomous Pick-and-Place of Pneumatically Attachable Flexible Rails

C. D'Ettorre[1], A. Stilli[1], G. Dwyer[1], M. Tran[2] and D. Stoyanov[1]

[1]Wellcome/ EPSRC Centre for interventional and Surgical Science (WEISS), UCL [2]Research Department of Surgical Biotechnology, University College London

c.dettorre@ucl.ac.uk (DOI10.31256/HSMR2019.10)

INTRODUCTION

In Robotic-Assisted Partial Nephrectomy (RAPN) tumours are excised from the kidney while aiming to preserve organ functionality. Ultrasound (US) imagining is used as an intraoperative technique to identify and outline of the tumour. During RAPN with the da Vinci Surgical System (Sunnyvale, CA), US images are acquired using a "drop-in" US probe which is passed through the instrument port. The EndoWrist® Pro-Grasp Forceps Gripper is commonly used to grasp this kind of probe and to swipe it on the surface of the kidney. During scanning, given the morphology of the kidney, slippages are common, and repositioning of the probe is often needed.

In this paper, we build on previous work [1] where Pneumatically Attachable Flexible (PAF) Rails were introduced. We propose a software architecture customized for PAF to automate track-guided US scanning leading towards better workflow. Our architecture is designed to automatically grasp the PAF rail and to place it on the tissue. After autonomous pick-and-place of the system, the probe can be used for scanning, sliding the probe along the PAF rail. The architecture relies on a calibrated environment and on vision as input of a gradient-based planning algorithm.

MATERIALS AND METHODS

Calibration and Visual Feedback - Calibration is needed to link the vision system and measurements from it with robot kinematics data. The stereo endoscope is calibrated using conventional camera calibration [2]. For the transformation between the camera and robot frame, we select a specific point cloud and, knowing the coordinate of points in the different reference frames, the calibration problem can be formulated as a point cloud registration problem [3]. The proposed system presents a visual interface which allows the surgeon to select the current position of the PAF rail and the location where it should be placed on the organ's surface. Selection of the grasping site represents the input to the system.

The coordinates of the selected points are then triangulated and reconstructed in the 3D space using the stereo endoscope. They can then be used as targets for the pick and place task using the calibration transformations. In parallel, the kidney is segmented both in the left and right frame and the local features are extracted using the SURF algorithm [4] for both frames. The two points clouds are triangulated, reconstructed and translated in the robot reference frame and used as the target for the placement phase.

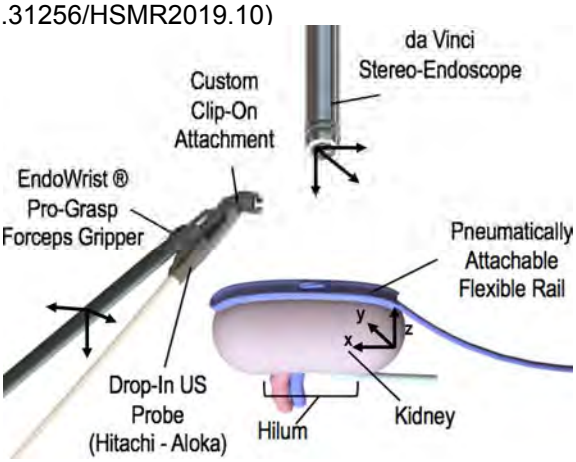

Figure 1 – Schematic representation of the proposed system. The PAF rail is located on the kidney surface and the model of US-probe is equipped with an adaptor. This allows the surgeon to properly grasp the probe with the Pro-Grasp tool and slide the probe in the rail.

Gradient-based Planning - Our algorithm takes as input the current and desired positions of the PAF rail defined by the surgeon and allows the robot to grasp it and position it on the kidney's surface accordingly. Notably, we have not considered the effects of physiological motion on the organ. However, in consideration of the future work we will conduct in this direction, we have decided to choose a fast planning algorithm to allow rapid re-planning, hence, to tackle the position uncertainty associated with motion in vivo.

At each time step, given the current location of the tooltip in the Cartesian space, we computed an intermediate position, through the gradient-based approach, located at a distance called *next-translation.* If the target is within the *next-translation* distance, the new Cartesian position is the target itself. Similarly, for the orientation, we compute an intermediate target as the rotation necessary to change the current orientation of the tooltip to the target one. Given the morphology of the system paired with the organ we defined as the target orientation the one along the x-axis (direction shown in Fig. 1). The intermediate rotation, the *next-rotation*, is parameterized as the angular rotation that needs to be performed to reach the target orientation. Due to the design of the grasping slot of the PAF rail, it is important to correctly grasp the system with the tooltip in the proper orientation, to guarantee an effective grasp. Hence, after the grasp-acquisition step, the orientation is never more than a small angle away

from the desire targeted organ surface orientation. We assume that the orientation of the PAF rail in the operating area before the grasp can be controlled by the surgeon's assistance through the pressure pipe. Using *cisst-saw* library [5], we compute the Cartesian Jacobian and the rotational Jacobian, which show how the changes in the joint angles effect the final pose of the tooltip in the Cartesian space. Rotations are given in angle-axis representation. The parameters *next-transl* and *next-rot*, associated with the *next-translation* distance and the *next-rotation* angles respectively, guarantee that the intermediate tool tip pose is close to the current one. Hence, it is possible to linearize our problem using Equation 1, where $\mathbf{J_{tr}}$ and $\mathbf{J_r}$ are the Cartesian and rotational Jacobian defined above, and $\mathbf{\Delta_{tr}}$ and $\mathbf{\Delta_r}$ the desired translation and rotation to move the end effector to the intermediate target. The da Vinci robotic arm has 6 DoFs and an ordinary least-squares regression is used to compute the required joint changes necessary to satisfy the equation.

$$\begin{bmatrix} J_{tr} \\ J_r \end{bmatrix} \theta = \begin{bmatrix} \Delta_{tr} \\ \Delta_r \end{bmatrix} \quad (1)$$

RESULTS

A dataset of 40 acquisitions has been recorded to test the overall architecture. To recreate the surgical scenario, the experiment was defined as follows (see Fig. 2): 1 - the PAF rail is randomly inserted inside the field of view of the stereo-endoscope; 2 - the operator triggers the motion of the robot selecting on screen the desired position of the PAF rail on the targeted kidney; 3 - The robot grasps the PAF rail; 4 – it moves toward the target organ; 5 - The robot place the PAF rail on the organ surface according to the position previously selected through the interface. The task in consider successfully completed once the PAF rail is in suction and is correctly positioned on the kidney's surface. The experiment had a success rate of 35 acquisitions over 40 (Fig. 3), while in the remaining 5/40 the tooltip was not able to reach the rail to complete the grasp. The average completion time among all the successful acquisitions was 42 seconds.

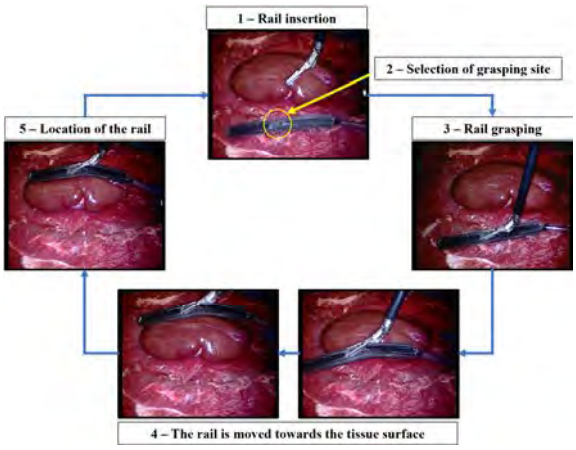

Figure 2 – Representation of the different step of the pick and place task.

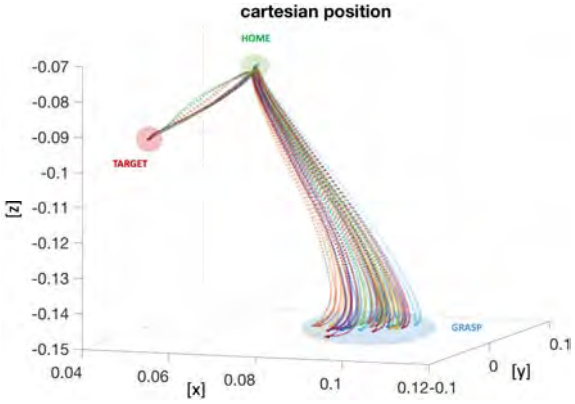

Figure 3 – Representation of the Cartesian position of the tooltip in the workspace in meters. The 35 successful acquisitions are represented.

DISCUSSION

The experiments presented in this paper show that the autonomous pick-and-place of the PAF rail system is feasible. We showed that the proposed software architecture can be successfully used to locate the PAF rail in the environment, to place it in a desired position, as well as to move the robotic instruments accordingly based on the calibrated environment and on a gradient-based trajectory planned on the fly. The results obtained show a success rate of 87.5%. Regarding the rest of executions, the system fails the correct execution for reasons related to the accuracy of the reconstruction of the grasping site. As a matter of fact, the small baseline between the two cameras of the stereo endoscope makes really challenging to precisely estimate of the 3D-position of points in space. Several challenges remain: one is increasing and incorporating mitigation strategies for the uncertainties coming from the real clinical environment, e.g. kidney motion and deformation and a highly vascularized environment where bleeding can cause occlusion, thus the failure of the vision system. This could have potentially adverse effects also on the surface registration process.

REFERENCES

[1] A. Stilli *et all*, "Pneumatically Attachable Flexible Rail for Track-Guided Ultrasound Scanning in Robotic-Assited Partial Nephrectomy. A Preliminary Design Study." *IEEE Robotics And Automation Letters*, Vol. 4, no. 2, pp. 1208-1215, 2019.

[2] Z. Zhang, "A Flexible New Technique of Camera Calibration.", *IEEE Translation of Pattern Analysis And Machine Intelligence*, vol. 22, pp. 1330-1334, 2000.

[3] C. D'Ettorre *et all*, "Automated Pick-up of a Suturing Needle for Robotic Surgical Assistance", *ICRA*, pp. 1370-1377, 2018.

[4] H. Bay *et all*, "SURF: Speeded up Robust Features", 2006.

[5] P. Kazanzides *et all*, "An Open Source Research Kit for the da Vinci Surgical System", in *ICRA*, 2014, pp. 6434-6439.

Design of the MUSHA Hand II for Robotic-Assisted Laparoscopic Surgery

H. Liu[1], P. Ferrentino[1], M. Selvaggio[1], S. Pirozzi[2], F. Ficuciello[1]

[1]*University of Naples Federico II*

[2]*University of Campania "Luigi Vanvitelli"*

hzauliuhuan@gmail.com (DOI 10.31256/HSMR2019.11)

INTRODUCTION

Robot-assisted laparoscopic surgery has been widely preferred since its introduction, as it reduces blood loss, hospital stay and mortality of patients. Various Multi-Port Laparoscopy (MPL) robotic system, Single-Port Laparoscopy (SPL) systems and Natural Orifice Transluminal Endoscopic Surgery (NOTES) systems[1-3] were developed.

Although those surgical systems demonstrated impressive dexterity, the end-effectors (graspers, retractors, etc.) installed to the distal of the systems remain similar to the tools used in manual laparoscopic surgery. For example, most of the EndoWrist graspers and retractors for the da Vinci surgical system share similar two-jaw design. Limited dimension of access port might be the major reason that restrained surgical end-effector to simple and compact design.

Since human organ/tissues are generally slippery and existing graspers could not provide prehensile grasp, a high gripping force need to be applied on the tissue to secure reliable pinch grasp. Inappropriate grasp force may cause tissue injury, especially for handling larger organs like the bowel, liver and spleen. Moreover, the missing of tactile sensation of current grasper may worsen the situation, as the surgeon could not know the contact force he/she is applying on the organ via the robotic system.

Aimed at a miniature hand with human-like functionality for robot-assisted laparoscopic surgery, the three-fingered MUSHA Hand (MUltifunctional Smart HAnd) have been developed as our first effort [4]. Based on the obtained result, the MUSHA Hand II was developed, as shown in Fig. 1, with significant improvement on dimension, integrity and compatibility with the da Vinci Research Kit (dVRK) surgical system. This paper presents the design, development and preliminary experimentation of the new hand.

MATERIALS AND METHODS

The MUSHA Hand II, was designed and developed, as shown in Fig. 1(a)~(d). The hand is composed of an actuation unit, a ϕ12mm tube and three identical snake-like fingers. The fingers are remotely actuated by the actuation unit through multiple tendons inside the tube.

Driven by the actuation unit, the hand can be folded to a ϕ12mm cylinder shape, as shown in Fig. 1(a). Then, the hand can be inserted into an abdominal cavity through a ϕ13mm trocar. After the insertion, it can be configured to the grasper or the retractor mode, as shown in Fig. 1(b) and (c), respectively. In addition, three-dimension force sensor was integrated to each fingertip. Thus the hand can also perform palpation, as shown in Fig. 1(d).

The hand is designed to be installed to one of the Patient Side Manipulators (PSMs) of the dVRK, as shown in Fig. 1(e). Therefore, the original dVRK interface was adopted and the four channels of actuation from the dVRK were utilized. In addition, two DC motors (Maxon DCX12S) were used to augment the dexterity and functionality of the hand.

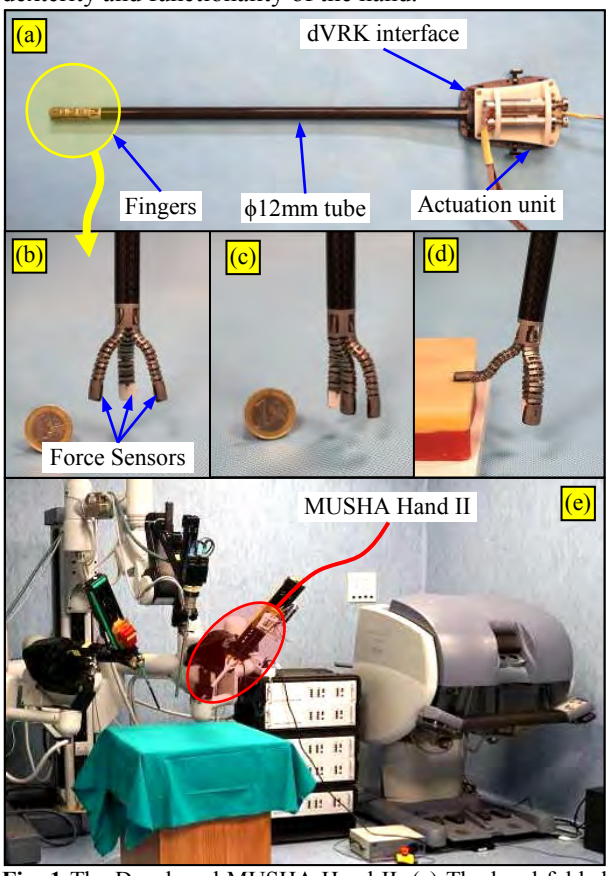

Fig. 1 The Developed MUSHA Hand II. (a) The hand folded to a ϕ12mm cylinder shape. (b) The hand in grasper mode and (c) retractor mode. (d) Fingertip sensor can be utilized for palpation. (e) The Hand install in the dVRK system.

The MUSHA Hand II has three identical underactuated fingers. Design details of the finger is shown in Fig. 2. The finger is consisted of a proximal segment and a distal segment, which connected by a passive abduction/adduction joint.

The distal segment consists of four vertebrae and one sensorized fingertip, connected by four revolute joints. The segment is driven by two antagonistic

tendons (red ones) made from ϕ0.4mm steel cable, as shown in Fig. 2.

The proximal segment has six vertebrae, which can be further divided to the P1 sub-segment and the P2 sub-segment. Two tendons (blue ones) are used to drive the P1 subsegment. Another two tendons (green ones) are used to couple the motion of the two sub-segments, as two ends of each tendon were anchored on the hand base and the most distal vertebra of the P2 sub-segment. Therefore, as the P1 sub-segment is driven to bend outward or outward, the P2 sub-segment is bent to the opposite direct.

Two ϕ0.4mm nitinol rods are inserted in the holes of each vertebra, from the fingertip to the hand base, to bring all the joints compliance, including the passive abduction/adduction joint.

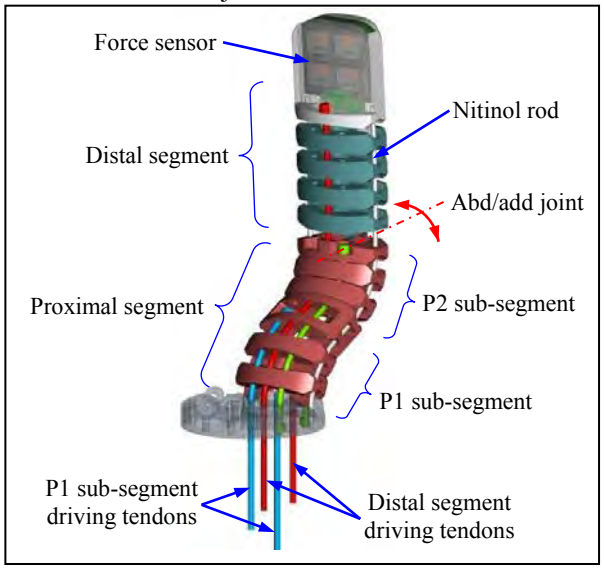

Fig. 2 Design of the underactuated finger

RESULTS

Preliminary teleoperated grasping experiment were conducted.

The hand was mounted on one of the PSM of the dVRK system, as shown in Fig. 1(e). After been inserted through a trocar, the hand was switched to the grasper mode shown in Fig. 1(b).

Control of the hand is also integrated with the dVRK system through ROS (Robot Operating System). Motion of the master tool manipulator (MTM) was mapped to the MUSHA Hand II. Specifically, the rotation of the most distal joint of the MTM was mapped to the rotation of the whole hand along the tube. The open/close of the MTM gripper was mapped to the flexion/extension of the distal segments of the three fingers.

A ϕ15mm ball made from plasticine was placed within the view of the dVRK endoscope, as shown in Fig. 3(a). Then hand was teleoperated by a subject operating the MTM of the dVRK (see Fig. 3(b)). Fig. 3(c)~(e) show the sequence of the MUSHA hand reaching, grasping and lifting the object, respectively. Fig. 3(f) shows a clos-up of the fingers pinching the object by its fingertips.

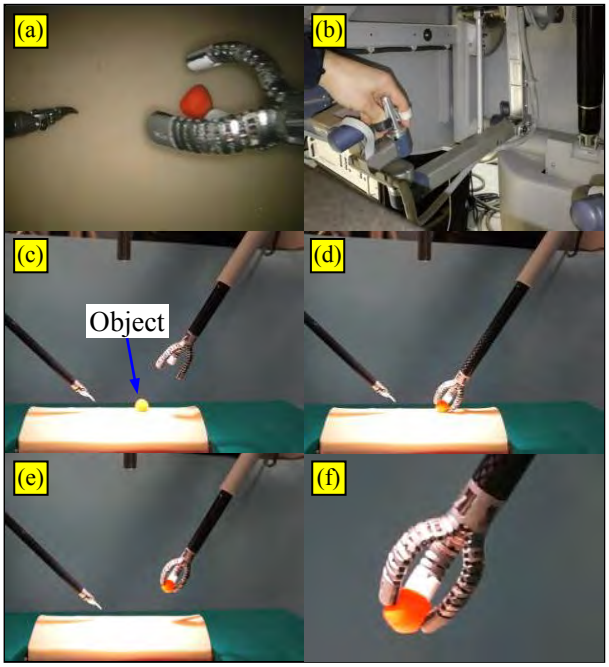

Fig. 3 Preliminary teleoperated grasping experiment. (a) The view from the dVRK endoscope. (b)The MTM of the dVRK. (c)~(e) Sequence of the hand grasping an object. (f) Close-up view of the hand grasping the object.

DISCUSSION

This paper presents the design and preliminary experiment of the MUSHA Hand II, which is a miniature three-fingered hand with fingertip force sensor for robot-assisted laparoscopic surgery. After been inserted through a ϕ13mm trocar, the hand can be switched to different configuration to perform various tasks. The hand was integrated with the dVRK system and preliminary teleoperated grasping was successfully performed. Further experimentation, including quantitative organ manipulation and palpation, will be performed to verify the dexterity and functionality of the hand.

REFERENCES

[1] S. Thielmann, U. Seibold, R. Haslinger, G. Passig, T. Bahls, S. Jörg, et al., "MICA - A new generation of versatile instruments in robotic surgery," in 2010 IEEE/RSJ International Conference on Intelligent Robots and Systems, 2010, pp. 871-878.

[2] K. Xu, J. Zhao, and M. Fu, "Development of the SJTU Unfoldable Robotic System (SURS) for Single Port Laparoscopy," IEEE/ASME Transactions on Mechatronics, vol. 20, pp. 2133-2145, Oct 2015.

[3] J. Zhao, X. Zheng, M. Zheng, A. J. Shih, and K. Xu, "An endoscopic continuum testbed for finalizing system characteristics of a surgical robot for NOTES procedures," in 2013 IEEE/ASME International Conference on Advanced Intelligent Mechatronics, 2013, pp. 63-70.

[4] M. Selvaggio, G. A. Fontanelli, V. R. Marrazzo, U. Bracale, A. Irace, G. Bregio, et al., "The MUSHA underactuated hand for robot-aided minimally invasive surgery," The International Journal of Medical Robotics and Computer Assisted Surgery, p. e1981, 2018.

Toward an ontology for automation in surgery: application to peg-and-ring task

Hirenkumar Nakawala, Paolo Fiorini

Department of Computer Science, University of Verona, Verona, Italy
hirenkumarchandrakant.nakawala@univr.it (DOI10.31256/HSMR2019.12)

INTRODUCTION

Creating an ontology for automation in surgery will impact the way information is currently exchanged between human and surgical robots. Human and robot both represent two different cognitive models and exhibit different spatiotemporal interactions, the knowledge gap that still needs to be addressed for automation in surgery. For autonomous task execution in a safety-critical scenario like surgery, efficient low-level data processing, e.g., recognition of *surgemes* – primitive gestures, as well as robust representation of abstract interventional models are necessary in order to guarantee safety in all conditions and to cope with unknown and failure situations. The objective of this work is to provide a generic symbolic knowledge model which should be generalized to any surgical procedure to achieve a level of maximum autonomy for executing surgical tasks in variable environments. We developed an ontology representing generic high-level entities toward task automation in surgery. For prototyping, an ontology for surgical automation is developed focusing on "peg-and-ring" task, a surgical training task, from the Fundamentals of Laparoscopic Surgery (FLS) [1]. Furthermore, we validated the developed ontology by using it in a supervisory control framework.

MATERIALS AND METHODS

An ontology is a formal and explicit specification of a shared conceptualization [2]. Conceptualization refers the concepts related to the types of entities, with relationships and constraints that exist in a given domain. A *task* is defined as a concrete decomposition of actions into robot behaviors. Robot behavior, a low-level goal-directed movement, can be pre-defined in any computational model, e.g. Finite State Machine (FSM) and allow robot to interpret based on the instructions from the high-level supervisory layer, e.g. ontology. Ontology for surgical automation is expected to provide a knowledge base on the surgical intervention, high-level description on the surgical task and behavior of the system, and semantic interoperability to interact with the execution layers, which are used for robot control, to aid in low-level reasoning, e.g. motion planning.

Developed ontology is based on Suggested Upper Merged Ontology (SUMO) [3]. SUMO particularly divides all entities in physical and abstract groups that exist in the domain of discourse. Entities that exist in space-time are defined as "physical", whereas other entities which are not as "abstract", e.g. including mathematical and epistemological constructs. Physical entities are separated into objects and processes. An object, a type of task resource, is an entity that has spatiotemporal parts like objects and spatial regions. A process contains entities for mechanical operations and is expected to unfold over a finite time duration.

The ontology for peg-and-ring task defines what a peg-and-ring task is, and specifies the properties of task as well as task resources, e.g., objects and entities for a state machine. To develop the ontology, we understood peg-and-ring task based on the recorded videos and using the previous literature [4] which explains peg-and-ring task using two manipulators. The ontology is developed using a top-down methodology, following a method described in [5], where we separated object and process branches based on SUMO. Object branches, i.e. *Object,* are used to present peg-and-ring task resources, e.g., a set of needed physical objects for the task - "pegs", "rings", "robot", "end-effector" and so on, while process branch is used to specify entities representing surgical *actions*, e.g. "move", "carry" and so forth. The logical propositions are specifically defined for the processual entities, *Action* and *State. Action* defines the specific *Goal*-directed movement*,* an externally defined behavior or state of the system, which ideally pre-defined in the FSM, that robot is trying to accomplish. *State* represents whether the state machine is in the initial, transition, or final state. If the overall *Goal* is to move, i.e. "move" state in FSM which was used to reach the ring, the robot may be told to have a goal of reaching an intermediate pose which is derived implicitly analyzing the sensor data, e.g., vision using the ontology. To define the temporal relations inside the ontology, we followed Allen's temporal interval algebra. Temporal relations are especially specified between the entities representing *Action.* Spatial information is represented with the abstract concepts, e.g. *position*, *orientation, etc*., which are defined especially for *object.* The ontology was developed using the Protégé knowledge management tool, serialized in RDF/XML, and processed in OWL API.

RESULTS

The resulted ontology has 211 axioms, 113 logical axioms, 40 classes, 14 object properties and 17 data properties. The classes, i.e. *State*, *Action*, *Object*, *Exit conditions, MathematicalOrComputationalThing* and *spatial information*, to derive the surgical task is shown in Fig. 1. The normative knowledge represented in the ontology defines the structure and content of the task

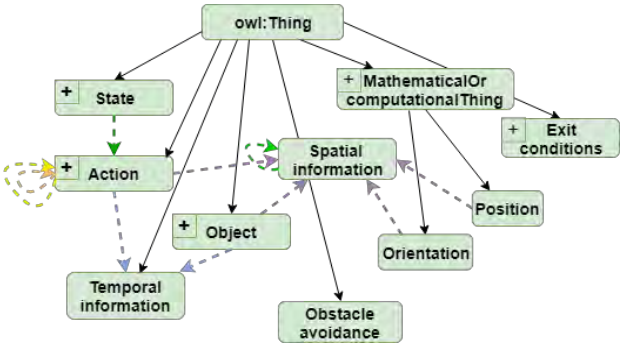

Fig. 1 High-level conceptual structure representing entities of the ontology. The rectangles represent the classes of ontology. Black arrows show the class hierarchies and other colored arrows represent relations between the classes.

which enables communication of task-related data, categorization of states and vision data, e.g., assigning percepts to classes' instances, called "symbol grounding", decomposition of the action sequence, and high-level reasoning using the semantic/production rules. Production rules were defined using the pre- and post-conditions and used to derive axioms for action instances inside the ontology during the task execution.

A prototypical peg-and-ring task scenario consisted of 3 different colored pegs and rings. The task consists of multiple pick-and-place in various sequences and spatial configurations using an anthropomorphic manipulator (Panda from Franka Emika, Germany). The ontology was validated by using it in a supervisory control framework [6] consisting of four components - a predefined task *model* (FSM), an *ontology-based reasoner* to drive the execution, a RGBD *camera* for sensing, and *Dynamic Movement Primitives (DMPs)* as a motion planner. Temporal relations were used to do the qualitative temporal planning between two actions, e.g. "move", to the ring, takes place before "carry" the ring. Spatial reasoning was achieved by associating spatial objects in the environment considering the "colorID", which was specified for the objects as a data property. For example, if environment contains the object with "colorID" "0" and "0" is associated "redring", where "colorID" is specified as an axiom for each ring, then the environment contains the "redpeg" with the exact coordinates, which was also included inside the ontology by analyzing the vision data. The ontology also infers that the "redring" and "redpeg" are objects and contains some spatial information, i.e. object poses. A total of 5 different type of rules were implemented. An exemplary rule which was used on the ontological entities to execute the task is as below:

***Preconditions*:** End-effector at some spatial location and gripper status is open

***Effects*:** Classification of rings, decomposition of states (of FSM's), i.e. obtaining action sequences, assignment of colorIDs to rings

In the exemplary rule, the end-effector is an instance of *object* class, while the status of gripper is obtained implicitly by analyzing the vision data. The expected effects are classification of rings based on the "colorIDs", i.e. if an object is associated with colorID "0" then it is a "redring". It also allows to decompose the action sequences based on the sequences of the IDs of colors. Ontology was processed in 258 ms by a description-logic (DL) based reasoner i.e. "Pellet" to autonomously execute the peg-and-ring task with 100% success rate, also in a failure condition when drop of a ring occurs while carrying it to the peg.

DISCUSSION AND FUTURE WORK

The ontology could indeed be used to represent the entities and logical axioms for mapping high-level states to low-level actions and efficient high-level task planning for automation in surgery. The low-level action models are executed based on the abstract specifications by extending class taxonomy with action-related concepts. While it is evident that ontologies can be a promising knowledge and information model to be used in supervisory control architectures, the knowledge model should be evolved intraoperatively to handle the dynamic nature of surgery and to do efficient task planning. Future work includes extension of the proposed ontology including domain ontologies, OntoSPM (Ontology for Surgical Process Modelling) [7] for surgery and CORA (Core Ontology for Robotics and Automation) [8] for automation and robotics, and realization of a reasoning engine which will be able to efficiently compute the task and action description in the ontology during dynamic situations. Furthermore, we will validate the ontology with the execution of peg-and-ring task using the da Vinci Research Kit (dVRK).

ACKNOWLEDGEMENT This research is funded by the European Research Council (ERC) under the European Union's H2020 research and innovation programme (grant agreement No. 742671 "ARS").

REFERENCES

[1] Sopar NJ, Fried GM. The fundamentals of laparoscopic surgery: its time has come. Bull Am Coll Surg, 2008; 93(9): 30-32.

[2] Gruber TR. A translation approach to portable ontologies, Knowledge Acquisition, 1993; 5(2): 199-220.

[3] Ian N, Pease A. Toward a Standard Upper Ontology. Formal Ontology in Information Systems. Proceedings of the 2nd International Conference. 2001; 2-9.

[4] Hong M, Rozenblit JW. Modeling of a transfer task in computer assisted surgical training. MSM16-proceedings of the modelling and simulation in medicine symposium. 2016; 4.

[5] Natalya NF, McGuiness DL. Ontology Development 101: A guide to creating your first ontology, Stanford medical informatics technical reports - SMI-2001-0880, 2001.

[6] Ginesi M, Meli D, Nakawala H et al., Toward a knowledge-based framework for task automation in surgery, CRAS 2019, Genova, Italy.

[7] Gibaud B, Forestier G., et al., Toward a standard ontology of surgical process modelling. Int J. CARS, 2018; 13(9): 1397-1408.

[8] Prestes E, Carbonera JL., et al., Towards a core ontology for robotics and automation. Robotics and Automation Systems, 2013; 61(11): 1193-1204.

Deployable shape sensors for minimally invasive surgery using Frequency Division Multiplexed Electrical Impedance Tomography

J Avery[1], M Runciman[2], G Mylonas[2], A Darzi[1]

[1]*Department of Surgery and Cancer, Imperial College London, London, UK,*

[2]*HARMS Lab, Department of Surgery and Cancer, Imperial College London, UK*

james.avery@imperial.ac.uk (DOI10.31256/HSMR2019.13)

INTRODUCTION

Through the reduction of soft tissue trauma, and navigation through tortuous paths inside the body, soft robots have the potential to improve upon conventional rigid devices [1]. However, the controllability of these soft systems is limited given the deformability of the compliant structures and the challenges in integrating sufficient shape or pose sensing. Many proposed sensing methods either compromise the desirable mechanical properties or require line of sight [2]. Soft tactile and pose sensors have been proposed wherein shape related electrical impedance changes are imaged using Electrical Impedance Tomography. However, these elastomer sensors are often not suitable for minimally invasive surgery (MIS), as they have low packing efficiencies or are not biocompatible [3]. This work describes a deployable shape sensing technique, Frequency Division Multiplexed Electrical Impedance Tomography (FDM-EIT), suitable for integration with soft robotics for minimally invasive surgery. Due to the low-profile of the structure when unpressurised, large changes in volume are possible when transitioning between the undeployed and deployed states. The conductive fluid within the sensing chambers is added after deployment inside the body, and thus does not add to the volume of the system during insertion.

MATERIALS AND METHODS

A soft actuator was created based on the "aeroMorph" fluid actuated hinges [4] that bend to an angle pre-defined by the aspect ratio of the diamond weld pattern at their centre, Fig 1. Thermoplastic films were welded together using a robotically guided laser welding system developed in-house. The pneumatic actuator was created using a single planar weld pattern, and another chamber was added to one half of the hinge to form the tactile sensor. Copper wires of 0.15 mm diameter were affixed inside the sensing chamber prior to welding, and electrodes created by removing 0.5 mm of insulation. Thus, the wires were held in a stable position during deployment and actuation. The pneumatic chamber was then pressurised using a syringe pump. Then the sensing chamber was filled with 0.1 % saline solution through a separate inlet, Fig 2.

In FDM-EIT, current at different frequencies is injected between different electrode pairs simultaneously. The system was constructed from a parallel current source with six injection channels [5], and a USB-6363 16 bit DAQ at 60 kHz sampling rate. Current was injected at six frequencies between 2 and 11.25 kHz, with 1.85 kHz spacing, to reduce harmonic interference. The current amplitude of 120 μA was well below the IEC60601 patient safety limits. One of six electrodes was used as a common reference, giving five measurements per current injection frequency, yielding a total of 30 EIT measurement channels. A single measurement consisted of the average demodulated amplitude of multiple sine waves, controllable from 3 to 250ms.

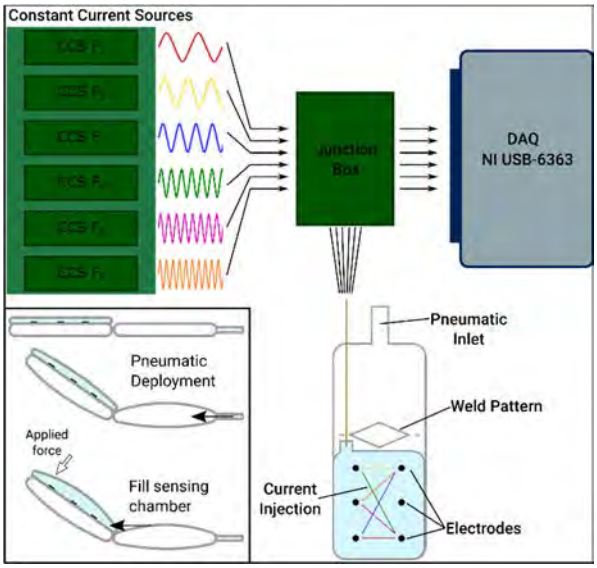

Fig. 1 Measurement setup of FDM-EIT system. 6 simultaneous current injections and voltage measurements within tactile sensing camber. Insert – Sensor deployment, pneumatic unfolding and actuation followed by filling of sensing chamber

To generate the EIT images, a solid model of the tactile pad was created in SolidWorks (Dassault Systèmes), and a Finite Element Model, Fig 3A, of 570k elements was created using bespoke meshing software based on CGAL (Computational Geometry Algorithms Library). The electric currents were simulated and a sensitivity matrix, Fig 3B, obtained using the PEITS solver. The images were reconstructed using Zeroth Order Tikhonov regularisation in a hexahedral subdomain, using cross-validation to select the hyper parameter λ [6]. The actuator was used in an experiment simulating a grasping task common in soft robotics, to test the exteroception of the sensor. The hinge was actuated such that the sensing chamber was deflected by a rigid object, mimicking a grasping target, in three locations.

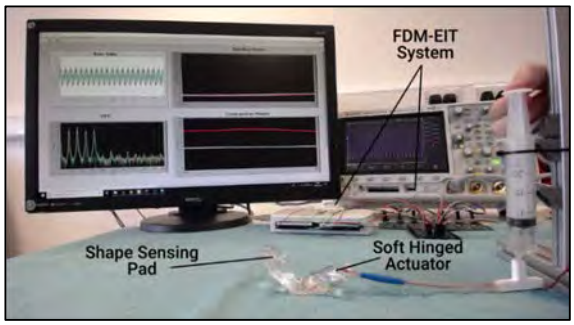

Fig. 2 Deployable shape sensor, FDM-EIT system connected to soft "aeroMorph" hinged actuator, with attached tactile pad [7]

RESULTS

With pressurisation, the bending angle of the hinge increased in a repeatable manner. The compression of the sensing pad resulted in a clear apparent conductivity decrease in the reconstructed images, Fig 3C, as a result of local volume reduction. Whilst there is a high point spread function evident in the images, each location produced distinct profiles and the intensity was focused in the correct area. A maximum of 10 ms temporal resolution was possible using this system, whilst still yielding sufficient SNR (> 60 dB) to generate images.

DISCUSSION

The proposed shape sensor is novel, low profile and suitable for endoscopic insertion, giving a high packing density, whilst still maintaining sensing capabilities. The FDM-EIT technique is beneficial in MIS applications as it uses safe currents and is made MR conditional by using non-ferromagnetic materials. Further, the device uses low pressures and biocompatible fluids for actuation and sensing. Whilst the temporal resolution of the data collection is 10 ms, the image reconstruction is currently limited to ~100 ms as it is not optimised for real-time applications. However, this is sufficient for use in a closed loop control scheme with the existing devices, given the low actuation speeds.

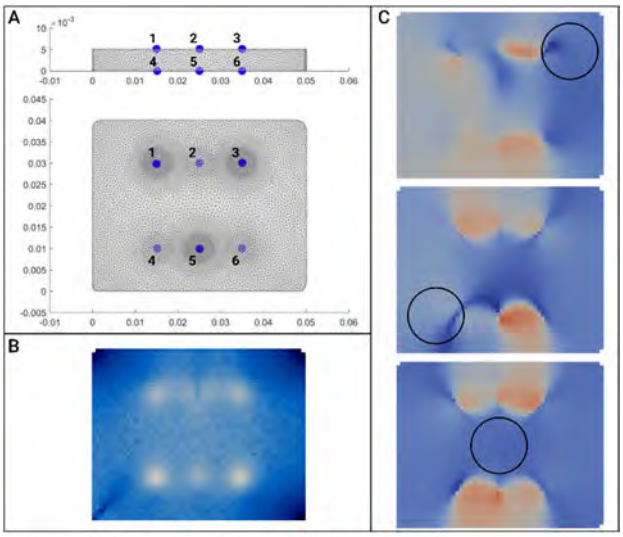

Fig. 3 EIT reconstructions of shape changes in tactile sensor. FEM A) and Sensitivity matrix B) used in forward model, C) Reconstructions of deformations in three target locations, blue regions represent apparent conductivity increases

The reconstructed images could be improved through the optimisation of the electrode locations, and increased electrode count. Work is ongoing to deposit MR conditional tracks directly onto the thermoplastic itself, to create a higher number of electrodes with a wider diameter. The supporting pneumatic beam was not totally rigid under the pressures used. Thus, the actual shape change was much more complicated than just a localised point, as the support chamber also deformed. Further improvements could be made to the EIT methods, as the regularisation used is not specific to this application. The reconstructions could be improved either through an existing algorithm, or development of one targeted to shape sensing devices. Finally a feature extraction step is necessary to integrate the sensor output with existing object localisation and classifiers [8].

REFERENCES

[1] M. Cianchetti, C. Laschi, A. Menciassi, and P. Dario, "Biomedical applications of soft robotics," *Nat. Rev. Mater.*, vol. 3, no. 6, pp. 143–153, Jun. 2018.

[2] C. Shi, X. Luo, P. Qi, T. Li, S. Song, Z. Najdovski, T. Fukuda, and H. Ren, "Shape sensing techniques for continuum robots in minimally invasive surgery: A survey," *IEEE Trans. Biomed. Eng.*, vol. 64, no. 8, pp. 1665–1678, 2017.

[3] J.-B. Chossat, H.-S. Shin, Y.-L. Park, and V. Duchaine, "Soft Tactile Skin Using an Embedded Ionic Liquid and Tomographic Imaging," *J. Mech. Robot.*, vol. 7, no. 2, p. 021008, May 2015.

[4] J. Ou, M. Skouras, N. Vlavianos, F. Heibeck, C.-Y. Cheng, J. Peters, and H. Ishii, "aeroMorph - Heat-sealing Inflatable Shape-change Materials for Interaction Design," in *Proceedings of the 29th Annual Symposium on User Interface Software and Technology - UIST '16*, 2016, pp. 121–132.

[5] J. Avery, T. Dowrick, A. Witkowska-Wrobel, M. Faulkner, K. Y. Aristovich, and D. S. Holder, "Simultaneous EIT and EEG using frequency division multiplexing," *Physiol. Meas.*, 2019.

[6] K. Y. Aristovich, G. S. dos Santos, B. C. Packham, and D. S. Holder, "A method for reconstructing tomographic images of evoked neural activity with electrical impedance tomography using intracranial planar arrays.," *Physiol. Meas.*, vol. 35, no. 6, pp. 1095–109, Jun. 2014.

[7] J. Avery, M. Runciman, A. Darzi, and G. P. Mylonas, "Shape Sensing of Variable Stiffness Soft Robots using Electrical Impedance Tomography," in *IEEE International Conference on Robotics and Automation*, 2019.

[8] A. Schneider, J. Sturm, C. Stachniss, and M. Reisert, "Object identification with tactile sensors using bag-of-features.," in *IROS*, 2009, pp. 243–248.

Real-time prediction of breast lesions displacement during Ultrasound scanning using a position-based dynamics approach

D. Dall'Alba[1], E. Tagliabue[1], E. Magnabosco[1], C. Tenga[1], P. Fiorini[1]

[1]*Dept. of Computer Science, University of Verona,*

eleonora.tagliabue@univr.it (DOI10.31256/HSMR2019.14)

INTRODUCTION

The non-invasiveness and real-time capabilities of ultrasound (US) imaging make this technique appealing for guiding the needle towards suspicious areas during breast biopsy procedures. However, the fact that certain malignant lesions are often challenging to be distinguished on US has raised interest in finding some ways to combine knowledge about lesions position obtained from pre-operative modalities with real-time information provided by intra-operative US. In order to correctly estimate lesions displacement, it is essential to account for the large deformations the breast undergoes due to the compression forces applied with the US probe by the physician, to guarantee proper probe-tissue coupling and obtain acceptable image quality. An additional challenge is posed by the fact that breast behavior varies a lot across the population, thus requiring patient-specific models [1].

Biomechanical models represent a valuable tool to account for anatomical deformations resulting from US probe interaction. Although the finite element method (FEM) has been extensively used in breast biomechanics, it was never employed to compensate for US probe-induced deformations, due to its incompatibility with real-time computation. In addition, the main bottleneck of FE simulations is the generation of 3D mesh of the anatomy, a process which has to be repeated for every subject in a patient-specific context [2]. A valuable alternative to FEM is represented by geometry-based approaches, like the position-based dynamics (PBD). The PBD approach models objects as an ensemble of particles whose positions are directly updated as a solution of a quasi-static problem subject to geometrical constraints, thus making the method stable, robust and able to achieve real-time performances [3]. An additional advantage of this approach is that it does not require the construction of a 3D mesh of patient anatomy, which simplifies its translation into the clinical workflow. The PBD scheme has been used by Camara et al. to create a patient-specific biomechanical model of the kidney for the real-time simulation of intra-operative US [4]. In their work, optimal PBD parameters are estimated as those describing the deformation of kidney phantom subject to different levels of probe-induced deformations.

In this work, we present a biomechanical model of the breast based on the PBD formulation available in NVIDIA FleX. To the best of our knowledge, this is the first model able to predict in real-time the displacement of internal lesions due to the interaction with US probe. In order to obtain a patient-specific description of the deformation, PBD parameters are fine-tuned on the anatomy of interest (in our case, a realistic breast phantom) by tracking the displacement of a US-visible landmark. In this way, we obtain a patient-specific model that can accurately predict in real-time the displacement of the other internal areas during US scanning.

MATERIALS AND METHODS

The experimental data are acquired from a Freehand Ultrasound System (FUS) based on a MicrUs US device (Telemed, Vilnius, Lithuania) equipped with a linear probe (model L12-5N40) and an optical tracking system MicronTracker Hx40 (Claron-Nav, Toronto, Canada) (Figure 1). The overall probe spatial calibration error achieved is below 1mm (±0.7147).

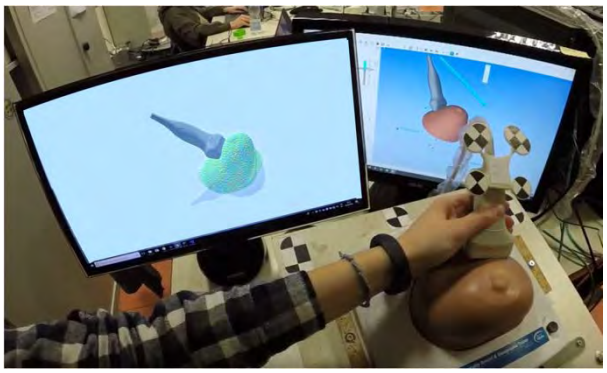

Fig 1. The FUS system allows to map the real positions of the CIRS breast phantom and the US probe to the 3D Slicer scene (right monitor). Information about probe spatial transformation is communicated to the simulated environment in Unity (left monitor).

A realistic multi-modality breast phantom (Model 073; CIRS, Norfolk, VA, USA), which has several dense and stiff internal masses of diameter 5-10mm, is used to evaluate the capability of the PBD model to provide correct estimates of biopsy targets. Before applying the model to predict lesions displacement, PBD parameters are tuned to account for the specificity of the anatomy of interest. In particular, we optimize the value of *cluster spacing, cluster radius* and *cluster stiffness* parameters, while we set other parameters in accordance to values reported in [4]. Considered parameters are controlling the deformable behavior of soft objects through the PBD constraint called "region-based shape matching". Optimal parameter values are estimated with a greedy strategy as those minimizing the average localization error on a US-visible landmark (in our case,

one of the internal lesions), when applying four different input deformations with the probe (5, 10, 15, 20 mm). Localization error is computed as Euclidean distance between the model-predicted and the real displacement provided by the FUS of corresponding fiducial points. It's worth mentioning that any internal structure which is detectable on US can be used for this tuning process. The PBD model with updated optimal parameters is then used to infer the displacement of 9 segmented lesions under four deformations as done previously. To evaluate the performances of the proposed approach, we compare it with both a FE and a rigid model. The FE simulation is performed on a mesh of 26,220 linear tetrahedral elements, exploiting SOFA framework[1]. The breast is modelled as a homogeneous Neo-Hookean material, whose elastic properties are set in accordance with the work in [6].

RESULTS

Optimal values for the cluster spacing, cluster radius and cluster stiffness parameters obtained with the calibration procedure are 11.2, 8.5 and 0.46 respectively.

Figures 2 and 3 compare the performances of the proposed deformation model with a FE and a rigid model. Localization errors relative to both PBD and FEM are computed as difference between the model-predicted position and the real lesion position (extracted from US image), at each deformation level. On the other hand, in the rigid case, lesion position at rest always corresponds to the predicted position. The green, purple and orange lines in Figure 2 show the trend of the localization error at increasing deformation levels for the PBD, FEM and rigid model. It's immediately possible to notice that errors obtained with the PBD model are aligned with FE models, with no significant differences. Both PBD and FEM outperform the rigid case by at least halving the prediction error on all the tumors, as emerges from Figure 3.

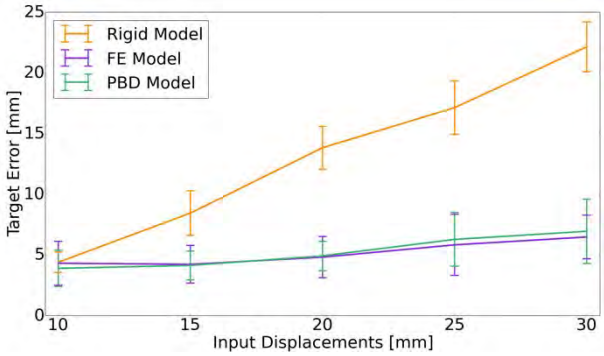

Fig 2. Average target error in mm at different levels of applied deformations for PBD (green), FEM (purple) and rigid (orange) models.

Considering computation times, the average time needed for the PBD model to predict anatomical deformations following the 4 input displacements is 6.99s (±0.36), which approximately corresponds to 1.75s for simulating each input deformation. On the other hand, the FE model takes 16.37s (±0.73) on average, which corresponds to nearly 4.09s for each input deformation. Therefore, FEM takes more than twice the time needed by the proposed PBD approach to perform the simulation, even without a significant improvement in prediction accuracy.

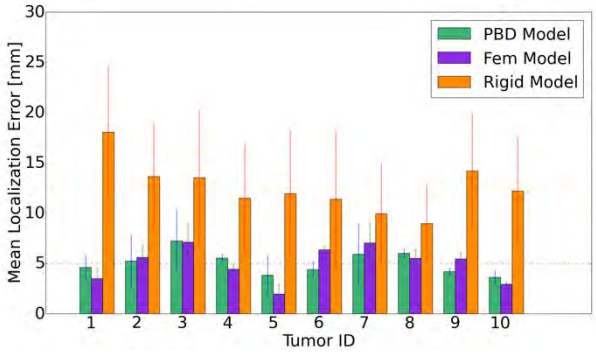

Fig 3. Average localization error in mm obtained for each tumor with the PBD (green), FEM (purple) and rigid (orange) model. Horizontal dashed lines represent the corresponding average error.

CONCLUSION AND DISCUSSION

Exploiting PBD formulation for modelling breast deformations has proved successful in predicting in real-time probe-induced displacement of internal lesions during US scanning. The proposed approach achieves comparable accuracy with FE models, but with faster computational performance and without even requiring tedious 3D mesh generation. Furthermore, it outperforms rigid models usually employed for lesion tracking in biopsy procedures. As future work, we will make the model able to describe heterogeneous structures of breast tissues. We expect this improvement to have a significant impact on simulation accuracy, especially when dealing with real clinical cases. Eventually, we will include the real-time PBD deformation model within a robotic framework able to perform an autonomous US-based guided percutaneous procedure, from the US scanning to the needle insertion.

REFERENCES

[1] R. Guo, G. Lu, B. Qin, and B. Fei, "Ultrasound Imaging Technologies for Breast Cancer Detection and Management: A Review," *Ultrasound Med. Biol.*, 2017.

[2] J. Zhang, Y. Zhong, and C. Gu, "Deformable Models for Surgical Simulation: A Survey," *IEEE Reviews in Biomedical Engineering*. 2018.

[3] M. Müller, B. Heidelberger, M. Hennix, and J. Ratcliff, "Position based dynamics," *J. Vis. Commun. Image Represent.*, 2007.

[4] M. Camara, E. Mayer, A. Darzi, and P. Pratt, "Soft tissue deformation for surgical simulation: a position-based dynamics approach," *Int. J. Comput. Assist. Radiol. Surg.*, 2016.

[5] R. Amini, "A novel and inexpensive ballistic gel phantom for ultrasound training," *W. J. E. Med.*, 2015.

[6] F. Visentin, V. Groenhuis, B. Maris, D. DallAlba, F. Siepel, S. Stramigioli, P. Fiorini, "Iterative simulations to estimate the elastic properties from a series of mri images followed by mri-us validation," *Medical & biological engineering & computing.*, 2018.

[1]www.sofa-framework.org

Needle Segmentation in 3D Ultrasound Volumes Based on Machine Learning for Needle Steering

G. Lapouge[1,2], H. Younes[1], P. Poignet[2], S. Voros[1], J. Troccaz[1]

[1]Univ. Grenoble Alpes, CNRS, Grenoble INP, TIMC-IMAG, F-38000 Grenoble, France

[2]Univ. Montpellier, CNRS, LIRMM, F-34090 Montpellier, France

{hatem.younes ; guillaume.lapouge}@univ-grenoble-alpes.fr (DOI10.31256/HSMR2019.15)

INTRODUCTION

To achieve needle steering and guide a flexible needle, it is necessary to localize it first. In the case of 3D ultrasound (US) in B-mode, the poor imaging quality and artefacts make it difficult to determine the needle pose. Needle localization issues specific to needle steering are reviewed in [1]. In [2], we proposed an observer of the needle tip pose. In [3], we detailed a machine learning approach for needle localization in 3D US volumes. In this paper, we describe the interconnection of both methods for precise curved needle localization in the context of needle steering.

MATERIALS AND METHODS

Approach

3D US compatible needle localization algorithms are reviewed in [4]. Localizing the needle in the whole US volume is computationally expensive. To manage real-time localization, we propose the interconnection of an observer that automatically provides a volume of interest (VOI), and a segmentation algorithm. Because the needle visibility in 3D US volume changes during the insertion, we propose machine learning to select adaptively needle voxels among the VOI voxels.

Needle Pose Estimation

The needle tip behavior is modeled by a unicycle kinematic model. The tip follows a circular path when it is inserted without rotation. In this work, we consider that the needle shaft follows the path of the needle tip. In this hypothesis, segmenting the needle tip over time is equivalent to segmenting the whole needle shaft. This hypothesis is validated experimentally.

The needle tip position and orientation are estimated in real time by the multi-rate unscented Kalman filter (MUKF) described in [2]. It takes as inputs the robot control commands and the measurement coming from the robot's sensors, needle tip segmentation results in the 3D US volumes and stiffness information of the surrounding tissue. The estimated path traced by the needle tip $\widehat{\Phi}$ defines a tubular volume of interest, of radius set by the user, for needle segmentation.

If the needle cannot be segmented in the ultrasound volume, the estimation continues until the needle becomes visible again. The segmentation results are then considered as measurements to update the estimation.

This work was partly supported by the Investissements d'Avenir programme (Labex CAMI, ANR-11-LABX-0004) and by the FOCUS project (ANR-16-CE19-0011).

Naïve Bayes classification

As explained in [3], the VOI histogram can be modeled using an additive Gaussian Mixture Model (GMM):

$$P(I(v)) = \sum_{i=1}^{M} \pi_{V_i} P_i(I(v))$$

Where v is a voxel and $I(v)$ its intensity value, M is the number of mixed components, π_{V_i} represents the coefficient of the i^{th} component and P_i is the Gaussian probability density function that defines the i^{th} component. Here we consider two classes (i=2):

$$Cl = \{\text{Needle } (X_n), \text{Background } (X_b)\}.$$

Given the observed feature $I(v)$, the Bayesian classifier assigns the most likely class as next equation:

$$C_{Bayes}(I(v)) = \arg\max_{v_i} P(Cl = X_i | I(v)).$$

In the case of binary classification, Bayesian classifier is summarized by the followed inequalities:

$$\pi_{x_n} P(I(v) | Cl = X_n) \underset{X_b}{\overset{X_n}{\gtrless}} \pi_{x_b} P(I(v) | Cl = X_b).$$

Each voxel of intensity $I(v)$, is classified as a needle member if the posterior probability of X_n is larger than that of X_b. Several parameters are required to establish this probabilistic model. They vary from GMM to another, even in the same image. Though, each needle localization starts with the prediction of the required parameters.

Expectation Maximization algorithm (EM)

The unknown parameters representing the GMM are estimated by an EM algorithm. This iterative process computes the maximum likelihood of an observed feature for each iteration. The following equations represent the main instructions done iteratively to estimate the parameters.

$$\pi_{X_i}^{new} = \frac{1}{N} \sum_{j=1}^{N} P(X_i | v_j, \theta^k)$$

$$\mu_{X_i}^{new} = \frac{\sum_{j=1}^{N} v_j P(X_i | v_j, \theta^k)}{\sum_{j=1}^{N} P(X_i | v_j, \theta^k)}$$

$$\sigma_{X_i}^{new} = \frac{\sum_{j=1}^{N} v_j P(X_i | v_j, \theta^k)(v_j - \mu_{X_i}^{new})^2}{\sum_{j=1}^{N} P(X_i | v_j, \theta^k)}$$

Where N is the number of voxels and θ^k is the parameters vector to be estimated at the k^{th} iteration.

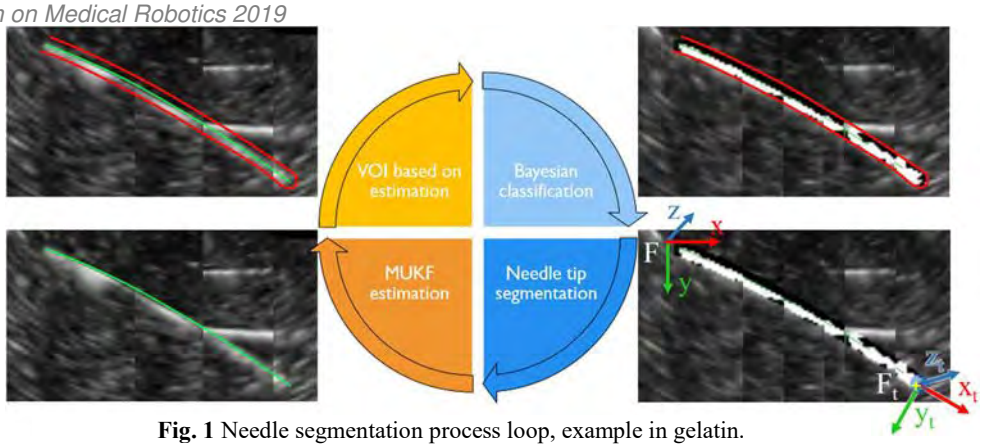

Fig. 1 Needle segmentation process loop, example in gelatin.

Starting from an initial set of values for θ, the algorithm uses the newly derived parameters as the guess for the next iteration. The iteration stops when the parameters values stabilize: $|\theta^k - \theta^{k+1}| < \varepsilon$. A meaningful initialization of θ is necessary for suitable convergence. More details can be found in [3].

Needle tip segmentation

The needle visibility depends on its location in the US volume. Before applying Bayesian classification, the VOI is cropped to keep the 40% of its original length which contain the needle extremity. In this way, we ensure that the tip and shaft voxel intensities are similar (i.e. can be considered as belonging to the same class Xn).

The needle tip search is then done in a spherical neighborhood around the estimated needle tip. In that neighborhood, if there is no voxel belonging to Xn, the segmentation fails. Else, the segmented tip is computed as the weighted centroid of the voxels in Xn. The weighting w_p of a voxel p verifies:

$$w_p \propto w_{p_1} x_t - w_{p_2}(y - y_0)$$

Where $w_{p_1}, w_{p_2} \in \mathbb{R}_+^2$ are set by the user (resp. 3 and 1 here); x_t is the abscissa of the voxel in the estimated tip frame F_t (see Fig. 1); y (resp. y_0) is the ordinate of the voxel (resp. estimated tip) in the image frame F (see Fig. 1). The needle tip is therefore researched preferentially in the direction of the insertion (x_t), and in the opposite direction of expected tip reverberation artefacts $(-y)$.

RESULTS

The proposed solution has been implemented in the context of automated needle insertions to reach a target. A beveled-tip 24 Gauge Nitinol needle was inserted and rotated into gelatin phantoms and pork tenderloin with a robot. The needle surface was either coated with polyurethane foam or etched with a laser. The ultrasound volumes were acquired at 1 Hz with a 3D end-fire probe 4DEC-9/10 used with the Ultrasonix Sonix RP ultrasound system. The US volume voxels are cubes with 0.4 mm edges. Running on an Intel® Core™ I5-8300H CPU, an iteration of the algorithm takes between 20 ms and 30 ms depending on the VOI size.

60 manual needle tip segmentation (0.3 mm repeatability) have been done by a non-expert individual among 4 different needle insertions (2 in pork tenderloin and 2 in gelatin phantoms). The 3D segmentation error Δ was computed as the Euclidean distance between manual and automatic tip segmentation. Axial segmentation errors were computed as the Euclidean distance on each axis between manual and automatic tip segmentation. Results are reported in Table 1.

Difference	Δx	Δy	Δz	Δ
Gelatin	0.5±0.3 [0.0;1.2]	0.2±0.2 [0.0;0.8]	0.5±0.3 [0.0;1.2]	0.8±0.3 [0.1 ;1.5]
Pork	0.3±0.2 [0.0;0.5]	0.3±0.2 [0.0;0.8]	0.4±0.3 [0.0;0.6]	0.5±0.2 [0.2 ;1.0]

Table 1 Difference between manual and automatic needle segmentation (mm). Format: mean±std [min;max].

The mean segmentation error in each direction is generally inferior to the spatial resolution of the probe. The results are therefore very close to voxel size precision and satisfactory for needle tip segmentation. Needle segmentation is more precise in pork than in gelatin. Indeed, in gelatin, the needle can be seen with a better contrast but suffers from greater reverberation artefacts than in pork.

Momentary needle loss occurred in 2 of the pork insertions with no significant impact on automatic segmentation error when the needle becomes visible again.

DISCUSSION

We have proposed an automated needle localization in 3D ultrasound volumes. The solution is composed of interconnected observer and segmentation algorithms. The solution is fully automatic and adapts to the conditions of insertions (i.e. different needles or insertion media). This interconnection allows for precise tip localization despite changing needle visibility in noisy 3D US volumes. It is also robust to momentary needle loss. This makes it suitable for clinically compatible needle steering.

REFERENCES

[1] C. Rossa, M. Tavakoli. Issues in closed-loop needle steering, Control Engineering Practice. May 2017; 62: 55-69.

[2] G. Lapouge, J. Troccaz, P. Poignet. Multi-rate unscented Kalman filtering for pose and curvature estimation in 3D ultrasound-guided needle steering. Control Engineering Practice. Nov. 2018; 80: 116-124.

[3] H. Younes, S. Voros S, J. Troccaz. Automatic needle localization in 3D ultrasound images for brachytherapy. IEEE 15th International Symposium on Biomedical Imaging (ISBI 2018). 2018; 1203-1207.

[4] Y. Zhao, Y. Shen, A. Bernard, C. Cachard, H. Liebgott. Evaluation and comparison of current biopsy needle localization and tracking methods using 3D ultrasound. Ultrasonics. Janv. 2017; 73: 206-220.

Robotically assisted electrical bio-impedance measurements for soft tissue characterization: a feasibility study

Kim L. Schwaner[1], Diego Dall'Alba[2], Zhuoqi Cheng[3], Leonardo S. Mattos[3], Paolo Fiorini[2] and Thiusius R. Savarimuthu[1]

[1]*The Mærsk Mc-Kinney Møller Institute, University of Southern Denmark*
[2]*Department of Computer Science, University of Verona*
[3]*Department of Advanced Robotics, Istituto Italiano di Tecnologia*
kils@mmmi.sdu.dk (DOI10.31256/HSMR2019.16)

INTRODUCTION

The incorporation of advanced sensing technologies (STs) for tissue discrimination during complex procedures is an essential component of future surgical robot systems (SRS). Real-time STs are required to further improve the surgeons' performance in tissue discrimination and manipulation [1]. In the future, these novel STs will also enable an autonomous SRS to recognize contact with different tissue types in different conditions [2]. This information could be of enormous importance in the correct autonomous execution of complex procedures when other sensory data are not providing enough information for estimating the actual surgical conditions.

This work presents the application of a compact electric bio-impedance (EBI) measurement device that can be integrated into standard surgical instruments [3]. EBI measurements have been demonstrated to be a valuable supporting ST in a range of clinical applications, for instance in the localization of pathological areas in breast [4], or for detecting venous entry of catheters [5]. It is a challenging task, however, to obtain stable and robust measurements with a standard bipolar surgical instrument.

In [6], Cheng et al. identify the two main parameters that impact EBI measurements: the distance L between forceps jaws and tissue compression depth d. A graphical user interface was integrated into the standard endoscopic view to support the human operator in correctly controlling these critical acquisition parameters. Even with this interface, stable EBI acquisition between different measurements, i.e. almost constant L and d values, was difficult for a human operator to achieve.

To overcome this problem, we propose a robotically assisted EBI acquisition system (REAS), able to obtain stable EBI measurement over a regular sampling grid in a user-defined region of interest (ROI), with very limited a priori knowledge of the region properties (e.g. no knowledge about geometrical, anatomical and tissue properties). We demonstrate the feasibility of the REAS in an ex-vivo experiment based on the da Vinci Research Kit (dVRK) [7]. The results confirm the capabilities of the proposed method of performing robust EBI data acquisition. This could be a step toward improving the sensing capabilities of future autonomous SRS.

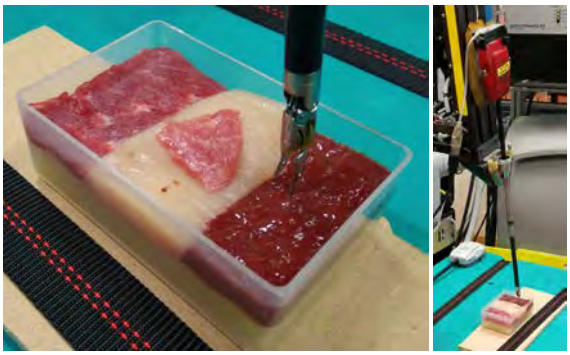

Fig. 1 Left: The phantom made of 3 different ex-vivo animal tissue samples, pork muscle (left), chicken breast (centre) and beef liver (right). We added a triangular piece of pork muscle on top of centre chicken section to increase the complexity of the acquisition. The rough phantom dimensions are $88 \times 55 \times 25$ mm. Right: The bipolar forceps with integrated EBI sensor.

MATERIALS AND METHODS

The EBI sensor used in this work is an embedded device based on an AD5933 (Analog Devices, Inc.) impedance converter IC. Please refer to [6] for a more detailed description of the sensor and its calibration. The sensor is mounted on the housing of an EndoWrist Maryland Bipolar Forceps (Intuitive Surgical, Inc.) and the bipolar leads of the instrument are used to connect the sensor circuit to the forceps grasper jaws. The jaws are placed in contact with the tissue sample under test (see Fig. 1) and the EBI sensor samples the complex impedance $|Z|\angle\theta$ with an excitation frequency of 100 kHz, jaw opening $L = 6$ mm and tissue pressing depth $d = 2$ mm. Impedance measurements are obtained at a rate of 50 Hz.

We propose a measurement planning algorithm that requires only minimum input information. The algorithm is initialized with an orientation (vector $\boldsymbol{n}$) and a bounding box representing the ROI to be analysed. The algorithm then generates a regular grid in a plane with normal $\boldsymbol{n}$, above the tissue surface. The forceps is moved between each point in the grid, and at each point toward the surface, keeping the wrist aligned with $\boldsymbol{n}$. Surface contact is detected when the measured impedance magnitude $|Z|$ crosses a given threshold level. Once surface contact is detected the instrument is pushed against the surface along direction $\boldsymbol{n}$ to obtain the desired pressing depth d. Finally, the instrument is held steady for 0.4 s to

collect 20 impedance measurements at that point.
An ex-vivo experiment was conducted with the dVRK platform to evaluate whether the sensor is indeed capable of autonomously detecting tissue surface and map impedance measurements to contact points. Fig. 1 shows the experimental setup in which a phantom made of three different animal tissues (beef liver and pork muscle and chicken breast) is used to test the proposed system. The measurement planning algorithm was initialized with acquisition orientation roughly aligned with the surface normal and a bounding box of 76×40 mm centred with respect to the phantom. A grid of 21×12 evenly spaced measurements across the ROI is acquired. The threshold level for contact detection was set to 2000 Ω.

RESULTS

Fig. 2 shows the surface map generated using the impedance measurements collected at the contact points. Specifically, the axes show the Cartesian positions (relative to the robot kinematic frame) where instrument-tissue contact was detected. Surface triangle (x, y) coordinates are determined from the Delaunay triangulation between contact points and the z coordinates are found by linear interpolation. The surface colour is mapped to the mean of the magnitude of the impedance measurements $|\bar{Z}|$ taken at that point. The black lines represent ground-truth boundaries. The map shows a clear separation of impedance values between tissue types. The triangle piece of porcine muscle in the middle is clearly visible in the map. However, its impedance values are not significantly different from the surrounding tissues except at three points.

DISCUSSION

The fact that tissue-instrument contact detection was successful at every sample point demonstrate that contact detection is robust and reliable. Since we use a bipolar instrument, contact detection is limited to when both grasper jaws are open and in contact with the tissue.
A qualitative assessment of the resulting surface map confirms that we are able to distinguish between different tissue types. Autonomously measurements using a robot lets us accurately control sample positions, pressing depth d and grasper jaw opening L. However, other factors such as blood on the tissue surface can greatly reduce the trustworthiness of measurements. Although we can distinguish between different tissue types, further studies are required to evaluate how the method will perform in distinguishing pathological tissues from healthy ones.
In this work, we demonstrated the feasibility of an autonomous REAS and experimentally evaluated its performance in ex-vivo conditions. The preliminary results are encouraging but also affected by many limitations. The results motivate future research to improve the actual acquisition performance and push the system closer to clinical applicability.
Future work will improve the scanning pattern by substituting the evenly-spaced grid with an adaptive grid to sample more densely in regions with significant EBI measurement difference, which could correspond to

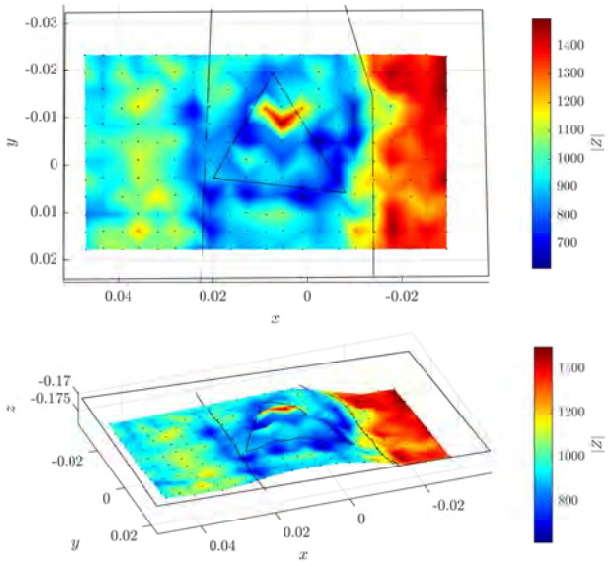

Fig. 2 Surface map (seen from different viewing angles) showing the result of the phantom acquisition. Surface points are extracted from robot kinematics and the surface colour is mapped to the mean of the corresponding impedance magnitude values $|\bar{Z}|$, measured in Ω. Black lines represent boundaries between different tissue types and the outer edge.

pathological regions. Another improvement will be related to multi-modal data fusion, in particular, the integration with stereo endoscopic images to obtain information about surface properties in the ROI thus optimize acquisition parameters, e.g. by adapting instrument tip orientation to surface normal estimation. Finally, we aim to test the proposed system in more realistic conditions, such as in-vivo animal trials and to discriminate between healthy and pathological areas of the same organ.

ACKNOWLEDGEMENT

This research is funded by the ERC project ARS under the EU H2020 research and innovation programme (grant agreement No 742671).

REFERENCES

[1] R. H. Taylor *et al.*, 'Medical Robotics and Computer-Integrated Surgery', in *Springer Handbook of Robotics*, 2nd ed., 2016.

[2] G.-Z. Yang *et al.*, 'Medical robotics—Regulatory, ethical, and legal considerations for increasing levels of autonomy', *Science Robotics*, 2017.

[3] D. Dall'Alba *et al.*, 'EL.I.S.A.: Electric Impedance Sensing for Surgical Applications', *Hamlyn Surgical Robot Challenge*, 2018.

[4] Y. Zou *et al.*, 'A review of electrical impedance techniques for breast cancer detection', *Med. Eng. & physics*, 2003.

[5] Z. Cheng *et al.*, 'A New Venous Entry Detection Method Based on Electrical Bio-impedance Sensing', *Annals of Biomedical Engineering*, 2018.

[6] Z. Cheng *et al.*, 'Design and integration of electrical bio-impedance sensing in surgical robotic tools for tissue identification', *Workshop on New Technologies for Computer/Robot Assisted Surgery*, 2018.

[7] P. Kazanzides *et al.*, 'An open-source research kit for the da vinci surgical system', in *IEEE Intl. Conf. on Robotics and Auto. (ICRA)*, 2014.

Surgical Action Recognition with Spatiotemporal Convolutional Neural Networks

Giacomo De Rossi[1], Nicola Piccinelli[1], Francesco Setti[1], Riccardo Muradore[1], Fabio Cuzzolin[2]

[1]*University of Verona;* [2]*Oxford Brookes University*

[giacomo.derossi, nicola.piccinelli, francesco.setti, riccardo.muradore]@univr.it

fabio.cuzzolin@brookes.ac.uk (DOI10.31256/HSMR2019.17)

INTRODUCTION

The ability to recognize gestures in a minimally-invasive surgical scenario is key towards greater integration of automated systems that could support surgeons during everyday operations. For instance, it can act as a post-operational tool for quality assessment and surgeons training or it can be integrated as a high-level supervisor over both manual and fully autonomous surgeries. To this end, the implementation of a real-time recognition algorithms capable of distinguishing among fine-grained surgical gestures, which are instances of generic representations called "*surgemes*" [1], becomes necessary. This work applies a combined *Spatiotemporal Convolutional Neural Network* that interpolates temporal features to correctly pinpoint the occurrence of gesture variations and provides the overall segmentation confidence for further analysis. Thanks to its reduced computational profile and overall performance, it allows for real-time action segmentation specifically tuned on surgical gestures.

MATERIALS AND METHODS

We tested our neural network on both the suturing subset of the *JHU-ISI Gesture and Skill Assessment Working Set* (JIGSAWS) [2] and a simplified dataset of human-robot cooperation tasks recorded on the premises to test the viability as a supervisory control. Both datasets are recorded in a more controlled environment than a real Robotic Minimally-Invasive Surgery (R-MIS) laparoscopy, still they contain the main gestures required from a surgeon to perform most real-world tasks.

The system analyses each video frame in the RGB colour space augmented by a *Motion History Image* (MHI) computed as a difference of previous frames over 2 seconds. This simple augmentation technique helps in maintaining a temporal relationship during the frame-by-frame feature extraction phase. After the extraction of each set of features $\mathbf{u}_i, i = 1 \dots t$ by the spatial convolutional network, these are processed by a second network focussing on temporal filtering to identify the changes in action in the entire video stream. Whereas the spatial network is a straightforward variation on a VGG-16 [3] structure to include an additional image layer (**Fig.1**, bottom), the temporal network is a novel approach that modifies the standard *autoencoder* hourglass structure found in [4] to improve its filtering performances by the introduction of an interpolating layer in place of the

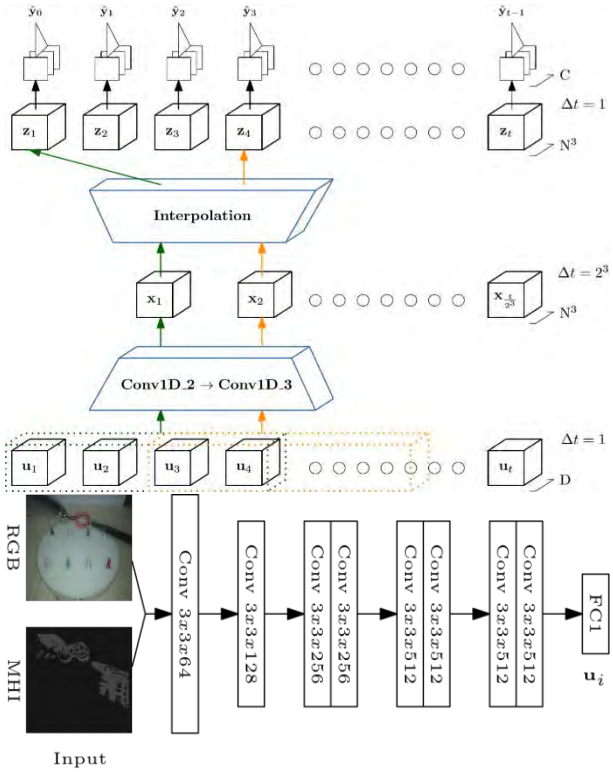

Fig.*1* Spatial (bottom) and Temporal (top) convolutional networks operating on augmented images of laparoscopy tools manipulation tasks.

decoder phase (**Fig.1**, top). Additionally, all pooling operations used for dimensional reduction have been replaced by convolutional stride operations to maintain sampling consistency over temporal data. For these reasons, we call the network *Time-Interpolated Fully-Convolutional* (*TIFC*).

The interpolating function is a piecewise linear approximation composed of segments $S(t) = \{s_1(t), \dots, s_k(t)\}$ such as $s_k(t) = (\boldsymbol{x}_{k+1} - \boldsymbol{x}_k)(t - k) + \boldsymbol{x}_k$ given a reconstructed timeline on

$$t \in \left\{ t_i \in \mathbb{Q}^+ \mid t_i = \frac{|x|}{|\hat{\boldsymbol{y}}|} i, i = 0, \dots, |\hat{\boldsymbol{y}}| \right\},$$

where $\boldsymbol{x}_k$ is the input vector at sample index k, $|\hat{\boldsymbol{y}}|$ is the desired size for the estimated output vector. The expression of $S(t)$ becomes

$$S(t) = \sum_{k=1}^{|\hat{y}|} s_k(t)\chi_{[k,k+1)}(t)$$

assuming χ as an indicator function which is non-zero only in the specified interval. The output is the response of the network at its middle layer expanded over the temporal dimension, called $\hat{\boldsymbol{Y}} = \{\boldsymbol{y}_i\}_1^t$, thus comparable with the desired response $\boldsymbol{Y}$.

RESULTS

The proposed solution has been tested against alternative algorithms available in literature to solve the action segmentation problem from video streams. The test focussed primarily on the JIGSAWS dataset given its widespread usage and availability of first-hand results. The evaluation strategy follows a *Leave One User Out* approach for cross-validation to both maximize the adaptability to different gesture styles as performed by multiple users and to minimize the incidence of overfitting. The results presented in **Tab.1** for our network are the mean of all the cross-validations. The compared metrics are:

- the *accuracy*, which is the percentage of true positives and negatives identified by the model;
- the *edit score* [5], which is the percentage of correctly segmented actions evaluated over non-repetitive label sequences (for example, the sequence *{ABC}* compared with *{AAABBC}* would obtain a score of 100%, since the amount of repetitions is irrelevant)
- the *F1*, which is the harmonic mean between precision and recall.

Algorithm	Accuracy	Edit Score	F1
MsM-CRF[2]	77.29	n.a.	n.a.
ED-TCN[4]	81.4	83.1	87.1
TricorNet[6]	82.9	86.8	n.a.
TIFC [our]	81.97	86.9	91.1

Tab.1 Comparison between comparable approaches for action segmentation available in literature (results are percentages).

The most similar network structure, the *ED-TCN* [4], reaches a top score of 83.1% with the same *leave one user out* validation; the closest results are achieved by the more complex hybrid convolutional and recurrent network *TricorNet* [6] that does not use a user-focused validation technique but a more generic random split between training and testing data.
Figure 2 presents visually a segmentation operated on one sample of the JIGSAWS dataset.

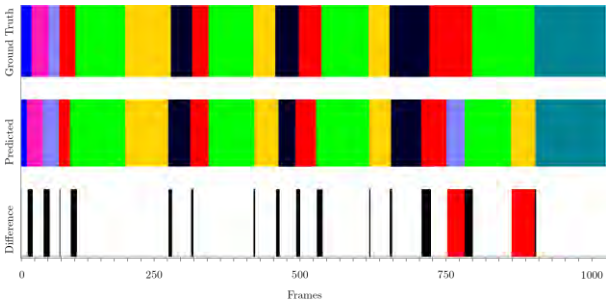

Fig. 2 Result of the temporal segmentation over one sample of the JIGSAWS dataset: the top two plots illustrate the sequences of true and predicted gestures; in the bottom plot, the black lines indicate temporal shift while the red lines indicate mispredicted labels.

DISCUSSION

The *TIFC* improves the state of the art for fine-grained action recognition and reaches the limit imposed by manually-annotated action labels in videos. It introduces a novel topology that incorporates an interpolation procedure following a filtering via linear convolution layers with re-sampling. It improves, additionally, on the overall time required to evaluate the sequences, once the network is trained. The combined improvements represent another step towards high-level, real-time semi-autonomous control systems based on gesture recognition within the operating rooms.

REFERENCES

[1] C. E. Reiley and G. D. Hager, "Task versus subtask surgical skill evaluation of robotic minimally invasive surgery," *Lect. Notes Comput. Sci. (including Subser. Lect. Notes Artif. Intell. Lect. Notes Bioinformatics)*, vol. 5761 LNCS, no. PART 1, pp. 435–442, 2009.

[2] N. Ahmidi *et al.*, "A Dataset and Benchmarks for Segmentation and Recognition of Gestures in Robotic Surgery," *IEEE Trans. Biomed. Eng.*, vol. 64, no. 9, pp. 2025–2041, 2017.

[3] K. Simonyan and A. Zisserman, "Very deep convolutional networks for large-scale image recognition," *arXiv Prepr. arXiv1409.1556*, 2014.

[4] C. Lea, M. D. Flynn, R. Vidal, A. Reiter, and G. D. Hager, "Temporal convolutional networks for action segmentation and detection," *Proc. - 30th IEEE Conf. Comput. Vis. Pattern Recognition, CVPR 2017*, vol. 2017–Janua, pp. 1003–1012, 2017.

[5] L. Yujian and L. Bo, "A Normalized Levenshtein Distance Metric," *IEEE Trans. Pattern Anal. Mach. Intell.*, vol. 29, no. 6, pp. 1091–1095, 2007.

[6] L. Ding and C. Xu, "TricorNet: A Hybrid Temporal Convolutional and Recurrent Network for Video Action Segmentation," pp. 1–10, 2017.

Deep Q Reinforcement Learning for Autonomous Navigation of Surgical Snake Robot in Confined Spaces

S. Athiniotis, R. A. Srivatsan and H. Choset

Robotics Institute, Carnegie Mellon University,

sathinio@andrew.cmu.edu (DOI10.31256/HSMR2019.18)

INTRODUCTION

Airway management is fundamental for all anesthetic as well as emergency medicine procedures to maintain airway patency, prevent aspiration and permit ventilation without leakage. While endotracheal intubation and tracheostomy are regarded as the go-to procedures in such incidents, they are reportedly correlated with numerous side effects which can sometimes even be life-threatening [1]. These complications stem from the fact that essentially a human is blindly and manually maneuvering the intubation tube. In order to mitigate the ensued risks and aftereffects of currently employed methods, this work uses a surgical snake robot [2] to autonomously navigate down the airway.

The contribution of this paper is developing the navigation policy that utilizes images from a monocular camera mounted on its tip. We use Q Reinforcement Learning in Deep Convolutional Neural Networks (DCNN) [3], widely referred to as Deep Q Reinforcement Learning Neural Networks (DQNN), to produce these policies. The system can serve as an assistive device for medical personnel to perform endoscopic intubation, with minimal to no human input.

MATERIALS AND METHODS

Reinforcement learning (RL) has proven to be a successful tool for autonomous navigation and control over the past years. The objective of RL is to learn good policies for sequential decision problems by optimizing accumulated reward indicators [4]. In particular, learning to control agents from sensory data like vision, had been of great interest to the community [5, 6], including advancements introduced by Google DeepMind [3]. Most methods employ DCNN in Q learning implementations of RL algorithms. These innovative approaches empower agents to accurately predict optimum courses of thousands of sequential actions, in the presence of noisy input data in dynamic environments.

Although deep RL is currently facing an unprecedented resonance in the majority of engineering fields, it has not yet been used widely in the medical domain. To the best of our knowledge, no existing literature suggests its deployment for endoscopic intubation. This paper demonstrates that a DQNN framework can accurately enable a flexible snake robot to navigate inside a patient's airway using camera images (Fig 1 (b)).

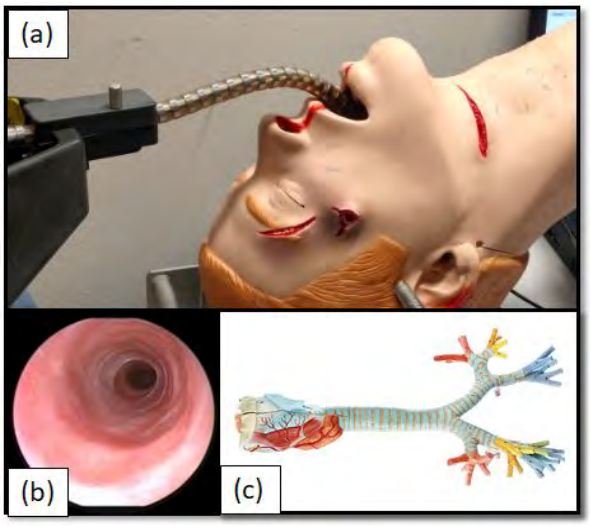

Fig. 1 (a) Surgical snake robot in assistive respiration. (b) Image of trachea as seen from the camera on the head of the robot. (c) The trachea is a non uniform curved tube of length 100-120 mm and diameter 18-20 mm.

Given the inter-patient variability as well as poor lighting and featureless environment, conventional motion planning and computer vision algorithms do not produce results with high levels of confidence. However, data driven RL algorithms rely solely on information from the unknown Markovian[1] environment. Hence, eliminating the prevalent need of most machine learning methods for large labeled datasets. Therefore we consider RL.

In this work, a surgical snake robot (see Fig. 1 (a)) plays the role of the agent[2]. The underline control algorithm interprets its state by propagating the camera's live feed through the DCNN and predicting the optimum action. In order to train the network in a realistic context, we formulated a Gazebo simulation as shown in Fig 2. Since the robot is a follow-the-leader mechanism [2], we restrict our learning to the actions of the tip of the robot alone. This helps reduce the computational complexity of the model and significantly accelerates the training time.

The sensory input supplied to the system are 84×84×3 RGB images from a camera mounted at the tip of the robot's head which carries its own light source.

[1]Markovian is used to describe a fully observable environment where the state transition probability function depends on the future state given the present state [4].

[2]In RL, agent is the entity that learns how to perform the intended task (for example robot, vehicle, etc.) [4].

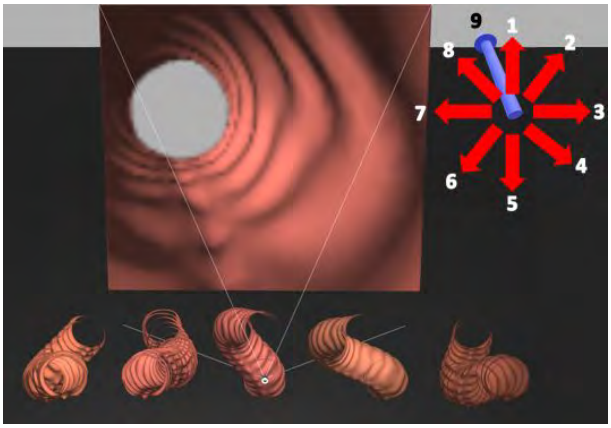

Fig. 2 Gazebo training environment including the agent (snake scope head), five different trachea models on which the DCNN was trained, the projection of the camera frame and the 9 discrete actions the agent is allowed to take.

The DCNN has 4 convolutional hidden layers followed by 2 fully connected layers which are split into two to form the proposed dueling structure [6]. The number of outputs is equal to the discrete number of possible actions that the agent is allowed to take, which in our case is 9 (See Fig. 2). In each of the defined actions, the head of the snake is oriented to the desired pitch/yaw by 5 deg and then advanced one step in the forward direction by 0.5 mm.

The network is iteratively trained for 80,000 episodes using stochastic gradient descent to update the weights over a batch of 32 experiences. The exploration rate, which reflects to the randomness of the selected actions, is linearly decreased from 100% to 1% after 70,000 episodes (see Fig. 3). The reward function is defined such that the further the distance traversed, higher the assigned reward. The termination conditions for each episode are - (1) Reaching the end of the trachea, (2) completing more steps than allowed, and (3) colliding with the walls. In order to detect collision between the solid bodies, two 2D lasers were mounted on the coronal and transverse plane of the agent. However, they will not be included in the actual experiment and they are only used for ease of collision detection in simulation.

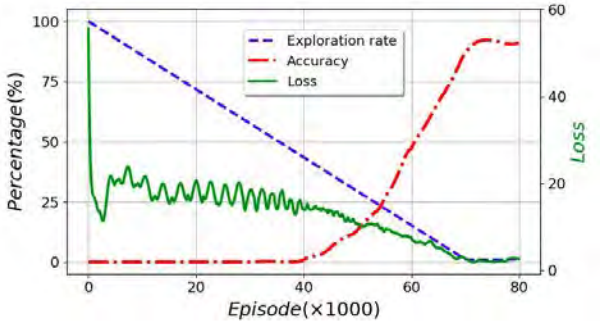

Fig. 3 Accuracy and loss versus number of training episodes.

In order to improve the robustness to different environments, and smoothly transfer to real world scenarios, domain normalization [7] is implemented by:

- Adding Gaussian noise to the camera data
- Varying the color of each model
- Randomizing agent's initial position and pose
- Randomly selecting a trachea model every 10 episodes

The following hyperparameters for the learning algorithm were hand-tuned through iterative trainings: discount rate=0.98, learning rate=0.0005, collision penalty=40, completion reward=100, buffer memory size=60,000 and batch size=32.

RESULTS

In Fig. 3 we present the resulting accuracy over training episodes, which eventually converged to 92%. In our setup, accuracy is calculated as the number of successes in 100 consecutive episodes, where success is counted only if the agent reaches the end of the trachea without meeting any of the other two terminating conditions [3]. We also present the mean loss of each episode of our training in Fig. 3, which is calculated as the average of the quadratic loss values over all steps of an episode.

DISCUSSION

We have implemented an autonomously navigating agent within a trachea using DQNN. This is challenging because the trachea is highly confined and thus two consecutively wrong actions could have inevitably lead to unwanted collision, i.e. failure. To address this challenge, we implemented a reinforcement learning approach, which produces policies that only select the appropriate action to navigate. We believe the approach in this paper can serve as an assistive device for a broad spectrum of endoscopic procedures. Of particular interest to the authors involve extending this approach to natural orifice transluminal surgery (NOTES) and endoscopic submucosal dissection (ESD).

REFERENCES

[1] J. Divatia and K. Bhowmick. Complications of endotracheal intubation and other airway management procedures. *Indian J Anaesth*, 49(4):308-318, 2005.

[2] A. Degani, H. Choset, A. Wolf, and M. A. Zenati. Highly articulated robotic probe for minimally invasive surgery. In *Proceedings ICRA,* 2006. (pp. 4167-4172).

[3] V. Mnih, K. Kavukcuoglu, D. Silver, A. Graves, I. Antonoglou, D. Wierstra and M. Riedmiller. Playing Atari with Deep Reinforcement Learning. *arXiv preprint arXiv:1312.5602,* 2013.

[4] R. S. Sutton and A. G. Barto. Reinforcement learning: An introduction. *MIT press,* 2018.

[5] V. H. Hado, A. Guez, and D. Silver. Deep Reinforcement Learning with Double Q-Learning. In 30th *AAAI Conference on Artificial Intelligence*, 2016.

[6] Z. Wang, T. Schaul, M. Hessel, H. V. Hasselt, M. Lanctot, and N. De Freitas. Dueling Network Architectures for Deep Reinforcement Learning. *arXiv preprint arXiv:1511.06581,* 2016.

[7] V. H. Hado, A. Guez, M. Hessel, V. Mnih and D. Silver. Learning values across many orders of magnitude. *arXiv preprint arXiv:1602.07714,* 2016.

[3] See experimental result in this Video link

Autonomous Detection of *C. diff* Toxins in Clinical Stool Using A Magnetic Microrobotic System

Lidong Yang, Yabin Zhang, and Li Zhang

Department of Mechanical and Automation Engineering, The Chinese University of Hong Kong (CUHK), Shatin NT, Hong Kong SAR, China (DOI10.31256/HSMR2019.19)

INTRODUCTION

Clostridium difficile (*C. diff*) is a gastrointestinal pathogen and the leading cause of health-care-associated infection (e. g. diarrhea and pseudo-membranous colitis) in the USA and developed countries [1]. Since the year of 2000, more than 300,000 hospitalizations involve *C. diff* infection (CDI) each year with an annual cost of 1.0 to 4.9 billion to the US health care system [2]. CDI is a toxin-mediated disease and *C. diff* secretes two major toxins, i.e. toxins A (TcdA) and B (TcdB), that are clearly responsible for diarrhea and colitis. Therefore, a timely and accurate detection method for these toxins is significant for early diagnosis of CDI, timely infection control and pharmacological treatment. To date, a series of detection methods targeting one or both toxins through conjugation techniques have been developed, such as the enzyme immunoassays, cell culture cytotoxicity neutralization assay, glutamate dehydrogenase assay, and molecular assays [3]. However, these approaches have limitations, such as high analytical cost, strong dependence on reference, long turnaround time (usually 24-28 h for cell cytotoxicity assay), specificity in the laboratory diagnosis setting and professional skills. In view of the current situations, an automated, rapid and low-cost detection method for *C. diff* toxins is highly required for the clinician to make an early diagnosis and timely treatment.

MATERIALS AND METHODS

This paper presents a magnetic microrobotic system and related methods that enable the autonomous and rapid detection of toxins secreted by *C. diff* that exist in patient's stool. The fluorescent magnetic spore-based microrobot (FMSM), as a microscale mobile sensing tool, is used to efficiently detect *C. diff* toxins by utilizing its property of selective fluorescence responses: the contact and reaction with *C. diff* toxins cause its fluorescence decay. The obtained FMSMs are shown in Fig. 1(a) by batch fabrication. The fluorescence images in Fig. 1(b) demonstrate the high fluorescence performance of the FMSMs. Very recently, our report [4] has confirmed that the FMSM has fluorescence response selectivity.

This selectivity is mainly caused by the oligosaccharide and related groups on the FMSMs that are formed on the surface of carbon dots during the hydrothermal process. The interaction between oligosaccharide and related groups and combined repetitive oligopeptides (CROPs) on the C. diff toxins would cause the fluorescence decay of the carbon dots. The Smart BLAST (provided by National Center for Biotechnology Information online) survey result indicates that, in gastrointestinal (GI) tract, the CROPs segment and its high matched sequences can only be observed in TcdA/TcdB and cell wall proteins of *C. diff* [4]. These results support the specific detection capability of FMSMs to *C. diff* toxins and exclude the possibility of false positive detection caused by the interference of other toxins and bacteria in clinical samples.

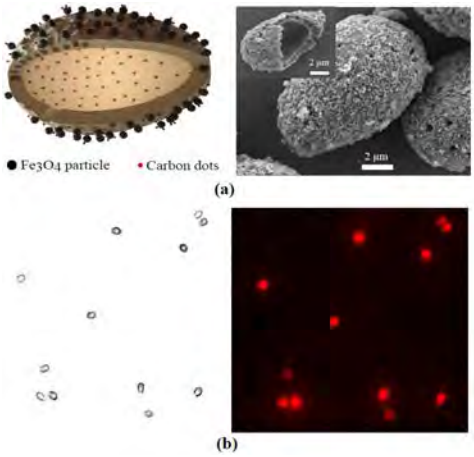

Fig. 1 (a) Schematic diagram (left) and scanning electron microscopy (SEM) images (right) of the fabricated FMSMs. The Fe_3O_4 nanoparticles coated on the outside wall is for magnetic actuation. The carbon dots coated on the outside and inside walls are for fluorescence imaging based C. diff toxins detection. Please note that, in the schematic diagram, the particles are not with the real size. (b) Bright-field image and dark-field fluorescence image of the FMSMs with red light emission under green light excitation [4].

The overall magnetic microrobotic system is illustrated in Fig. 2. The electromagnetic coil system, i.e. MagDisk [5], consists of five independent electromagnets enabling its capability of generating the rotating fields for actuation of FMSM with tumbling motion with over 20 Hz. An inverted fluorescence microscope with a fluorescence illuminator is for fluorescence imaging of the FMSMs. An sCMOS camera provides vision feedback to the host computer, which implements the image processing, automated motion control, magnetic field control and data processing algorithms. The FMSMs and sample solution are placed in a glass tank. The glass tank locates in the middle of the MagDisk workspace (about 20 mm*20 mm), and it is connected to a 2 degree-of-freedom (DoF) sample positioning stage for adjusting the field of view of the microscope. The relevant magnetic field parameters are computed and delivered to the servoamplifier for driving the electromagnetic coils.

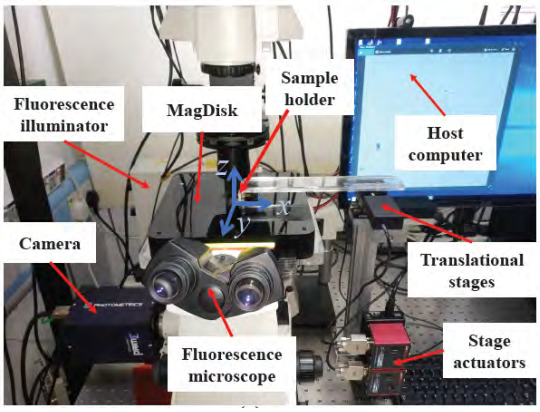

Fig. 2 The lab-constructed magnetic microrobotic system for autonomous detection of *C. diff* toxins in clinical stool.

In order to automatically control the microrobot navigation and obtain the fluorescence parameter variation of the FMSM, a simultaneous motion tracking and fluorescence extraction method is proposed. Then a navigation trajectory and a trajectory following control method are proposed to let the FMSM autonomously navigate in the entire workspace to contact with the toxins. After at most 20 minute's navigation, the detection result is given immediately based on the recorded fluorescence data.

RESULTS

Clinical stool samples are provided by healthy volunteers and C. diff -positive patients from the Prince of Wales Hospital (Shatin, Hong Kong). Similar to the treated supernatants of clinical stool samples that commonly used for ELISA (TGC-E002-1, tgcBIOMICS GmbH, Germany), stool specimens (about 2 g) are cut, re-dispersed in PBS (about 2 mL) and then made to supernatants for use. The toxin concentration of the infected sample is determined as C = 8.66 ng/mL by ELISA. Then, the stock solution is diluted into different concentration groups (form 0.01C to 0.5C) for use in the autonomous detection experiments.

Fig. 3 shows that the proposed method can well extract the FMSM although the background noise varies. By using this method, the fluorescence inensity of the FMSM is accurately obtained in real-time. Baesd on the variation of the data, the qualitative detection result is obtained as illustrated in Fig. 4 where the dramatic fluorescence decrease is only captured in the infected stool sample.

CONCLUSION

An autonomous, rapid and low-cost *C. diff* toxin detection technique for clinical stool has been presented. The magnetic microrobotic system and image processing method are introduced whose effectivenees is validated by experiments on clinical stool. The autonomous detection finishes within 20 min which is at least 8 times shorter than that of the ELISA used in Prince of Wales Hospital (Shatin, Hong Kong). The proposed technique has good competency for future clinical use.

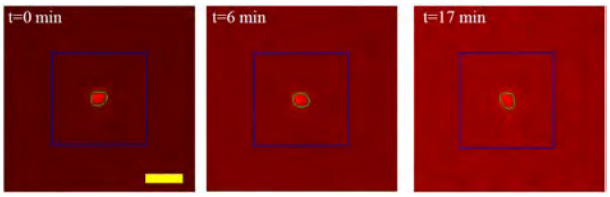

Fig. 3 Effectiveness test and performance of the proposed image gradient-based method for accurately extacting the FMSM from feedback images with varied background noise. Length of the scale bar is 15 um.

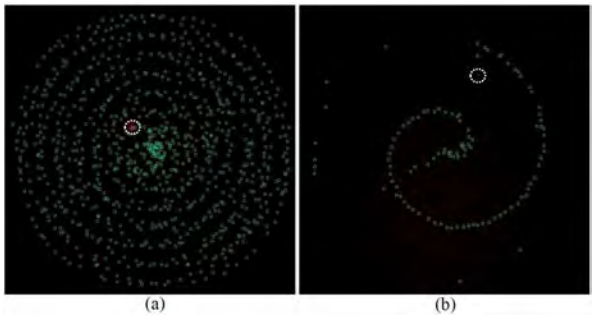

Fig. 4 Autonomous detection results for clinical normal stool (a) and infected stool (0.5C) (b). Small green circles represent the navigation points where fluorescence intensity of the FMSM are above the threshold value (50) of the qualitative detection criterion. White dashed circles mark the FMSMs when the navigation process finishes.

ACNOWLEDGEMENT

The research leading to these results has received funding support from the Hong Kong Research Grants Council (RGC) with Project No. 14203715 and 14218516.

REFERENCES

[1] S. S. Magill, J. R. Edwards, W. Bamberg, Z. G. Beldavs, G. Dumyati, M. A. Kainer, R. Lynfield, M. Maloney, L. McAllister-Hollod, J. Nadle, et al., "Multistate point-prevalence survey of health care–associated infections," *N. Engl. J. Med.*, vol. 370, no. 13, pp. 1198–1208, 2014.

[2] C. R. Polage, C. E. Gyorke, M. A. Kennedy, J. L. Leslie, D. L. Chin, S. Wang, H. H. Nguyen, B. Huang, Y.-W. Tang, L. W. Lee, et al., "Overdiagnosis of clostridium difficile infection in the molecular test era," *JAMA Intern. Med.*, vol. 175, no. 11, pp. 1792–1801, 2015.

[3] L. Alcala, L. Sanchez-Cambronero, M. Catalan, M. Sanchez-Somolinos, M. Pelaez, M. Marin, and E. Bouza, "Comparison of three commercial methods for rapid detection of clostridium difficile toxins a and b from fecal specimens," *J. Clin. Microbiol.*, vol. 46, no. 11, pp. 3833–3835, 2008.

[4] Y. Zhang, L. Zhang, L. Yang, C.-I. Vong, K.-F. Chan, W. K. K. Wu, T. N. Y. Kwong, N. W. S. Lo, M. Ip, S. H. Wong, J. J. Y. Sung, P. W. Y. Chiu, and L. Zhang, "Real-time tracking of fluorescent magnetic sporebased microrobots for remote detection of c. diff toxins," *Sci. Adv.*, vol. 5, no. 1, p. eaau9650, 2019.

[5] L. Yang, Y. Zhang, C.-I. Vong, and L. Zhang, "Automated control of multifunctional magnetic spores using fluorescence imaging for microrobotic cargo delivery," in *2018 IEEE/RSJ Int. Conf. Intell. Robot. Syst. (IROS)*. IEEE, 2018, pp. 6180–6185.

Gaze-contingent Robotic Flexible Endoscopy

A. A. Kogkas[1], B. Glover[3], N. Patel[3], A. Darzi[2], G. P. Mylonas[1]

[1]HARMS Lab, [2]Department of Surgery and Cancer, Imperial College London, UK

[3]Department of Gastroenterology, Imperial College London, UK

a.kogkas15@imperial.ac.uk (DOI10.31256/HSMR2019.20)

INTRODUCTION

Flexible endoscopy is a common medical technique used for diagnosis in the upper and lower gastrointestinal (GI) tract. The flexible endoscope consists of a flexible tube, up to two working channels for insertion of flexible instruments, a camera and a light source at the distal end (tip). Bending the tip left-right and up-down, is achieved by rotating two dials with one hand, whilst the other hand is used for rotating, inserting and retracting the endoscope shaft. Often, more than one operator is needed for effective manipulation. As a result, the conventional control of a flexible endoscope creates challenges, such as poor ergonomics, inefficient handling of the endoscopic tip and suboptimal collaboration [1].

Therefore, the development of an intuitive interface to overcome these challenges is deemed necessary. Robotization of the existing flexible endoscopes has been attempted in previous studies [2, 3]. In [4] we proposed a gaze-controlled robotized system, which allows hands-free control of the endoscopic view in an intuitive fashion, using the natural gaze of the user to steer the endoscope tip. Evaluation with novice users showed improved performance and preference over traditional hand control. Limitations of this system include the lack of motorization of the rotation, insertion and retraction of the shaft of the endoscope and the restricted positioning of the user in front of a screen, due to the use of screen-based eye-tracking sensors.

In this study, we propose a fully motorized gaze-controlled system for non-restricting, free-view flexible endoscopy. The feasibility and comparison against traditional hand control are assessed. Simulated examination of the upper GI tract is performed by novice users.

SYSTEM OVERVIEW

The system presented here allows a user to remotely control the endoscope movements without handling the device, while expert endoscopist studies art currently ongoing. A flexible gastroscope is attached to an articulated robotic arm, mounted onto a rail and placed on top of a surgical table (Fig. 1). The dials used to control the distal tip steering are motorized using two 3D printed gears and two motors, controlled by a gaze-contingent closed loop velocity controller. Gaze on the screen is estimated based on a 3D gaze reconstruction framework we developed [5] with the synergy of conventional wearable eye-tracking glasses, a motion capture system and fixed in space RGB-D cameras for real-time 3D reconstruction of the environment. The robot controls the endoscope shaft rotation and insertion/retraction. The former is controlled with the head sideways rotations and the latter with a joystick handle, which also allows features such as system pause and automatic retroflexion. Audio feedback is provided when the user enables rotation, pauses the system or enables retroflexion.

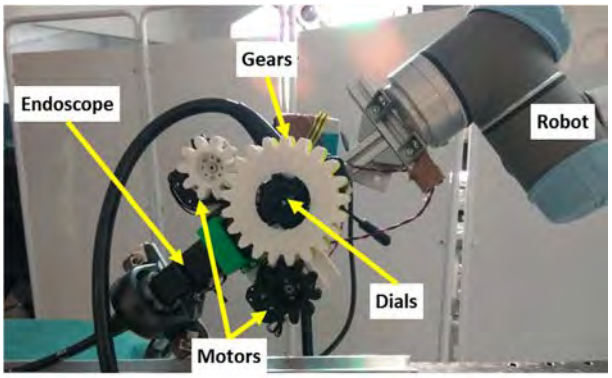

Fig. 1 The robotized flexible endoscope mounted on the UR5.

MATERIALS AND METHODS

Free-view gaze interaction with the screen is achieved with the real-time framework presented in [5]. Its core functionality is to provide the user's 3D point of regard in space. It relies on estimating the pose of the eye-tracker scene camera in the world frame, and tracing the gaze ray provided on the head frame of reference, onto the 3D reconstructed space. For the work presented here, the head pose is estimated with the employment of the OptiTrack motion capture system. Spherical markers are mounted on the eye-tracker to form an asymmetric rigid body and allow OptiTrack to provide its unique 6 degrees of freedom (DOF) pose in space. The rigid transformations between the rigid body –eye-tracker scene camera and OptiTrack– world coordinate system are calibrated. By using the hybrid macro/micro-scale model presented in [6], the mode (macro or micro) and the 2D screen fixation (for micro mode) is provided as output.

For gaze control, the PID controller presented in [4] is employed, which relies on the distance between the fixation point on the screen and the center of the screen.

The rotation of the endoscope is achieved by rotating the end-effector of the robot with a constant speed. It is initiated with the rotation of the user's head on the eye-tracker's scene camera's z-axis, above a predefined angular threshold. The head orientation reference is defined at the beginning of the experiment.

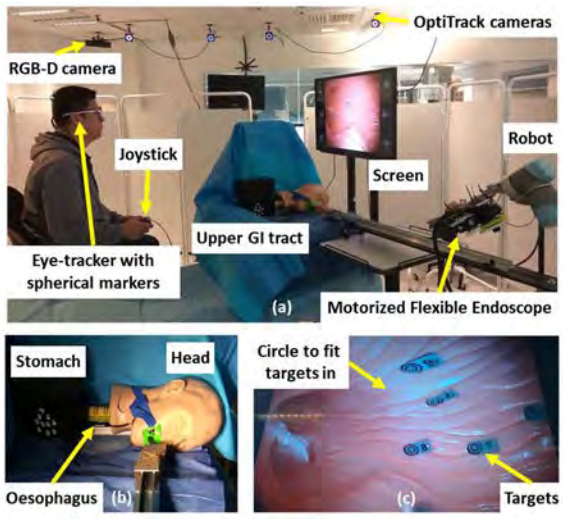

Fig. 2 (a) The experimental setup. (b) The upper GI tract phantom and (c) the camera view of the targets.

Insertion and retraction of the endoscope is implemented with the linear movement of the robot with constant velocity. It is triggered by a joystick (up/down respectively) connected to an Arduino Uno which streams data to the system PC.

Retroflexion of the distal tip is activated by holding the joystick to the right for 1 *s*. The system is paused (motors and robot remain idle) by pushing the joystick handle and is enabled by pushing the joystick again. No action is performed when user's gaze is outside the screen.

For eye-tracking, the SMI (SensoMotoric Instruments GmbH) glasses are used. For RGB-D sensing, the Microsoft Kinect v2 is used and for head pose tracking the OptiTrack motion capture system with four Prime 13 cameras. The robot arm is a UR5 by Universal Robots. Two Dynamixel RX-24F motors were employed for the motorization of the endoscope. For the endoscopic task view, a 42″ LG screen with 1920x1080 px resolution is used. The endoscope is a flexible gastroscope (Karl Storz 13801 PKS).

EXPERIMENTAL SETUP

The evaluation task simulates a diagnostic gastroscopy using gaze or hand (conventional) control. The experimental setup involves a head phantom, a silicon tube to simulate the oesophagus and a stomach phantom filled with 10 numbered targets (Fig. 2b,c). Seven subjects, 6 males and 1 female, between the ages of 26 and 35 with normal uncorrected vision, were invited to take part in the study. After informed consent, the subjects were taken through the experimental setup, starting either with the gaze- or hand-control setup, in randomized order, and given time to familiarize themselves with it. Each subject was then instructed to intubate the oesophagus, locate and fit the targets in ascending order within a circle drawn at the center of the screen (Fig. 2c).

RESULTS

All the subjects were able to independently intubate the oesophagus and accurately locate ten targets placed in the stomach using the gaze-controlled system and the traditional hand control. The average time to complete the task with gaze was 2:04±0:30 minutes vs 03:40±01:00 with hand control. Significant difference between the two modalities at the $p<.05$ level [$F(1, 14) = 16.32$, $p = 0.001$] is found. NASA-TLX questionnaires show preference in gaze control (84±12%) over hand control (33±17%) and significant difference at the $p<.05$ level [$F(1, 12) = 41.55$, $p<.001$] (Fig. 3).

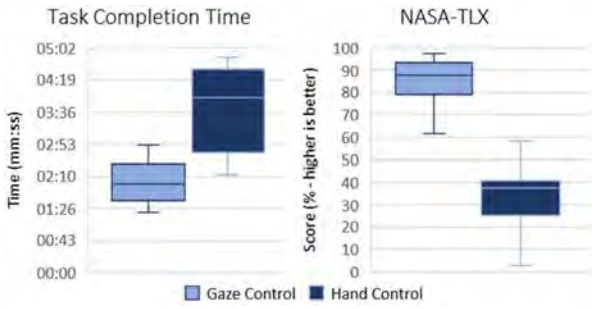

Fig. 3 Results of task completion time (left) and NASA-TLX (right) for both gaze- and hand-control modalities.

DISCUSSION

A fully robotized gaze-contingent flexible endoscope has been presented, which allows touchless control of a flexible endoscope in a free-viewing fashion. Testing with non-endoscopist subjects in a simulated diagnostic gastroscopy (upper GI) showed that gaze controlled endoscopy is a feasible concept. It allows ergonomic, user-friendly and intuitive control whilst maintaining the benefits of a flexible endoscope. Further experiments involving expert endoscopists are ongoing.

AAK is supported by the NIHR Imperial Biomedical Research Centre (BRC).

REFERENCES

1. Cao, C.G.L., Milgram, P.: Disorientation in minimal access surgery: A case study. In: Proceedings of the Human Factors and Ergonomics Society Annual Meeting. pp. 169–172 (2000).
2. Kume, K., Kuroki, T., Sugihara, T., Shinngai, M.: Development of a novel endoscopic manipulation system: The Endoscopic operation robot. World J. Gastrointest. Endosc. 3, 7, 145 (2011).
3. Pullens, H.J.M., van der Stap, N., Rozeboom, E.D., Schwartz, M.P., van der Heijden, F., van Oijen, M.G.H., Siersema, P.D., Broeders, I.A.M.J.: Colonoscopy with robotic steering and automated lumen centralization: a feasibility study in a colon model. Endoscopy. 48, 03, 286–290 (2016).
4. Vrielink, T.J.C.O., Puyal, J.G.-B., Kogkas, A., Darzi, A., Mylonas, G.: Intuitive Gaze-Control of a Robotized Flexible Endoscope. In: 2018 IEEE/RSJ International Conference on Intelligent Robots and Systems (IROS). pp. 1776–1782 (2018).
5. Kogkas, A.A., Darzi, A., Mylonas, G.P.: Gaze-contingent perceptually enabled interactions in the operating theatre. Int. J. Comput. Assist. Radiol. Surg. 1–10 (2017).
6. Kogkas, A.A., Sodergren, M.H., Darzi, A., Mylonas, G.P.: Macro- and Micro-Scale 3D Gaze Tracking in the Operating Theatre. In: The Hamlyn Symposium on Medical Robotics. p. 100 (2016).

Wave-Shape Notched Compliant Joint with High Rigidity

Seunguk Kim[1], Seongbo Shim[1], Daekeun Ji[1] and Jaesung Hong[1]

[1]DGIST

jhong@dgist.ac.kr (DOI10.31256/HSMR2019.21)

INTRODUCTION

The notched compliant joint has been increasingly used in continuum manipulators for minimally invasive surgical applications. The notched compliant joint has advantages of small size, large bending angle, small bending radius and constant curvature as well as high bending rigidity against external force applied perpendicularly to the bending plane [1].

Neverthless, the notched compliant joint has low bending rigidity against external force *parallel* to the bending plane, thus leading to undesired bending posture. This undesired bending posture results in a position error of tip in the joint, which increases the risk of surgery by wrong manipulation of an instrument attached to the joint.

To overcome this drawback, we proposed a mechanism by changing the shape of the notch. Although various shapes of notch have been reported, including rectangular shape with corner-filleting, which is a typical shape of notch, triangular shape, tapered shape and rounded shape, they were designed not for improving bending rigidity but for enhancing stress distribution or avoiding permanent deformation caused by exceeding strain limit. To the best of our knowledge, the recent researches have not focused on the shape of notch to improve the rigidity to bending force.

In this study, we propose a new type of notched compliant joint based on the modified shape of the notch, which has thick spacer without losing the height of the notch. The proposed notched compliant joint showed the improved bending rigidity while maintaining maximum bending angle compared to the typical-shape notched compliant joint.

MATERIALS AND METHODS

Maximum bending angle and bending rigidity of the notched compliant joints are mainly affected by l_n, height of notch, and l_s, thickness of spacer, respectively [1] [2]. In a typically shaped notched compliant joint, if L, length of bendable section in the joint, and N, numbers of notch in one side, are determined by constrained space, l_s cannot be increased without decreasing l_n.

To solve this limitation of the typical shape of notch, by defining a new parameter h, height in the middle part of the notch, we proposed increasing l_s without decreasing l_n to improve rigidity without reducing maximum bending angle. The reason why we used the new parameter is as follows. Maximum bending angle is mainly determined by heights of inner and outer parts of the notch. From this, we found that height in the middle part of the notch is irrelevant to determining maximum bending angle.

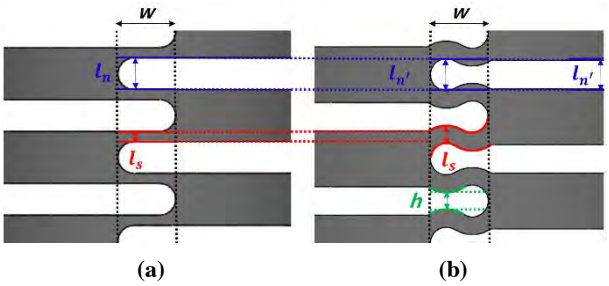

Fig. 1 Comparison of notch design between (a) typical shape and (b) wave shape

Therefore, we separated $l_{n'}$, height in the inner and outer parts of the notch, and h, height in middle part of the notch, as shown in Fig. 1(b). Then we added a protrusion in the middle part of the notch. The value of h can be adjusted by determining height of protrusion. As a result, l_s can be increased by decreasing h instead of reducing $l_{n'}$. Further, in order to enhance stress distribution and make l_s constant along the neutral line of spacer, we designed the protrusion to have a round shape with the same size of curvature in the fillet of the inner part of notch. As shown in Fig. 1, by decreasing h through adjusting height of the protrusion, the wave-shaped notch has higher l_s with same $l_{n'}$ compared to typical-shaped notch.

In addition, we demonstrated this characteristic of the wave-shaped notch mathematically. If L and d are determined, l_s and l_n have relationship of inverse proportionality in equation (2) induced from equation (1) which is the design equation of a typical-shaped notch [1]. However, equation (3) is the modified design equation of the wave-shaped notch having the new parameter, h, added by the protrusion in the middle part of the notch. Equation (4), simplified from equation (3), describes that l_s can be increased by decreasing h instead of decreasing $l_{n'}$ in a wave-shaped notch.

$$L = (2N + 1)(l_n + l_s) \tag{1}$$

$$\Delta l_s = -\Delta l_n \tag{2}$$

$$L = \frac{1}{2}(2N + 1)(l_{n'} + 2l_s + h) \tag{3}$$

$$\Delta l_s = -\frac{\Delta l_{n'}}{2} - \frac{\Delta h}{2} \tag{4}$$

Through proposed design equation for the wave-shaped notch, by setting variation of h to 0.4 *mm*, l_s increase from 0.3 *mm* to 0.5 *mm* compared to the typical-shaped

notch, while maintaining $l_{n'}$ to 0.91 *mm*, with L, OD and ID of the tube to 30 *mm*, 12 *mm* and 6 *mm* respectively.

SIMULATION RESULTS

We used the finite element modeling (FEM) package ANSYS Workbench Release 17.1 to demonstrate that the proposed wave-shape notched compliant joint has higher rigidity than the typical-shape notched compliant joint.

First, we used simplified geometry models of wave-shape and typical-shape notched compliant joints for decreasing time to solve the deformations of the joint by reducing total size and maintaining other design condition. However, all conditions of both models were identical except for shape of notch. Without external force, both models have a same displacement of tip position, d, between base and 100° bended position as much as 16.8 mm. After applying 5 N external force to the tip, The displacements in typical type, d_R and proposed type, d_W are 17.4 *mm* and 17.1 *mm* respectively, as shown in Fig.2. The result of simulation showed that the value of $|d - d_W|$, which is 0.3 *mm* as position error in tip of the wave-shape notched model, is 50 % lower than the value of $|d - d_R|$, which is 0.6 *mm* as position error in the tip of the typical-shape notched model.

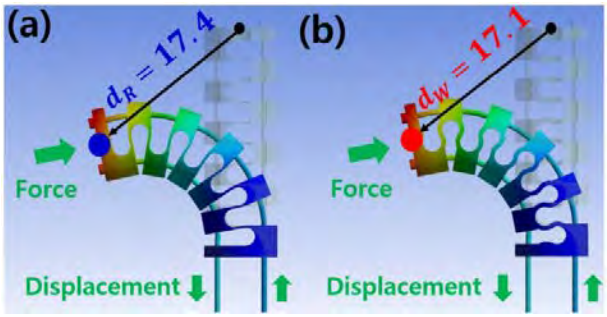

Fig. 2 Rigidity comparison between (a) typical-shape notched compliant joint and (b) wave-shape notched compliant joint

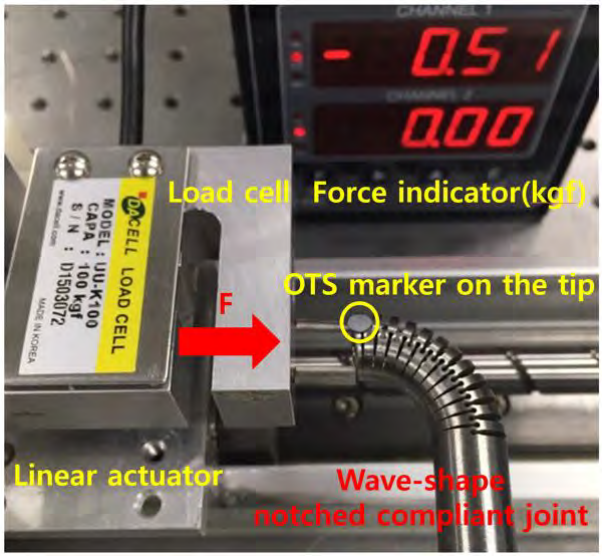

Fig. 3 Experiment for measuring position error of wave-shape notched compliant joint against external force

EXPERIMENTAL RESULTS

To measure actual positioning error of the proposed design, we manufactured a proposed wave-shape notched compliant joint in nitinol and performed the experiment. First, we bent the proposed notched compliant joint with 100° angle and applied 5 N external force to the tip by linear guide equipped load cell (UU-100K, CAS corp., Yangju, Korea). Next, we measured position error in the tip of our proposed joint between when applying no external force and applying external force by using an optical tracking system (OTS) (Polaris spectra, Nothern Digital Inc., Waterloo, Cananda), shown in Fig. 3.

In the result of 5 repetitions of the experiment, the average position error is 0.56 *mm* with 0.04 *mm* standard deviation.

DISCUSSION AND CONCLUSION

The results of FEM simulation demonstrated that the proposed wave-shape notched compliant joint has higher rigidity than the typical-shape notched compliant joint by the former showing relatively small position error against external force compared to the latter. The results of the experiment showed the proposed notched compliant joint can withstand applied 5 N external force with 0.56 *mm* position error. Because the simulation used a small model than manufactured joint and did not consider of friction force between wires and the joint, different results appeared between the simulation and the experiment. With the proposed notched compliant joint, position accuracy for the manipulating instrument can be increased without employing any control method. However, the proposed notched compliant joint has limitation on amounts of increasing rigidity. Because the parameter, h, can be decreased until allowing closure of the notch to occur in the outer part of the notch for achieving maximum bending angle, which leads to limitation for increasing l_s affected rigidity.

In the future, we will perform the animal and cadaver experiments with the proposed mechanism to treat bone tumor.

ACKNOWLEDGEMENT

This material is based upon work supported by the Ministry of Trade Industry & Energy(MOTIE, Korea), Ministry of Science& ICT(MSIT, Korea), and Ministry of Health & Welfare(MOHW, Korea) under Technology Development Program for AI-Bio-Robot-Medicine Convergence(20001688).

REFERENCES

[1] Murphy, R., Kutzer, M., Segreti, S., Lucas, B., & Armand, M. (2014). Design and kinematic characterization of a surgical manipulator with a focus on treating osteolysis. *Robotica*, *32*(6), 835-850.

[2] A. Gao, R. J. Murphy, H. Liu, I. Iordachita, & M. Armand, Evaluating the deflection of dexterous continuum manipulators with unevenly distributed compliant joints, *38th Annual International Conference of the IEEE Engineering in Medicine and Biology Society (EMBC)*, Orlando, FL, 2016, pp. 5099-5102.

Estimating the Complete Shape of Concentric Tube Robots via Learning

A. Kuntz, A. Sethi, R. Alterovitz

Department of Computer Science, University of North Carolina at Chapel Hill adkuntz@cs.unc.edu (DOI10.31256/HSMR2019.22)

INTRODUCTION

Concentric tube robots, needle diameter robots composed of nested pre-curved tubes, are capable of curving around anatomical obstacles to perform surgical procedures at difficult-to-reach sites. Concentric tube robots have the potential to enable less invasive surgeries in many areas of the human body, including the skull base, the lungs, and the heart [1]. For these robots, in order to safely control and plan motions that automatically prevent unintended collisions with the patient's anatomy, an accurate shape model of the entire robot's shaft is required. Accurate prediction of the entire shape of a concentric tube robot from its control inputs is challenging, and current state-of-the-art shape models are often unable to accurately account for complex and unpredictable physical phenomena such as inconsistent friction between tubes, non-homogenous material properties, and imprecisely shaped tubes [2][3]. In this work, we present a data driven, deep neural network-based approach for learning a more accurate model of a concentric tube robot's entire shape.

Machine learning enables a data driven approach to the shape estimation of concentric tube robots. Neural network models have been successfully used to more accurately model the forward kinematics and inverse kinematics of concentric tube robots [4][5], and an ensemble method has been applied to learn and adapt a forward kinematics model online [3]. However, these models only consider the pose of the robot's tip. In order to successfully plan and execute motions that avoid unwanted collisions between the robot's shaft and patient anatomy, a model must accurately predict the *entire shape* of the robot.

In this work, we present a deep neural network approach that learns a function that accurately models the entire shape of the concentric tube robot, for a given set of tubes, as a function of its configuration (see Fig. 1). The neural network takes as input the robot's configuration, and the network outputs coefficients for orthonormal polynomial basis functions in x, y, and z parameterized by arc length along the robot's tubular shaft. In this way, a function representing the entire shape of the robot can be produced by one feed forward pass through the neural network.

The key insight behind our parameterization is that the uncertainty in the physics-based shape models is due mainly to uncertainty in curvature and torsion. The *arc length* of the robot's shape, however, is independent of these and as such is generally not subject to the same sources of uncertainty. We can leverage this known state by parameterizing our shape function by arc length.

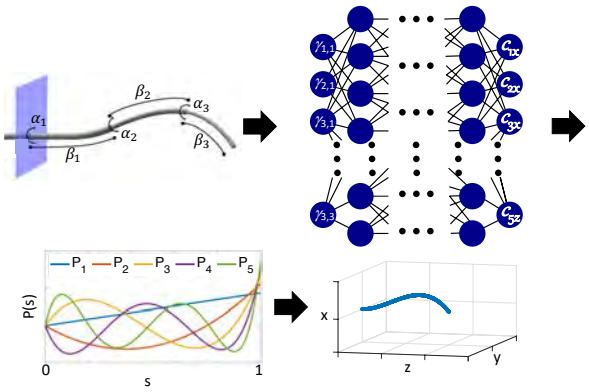

Fig. 1 Given a concentric tube robot configuration defined by the translations and rotations of the tubes (upper left), our neural network (upper right) outputs coefficients for a set of polynomial basis functions (lower left) that are combined to model the backbone of the robot's 3D shape (lower right).

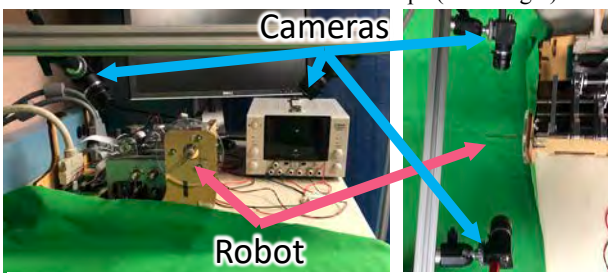

Fig. 2 We train the neural network using data from a physical robot. By taking images from multiple cameras (blue arrows), the shape of the robot's shaft (pink arrows) can be reconstructed in 3D using shape from silhouette.

MATERIALS AND METHODS

In order to learn a shape function for the concentric tube robot, data representing the robot's shape as a function of its configuration must be gathered. To gather shape data, we utilize a multi-view 3D computer vision technique called shape from silhouette [6], in which multiple images of the robot's shape for a given configuration are collected from cameras with known position (see Fig. 2). The robot's shaft is then segmented in each image and for each pixel in the segmentation a ray is traced out from the camera's position through its image plane. These rays then pass through a voxelized representation of the world, and voxels that are intersected by rays from every camera represent the robot's shape in the world. We then fit a 3D space curve to the voxels using ordinary least squares, resulting in a curve that represents the true, sensed backbone of the robot. We then train the neural network using the sensed backbone as ground truth.

Our neural network architecture consists of a feed forward, fully connected network, with 5 hidden layers of 30 nodes each. We utilize the parametric rectified

linear unit as our non-linear activation function between layers, which we noted provided a slight performance improvement over the standard rectified linear unit.

For a robot consisting of k tubes, we parameterize the i'th tube's state as $\boldsymbol{\gamma}_i := \{\gamma_{1,i}, \gamma_{2,i}, \gamma_{3,i}\} = \{\cos(\alpha_i), \sin(\alpha_i), \beta_i\}$ where $\alpha_i \in (-\pi, \pi]$ is the i'th tube's rotation and $\beta_i \in \mathbb{R}$ is the i'th tube's translation, as in [5]. We then parameterize the robot's configuration as $\mathbf{q} = (\boldsymbol{\gamma}_1, \boldsymbol{\gamma}_2, \ldots, \boldsymbol{\gamma}_k)$. This serves as the input to the neural network.

The network outputs 15 coefficients, $c_{1x}, c_{2x}, \ldots c_{5x}, c_{1y}, c_{2y}, \ldots c_{5y}, c_{1z}, c_{2z}, \ldots c_{5z}$, which serve as coefficients for a set of 5 orthonormal polynomial basis functions in x, y, and z parameterized by arc length, shown in Table 1. This results in three functions, $x(\mathbf{q}, s)$, $y(\mathbf{q}, s)$, and $z(\mathbf{q}, s)$, where $x(\mathbf{q}, s) = \text{len}(\mathbf{q}) * (c_{1x}P_1(s) + c_{2x}P_2(s) + \ldots + c_{5x}P_5(s))$, where s is a normalized arc length parameter between 0 and 1, and len($\mathbf{q}$) is the total arc length of the robot's backbone in configuration $\mathbf{q}$. Then $y(\mathbf{q}, s)$ and $z(\mathbf{q}, s)$ are defined similarly with their respective coefficients. The resulting shape function is $\texttt{shape}(\mathbf{q}, s) = \langle x(\mathbf{q}, s), y(\mathbf{q}, s), z(\mathbf{q}, s)\rangle$. To evaluate the shape of the robot at a given configuration, the neural network can be evaluated at $\mathbf{q}$, and the resulting coefficients define a space-curve function that can then be evaluated at any desired arc length. This, combined with knowledge of the robot's radius as a function of arc length, results in a prediction of the robot's geometry in the world.

We first pretrained our model on 100,000 data points (configuration and backbone pairs) generated by the physics-based model presented in [2]. Such pretraining allows us to prevent overfitting on the smaller amount of sensed, real world data.

We then trained our network on 8,000 data points, and we evaluate the network on 1,000 different test data points (both sets generated via shape from silhouette). We utilize a pointwise sum-of-squared-distances loss function and the ADAM [7] optimizer during training.

	s	s^2	s^3	s^4	s^5
$P_1(s)$	1.7321	0	0	0	0
$P_2(s)$	-6.7082	8.9943	0	0	0
$P_3(s)$	15.8745	-52.915	39.6863	0	0
$P_4(s)$	-30.0	180.0	-315.0	168.0	0
$P_5(s)$	49.7494	-464.33	1392.98	-1671.6	696.4912

Table 1 Coefficients for the orthonormal polynomial basis functions generated using Gram-Schmidt orthogonalization. $P_1(s) := 1.7321s$, $P_2(s) := -6.7082s + 8.9943s^2$, etc., plotted in Fig. 1 (lower left).

RESULTS

We compare our neural network's shape computation to that of the physics-based model presented in [2]. In Fig. 3 we plot a histogram of the errors across the 1,000 test configurations. For each configuration of our 3-tube robot we evaluate the shape of the physics-based model, the learned model, and the ground truth from the vision system at 20 evenly spaced points along the robot's shaft. We then present the maximum error—the L_2 distance of the point that deviates from the ground truth the most. The error distribution of the learned model is shifted to the left compared with that of the physics-based model, indicating that the learned model is more likely to produce lower error values than the physics-based model.

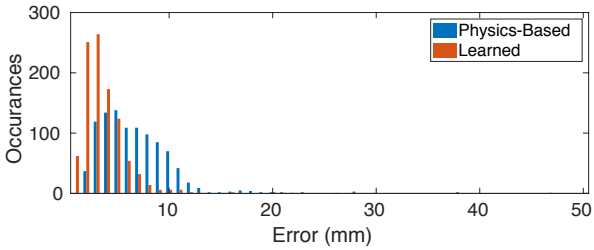

Fig. 3 A histogram of the maximum error along the robot's shaft for the learned model and the physics-based model, for each of the 1,000 test points. The distribution is shifted to the left in the learned model, indicating that it is more likely to produce lower error values. The maximum error is 26mm for the learned model and 47mm for the physics-based model.

DISCUSSION

In this work we present a learned, neural network model that outputs an arc length parameterized space curve. This allows us to take a data driven approach to modeling the shape of the concentric tube robot and improve upon a physics-based model. This may allow for safer motion planning and control of these devices in surgical settings that require avoiding anatomical obstacles. The model is only trained on cases where the robot is operating in free space. Accounting for interaction with tissue is the subject of future work. We also intend to investigate other models and augment the learned model to account for other sources of uncertainty in concentric tube robot shape modeling, including hysteresis, and plan to integrate the learned model with a motion planner and evaluate its use in automatic obstacle avoidance during tele-operation or automatic execution of surgical tasks.

ACKNOWLEDGEMENTS

This research was supported in part by the National Institutes of Health under Award R01EB024864.

REFERENCES

[1] Burgner-Kahrs J., Rucker D.C., Choset H. Continuum robots for medical applications: a survey. IEEE Trans. Robotics 2015 31(6):1261-80.

[2] Rucker D.C. The mechanics of continuum robots: model-based sensing and control. Ph.D. dissertation, Vanderbilt University, 2011.

[3] Fagogenis G., Bergeles C., Dupont P.E. Adaptive nonparametric kinematic modeling of concentric tube robots. IEEE/RSJ Int. Conf. on Int. Robots and Systems (IROS), Oct. 2016, 4324-29.

[4] Bergeles C., Lin F.Y., Yang G.Z. Concentric tube robot kinematics using neural networks. Hamlyn Symp. on Med. Robotics, 2015, 1-2.

[5] Grassmann R., Modes V., Burgner-Kahrs J. Learning the forward and inverse kinematics of a 6-DOF concentric tube continuum robot in SE(3). IEEE/RSJ Int. Conf. on Int. Robots and Systems (IROS), Oct. 2018, 5125-32.

[6] Baker S., Kanade T. Shape-from-silhouette across time part I: Theory and algorithms. Int. Journal of Comp. Vis. 2005 62(3):221-47.

[7] Kingma D.P., Ba, J. Adam: A method for stochastic optimization. arXiv preprint, 2014. 1412.6980.

Design and Modeling of a Multi-segment Steerable Sheath for Single-port Endoscopic Procedures

Jiaole Wang[1], Pierre E. Dupont[1]

[1]Boston Children's Hospital, Harvard Medical School, Boston, USA

jiaole.wang@childrens.harvard.edu (DOI10.31256/HSMR2019.23)

INTRODUCTION

This paper presents a steerable continuum sheath for use in single-port minimally invasive procedures. The sheath is designed to not only deliver multiple robotic arms through its working channels or lumens, but also to be steerable such that the endoscope can follow a curved path to the surgical site (see Fig. 1). The goal is to provide a means to increase the dexterity that can be achieved by multi-armed straight endoscopic systems such as proposed in [1, 2].

Several methods for steering multi-armed endoscopic systems have been previously proposed: a push-pull rod-driven mechanism was described in [3], and a concentric-tube mechanism was introduced in [4]. The push-pull rod-driven mechanism is effective in producing significant bending of the sheath, however, this approach requires reserving a portion of the cross section for routing of the rods or tendons. The challenge of designing a steerable sheath using concentric tubes [5] is that the maximum curvature of the sheath is limited by its relatively large outer diameter. The alternative approach of this paper is to produce bending of the sheath using precurved working channels. The smaller diameter of the working channels with respect to the overall sheath means that significantly larger precurvatures can be used with this approach. This idea, first introduced in [6] for a single-section sheath, is extended and demonstrated here for two-section sheaths.

Articulation of the sheath is achieved by using one or more precurved superelastic tubes lining the working channels used for arm delivery. These tubes can accomplish shape change of the sheath through any combination of pushing, pulling and rotation. The sheath can be modeled using Cosserat rod theory to describe each working channel. These rod models are constrained along their length by a central backbone that can also be modeled as a Cosserat rod. The specific case of 2-armed 2-segment sheath is investigated here. Each working channel is comprised of a single precurved tube and actuation is achieved solely by rotation of the two precurved tubes relative to the central backbone. Simulation and experiment are used to investigate the concept and to evaluate the kinematic model.

MATERIALS AND METHODS

The main structure of a single-segment two-channel steerable sheath is shown in Fig. 1. The two pre-curved tubes lining the working channels can be rotated at the proximal end with respect to the central backbone of the sheath to produce sheath bending. A multi-segment steerable sheath can be formed when there are multiple precurved tubes telescopically inserted together. It is noted that the tool-mounted arms delivered through these working channels can be actuated by tendons, rods, concentric tubes, etc. As depicted, disks spaced along the length of the sheath are attached to a central backbone. These disks constrain the relative positions of the channel tubes. Since the channel diameters are typically at least a factor of two smaller than the sheath diameter, the maximum precurvature is proportionally larger than what could be achieved with a sheath constructed from concentric tubes. This design is also spatially efficient by utilizing the working channels, traditionally passive elastic components, for actuation.

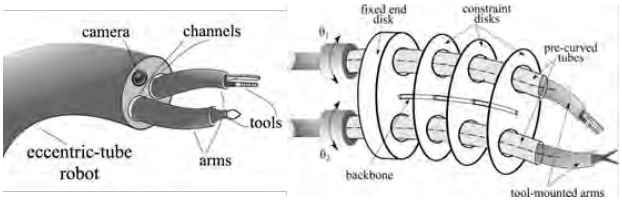

Fig. 1. Steerable endoscopic sheath actuated by rotation of two precurved tubes forming the working channels for the two robotic arms.

Kinematic modeling consists of solving for the shape of the backbone and precurved tubes by integrating a set of differential equations. The shapes of backbone and tubes is represented by $\mathbf{p}_i(s_i)$, where $s_i \in [0, \ell_i]$ is the independent arc length variable, ℓ_i is the tube length. The orientation of the body local frame is represented by a rotation matrix $\mathbf{R}_i(s_i)$which is defined as a Bishop frame moving along the tubes. The shape of the entire tube can be obtained by integrating $\dot{\mathbf{p}}_i(s_i) = \mathbf{R}_i(s_i)\mathbf{e}_3$ and $\dot{\mathbf{R}}_i(s_i) = \mathbf{R}_i(s_i)\hat{\mathbf{u}}_i$ from the proximal end to the distal end, where $\mathbf{u}_i(s_i)$ is defined as the local curvature and $\hat{\mathbf{u}}_i$ is a skew-symmetric matrix derived from $\mathbf{u}_i$.

For a single-segment sheath as introduced in [6], each precurved tube and the central backbone can be modeled as Cosserat rods subject to forces and moments applied to each other via the disks. The disks divide the tubes into sections over which integration is performed. According to Cosserat rod theory, the differential equation of curvature is given by

$$\dot{\mathbf{u}}_i = -\mathbf{K}_i^{-1}[\hat{\mathbf{u}}_i\mathbf{K}_i(\mathbf{u}_i - \mathbf{u}_i^*) + \mathbf{e}_3\mathbf{R}_i^{\mathrm{T}}\mathbf{n}_i], \quad (1)$$

where the subscript $i \in [0, \cdots, n]$ denotes the index for the tubes, and $i = 0$ stands for the backbone. The internal force is denoted as $\mathbf{n}_i$, and $\dot{\mathbf{n}}_i = 0$ since there is

no external force exerted on the tubes between disks. The tube stiffness is denoted as $\mathbf{K}_i = \mathrm{diag}([K_b, K_b, K_t])$, where K_b, K_t are the bending and torsional stiffness of the tube.

For the multi-segment sheath, the modeling of the central backbone is the same as for a single segment. With the working channel tubes, however, one must consider the relative twisting of the tubes. This matches the case of concentric tube robot modeling introduced in [5] since the telescopically aligned tubes can twist independently. This twist can be captured by the relative angle α_{ij} in local Z-axis with respect to the innermost (j=1)-th tube, where i and j are indexes for arm and tube, respectively. Therefore, the orientation of the j-tube of i-arm is $\mathbf{R}_{ij}(s) = \mathbf{R}_{i1}(s)\mathbf{R}_{\alpha_{ij}}(s)$ and $\mathbf{R}_{\alpha_{ij}}(s) = \exp(\alpha_{ij}(s)\hat{\mathbf{e}}_3)$. After some manipulation, the derivative of α_{ij} in terms of local torsional curvature $\mathbf{u}_{ij}(s)|_z$ is found to be $\dot{\alpha}_{ij}(s) = \mathbf{u}_{ij}(s)|_z - \mathbf{u}_{i1}(s)|_z$. As a result, the arm curvature can be integrated separately from bending and torsion. The bending curvature of i-th arm can be found as the 1-st tube as

$$\dot{\mathbf{u}}_{i1}|_{x,y} = -\mathbf{K}_i^{-1}\Big[\sum_{j=1}^{m}[\hat{\mathbf{u}}_{i1}\mathbf{K}_{ij}(\mathbf{u}_{i1} - \mathbf{R}_{\alpha_{ij}}\mathbf{u}_{ij}^*) - \dot{\alpha}_{ij}\mathbf{K}_{ij}\mathbf{R}_{\alpha_{ij}}\hat{\mathbf{e}}_3\mathbf{u}_{ij}^*] + \hat{\mathbf{e}}_3\mathbf{R}_{i1}^{\mathrm{T}}\mathbf{n}_i\Big]\Big|_{x,y}, \quad (2)$$

where the external forces applied to each tube can be expressed collectively as $\mathbf{n}_i(s) = \sum_{j=1}\ \mathbf{n}_{ij}(s)$ and collective stiffness is defined as $\mathbf{K}_i = \sum_{j=1}\ \mathbf{K}_{ij}$. Assuming no friction between tubes and disks, the differential equation for the torsional curvature of each tube takes the form

$$\dot{\mathbf{u}}_{ij}|_z = \frac{K_{bij}}{K_{tij}}[\mathbf{u}_{ij}^*|_x(\mathbf{u}_{i1}|_x\sin(\alpha_{ij}) - \mathbf{u}_{i1}|_y\cos(\alpha_{ij})) + \mathbf{u}_{ij}^*|_y(\mathbf{u}_{i1}|_x\cos(\alpha_{ij}) + \mathbf{u}_{i1}|_y\sin(\alpha_{ij}))]. \quad (3)$$

All differential equations are integrated simultaneously along the length of tubes to calculate the shape of each working channel. The boundary conditions, the compatibility condition imposed by disks, and solution approach are the same as those in [6]. Convergence in simulation is assumed when compatibility error is less than 0.6mm.

Table I. Prototype Parameters.
(Fig. 2-3 Parameters / Fig. 4 parameters)

	Segment 1	Segment 2	Backbone
Disk spacing (mm)	8		
Length (mm)	35 / 55	35 / 50	64 / 100
Radius of curvature (mm)	83.33 / 26.79	93.33 / 34.29	∞
Outer diameter (mm)	2.5 / 1.875	2.8 / 2.4	0.762mm
Inner diameter (mm)	2.2 / 1.6	2.6 / 2.0	--

RESULTS

Two 2-section steerable sheath prototypes were built as shown in Figs. 2-4 using the parameters of Table I. Initial validation of the model was performed by visual comparison of simulated and experimental shapes as shown in Fig. 3 for the low-curvature prototype. For this design, the model converged for a broad range of initial conditions while for the high curvature design, convergence was sensitive to initial conditions. Future work will focus on model solution techniques and calibration.

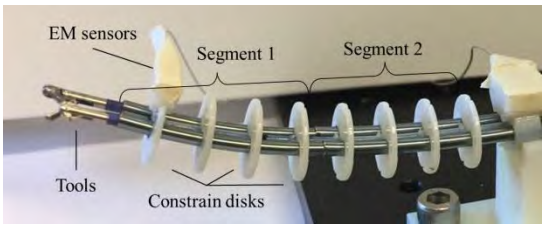

Fig. 2. Two-section sheath prototype accommodating two arms.

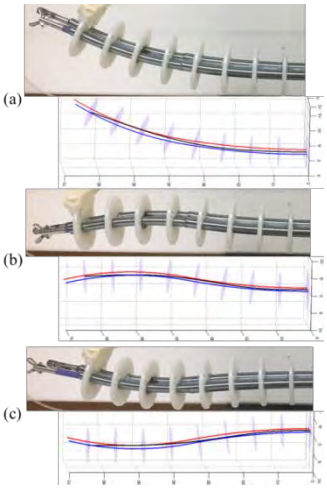

Fig. 3. Comparison of experimental and simulated shapes of low curvature tubes. Black curve is central backbone, blue and red curves are working channels corresponding to the left and right arms.

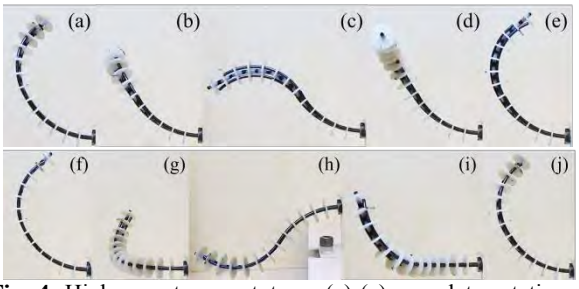

Fig. 4. High-curvature prototype. (a)-(e) complete rotation of distal section. (f)-(h) complete rotation of proximal section.

ACKNOWLEDGEMENTS

This work was supported by NIH grant R01NS099207.

REFERENCES

[1] H. Azimian *et al*. A Dual-arm Robotic Neuroendoscope: Early Results, *In HSMR*, 2016.
[2] R. J. Hendrick *et al*. Hand-held transendoscopicrobotic manipulators: A transurethral laser prostatesurgery case study, *Int*. *J*. *Robot*. *Res*. , 2015.
[3] N. Sarli *et al*. Preliminary Porcine In Vivo Evaluation of a Telerobotic System for Transurethral Bladder Tumor Resection and Surveillance, *J*. *Endourology*, 2018.
[4] Z. Mitros *et al*. Mechanics Modelling of Eccentrically Arranged Concentric Tubes, *In HSMR*, 2018.
[5] P. E. Dupont *et al*. Design and control of concentric-tube robots, *IEEE Trans*. *Robot*., 2010.
[6] J. Wang *et al*. Steering a multi-armed robotic sheath using eccentric precurved tubes, *In ICRA*, 2019.

Vessel Reconstruction using Multiple Forward Looking Sensors in A Steerable Needle

Vani Virdyawan[1], and Ferdinando Rodriguez y Baena[1]

[1]*Department of Mechanical Engineering, Imperial College London, UK,*
f.rodriguez@imperial.ac.uk (DOI10.31256/HSMR2019.24)

INTRODUCTION

During percutaneous intervention in the brain, the needle must avoid major blood vessels, as inadvertently puncturing one can pose a life-threatening complication. There is a risk that vessels with a size close to or smaller than the resolution of commonly used preoperative imaging modalities such as Magnetic Resonance Imaging (MRI, ~0.59 × 0.59 × 1 mm) would not be detected during procedure planning. To detect these vessels, Wardell et al. (2016) [1] had deployed a Laser Doppler Flowmetry (LDF) sensor in a rigid needle while performing Deep Brain Stimulation (DBS) implantation Procedures. The insertion path of a rigid needle, however, is limited to a straight line. Consequently, if a vessel is detected in front of the tip of the needle, the procedure must be interrupted. This limitation is driving the development of needles that can be steered around curvilinear paths to avoid obstacles.

In our previous study [2], [3], we have shown the feasibility of using LDF sensors for intra-operative vessel detection in a steerable needle. We used one type of steerable needle systems referred to as a Programmable Bevel Tip Needle (PBN). PBN offers a multi-segment flexible design, which is inspired by the egg-laying channel of certain insects [4]. Knowledge of vessel pose is crucial for the steerable needle system to execute and avoid obstacles.

The LDF sensor detects a vessel by measuring the Doppler shift effect in the light refracted by the moving blood cells flowing within it. Since the laser light is randomly scattered in the tissue, it is challenging to determine the source of the signal, and thus determining the perfusion value of blood flow is not possible [5]. Therefore, the perfusion measurements is a relative value with an arbitrary units (AU). Since a perfusion value corresponds to many vessel positions, in [2], successive measurements combined with a lookup table of the inverse perfusion value were used to determine the position of the vessel with respect to the tip of the sensor. However, this method only works for a given pair of tissue and vessel properties. In [3], relative measurements between each probe were used directly to classify the "no-go" area. Using relative measurements, the perfusion value of each probe was normalized so that this method is applicable to any set of tissue optical properties. However, there are several limitations in the algorithm, such as the inability to predict vessel diameter or the distance from the vessel to the probe.

Under real conditions, neither the vessel nor the tissue properties are known beforehand. Hence, in this paper, a feasibility study is presented where a Long Short-Term Memory (LSTM) network is used to directly predict the "no-go" area that was inferred from successive measurements from four laser Doppler probes.

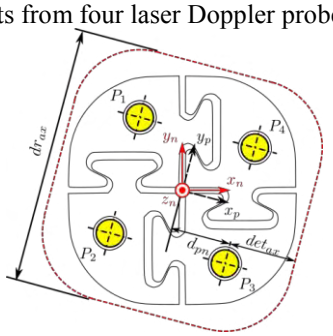

Fig. 1 The cross section of the PBN and the locations of the LDF probes in its working channels. The red-dash line represents the detection range of the probe.

MATERIALS AND METHODS

LSTMs require a large number of training data sets, which would be impractical to acquire experimentally. Therefore, we used Monte-Carlo simulations [6] to model measurements from the LDF system. The detection fiber was modelled using a ring detector. In each run, the simulation was stopped if there were 100,000 photons detected in the detector. The simulations were used to model the perfusion value for 0.3, 0.6, and 0.9 mm diameter vessels, with reduced scattering coefficient (μ_s') equal to 0.55, 0.75, and 0.95 mm. The flow velocities were set at 10, 15, and 20 mm/s. For each set of optical properties, the perfusion values were simulated at off-axis positions ranging from 2 to 0 mm in -0.2 decrements and at axial position ranging between 0.75 to 4.05 mm in 0.3 mm increments. In this proof-of-concept, we assumed that only a single vessel is ever detected by the probe.

Fig. 1 shows the location of the LDF probes in the PBN. As can be seen, we used two coordinate systems, needle coordinate system (x_n, y_n, z_n) and probe coordinate system (x_p, y_p, z_p). The probe coordinate system is placed at an angle of -14.8° with respect to the needle coordinate system. We then defined the detection area of the sensors. With the maximum axial detection range of the probes set at 2.4 mm, the detection volume was discretized into voxels, with the size of each voxel equal to 0.3 × 0.3 × 0.3 mm. Using this voxel size, there were 1805 voxels inside the detection range of the sensors, where each voxel was used to represent a label (class).

The network was then used to predict whether a voxel is safe (it is not occupied by a vessel) or it is not safe (it is occupied by a vessel). The voxel value is set into 0 if it is

safe, while the value of not safe voxel is set to 1. Since the vessel can occupy several voxels at once, the problem becomes that of a multi-label classification where several labels (classes) can have a value of 1. Four perfusion values from four probes were simultaneously fetched and fed to the network. The input was presented in this form

$$[Perf_{1t} \quad Perf_{2t} \quad Perf_{3t} \quad Perf_{4t} \quad F^T]^T$$

Where $Perf_{1t}, Perf_{2t}, Perf_{3t}, Perf_{4t}$ are the perfusion values for probe 1, 2, 3, 4 at time t, respectively. F^T is 3 × 1 vector that defines the movement direction of the probe ([1 0 0] backward, [0 1 0] static, [0 0 1] forward). Two layer LSTM with 100 LSTM cells in each layer were used. The training dataset consisted of 18,000 sequences with 30 positions in each sequence. 9,000 sequences were generated for validation, and another 9,000 for testing. The trained networks was then used to predict the "no-go" area for real insertion experiments.

RESULTS

The top part of Fig. 2 shows an example of the network's ability to predict the presence and pose of a vessel that was not in a plane perpendicular to the needle insertion axis. The average time required by the trained network to perform each prediction is less than 0.09 s. The successive perfusion values (A_1 to E_1) were generated using simulation. The blue area in Fig. 2 shows voxels that were predicted to be occupied by the vessel while the red circles represent the actual voxels occupied by the vessel. To ease comparison the voxels were projected in the $x_p y_p$-plane and $x_p z_p$-plane. Starting from Point C_1, the network predicted the vessel orientation and position accurately. The network was then used to predict the "no-go" area based on data from real insertion experiments. The bottom part of Fig. 2 shows the perfusion values for the four probes while the needle was advancing toward the vessel at seven example positions (A_0 – G_0). The prediction evaluation metrics for the experiments were found to be: Precision: 0.21, Recall: 0.54. It should be note that, if the evaluation metrics were performed only at Point G_0, the recall value increased to 0.77, which means a 77% prediction accuracy in the vessel volume at Point G_0.

DISCUSSION

The results show that the network can predict information about the vessel even though the optical properties of the tissue differ within a certain range (μ_s'=0.75 ± 0.2 mm^{-1}). If the optical properties range varies significantly, for example in the gray matter compared to white matter, the network may be unable to generalize. However, since the tissue greyness can be observed using a laser Doppler system based on the intensity of the detected light [1], light intensity could be added as a further network input to differentiate between white and gray matter. Even though the networks were trained using simulation data, the results show that these can be used to predict experimental measurements correctly. Use of the simulation data sped up the training process for different probes and needle properties.

ACKNOWLEDGEMENT

This project has received funding from the European Union's EU Research and Innovation programme Horizon 2020 under grant agreement no 688279, EPSRC Impact Acceleration Account (PSF795 MEME), and MRC Confidence in Concept Scheme (PS3311 MEME).

REFERENCES

[1] K. Wardell et al., "High-Resolution Laser Doppler Measurements of Microcirculation in the Deep Brain Structures: A Method for Potential Vessel Tracking," *Stereotact. Funct. Neurosurg.*, pp. 1–9, 2016.

[2] V. Virdyawan et al., "Laser Doppler sensing for blood vessel detection with a biologically inspired steerable needle," *Bioinspir. Biomim.*, vol. 13, no. 2, p. 026009, 2018.

[3] V. Virdyawan and F. R. Y Baena, "Vessel Pose Estimation for Obstacle Avoidance in Needle Steering Surgery Using Multiple Forward Looking Sensors," 2019, pp. 3845–3852.

[4] L. Frasson et al., "Experimental evaluation of a novel steerable probe with a programmable bevel tip inspired by nature," *J. Robot. Surg.*, vol. 6, no. 3, pp. 189–197, Jun. 2011.

[5] M. Larsson, "Model-based quantitative laser Doppler flowmetry," vol. 15, no. October 2010, pp. 1–12, 2016.

[6] F. de Mul et al., "Laser Doppler Velocimetry and Monte Carlo simulations on models for blood perfusion in tissue," *Appl.Opt.*, vol. 34, no. 28, pp. 6595–6611, 1995.

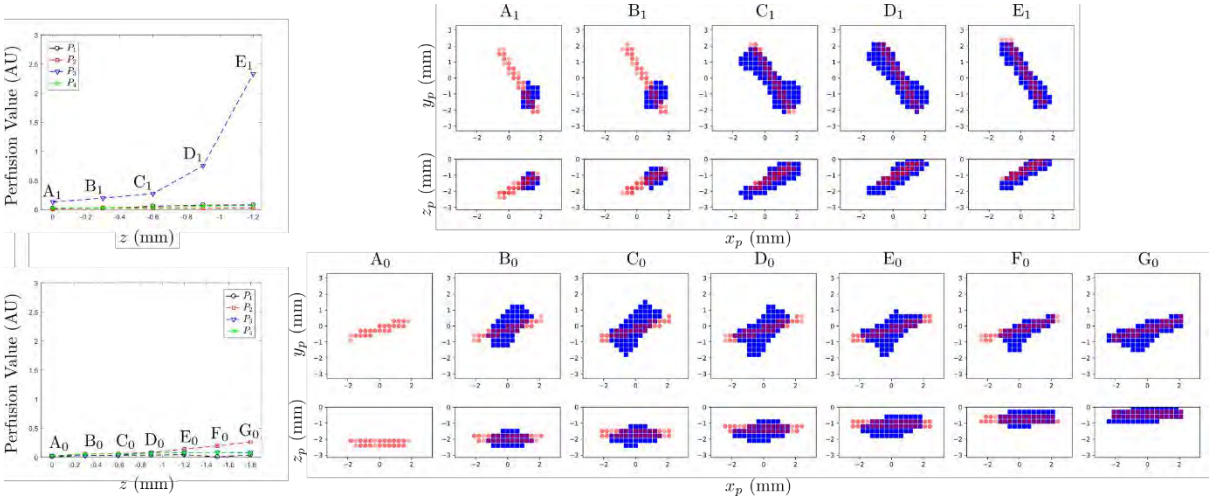

Fig. 2 Examples of perfusion values for a vessel and its corresponding actual (red-circles) and predicted (blue-squares) vessel area inside the detection area of the sensors. Top: from simulation data, bottom: real insertion data

Semi-Analytical Orientation Alignment with Joint Limit Constraints for Tele-Operated Surgical System

Yuanpei Cai[1], C. W. Vincent Hui[1], and K. W. Samuel Au[1]

[1]*Dept. of Mechanical & Auto. Eng., The Chinese University of Hong Kong*

samuelau@cuhk.edu.hk (DOI10.31256/HSMR2019.25)

INTRODUCTION

In tele-operated surgical system, orientation gimbal mechanisms with a "redundant" gimbal set up joint are commonly adopted in the Master Tool Manipulator (MTM) such as dVRK (Fig. 1) [1] . This setup joint (Fig. 1) is used to overcome the limited range of motion of other gimbal joints. With that, the user can input any desired orientation through their own hands without being obstructed by other gimbal joint limits during the tele-operation. For this reason, it is critical to choose the gimbal setup joint configuration wisely during the initial master and slave orientation alignment before the start of the tele-operation (Fig. 2).

The initial orientation alignment problem can be categorized as solving the inverse kinematics with joint limit constraints, which has been investigated extensively. For example, weighted pseudo-inverse, Null Space Projection Approach (NSPA), and Jacobian Transpose Approach (JTA) with joint velocity saturation are the typical local/reactive inverse approaches [3] [4], while [5] [6] proposed non-local or global optimal solutions. The former approaches rely on soft constraints and cannot guarantee if the alignment can always stay away from its mechanical limits at any desired orientation. The latter approaches require exhaustive computation effort and tuning, and often get stuck in local optima. Furthermore, the majority of the implementation of these approaches only focus on optimizing the alignment at the present status, they seldom consider how the selection of the "redundant" joint angle can reduce the chance of hitting the joint limits of other gimbal joints in the subsequent tele-operation (Fig. 2).

In this paper, we present a semi-analytical approach to address the orientation alignment problem with joint limit constraints in the orientation gimbal. We decouple the alignment problem into two steps: (1) Formulate the feasible solution set of the gimbal inverse problem as a function of the redundant joint analytically; (2) Choose the optimal redundant joint configuration that minimizes the likelihood of hitting the mechanical gimbal joint limits in the subsequent tele-operation. The proposed algorithm was implemented and integrated with C/C++ CISST-SAW library of the dVRK for experimental study. A comprehensive comparison was conducted against other typical methods in both simulations and experiments and the results demonstrated the effectiveness of our proposed algorithm.

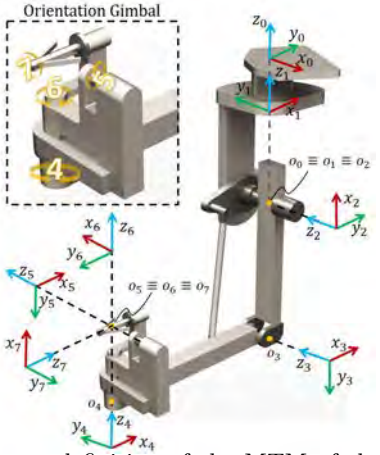

Fig. 1: Frame definition of the MTM of the da Vinci Research Kit(dVRK). Joint 4 is the redundant gimbal setup joint.

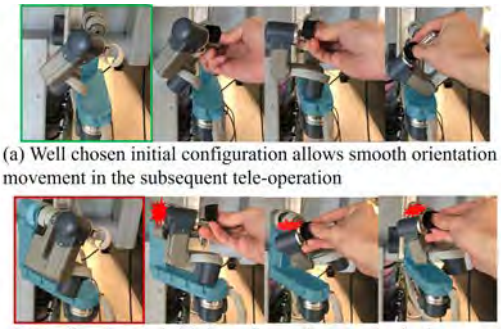

(a) Well chosen initial configuration allows smooth orientation movement in the subsequent tele-operation

(b) Badly chosen initial configuration results in frequently hitting on the joint limit

Fig. 2: Initial configuration of MTM can influence and bring nuisance to the subsequent tele-operation

METHOD

Step 1: Solution Set Formulation

The orientation gimbal of dVRK (Fig. 1) is an example of a typical gimbal mechanism used in a MTM. It has four degrees of freedom: gimbal set up joint(joint 4), gimbal pitch(joint 5), gimbal yaw (joint 6), and gimbal roll (joint 7), with mechanical limits $\boldsymbol{q}_o^{min} = [-90^\circ \ -90^\circ \ -45^\circ \ -480^\circ]^T$ and $\boldsymbol{q}_o^{max} = [200^\circ \ 180^\circ \ 45^\circ \ 450^\circ]^T$. The redundant set up joint allows the orientation gimbal to provide a complete spherical orientation workspace, i.e., it guarantees that there is at least one set of feasible gimbal joint solution for a given desired Cartesian orientation. Given a desired orientation ($\boldsymbol{R}^{dsr}$), gimbal set up joint, gimbal pitch/yaw joints are firstly moved to align the tip pointing direction ($\boldsymbol{z}$) with the desired one ($\boldsymbol{z}^{dsr}$),

$$\boldsymbol{z} = \left[z_x^{dsr} z_y^{dsr} z_z^{dsr}\right]^T. \tag{1}$$

Eq. (1) has multiple solutions for the redundancy in the orientation gimbal. We form a solution set($\mathcal{F}$)

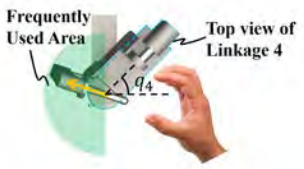

Fig. 3: Top view of the frequently used area

as a function ofl q_4, where

$$\begin{cases} q_6 = -\sin^{-1}\left(z_x^{dsr} c_4 + z_y^{dsr} s_4\right) \\ q_5 = \cos^{-1} \frac{z_y^{dsr} c_4 - z_x^{dsr} s_4}{c_6} \end{cases}. \tag{2}$$

Here, s_i and c_i are abbreviations for $\cos q_i$ and $\cos q_i$. Finally, the wrist roll joint is moved by

$$q_7 = axisAngle(\boldsymbol{R}^T \boldsymbol{R}^{dsr}), \tag{3}$$

where $\boldsymbol{R}$ is the tip orientation frame with $q_7 = 0$, and $axisAngle(\cdot)$ is an operator that gives the angle in Axis-Angle representation for a rotation matrix [4].

Step 2: Optimizing Redundant Joint Configuration:

Apart from achieving the desired orientation, the system redundancy also allows us to fulfill some additional requirements. As shown in Fig.2(b), bad MTM initial configuration can bring nuisance in the future tele-operation. In order to address this issue, we propose to optimize the MTM initial configuration. Based on the user experience (Fig. 3), by positioning the linkage 4 at the right-hand side ($q_4 < 90°$) helps to preserve the continuity of the most frequently used area of the orientation workspace (green half sphere), and avoid the tip disturbingly hitting on the mechanical structure in the future. This optimization problem can be formulated as follows

$$\begin{aligned} \min_{\boldsymbol{q}_o} \quad & \|\boldsymbol{q}_o^{dsr} - \boldsymbol{q}\|_W^2 \\ \text{s.t.} \quad & \boldsymbol{q}_o \in \mathcal{F} \end{aligned}, \tag{4}$$

where $\boldsymbol{q}_o^{dsr} = [45° \ 0 \ 0 \ 0]^T$ is the preferable configuration and $\|\cdot\|_W$ is the induced norm with $W = diag([2 \ 0 \ 0 \ 0])$. Considering the set $\mathcal{F}$ is finite, this optimization problem can be solved in real-time by exhaustive search.

RESULTS AND DISCUSSIONS

The proposed algorithm was compared with JTA and NSPA approaches. We tested these algorithms with 2592 randomly generated, target rotation matrices. Three performance indices were defined for comparison: 1) failure rate(tip orientation different from desired); 2) the angle distribution of q_4; 3) average computation time. As shown in Fig. 4, NSPA obtained a better result than JTA in terms of keeping joint 4 around 45° and computation speed, but the failure rate was unacceptably high (30%). Our approach had zero failing rate, the fastest computation speed, and the highest likelihood to maintain joint 4 at around the preferable configuration as compared to other methods. Fig. 5 showed an example of the orientation tracking performance of these algorithms. It is observed that both NSPA and JLA approaches got stuck at their local optima with non-zero orientation errors, while our approach was able to move to the desired orientation.

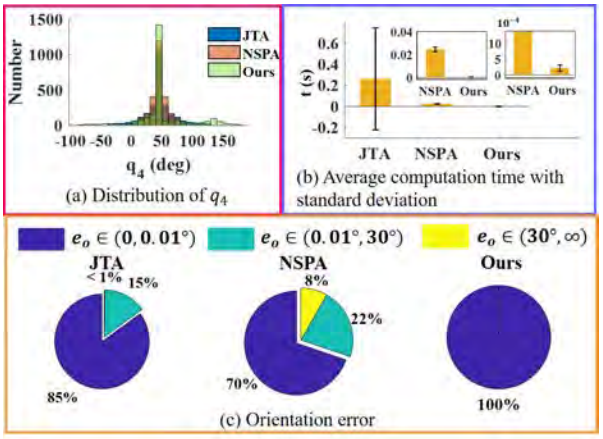

Fig. 4: Performance Comparison

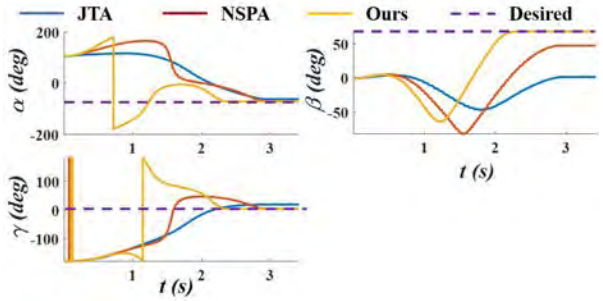

Fig. 5: Comparison of the orientation trajectory (represented by Euler angle) based on three different methods

SUMMARY

A semi-analytical orientation alignment algorithm was proposed and verified in both simulations and experiments. Initial results demonstrated the proposed algorithm can effectively use the redundant joint to overcome the joint limit constraints. In the future, we will further conduct user studies to validate the proposed algorithm in addressing the alignment issues in different surgical scenarios, such as endoscopic camera control and clutch operation.

REFERENCES

[1] A. A. Raheem et al., "Robot-assisted Fallopian tube transection and anastomosis using the new REVO-I robotic surgical system: feasibility in a chronic porcine model," *BJU Int.*, vol.118, pp. 604-9, 2016.

[2] P. Kazanzides et al., "Surgical and Interventional Robotics - Core Concepts, Technology, and Design," *IEEE Rob. Aut. Mag.*, vol.15, pp. 122-130, June, 2008.

[3] Y. Nakamura et al., "Robotics: modelling, planning and control," *Spr. Sci. & Bus. Media*, pp.3-15, 1987.

[4] S. Bruno et al., "Task-Priority Based Redundancy Control of Robot Manipulators," *Int. J. on Rob. Res.*, pp. 3-15, 1987.

[5] M. Faroni et al., "Predictive Inverse Kinematics for Redundant Manipulators With Task Scaling and Kinematic Constraints," *IEEE Trans. on Rob.*, vol.35, no. 1, pp. 278-285, Feb, 2019.

[6] H. Dai et al., "Global inverse kinematics via mixed-integer convex optimization," *Int. Sym. on Rob. Res.*, pp. 1-16, 2017.

Soft, Deployable, Cable Driven Robot for Minimally Invasive Surgery

Mark Runciman[1*], James Avery[2], Ming Zhao[1], Ara Darzi[2], George Mylonas[1]

[1]*HARMS Lab, Department of Surgery and Cancer, Imperial College London*

[2]*Department of Surgery and Cancer, Imperial College London*

*m.runciman@imperial.ac.uk (DOI10.31256/HSMR2019.26)

INTRODUCTION

En bloc removal of colon cancers with diameters larger than 20 mm and at an early stage can be achieved by Endoscopic Submucosal Dissection (ESD) [1], which results in lower recurrence rates than piecemeal Endoscopic Mucosal Resection (p-EMR) [2]. ESD is highly challenging to perform, however, resulting in long operation times and higher complication rates than p-EMR [3]. This work describes a deployable cable driven parallel robot that acts as an attachment to a flexible endoscope and provides bimanual control of two additional instruments, providing a soft robotic approach to previous work [4][5]. Haptic controllers in each of the user's hands allow the user's motions to intuitively guide the surgical instruments in the end-effectors to perform surgical tasks, such as ESD.

If ESD can be made simpler, safer and quicker to perform then the uptake of this technique might increase, and higher numbers of patients could benefit from the removal of large early gastric cancers in one piece, as opposed to piecemeal. Between 30 and 80 supervised procedures are required to learn the ESD technique [6], so if ESD can be made easier and the learning curve reduced, then a greater number of endoscopists will be able to perform it. In the UK in 2015 colon cancer was the second most deadly cancer and the fourth most common [7]. There is a need, therefore, for higher accessibility to advanced cancer treatments.

The support structure of the robot is in the shape of a hollow hexagonal prism and is based on inflatable load bearing structures that can be rapidly and inexpensively manufactured using a laser welding technique [8]. Due to the low-profile of the structure when unpressurised, large changes in volume are possible when transitioning between the undeployed and deployed states. Furthermore, the rigidity of the structure increases as the internal chambers of the thermoplastic sheet it is made of are pressurised. Transitioning from a low volume, flexible state to a larger volume, rigidified state prevents impediment of the endoscope's tip control when the robot is not in use. Force-transmission cables are routed to attachment points on the end-effectors through a sheath that fits around the inflatable structure, which is also manufactured by laser welding to ensure accuracy of the entry points of the cables into the structure's hollow interior. By controlling the length of the cables, the pose of each of the two end-effectors are controlled. The novel design and innovative manufacturing method deliver low wall thickness of the inflatable structure while maintaining sufficient rigidity, permitting a large workspace. The soft robotic robot is displayed in Fig 1.

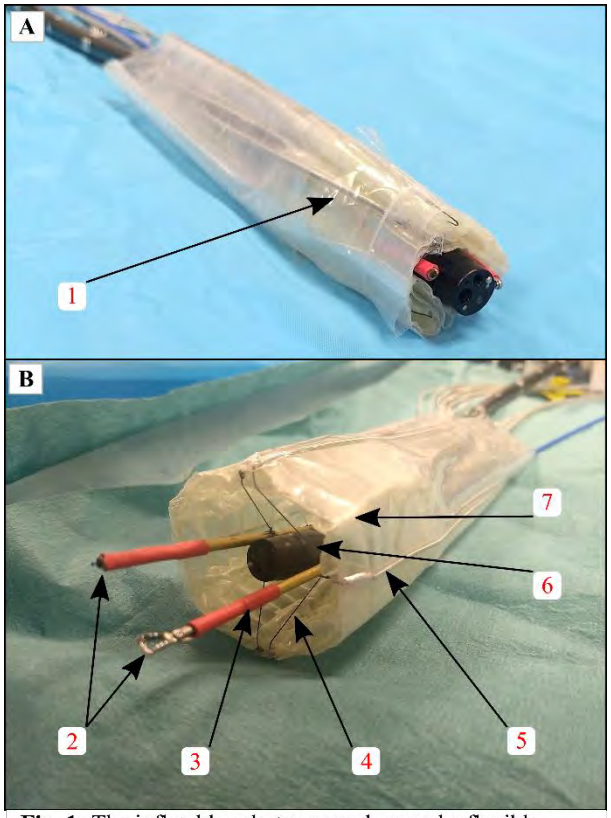

Fig. 1: The inflatable robot wrapped around a flexible endoscope in its A) undeployed and B) deployed state. 1) Undeployed inflatable structure 2) Surgical tools 3) End effector 4) Force transmission cable 5) Bowden cable within plastic sheath 6) 12 mm diameter colonoscope 7) Deployed inflatable structure.

MATERIALS AND METHODS

The inflatable structure and the cable routing sheath were both manufactured using a laser welding system similar to [8]. A Cartesian robot guides the optics of a high power 940 nm laser diode (LuOcean Mini LU0940D250-D, Lumics, Germany) that collimate and focus the beam at the surface of a vacuum table upon which multiple sheets of thermoplastic material are clamped together. A dye (Clearweld LD940B, TWI, UK) that absorbs infrared light is deposited onto the thermoplastic sheets in the desired weld pattern before exposure to the 1 mm diameter beam that locally heats and welds the sheets together. In this way, airtight chambers are formed between sheets. Weld patterns are easily customised by changing the parameters of a base design that relies on two layers that are themselves welded together. One layer contains a single chamber consisting of a series of beams

that forms the circumference of the hollow prism shape when inflated, while the second layer consists of another series of beams that pass along the length of the prism at each corner and stiffens the structure. Not only are these inflatable structures customisable, but they are also rapid to manufacture: it took under 5 minutes to apply the dye and weld the first pattern used for this robot, under 4 minutes for the second pattern and under 4 minutes for the weld pattern to join the two layers. Similarly, the cable-routing sheath was laser welded as this provided a low-profile shape and ensured accurate placement of the cable entry points around the inflatable structure. The welded sheets were manually welded to form cylinders and the cables and tubular end-effectors were attached to the sheath, with the inflatable structure placed inside it. Surgical tools were anchored inside the end-effectors and the force transmission cables connected to the motor unit as in [5]. This gives the user control of two parallel manipulators.

RESULTS

When wrapped around a 12 mm diameter colonoscope the entire robot assembly has a diameter of 25 mm. After deployment, the robot approximates a hollow hexagonal prism of side length 28.5 mm, resulting in a maximum width of 57 mm.

After inflation to a gauge pressure of 1 bar, the rigidity of the inflatable structure increased sufficiently to achieve tension forces in the cables of up to 26 N. Using a 6 Degree of Freedom (DOF) force transducer (Nano 17, ATI Automation) the forces exerted by one end-effector in its local X, Y and Z axes were measured and magnitudes greater than 8 N, 2 N and 6 N observed in each axis respectively.

A procedure mimicking ESD was successfully performed on *ex-vivo* chicken breast tissue using the deployable robot equipped with a grasper and a diathermy tool (VIO 200D, Erbe Elektromedizin GmbH). The skin was marked, injected with saline and an area of it removed *en bloc*. This was possible because the working channels of the endoscope are unoccupied while using our robot and because the mechanism delivers high dexterity to both end effectors. The result is displayed in Fig. 2. The shape of the removed skin approximated an ellipse with major axis of 20 mm and a minor axis of 15 mm.

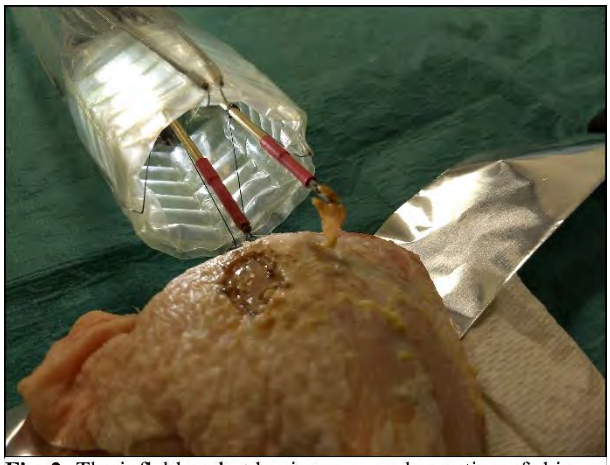

Fig. 2: The inflable robot having removed a section of skin from ex-vivo chicken breast tissue.

DISCUSSION

The manufacturing method enables fast and inexpensive production of customisable cable-driven parallel robots. The robot in this work is designed for applications in the cecum where the intestine diameter is largest, but the robot's size can be scaled up or down depending on the patient and the procedure to be performed. These robots are capable of large volume and stiffness changes, high force exertion and give the user dextrous control of two instruments.

A compliant outer layer may further reduce the potential for unwanted damage to the soft tissue of the colon, and thermoplastic elastomer sheet materials may provide a simple way of adding this functionality. The main difficulty may lie in finding laser welding parameters that permit sealing of distinct materials.

Future work focuses on integrating a sensor to measure the shape of the inflatable, as deformation of the support structure leads to errors in end-effector position and this affects the controllability. Diagnostic and exteroceptive sensors are also being investigated but problems with their bonding and integration into soft devices remain unsolved.

REFERENCES

[1] K. J. Kang, K. M. Kim, B. H. Min, J. H. Lee, and J. J. Kim, "Endoscopic submucosal dissection of early gastric cancer," *Gut Liver*, vol. 5, no. 4, pp. 418–426, 2011.

[2] S. J. Heitman and M. J. Bourke, "Endoscopic submucosal dissection and EMR for large colorectal polyps: 'the perfect is the enemy of good,'" *Gastrointest. Endosc.*, vol. 86, no. 1, pp. 87–89, 2017.

[3] S. Oka *et al.*, "Advantage of endoscopic submucosal dissection compared with EMR for early gastric cancer," *Gastrointest. Endosc.*, vol. 64, no. 6, pp. 877–883, 2006.

[4] G. P. Mylonas, V. Vitiello, T. P. Cundy, A. Darzi, and G. Z. Yang, "CYCLOPS: A versatile robotic tool for bimanual single-access and natural-orifice endoscopic surgery," *Proc. - IEEE Int. Conf. Robot. Autom.*, pp. 2436–2442, 2014.

[5] T. J. C. O. Vrielink, M. Zhao, A. Darzi, and G. P. Mylonas, "ESD CYCLOPS: A new robotic surgical system for GI surgery," *2018 IEEE Int. Conf. Robot. Autom.*, pp. 150–157, 2017.

[6] A. Najib Azmi *et al.*, "Endoscopic Submucosal Dissection Outcomes for Gastroesophageal Tumors in Low Volume Units: A Multicenter Survey," *Diagn. Ther. Endosc.*, vol. 2016, 2016.

[7] Cancer Research UK, "Cancer Statistics.pdf." 2019.

[8] M. Runciman, A. Darzi, and G. P. Mylonas, "Deployable, Disposable, Self-Propelling and Variable Stiffness Devices for Minimally Invasive Surgery," *2018 8th Joint Workshop on New Technologies for Computer/Robot Assisted Surgery*. pp. 17–18, 2018.

Design of Non-Circular Joint Contour for Continuum Robots

Z. Jin[1], A. Gao[1], N. Liu[1], Z. Wu[1], G. Z. Yang[1]

[1]*The Hamlyn Centre for Robotic Surgery, Imperial College London*
z.jin18@imperial.ac.uk (DOI10.31256/HSMR2019.27)

INTRODUCTION

Lung cancer is a life-threatening disease, and diagnosis relies on the bronchoscopy that is usually implemented by inserting the bronchoscope to go through the bronchi to perform the needle biopsy. To avoid the invasive damage, we have proposed a solution to use an optical imaging probe to go through the instrument channel of the bronchoscope to access distal airways and perform the optical biopsy [1-3]. In our previous work [4], a miniaturised laser-profiled continuum robot with interlocked circular joints was developed to help steering the imaging probe to access the desired targets. However, the centreline of continuum robot with circular joint will be changed during the deflection, which will inevitably affect the location of the imaging probe aligns with the centre. Therefore, it is necessary to adjust the joint contour to guarantee the constant centreline length during the deflection.

The motivation of this paper is to design a non-circular joint contour for enabling a constant-length centreline during the deflection of continuum robots. Fig. 1 (a) shows the comparison of continuum robots with circular and non-circular joint contours, where an imaging probe is assembled in the centre of the continuum robot. It shows that the probe tip will be out of the inner lumen of continuum robot with circular joints during the deflection when the probe's proximal end is fixed; while the continuum robot with non-circular joints will keep the probe's location unchanged. This paper is organized as follow. A design method is first introduced to calculate the non-circular contour; then the kinematics is built to describe the deflection of continuum robot with non-circular joints. Finally, simulations are carried out and a prototype is made to demonstrate the effectiveness.

MATERIALS AND METHODS

We design a non-circular joint contour shown in Fig. 2 to guarantee the constant centerline length. Different from the circular joint contact by surface, there is only two lines or points contact with each other on a joint. The trajectory of the top segment will follow joint contour of the bottom segment. A processing map to achieve the result is shown in Fig. 3. We can consider the shape changes of the imaging probe in the continuum robot when it starts to rotate. The part contacts with disk will keep straight, and the imaging probe will bend between two adjacent disks. In this case, the bending part of the fibre is an arc of a typical circle, and the centre of a circle can be estimated withthe distance between the disk planes and the rotational angle. When the continuum robot under the straight position, the central line of the

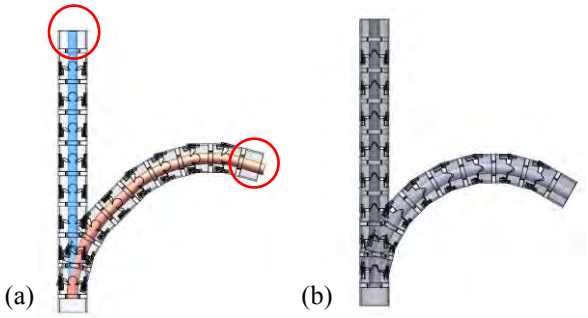

Fig. 1 Centreline comparison of continuum robots with circular and non-circular joints. An obvious centreline change can be observed in (a) compared with the continuum robot with non-circular joints in (b).

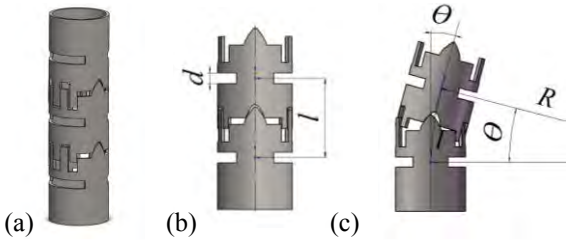

Fig. 2 Design of non-circular joint contour. (a) General 3D view with cover and base; (b) General dimension: l is the distance between the neighbour disks under the straight position, also is the length the of inner instrument; (c) The continuum robot diagram after bending.

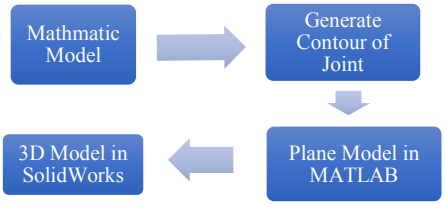

Fig. 3 An overview of the design processing.

continuum robot and the imaging probe aligned with each other, where the length between the disks can be recorded as l. The rotation angle (θ) equals to 0 under the straight condition. The shape function of the joint can be written as (1) and (2), and the contour is shown in Fig. 2 as the gear tooth. This contour structure aims to ensure that the central line's length of the imaging probe always equals to l. At the same time, it's necessary to avoid the gear tooth and the gear slot overlapped with each other, and the structure of the slot can cover the gear tooth with a gap.

$$x = \frac{l}{\theta} * (1 - \cos\theta) \quad (1)$$

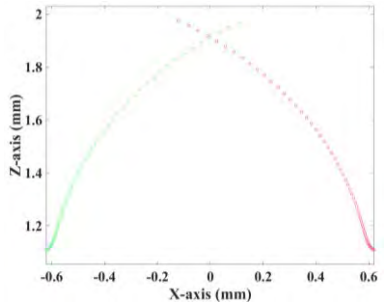

Fig. 4 The generated non-circular joint contour by the mathematical model.

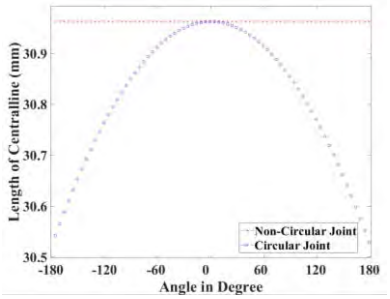

Fig. 5 The length comparison of the central line from top disk to base disk between the continuum robots with the non-circular and circular joint contours.

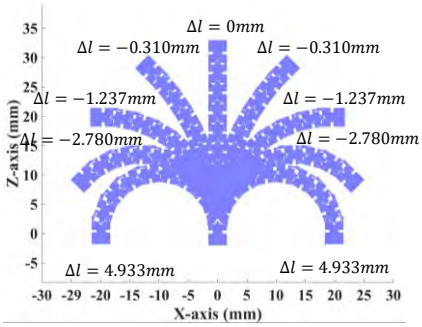

Fig. 6 Deflection of continuum robots under the cable length (Δl) from 0 mm to 4.933 mm.

$$y = \frac{l}{\theta} * sin\theta \tag{2}$$

For this joint, the motion combines rotation with translation. The forward kinematic can be derived from (3) and (4). The disk length (d) also needs to be taken into the transformation matrix. As Fig. 2 illustrates, the effect of the projection of disk length in x-y and x-z plane are neglected due to their small value.

$$T_G^n = T_G^1 \cdot T_1^2 \cdot T_2^3 \cdot T_2^3 \cdot \ldots \cdot T_{n-1}^n \tag{3}$$

$$T = \begin{bmatrix} R & d \\ 0 & 1 \end{bmatrix} = \begin{bmatrix} 1 & 0 & 0 & 0 \\ 0 & cos\theta & -sin\theta & x + d \cdot sin\theta \\ 0 & sin\theta & cos\theta & y + d \cdot cos\theta \\ 0 & 1 & 0 & 1 \end{bmatrix} \tag{4}$$

RESULTS

Fig. 4 shows the calculated joint contour based on the mathematic model in the last section, which is generated by equation (1) and (2). It indicates that the model derives a non-circular contour, and two contours in the left and right could form a closed joint contour.

Fig. 5 shows the comparison of centerline length between continuum robots with non-circular and circular joints bending from -180° to 180°. Result shows that the continuum robot with non-circular joints generates a constant centerline, compared to the one with circular joints.

Fig. 6 illustrates the continuum robot under the different cable lengths. Results show that the structure can keep the tip of the imaging probe on the last disk, and do not need further control by comparing with the circular joint continuum robot.

Fig. 7 presents a prototype which is manufactured by 3D printing base on these concepts, the inner optical fibre keeps aligning on the tip of the continuum robot and marked as red circles in Fig. 7 (a).

DISCUSSION

This paper has developed a continuum robot with the non-circular joints to derive a constant-length centreline. A detailed design procedure has been illustrated to show the non-circular contour generation . Simulation results and the preliminary prototype have validated the proposed structure. However, one potential limitation is that two adjacent segments have the sharp contact, which may introduce the wear. In future, the metal material based on CNC, metal printing or laser cutting could potentially avoid this. Also, the contact-aided mechanism used in [5] could be integrated with this robot to improve its performance.

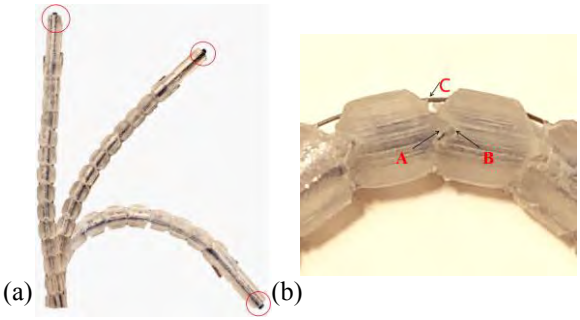

Fig. 7 (a) Bending of the prototypes of the non-circular continuum robot, and the tip of inner dark-blue optical fiber does not move during the deflection; (b) Details of the joint connection: A is the joint tooth; B is the joint cover; C is the driven-cable.

REFERENCES

[1] J. Shang, D. P. Noonan, C. Payne, J. Clark, M. H. Sodergren, A. Darzi, "An Articulated Universal Joint Based Flexible Access Robot for Minimally Invasive Surgery", *Proc. IEEE Int. Conf. Robot. Autom.*, pp. 1147-1152, 2011.

[2] S. KIM *et al.*, "Bronchoscopic Features and Bronchoscopic Intervention for Endobronchial Hamartoma", *Respirology*, vol. 15, no. 1, pp. 150-154, 2010.

[3] R. Webster and B. Jones, "Design and Kinematic Modeling of Constant Curvature Continuum Robots: A Review", *The International Journal of Robotics Research*, vol. 29, no. 13, pp. 1661-1683, 2010.

[4] N. Liu *et al.*, "Design and Kinematics Characterization of a Laser-Profiled Continuum Manipulator for The Guidance of Bronchoscopic Instruments", *Proc. Int. Conf. Robot. Automat.*, pp. 25-31, 2018.

[5] L. Ros-Freixedes *et al.*, " Design optimization of a contact-aided continuum robot for endobronchial interventions based on anatomical constraints", *International journal of computer assisted radiology and surgery*, pp. 1-10, 2019.

Ultrasound-based Safety Assessment during Moving Organ Tracking Towards In Vivo Focused Ultrasound Therapy

A. Mariani♦, L. Morchi♦, A. Diodato, A. Cafarelli, S. Tognarelli, A. Menciassi

The BioRobotics Institute, Sant'Anna School of Advanced Studies, Pisa, Italy
a.mariani@santannapisa.it ¨*Shared first author* (DOI 10.31256/HSMR2019.28)

INTRODUCTION

Focused Ultrasound (FUS) is coming to the forefront among the emerging therapeutic technologies, primarily in oncology [1]. High Intensity Focused Ultrasound (HIFU) consists of finely focusing high power acoustic energy on inner tissues from an external source (*i.e.* the HIFU transducer), in order to produce thermal or mechanical disruptive effects on the pathological target. To exploit its full potential as a non-invasive and intrinsically safe procedure, accurate targeting and energy transfer monitoring within the target volume have to be accomplished (*e.g.* by means of ultrasound imaging). However, the continuous physiological motion of organs – mainly due to breathing – makes this guidance challenging in abdominal targets (*e.g.* liver, kidney and pancreas), which linearly move up to 2 cm [2]. In the FUTURA framework (*www.futura-project.eu*), we introduced a novel method to compensate for the target motion by exploiting the feature of a ultrasound-guided robot-assisted platform [3]. This approach allows to track the target and keep the HIFU focus on it by rotating the transducer around a virtual pivot point and by adjusting the focal depth thanks to axial electronic steering. Such an approach overcomes the invasiveness of motion-suppression methods and it minimizes the acoustic window variations. The tracking accuracy of this system was validated in vitro during a simulated respiratory-induced motion: we reached a maximum motion compensation error always under 1 mm. However, to properly transfer energy to the moving target during an in vivo treatment, correct acoustic coupling between the transducer and the patient's skin has to be guaranteed all over the HIFU transducer motion. Fails in matching this condition introduce wave reflections at the interface and in turns dramatic efficiency loss, instrumentation damages and skin burns [4]. The current work aims at verifying the correct acoustic coupling during the angular tracking in a quantitative way by exploiting the Radio Frequency (RF) echo signals recorded by a US imaging probe confocal to the HIFU transducer. The synergy between tracking accuracy and correct coupling can pave the way to the HIFU clinical treatment also of moving organs.

MATERIALS AND METHODS

A) System overview

Test sessions were performed by using the FUTURA platform, whose architecture is reported in Fig. 1A: a 16-channel (1.2 MHz central frequency, 120 mm diameter, 20 W/channel maximum output capability) phased annular array HIFU transducer (Imasonic) and a confocally aligned 2D imaging Ultrasound linear phased

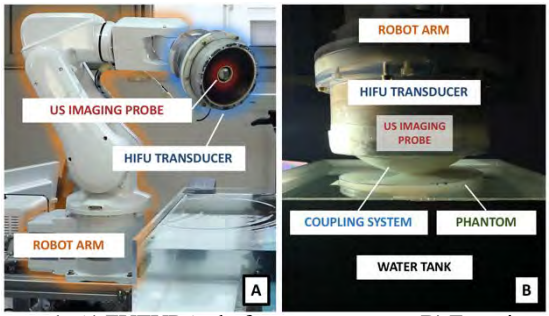

Figure 1: A) FUTURA platform components; B) Experimental setup.

array probe (Analogic Ultrasound PA7-4/12) are mounted on a robotic 6 degrees-of-freedom (DoFs) arm (IRB-120 robot, ABB). A 6 DoFs force/torque sensor (ATI mini 45, Industrial Automation) is attached to the robotic arm end-effector for force control. The transducer-patient coupling system is composed of a latex membrane (150 µm width) filled with deionized and degassed (dd) water and fixed to the HIFU transducer. A research Ultrasound system (SonixTABLET, Ultrasonix Medical Corporation) for raw RF data recording and system's parameters control is connected to the 2D imaging probe. Finally, an Agar-based phantom (140 mm in diameter and 15 mm in height) – 4% w/v agarose powder (Sigma-Aldrich) dissolved in dd water – was used as patient's body simulator, as its mechanical and acoustic properties are in line with those ones of human tissues [5]. To replicate the interface between the HIFU transducer and the patient's skin, the phantom was located above the water level of a dd water-filled tank (Fig 1B).

B) Experimental procedure

The purpose of this study is verifying that a correct acoustic coupling is maintained across each angular position – α – of the transducer during the angular tracking of moving targets. The idea is to accomplish this goal by performing safe, low-energy shots from the therapeutic transducer along the tracking trajectory in a preoperative phase, prior to the treatment. The derived coupling information acquired by the imaging probe can play as choice criterion to start the therapy or perform further adjustments. Specifically, we simulated the tracking of a linearly moving target (Δl = 2 cm, at a depth under the simulated skin corresponding to a maximum α = 12°) (Fig 2A); the coupling system was moved in contact with the Agar phantom, at 3 different heights (z) and associated contact force ranges – 1-2 N, 3-4 N and 5-6 N, respectively – within the safety range applicable to the patient's body [6]. For each configuration, the pivot point *P* (around which the transducer angular motion was

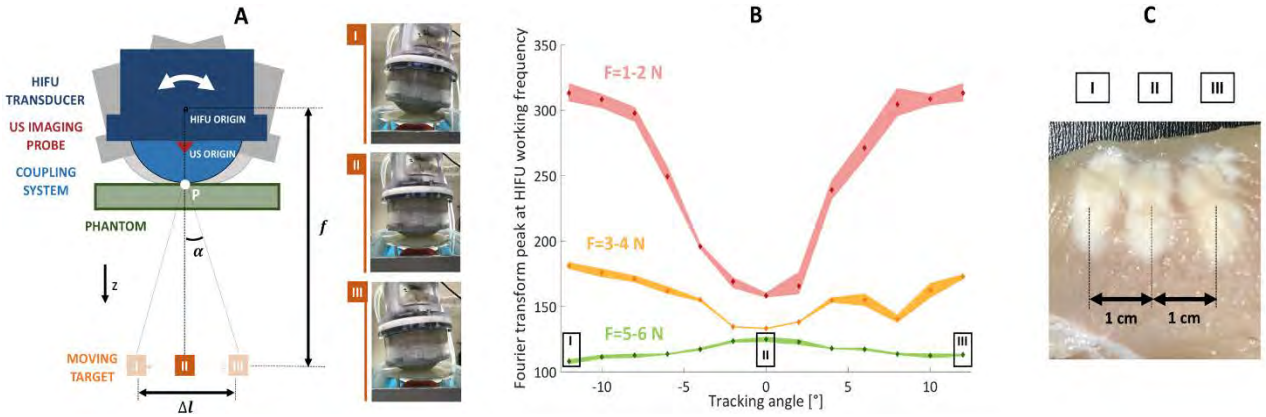

Figure 2 A) Schematic representation of the experimental procedure and real setup in 3 tracking configurations; B) Peak value of the Fourier transform of the RF signals during HIFU safe shots as a function of the tracking angle, in the 3 contact force configurations. The marked diamonds represent the mean across repetitions, while the shadow stands for data variability (maximum and minimum values). C) Lesions in the chicken breast in good coupling at α =-12° (I), 0° (II) and 12°(III).

performed) was set as the intersection between the optical axis of the transducer and the phantom upper plane. The transducer was then moved in different angular positions, ranging from -12° to 12° (with 2° steps), thus testing 13 different angular acoustic coupling conditions. Across all the configurations (both height and angle), the HIFU focus distance (*f*) was electronically adjusted to match the target centre.

For each angular condition, a safe low-energy sonication (1 W power; 1 s duration) was performed and the associated reflected waves were recorded through the confocal 2D imaging probe. The 2D probe was configured for working in receiving mode (no US waves transmission) at sampling frequency of 40 MHz.

The overall described experimental procedure was repeated 5 times.

Signal processing of RF data was performed to evaluate the quality of each coupling condition. Precisely, for each acquired RF signal, the Fourier transform peak – at the working frequency of the HIFU transducer – was computed as an index of wave reflections: lower the wave reflection, better the acoustic coupling quality.

In addition, in order to further demonstrate the correctness of the acoustic coupling at different transducer angular positions (α), three different thermal lesions were performed on a chicken breast in an estimated condition of good acoustic coupling (*i.e.* F=5-6 N). Specifically, a continuous sonication of 15 s duration at frequency and acoustic power of respectively 1.2 MHz and 115 W, was performed for α = -12°, α = 0°, and α = 12°.

RESULTS

Fig. 2B shows the Fourier transform peak of the reflected signal as a function of the tracking angle in the three analyzed configurations (*i.e.* contact forces). Increasing the contact force, a reduction in the peak value can be noticed, as well as a decrease in the variability across experimental repetitions. Considering the red curve, the larger the tracking angle, the larger the peak; on the contrary, the green curve features almost stationary peak values across the angular range. This phenomenon can be related to the variation of the contact surface between the coupling system and the phantom. Indeed, air interposition while tilting the transducer occurs in the first configuration (*i.e.* F=1-2 N), thus causing a reduction in the acoustic coupling.

Fig. 2C depicts the lesions performed on the chicken breast in the third condition (good coupling across all the angles, *i.e.*, contact force of 5-6N). Qualitatively, the lesions performed at the angular range boundaries and center appear very similar in size and shape.

DISCUSSION

This paper introduces a quantitative method to check the correctness of the acoustic coupling during FUS therapy while angular tracking of a moving target is performed. This technique is meant to work as a safety check in a preoperative phase in order to optimize the system positioning and thus the treatment efficiency and safety. Results showed the feasibility of the proposed method while performing the tracking of a linear motion up to 2 cm. Further investigations will be carried out in order to translate and test the proposed protocol in vivo.

ACKNOLEDGMENTS

Research supported by FUTURA2020 project (grant agreement n. 801451) and by River Global Scientific Lab srl.

REFERENCES

[1] J.-F. Aubry *et al.*, The road to clinical use of high-intensity focused ultrasound for liver cancer: technical and clinical consensus Current overview and unmet clinical need for treating cancer in and of the liver, *J. Ther. Ultrasound*, vol.1, p.1, 2013.

[2] S. C. Davies *et al.*, Ultrasound quantitation of respiratory organ motion in the upper abdomen, *Br. J. Radiol.*, vol.12, no. April, pp. 1096–1102, 1994.

[3] A. Diodato *et al.*, Motion compensation with skin contact control for high intensity focused ultrasound surgery in moving organs, *Phys. Med. Biol.*, 2018.

[4] T. Yu, J. Luo, Adverse events of extracorporeal ultrasound-guided high intensity focused ultrasound therapy, *PLoS One*, vol.6, no. 12, 2011.

[5] A. Cafarelli *et al.*, Tuning acoustic and mechanical properties of materials for ultrasound phantoms and smart substrates for cell cultures, *Acta Biomater.*, vol.49, pp. 368–378, 2017.

[6] N. Koizumi, M. Mitsuishi, A study on the construction methodology of remote ultrasound diagnosis system, *Robot. Soc. Japan*, vol.25, no.2, pp. 267–279, 2007.

Identification of the electrocautery state to enable spatially navigated intra-operative mass spectrometry tissue analysis

M. Asselin[1], A. Jamzad[1], A. Lasso[1], T. Ungi[1], J. Rudan[2], G. Fichtinger[1,2]

[1]*Laboratory for Percutaneous Surgery, School of Computing, Queen's University*

[2]*Department of Surgery, School of Medicine, Queen's University*

{mark.asselin, fichting}@queensu.ca (DOI10.31256/HSMR2019.29)

INTRODUCTION

In computer-assisted surgery situations arise when it is necessary to determine the status of tracked power tools, in order to perform accurate temporal and spatial monitoring of the tool within the navigation system. We need to detect what is often referred to as an "energy event", when the power tool, such as an electrosurgical cauterizer, is being activated within the tissue during surgery. What complicates the matter further is that an isolated sensing and feedback mechanism is required which does not interfere in any way with the clinically certified power tool. Electrosurgical devices are used during surgery to cut tissue and to apply coagulation to the surgical site. The two main modes of the device that need to be distinguished are cut and coagulation. In coagulation mode, the device induces a gradual temperature rise in the cells which causes the cells to dehydrate and shrink without bursting. This is particularly useful to seal minor blood vessels. The cut mode causes a more rapid heating of the tissue which results in the cellular water boiling and causes the cells to rupture, which is most useful to separate tissue while also sealing minor vasculature.

Precise knowledge of the electrocautery state is critical for spatially-navigated metabolomic analysis of the surgical aerosol, simply known as "smoke". Evaporative ionization mass spectrometry (REIMS) has been shown to have exquisite sensitivity and specificity in metabolomic tissue identification [1]. A major challenge for spatially-navigated mass spectrometry tissue typing is precise compensation for the time delay caused by the propagation of the surgical smoke from the dissection site to the mass spectrometer. This time delay is variable, owing to the varying length and curvature of the smoke evacuation tubing. In order to accurately resolve this variable time delay, one can temporally analyze the electrocautery burn, including the beginning and end of each cutting or coagulation action. Having captured the tracking data during the time period of the burn, we can map the mass-spectra to their spatial locations [2]. This paper presents a practical method for robust and accurate identification of the intra-operative state of the electrocautery, toward enabling navigated intra-operative mass spectrometry tissue analysis.

MATERIALS AND METHODS

We built on the approach of Carter *et al.* [3] and improved on it by placing an SCT-013 current sensor on both the live and return electrodes of the cautery. These sensors were connected to a PicoScope P2204A USB oscilloscope (Pico Technology, St Neots, UK) to amplify and digitize information about the current passing through the cautery (Fig 1.)

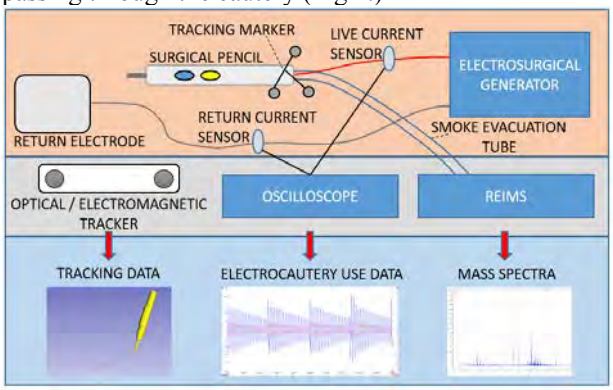

Fig. 1: Schematics of intra-operative time-delay compensation for spatially localized mass spectrometry tissue analysis. Note the current sensors placed on the cautery live and return electrodes and the oscilloscope digitizing these signals.

We can stream the current data via the PLUS Toolkit [4] to the SlicerIGT surgical navigation platform [5]. The signal wave analysis can be performed in MATLAB, which is bridged in real-time to SlicerIGT where the mass-spectra are mapped to their spatial locations.

Determining the electrocautery state (including the mode as well as whether the cautery is in contact with the patient or not) serves a double purpose in our system. Firstly, the mass spectra differ slightly between cut and coagulation modes, so these different diathermy modes must be distinguished. Using the external signals captured from the electrical properties of the cautery we can differentiate between these modes – and can thus apply machine learned models trained on data-specific to each cautery mode in real-time to improve tissue analysis accuracy. Secondly, being able to classify when the cautery is activated in the air, versus when it is being applied to the patient allows us to detect the precise beginning and end of every cautery burn. The air / tissue classification is necessary because surgeons often activate the cautery before their tool is in contact with the tissue they are dissecting.

To ensure generality and robustness for our cautery state detection method we performed the experiments twice, with electrosurgical generators from two different manufacturers. We used the Erbe VIO 50 C (Erbe Elektromedizin GmbH, Tuebingen, Germany) and the Valleylab Force FX C (Avante Health Solutions,

Illinois, USA) generators. For each generator, the electrical profile of five "burns" in air, and five cauterizing bovine tissue were recorded. This experiment was repeated 3 times collecting samples with temporal resolutions of 20us / division, 200us / division and 20ms / division. Some example signals from this experiment are shown in Fig 2. We divided the labeled data into 4 classes: cut-air, coag-air, cut-tissue and coag-tissue. We clustered these signals based on the magnitude of the live signal, the return electrode signal and the magnitude of the difference between them. Classification is straightforwardly performed by computing the distance between the unlabeled signal and the centroids of the clusters. Misclassified signals can be rectified by low-pass filtering since surgeons usually do not switch cautery mode within a single burn.

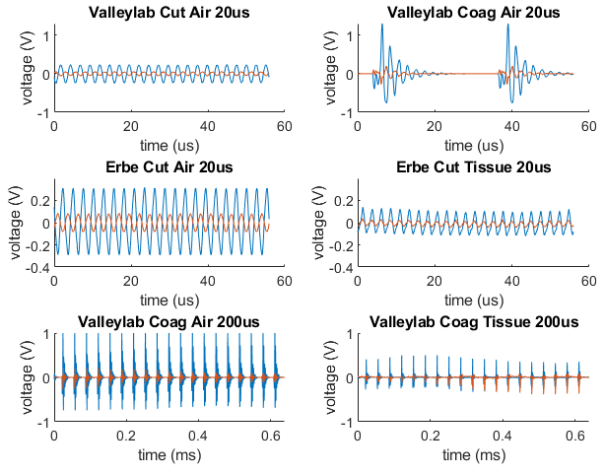

Fig. 2: Electrical signals of cautery live (blue) and return (orange) electrodes in cut (top left) and coagulation (top right) modes. Middle and bottom rows compare air burns (left) with tissue burns (right).

RESULTS AND DISCUSSION

Fig. 2 presents the signals captured from two different electrosurgical generators. Specific attention should be paid to the differences between cut & coagulation mode (top row) as well as the subtle low-frequency sinusoid present only in the envelope of signals from tissue burns. Fig. 3 presents a plot of the clustered signals, showing clear separation between the four classes. We tested the system with two different electrocautery generators. For each generator, the electrical profile of five pairs of burns in air and bovine tissue were recorded, each repeated three times with different temporal resolutions. The classification yielded clear identification of the electrocautery states and modes. It is of note that we purposely selected a straightforward training and classification model, since retraining may be necessary for different electrocautery generators or when energy settings are changed more drastically. This model can be updated with no disruption to the surgical workflow by processing a couple of additional cautery activations. Specifically, a single cut-air and coag-air sample must be provided, then we can label a handful of tissue burns using visible feedback from the surgical scene and the electrocautery generator. This recalibration and retraining, if necessary, can be done seamlessly using a few cutting and coagulation burns at the very beginning of the surgery, expectedly upon skin incision when tissue characterization is not yet necessary.

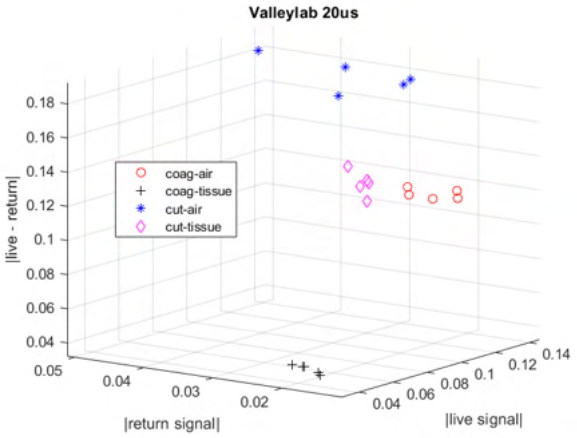

Fig. 3: Clustering of cut-air, coag-air, cut-tissue and coag-tissue samples collected on the Valleylab Force FX with 20us/ division temporal resolution, showing clear seperation.

We continue to optimize the implementation toward use in the clinical environment. To that end, our method needs to be faster than the shortest time delay between the cautery action and the appearance of mass spectra. In our experience [2] and that of Balog et al. [1], this time delay was never shorter than 1 sec. which is readily attainable in the integrated navigation system. In summary, we have shown the ability to differentiate the state and mode of the electrocautery action, as well as whether an activated cautery is in contact with the dissection site. The classifier is straightforward while being sufficiently robust and accurate, and it can also be seamlessly retrained during surgery. Future work will seek to validate this technique in the operating room and explore alternative detection algorithms using this translational data.

REFERENCES

[1] Balog J, Sasi-Szabo L, Kinross J, Lewis MR, …, Takats Z. Intraoperative tissue identification using rapid evaporative ionization mass spectrometry. Science Trans Medicine. 2013; 5(194): 194ra93.

[2] Asselin M, Kaufmann M, Wiercigroch J, Ungi T, …, Fichtinger G. Navigated real-time molecular analysis in the operating theatre, demonstration of concept. SPIE Medical Imaging 2019. 109512C.

[3] Carter K, Vaughan T, Holden MS, Gauvin G, …, Fichtinger G. Current sensing for navigated electrosurgery. SPIE Medical Imaging 2016. 97861Y.

[4] Lasso A, Heffter T, Rankin A, Pinter C, …, Fichtinger G. PLUS: Open-source toolkit for ultrasound-guided intervention systems. IEEE Trans Biomed Eng. 2014; 61(10): 2527-2537.

[5] Ungi, T., Lasso, A., Fichtinger, G. Open-source platforms for navigated image-guided interventions. Med Image Anal, 2016 Oct;33:181-186.

Preliminary Validation of Urethral Transection Simulation during RARP

Julien Abinahed[1], Nikhil Navkar[1], Georges Younes[1], Shidin Balakrishnan[1], Abdulrahman Alfayad[1], Waseem Palliyali[1], Gorune Ohannessian[2], Zherong Pan[3], Dinesh Manocha[4], George Turkiyyah[2], and Abdulla Al-Ansari[1]

[1]*Department of Surgery, Hamad Medical Corporation, Qatar,*
[2]*Department of Computer Science, American University of Beirut, Lebanon,*
[3]*Department of Computer Science, University of North Carolina, USA,*
[4]*Department of Computer Science, University of Maryland, USA*
jabinahed@hamad.qa (DOI10.31256/HSMR2019.30)

INTRODUCTION

Simulation of high-fidelity surgical cutting in real-time remains a major challenge for surgical simulators [1]. Current solutions typically simplify the cutting problem by generating large, unintended cuts, with simplified geometries and deformations leading to low fidelity cutting as shown in Fig. 1 and Fig. 2. This simplification of the cutting problem prevents specific cutting scenarios where high resolution and deformation models are required for the simulator to produce a meaningful learning outcome. This is for example the case of ureteral transection step during Robotic Assisted Radical Prostatectomy surgery (RARP) simulation, that requires high resolution and precise cutting steps. This scenario is not offered in current products perhaps due to the complexity of simulating a high fidelity cutting scenario in real-time [2]. Nonetheless urethral transection represents an important step in RARP as an unsuccessful urethral transection would have serious repercussions on surgical outcomes [3]. We developed a high-fidelity real-time cutting simulator for the urethral transection step during RARP surgery. Fig. 3 shows an overview of the simulator. In this paper, we present the initial clinical validation results performed on this simulator with surgeons.

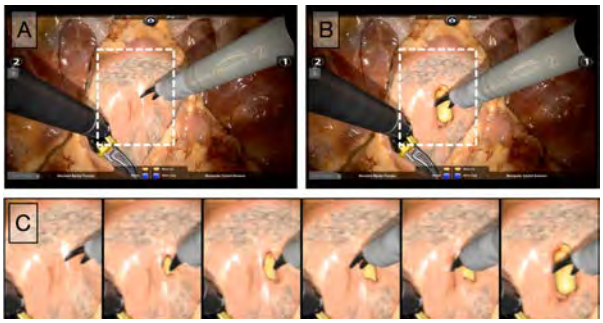

Fig. 1 Cut produced for bladder neck dissection on a simulator (RobotiX Mentor by 3D Systems Simbionix, Colorado, USA). Panel A shows intact anatomy before the cut, while Panel B shows tissue dissected after cut is produced by multiple snips as shown in series of images (left to right) of Panel C.

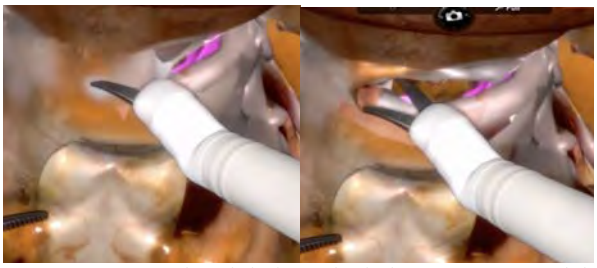

Fig. 2 One cut produced during robotic hysterectomy module on a simulator (RobotiX Mentor by 3D Systems Simbionix, Colorado, USA). Left picture show scene before cut just after closure of scissors, and right picture shows the cut after closure of scissors.

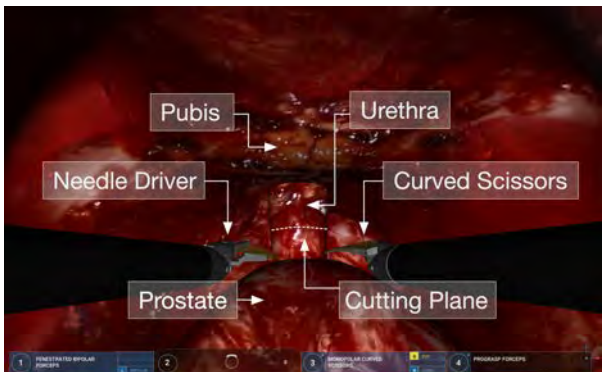

Fig. 3 Urethral transection simulator external view. Two haptic devices are used as interface to surgeons. Realistic textures and models are used to simulate the surgical scene.

MATERIALS AND METHODS

We developed a high fidelity realistic cutting simulator for the urethral transection step during robotic assisted prostatectomy simulation. The system includes real surgical textures, realistic geometric models, real-time, interactive, human in the loop, capable of continuous volumetric cutting merging advanced collision detection and finite element modelling all running at a limited computational budget of a typical high end laptop or workstation. In order to assess potential clinical value of our simulator we performed an initial validation study including face, content, and defined the metrics of

construct validity. We followed a user-centered approach for the design of the evaluation metrics that would measure qualitatively and quantitatively the performance of surgeons for the urethral cutting in RARP procedure. The approach was divided into two phases: formative and summative. Each phase comprised of techniques targeting the face, content and construct aspects of the simulation. The formative phase included observation and interviews with expert surgeons and medical doctors with a background in prostatectomy. Task analysis was performed to verify the assumptions about the surgeon's usage of a hypothetical simulator that allows urethral cutting. We conducted two formative evaluation tests: heuristics evaluation and think-aloud evaluation. We prepared a questionnaire on a Likert Scale of 1 (Strongly Disagree) to 5 (Strongly Agree) to assist in evaluating the subjective realism of the simulator, i.e. the face validity, and its appropriateness as a teaching modality, i.e. the content validity. We also identified 3 metrics that could be used to measure the performance of trainees [4], namely (1) The cut should lie on a plane that follows the surface of the prostate; (2) The size of the cut should be small to avoid unrecoverable damages; and (3) no damage to key organs such as rectum and nearby structures. In the summative phase, user tests were performed with surgeons (n = 7) with different experience levels (3 novice, 2 intermediate, and 2 expert level), using a think-aloud evaluation technique. Following the session, participants filled the Likert-scale questionnaire related to face and content validity and discussed the interface informally with the research team. The questionnaire was provided to the evaluators after allowing them to freely interact with the simulator. They were also engaged in discussions with the validity test moderator to assess the usability.

RESULTS

Table 1 summarizes the results. It shows that most participants rate the simulator high on face and content validation. The face validity average score was 4.05/5 while the content validity average score was 4.11/5.

Table 1 also shows the detailed feedback from each surgeon on each question related to face and content validity and that all questions averaged more than 3.5/5. Finally, Fig. 4 shows a sample cut, with the recorded key parameters used to generate evaluation metrics.

DISCUSSION

Initial validation results are encouraging. Results show that the simulator appear to be realistic and could be used as a teaching tool. In addition, the evaluation metrics that this urethral transection simulation can record are due to the high fidelity aspects of our simulator, namely high accurate geometries, collision handling and deformations all in real time. We did not observe specific trends among different group of surgeons, however since our sample size is relatively small, our future work will include larger sample size, with detailed construct validation with the metrics defined above along with face, and content validations, with larger cohort of surgeons with different background, and expertise level.

Table.1 Summary of face and content validation

	Questionnaire	Scores (1 - Strongly Disagree; 2 - Disagree; 3 - Undecided; 4 - Agree; 5 - Strongly Agree)							
		Surgeon 1	Surgeon 2	Surgeon 3	Surgeon 4	Surgeon 5	Surgeon 6	Surgeon 7	Average
Face Validity	The cutting mechanism represents a real world cutting task in a prostatectomy surgery	4	4	4	4	2	4	4	3.71
	The device is a sufficiently accurate representation of a real robotic system	4	5	4	4	3	4	3	3.86
	The hand controllers are effective for working in the simulated environment	5	3	5	4	4	4	5	4.29
	The user interface is efficient and minimalistic	5	5	3	4	4	4	4	4.14
Content Validity	The cutting task is effective for teaching the cutting skill for surgeons	4	4	3	4	4	5	4	4.00
	The scoring system effectively communicates the user's performance on the cutting exercise	4	5	5	4	4	4	4	4.29
	The scoring system effectively guides the user to improve the performance on the simulator	3	5	5	4	4	4	4	4.14
	The scoring system is effectively communicated to the user and messages are presented in plain language	5	5	4	4	4	4	5	4.43
	Learning the system is feasible by first-time users with minimal supervision and/or training	5	5	4	3	4	2	5	4.00

nf_0 = 13 faces, ne_0 = 44 edges | nf_1 = 17 faces, ne_1 = 27 edges | nf_2 = 7 faces, ne_2 = 18 edges

Fig. 4 Sample transection through consecutive cuts showing nf_i: the number of colliding faces, and ne_i the number of colliding edges between the urethral and tool meshes.

ACKNOWLEDGMENT

This work was supported by NPRP award [NPRP 5--995-2-415] from the Qatar National Research Fund (a member of The Qatar Foundation). The statements made herein are solely the responsibility of the authors.

REFERENCES

[1] Paulus, Christoph J., et al. "Virtual cutting of deformable objects based onefficient topological operations."TheVisual Computer 31.6-8 (2015): 831-841.

[2] Bielser, Daniel, and Markus H. Gross. "Interactive simulation of surgical cuts." Proceedings the Eighth Pacific Conference on Computer Graphics and Applications. IEEE, 2000.

[3] Pavlovich, Christian P., et al. "Urinary continence recovery after radical prostatectomy anatomical reconstructive and nerve-sparing techniques to improve outcomes." BJU international 120.2 (2017): 185-196.

[4] Y. Halwani, et al. "Evaluation Metrics for Urethral Cutting in Robot Assisted Radical Prostatectomy Simulation". Proceedings of the (IMSH), January 2019.

Towards smart oxygenation sensing implants using soft robotics and diffuse reflectance spectroscopy

J Avery[1], M Runciman[2], A J Thompson[1] G Mylonas[2], A Darzi[1]

[1]*Department of Surgery and Cancer, Imperial College London, London, UK,*

[2]*HARMS Lab, Department of Surgery and Cancer, Imperial College London, UK*

james.avery@imperial.ac.uk (10.31256/HSMR2019.31)

INTRODUCTION

Colorectal cancer is the 2nd highest cause of cancer death in the UK (42,000 diagnoses, 16,000 deaths annually). Over half of colorectal tumours arise in the rectum, where definitive management usually entails pre-operative chemoradiation (combined chemo- and radiotherapy) followed by surgical resection. However, predicting response to chemoradiation remains problematic [1], meaning some patients are delayed in having surgery and undergo the side effects of treatment without receiving any therapeutic benefit.

Hypoxia creates resistance to radio- and chemotherapy in colorectal (and other) tumours [2]. Therefore, continuous measurement of tumour oxygenation, and thus hypoxia, has the potential to track resistance to chemoradiation therapy and offer wide-ranging opportunities for personalisation and optimisation of treatments. Due to its ability to quantify the differing optical absorbance profiles of oxygenated and deoxygenated haemoglobin [3], [4], diffuse reflectance spectroscopy (DRS) is a good candidate technology for this application. However, in order to quantify the oxygen saturation within the tumour, the sensor must be in continuous contact with the tissue. This presents a particular challenge in colorectal applications, as the device must be both suitable for endoscopic insertion, as well as compatible with the surrounding soft tissue.

To meet these requirements, we are developing a DRS sensor on an inflatable soft robotics platform. The inflatable scaffold is designed to fold around an endoscope for insertion, before pneumatic deployment. The purpose of the scaffold is then to maintain contact between the DRS sensors and the colon wall without adversely occluding the lumen.

MATERIALS AND METHODS

Variable stiffness inflatable scaffolds were created from thermoplastic sheets using a robotically guided laser welding system. A 6 degree of freedom (DOF) UR5 robotic arm (Universal Robots, Denmark) guides a collimated infrared (IR) laser (940 nm, Lumics, Germany), which is focused to a spot size of 0.8 mm. Application of an IR dye along the welding sites was necessary as the triple-laminate polyethylene (PE, polyethylene terephthalate (PET), PE films used did not absorb the IR laser beam. Using this method, six interconnected circumferential beams were fabricated that could be inflated and stiffened using a single inlet, which were flexible enough to fold round an endoscope, Fig 1A. A hollow hexagon, approximating a ring, was constructed by connecting the two ends of this planar beam array, Fig 1B. The dimensions of the beams inside the scaffold were 30 mm by 20 mm. These were chosen as a trade-off between strength of the overall structure and ease of routing the electronics. When deployed the ring approximated a circle of 60 mm diameter, representative of the diameter of the ascending colon [5]. The inlet was heat sealed after inflation, and the tube removed.

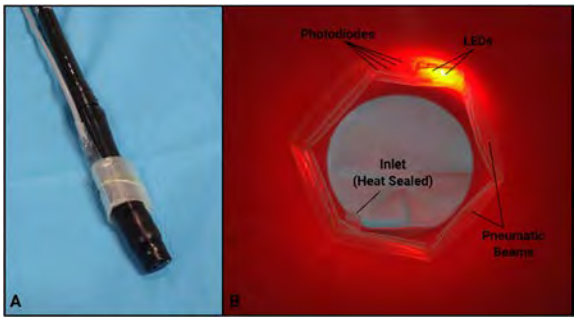

Fig. 1 Deployable inflatable scaffold incorporating prototype DRS sensor A) folded around endoscope during insertion B) deployed within a silicone rubber colon phantom

Optical sensing based on Near Infrared Spectroscopy (NIRS) was added to the scaffold. Using circuitry common to photoplethysmogram (PPG) systems, one red LED (660nm, Rohm semiconductor) and one IR LED (940nm, Kingbright) can be powered independently with a 20 mA operating current. These wavelengths are commonly chosen to provide the greatest contrast between the optical absorbance of oxygenated and deoxygenated haemoglobin. Four photodiodes (Rohm semiconductor) spectrally matched to the LEDs were connected via a multiplexer to a single transimpedance amplifier. The different sensor-detector spacing enables the interrogation of different depths within the tissue. To connect the optical sensors to the analogue front end, conductive traces (CircuitWorks Flex Conductive Pen, Chemtronics) were deposited onto the scaffold using a stencil. The stencil was laser cut using the same laser welding system used to create the inflatable scaffold. To reduce the strain and minimise the chance of delamination, the tracks ran parallel to the circumferential beams where possible. Finally, the optical sensors were affixed to the scaffold with silver epoxy. The analogue front end is a single circuit board, Fig 2, with dimensions 16mm x 8.5 mm.

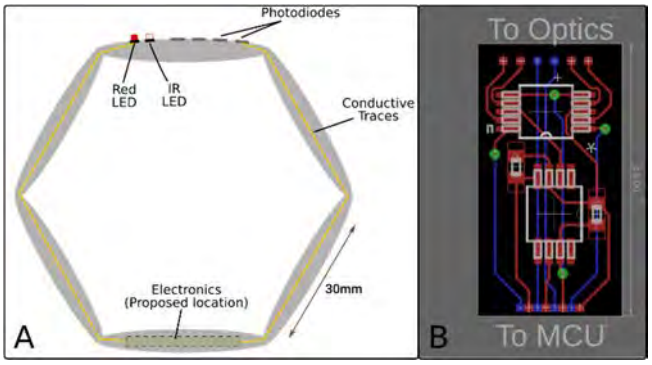

Fig. 2 A) Diagram of optical sensors incorporated within inflatable scaffold. B) PCB layout of analogue front end, to be incorporated within a beam of the scaffold

To assess the sensitivity of the proposed sensor, the TOAST++ software package [6] was used to simulate the diffuse light transport within a T3a rectal tumour [7]. Using custom meshing software based on the CGAL (Computational Geometry Algorithms Library) a finite element model was created based on a Magnetic Resonance Image (MRI) segmentation. Optical scattering and absorption values for the tissue were obtained from the literature [8]. The calculated Photon Measurement Density Function (PMDF) represents the sensitive volume for a single source/detector pair (Fig 3).

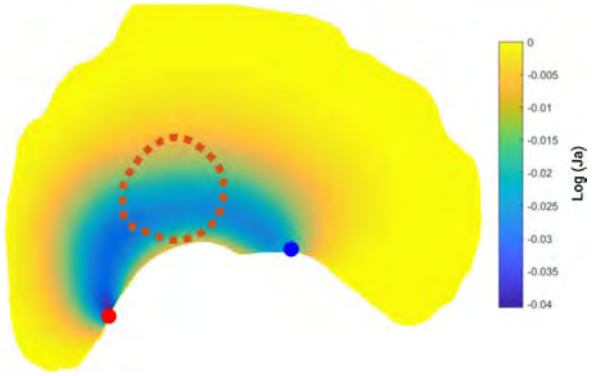

Fig. 3 Photon Measurement Density Function (PMDF) in a T3a rectal tumour illustrating how the sampling can be targeted to a chosen region (dashed line) using a single light emitting diode (LED, red dot) and photodetector (PD, blue dot). Yellow – low detection sensitivity; blue – high detection sensitivity.

RESULTS

The structure was deployed through pressurisation to approximately 500 mbar, to give an outer diameter of 60 mm. Using the heat seal, pressurisation and structure of the scaffold was maintained over the course of a week. The scaffold could be folded around and passed along an endoscope, before deployment with the conductive tracks intact. The optical sensors were successfully incorporated into the inflatable scaffold and continued to function after deployment. A spacing of 2 mm for the LEDs and 4 mm for the photodiodes was possible based on the limitations of the width of conductive tracks. The TOAST++ simulations demonstrated this sensor was sensitive to changes in oxygenation up to a depth of approximately 0.9 mm, sufficient to interrogate 5.6% of the tumour cross section.

DISCUSSION

Whilst the analogue front end presented here is limited to a single circuit design, the sensor itself is highly customisable, giving the potential for patient specific designs. Based on preoperative imaging, the size and shape of the scaffold could be readily adapted, and the optical sensor layout could be optimised. The ultimate goal is to incorporate the electronics into the stiffening chambers of the scaffold for a fully encapsulated device. This is not possible with the current analogue front end, which is constructed using a traditional rigid FR4 board. The next iteration of the design will use flexible PCBs and work is ongoing to improving the deposition of the conductive tracks, to reduce the minimum feature size to remove the separation between the LEDs. The proposed design has the potential to allow for continuous monitoring of oxygenation within a colorectal tumour during chemoradiation treatment. However, a soft compliant device that is capable of measuring oxygenation would also have a number of other monitoring applications, such as wound healing or anastomotic leaks.

REFERENCES

[1] I. Lindsey, "Predicting response to chemoradiotherapy in rectal cancer: Are we there yet?," *Color. Dis.*, vol. 15, no. 10, pp. 1199–1200, 2013.

[2] A. Challapalli, L. Carroll, and E. O. Aboagye, "Molecular mechanisms of hypoxia in cancer," *Clin. Transl. Imaging*, vol. 5, no. 3, pp. 225–253, 2017.

[3] E. Sevick, B. Chance, J. Leigh, S. Nioka, and M. Maris, "Quantitation of time- and frequency-resolved optical spectra for the determination of tssue oxygenation," *Anal. Biochem.*, vol. 195, pp. 330–351, 1991.

[4] A. A. Stratonnikov and V. B. Loschenov, "Evaluation of blood oxygen saturation in vivo from diffuse reflectance spectra," *J. Biomed. Opt.*, vol. 6, no. 4, p. 457, 2001.

[5] M. Khashab, P. Pickhardt, D. Kim, and D. Rex, "Colorectal anatomy in adults at computed tomography colonography: normal distribution and the effect of age, sex, and body mass index," *Endoscopy*, vol. 41, no. 08, pp. 674–678, Aug. 2009.

[6] M. Schweiger and S. Arridge, "The Toast++ software suite for forward and inverse modeling in optical tomography," *J. Biomed. Opt.*, vol. 19, no. 4, p. 040801, 2014.

[7] F. G. M. Taylor, R. I. Swift, L. Blomqvist, and G. Brown, "A systematic approach to the interpretation of preoperative staging MRI for rectal cancer," *Am. J. Roentgenol.*, vol. 191, no. 6, pp. 1827–1835, 2008.

[8] S. L. Jacques, "Optical properties of biological tissues: A review," *Phys. Med. Biol.*, vol. 58, no. 11, 2013.

Layer jamming pneumatic actuator for medical robotics

Michele Ibrahimi, Linda Paternò, Leonardo Ricotti, Arianna Menciassi

The BioRobotics Institute, Scuola Superiore Sant'Anna, Pisa, Italy

michele.ibrahimi@santannapisa.it (DOI10.31256/HSMR2019.32)

INTRODUCTION

The interest in stiffness-variable systems arises from the need of devices showing both high compliance and high load bearing capabilities. Traditional medical robots, such as manipulators, exoskeletons and prostheses, are usually made of rigid materials, not capable of stiffness or shape changes. In this field, jamming actuators and stiffening solutions appear as highly promising technologies: they are based on the application of vacuum inside envelopes of a flexible material, containing granular, fiber-based or layer structures. In its resting state, a layer jamming structure is highly compliant; on the other hand, when a vacuum pressure is applied inside the envelopes, the frictional interactions of the internal sheets significantly increase the bending stiffness of the whole system [1]. Generally, a layer jamming structure consists of flexible sheets of low cost materials, such as sandpaper, or sheets shaped through more expensive strategies to allow a more precise locking of the layers. This technology has been applied to haptics, surgical devices, as well as to soft actuators and sensors for assistance and rehabilitation purposes [2]. However, generally they lack a controlled shape and stiffness change capability. In the present work, a novel actuator made of layer jamming structures combined with inflatable chambers is proposed. The shape and stiffness change is activated by selectively pressurizing/ depressurizing the chambers through a control unit. The system can be portable/wearable: it can be integrated into a prosthesis/orthesis thus to adapt it to limbs, or it can be exploited in other domains, such as soft robotics or conformable grippers.

MATERIALS AND METHODS

The actuation concept consists of three chambers: two of them contain sandpaper sheets for the jamming actuation, while the other one is empty to allow inflation. The device is assembled by overlapping the two jamming chambers along their main dimension and by interposing the inflatable chamber transversally respect to the jamming chambers, and at mid-length. The three chambers are constrained together by three elastic bands made of a rubber-like material wrapped around the structure (Fig. 1a-0). All the chambers were obtained by welding foils of a PET/Nylon composite on their four sides. Starting from a planar state, the configuration can be changed as follows: (*1-2),* the bottom jamming chamber is stiffened by vacuum application, then the inflatable chamber is inflated, forcing the top jamming chamber to follow the shape imposed; (*3-4)* the top jamming chamber is stiffened, then the bottom one is softened by releasing the vacuum; *(5-6)* the inflatable chamber is deflated, forcing the bottom jamming chamber to adhere to the upper one, thanks to the elastic bands. The new configuration is then locked by applying vacuum to both layer structures. The system is activated through a control unit, which can be turned on by a mechanical switch. The micro-controller enables a micro-diaphragmatic pump to apply vacuum and pressurize the jamming and inflatable chambers by alternating the opening and closing of five 3 ports/ 2 ways normally closed solenoid valves and one 2 ports/ 2 ways normally closed solenoid valves (Fig. 1b).

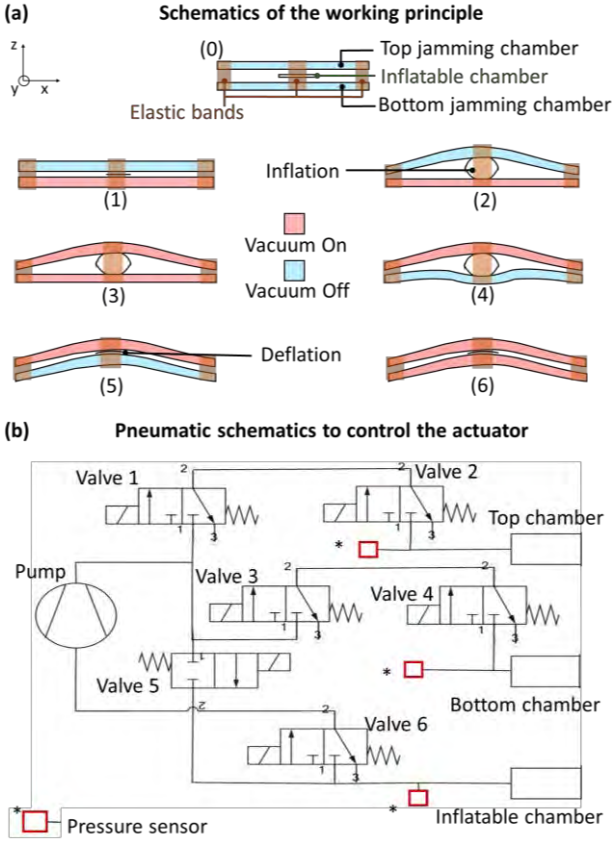

Fig. 1:(a) Lateral view of the actuation phases. Sample are 190x55 mm, containing sheets of 180 mm x 45 mm and an inflatable chamber of 30 mm x 45 mm. (b) Pneumatic circuit to activate the device.

The valve connections are assembled and activated during the different phases reported in Fig. 1a in such a way that the pump can be used as a compressor and vacuum source, since one of the two pump ports needs to stay opened during operation. Valves 2 and 4 are used to decouple the top and bottom chambers from the circuit, to maintain the vacuum after turning off the

pump. This mechanism highly depends on the stiffness variation of the jamming chambers, which need to be stiff enough to avoid buckling and soft enough to allow the maximum shape-change during the various phases. Hence, two-point bending tests were carried out on single jamming chambers, containing ten sheets of different sandpaper materials (P1000, P180 and P80). Each single jamming chamber was anchored at one extremity and its free end was bent with a six Degrees of Freedom robotic arm for a distance of 15 mm along the z axis (Fig. 1). The bending force was recorded with an ATI Nano 17 sensor, mounted on the robotic arm end-effector. Once assessed the bending characteristics of the jamming chambers, for each of the three types of sandpapers, an actuator was assembled, and its performance was verified (Fig. 2). For the activation, the inflatable chamber was pressurized at its maximum inflation pressure before breakage (180 kPa).

RESULTS

As reported in Table 1 illustrating results of the two-point bending tests, the highest maximum bending force of the single jamming chambers under vacuum is reported by the material with highest friction (P80).

Material	*Absolute Pressure*	*Max Bending Force (N)*	*Stiffness variation**
P80	101 kPa	0.221±0.001	11.09±0.076
	30 kPa	2.453±0.0027	
P180	101 kPa	0.151±0.001	11.72±0.123
	30 kPa	1.772±0.008	
P1000	101 kPa	0.051±0.001	16.54±0.233
	30 kPa	0.849±0.003	

Table 1: Forces averaged on three samples for each material. *Stiffness variation = $F_{30\,kPa}$ / $F_{101\,kPa}$.

However, this causes the material to be stiffer also without vacuum. In fact, it can be noticed that the stiffness variation is lower compared to P180, which in turn is lower than P1000. These materials have been used to assemble three actuators, not activated (phase 0 of Fig. 1a-0) and activated (phase 6 of Fig. 1a-6) configurations as showed in Fig. 2.

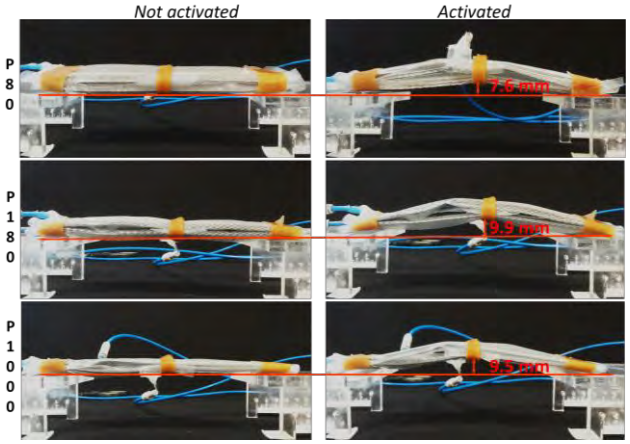

Fig. 2: Device samples with different internal sandpapers.

As depicted in Fig. 2, actuators displaced from phase 0 to phase 6 of 7.5 mm with P80, of 9.9 mm with P180 and of 9.5 mm with P1000, at mid-length.

DISCUSSION

In accordance with the layer jamming theory [1], it was verified that the bending force increases with vacuum and the maximum value is obtained with the P80 thanks to its highest interlayer frictional coefficient. The stiffness variation and maximum bending force are crucial in the different phases of the device working. Indeed, the bottom and top chambers in phases 2 and 4 need to be stiff enough to avoid the chambers buckling, respectively; in analogy, the top and bottom chambers in phases 2 and 5, respectively, need to be as soft as possible to guarantee the maximum shape change (Figure 1a). The actuator assembled with P80 displaced 7.6 mm, which is less than the others because the top chamber needs higher forces to be displaced during phase 2. On the other hand, P1000 displaced less than P180, because of a buckling downwards of the bottom chambers during phase 2. This behaviour may be avoided in the future by using interlocking sheets or by changing the samples shape, which can improve the stiffness variation and bending forces.

With a low-cost manufacturing, this working principle gives the possibility to change shape and stiffness at the same time. As shown in Fig. 3, playing with the constraints of the elastic bands, the device can be used for different purposes, such as gripping (Fig. 3a). Otherwise, a wearable pump can be used to activate a shape change of an orthotic brace, when a volume loss of a limb and/or loss of contact surface occur (Fig. 3b).

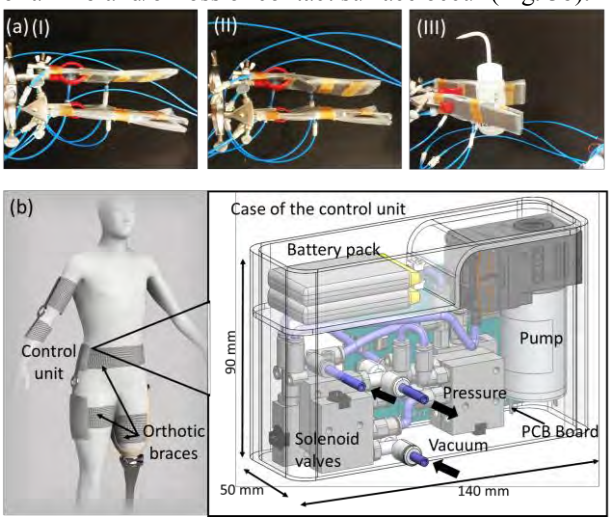

Fig. 3: (a), Gripper configuration lifting a 250g bottle and (b) control unit to activate the shape changes of the actuator in wearable devices.

REFERENCES

[1] Y. S. Narang, J. J. Vlassak, and R. D. Howe, "Mechanically Versatile Soft Machines through Laminar Jamming," *Adv. Funct. Mater.*, vol. 28, no. 17, pp. 1–16, 2018.

[2] M. Cianchetti, C. Laschi, A. Menciassi and P. Dario, "Biomedical application of soft robotics," *Nat. Rev. Mater.*, vol. 3, pp. 143–153, 2018.

Gaze-contingent Robotic Nurse Assistant

A. A. Kogkas[1], A. Ezzat[1], R. Thakkar[3], A. Darzi[2], G. P. Mylonas[1]

[1]HARMS Lab, [2]Department of Surgery and Cancer, Imperial College London, UK

[3]St George's, University of London, UK

a.kogkas15@imperial.ac.uk (DOI10.31256/HSMR2019.33)

INTRODUCTION

Meaningful integration of technology within surgery has been established as useful, while shortages in operating theatre personnel may increase patient mortality risk [1]. Assistive robotic devices enable to the surgical team touch-less interaction, information acquisition and task completion. This provides an extra "third hand" to empower staff to perform wider variety of tasks thereby improving efficiency and team work flow.

Robotic scrub nurses have been reported in the literature, which rely on hand gestures or voice commands to support the surgeon in selecting and delivering surgical instruments [2]. Whilst these examples are promising, some limitations have been reported relating to the practicality of gestures and voice recognition in the noisy operating theatre. We introduce a novel gaze controlled robotic scrub nurse which is supported by a perceptually-enabled Smart Operating Room (Smart-OR) platform [3]. This is based on a novel real-time framework for theatre wide and patient wise 3D gaze localization, to allow the surgeon to operate in a mobile fashion enabling further flexibility and freedom, as occurs traditionally. This framework enables dynamic gaze-based user interaction with the robotic scrub nurse to facilitate practical and user-friendly human-technology interaction intra-operatively.

SYSTEM OVERVIEW

The core functionality of the real-time framework presented here is to provide the user's 3D point of regard (PoR) in a world coordinate system (WCS), defined by multiple co-registered RGB-D sensors fixed in the theater. It relies on estimating the pose of the scene/RGB camera of the wearable eye-tracking glasses (ETG) in the WSC and tracing the gaze ray provided by the ETG on the head frame of reference, on the 3D reconstructed space. The ETG scene camera pose is estimated with the employment of a motion capture system (MCS) and spherical markers mounted on the ETG. The user's head pose (equivalent to the ETG's scene camera pose) can be used to map the 2D gaze to a unique 3D fixation in the WCS. The 3D gaze ray can be used to detect fixations on a screen fixed in space (micro fixation) and after a certain dwell time trigger the robot routine. The robot moves towards a surgical instrument selected by the user, grasps it with a magnetic gripper and transfers it to the user. When the force/torque sensor mounted on the robot end-effector senses the instrument is picked up, it returns to its homing pose (Fig. 1).

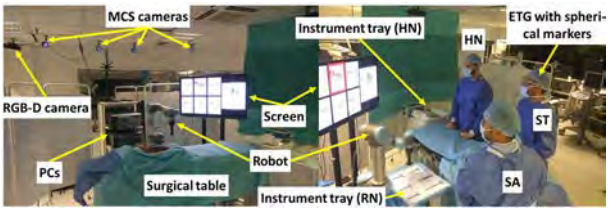

Fig. 1 The experimental setup. See Table 1 for definitions of abbreviations.

MATERIALS AND METHODS

Equipment: The wireless SMI (SensoMotoric Instruments GmbH) glasses are used for eye-tracking. Microsoft Kinect v2 cameras are employed for RGB-D sensing and the OptiTrack MCS, with 4 Prime 13 cameras for head pose tracking. The robot is a UR5 (Universal Robots), with the Robotiq FT-300 F/T sensor attached. A 42″ LG screen with 1920x1080 px resolution is used for the instrument selection GUI. A Windows 10 PC is used for acquiring and streaming ETG and MCS data and e Linux PC with Ubuntu 14.04 for all other modules.

Offline Calibration: In an offline calibration routine, the rigid transformations between the ETG rigid body–ETG scene camera and MCS CS – WCS are calibrated. The screen corners 3D coordinates in the WCS are manually selected on the Kinect RGB image and the 3D points are generated. The surgical instruments are positioned in fixed positions on a tray. The robot is manually moved over each instrument and the target pose is calibrated. 9-point eye-tracking calibration is performed before every task.

Interface Design: The GUI displayed on the screen consists of two parts: instrument selection (left 2/3) and the image navigation (right 1/3). *Left*: Six blocks equally split demonstrate common surgical instruments. Micro fixation on any of the blocks initiates a traffic light sequence (red-amber-green) followed by relevant audio feedback. Starting with red block borders, dwell time of 0.6 *s* into the same block turns the borders into orange and another 1 *s* turns the borders into green. The design is based on pilot experiments aimed to allow the user to have sufficient feedback (audio/visual) for the estimated micro fixation (red), be warned before finalizing the instrument selection (amber) and confirm the action (green). *Right*: Three slides are presented to provide information necessary for the task workflow. The user can navigate through them by fixating on the top and bottom 1/6 parts of the screen for previous and next slide respectively. Dwell time here is 1 *s*.

Robot Control: The selection of an instrument on the screen (server) triggers the robot (client) to handle the corresponding instrument to the user. TCP/IP is used to transmit the instrument ID to the robot client. The robot client has predefined poses for homing, instruments grasp and instruments delivery. The robot moves towards instruments grasping pose, grasps the instrument with the magnetic gripper and delivers it to the user. Then the robot stays idle until the force/torque sensor senses the instrument collection by the user and 2 *s* extra time to ensure proper instrument collection. Finally, it returns to its homing position.

EXPERIMENTAL SETUP

The abbreviations stated in Table 1 are used to describe the experimental setup. STs were recruited to perform ex vivo resection of a pig colon and hand sewn end-to-end anastomosis. Each surgeon performed two experiments in randomized order: (1) a HT with the assistance of a HN and (2) a RT with the assistance of both RN and HN.

Table 1 Abbreviations used to describe the experimental setup.

Ab.	Explanation	Ab.	Explanation
HT	Human nurse only task	RN	Robotic scrub nurse
RT	Robot and human nurse task	SA	Surgeon assistant
ST	Surgical trainee	NA	Scrub nurse assistant
HN	Human scrub nurse		

The instrument tray inventory consists of the 6 most frequently utilized instruments during this particular task. The RT starts with a 9-points eye-tracking calibration. Familiarization with the system setup is offered for 1 minute. During the task, the ST selects the desired instrument by gazing at the screen and once it is delivered and collected, the SA responds to verbal command or prior experience to return the instrument to its predefined position on the instrument tray. The ST addresses to the HN for further instruments. In case of wrong instrument delivery, the ST expresses the error verbally. If eye-tracking recalibration is necessary, the task continues after recalibration. During the HT the setup is identical, but the ST relies entirely on the HN to deliver instruments based on verbal commands. During both experiments, distractions are introduced to the HN. The NA asks the HN to stop and perform an instrument count twice and solve a puzzle at specific task stages.

10 STs participated (7 male and 3 female). Two had corrected vision. STs were between 30-40 years with at least 6 years surgical experience. 5 trained theater HN were recruited. One ST, with 2 years surgical experience, acted as SA and one medical student acted as NA for all experiments.

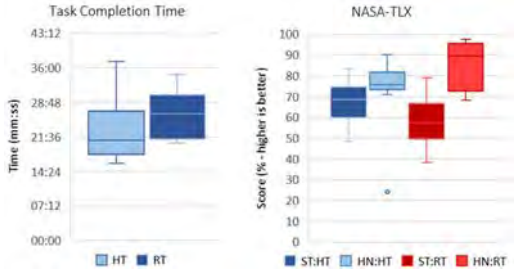

Fig. 2 Task completion time for HT and RT (left). NASA-TLX results for HT and RT responded by ST and HN (right).

RESULTS

After each task, the ST and HN were asked to complete a NASA-TLX questionnaire and the results are depicted in Fig. 2.

Overall time to complete the task was 22:35±6:30 minutes vs 26:04±4:50 minutes (HT vs RT, respectively) and no statistically significant difference was found.

ANOVA was used to compare preference of ST and HN on HT over RT (Table 2). Perception of HT and RT by ST and HN is also investigated. The only significant difference is shown on the perception of the RT by the ST (58±12%) and the HN (86±12%).

Table 2 ANOVA of paired NASA-TLX responses.

	95% confidence interval			
	ST on: HT vs RT	HN on: HT vs RT	HT by: ST vs HN	RT by: ST vs HN
F(1,18)	3.330	3.593	0.697	28.077
p	0.085	0.074	0.415	**<0.001**

DISCUSSION

A novel robotic scrub nurse, responsive to surgeon gaze, has been proposed. This platform allows the surgeon to visually select an instrument, using an ETG device, pick it up and deliver to complete a task. We tested the RN with 10 different surgical teams in a simulation of a common operative scenario, with similar theater staff representation and operative field set up.

Objectively, RT and HT showed no significant difference in overall experiment duration and all surgical experiments were completed. Subjectively, RN received positive feedback. NASA-TLX data demonstrated no significant difference between HN vs RN across perceptions. We aim to further develop our gaze-guided RN by enabling real-time recognition and tracking of the instruments and screen position in space. Practical aspects such as the RN delivering and returning the instruments will be implemented. Our goal is to develop a system to imitate the human nurse's most significant attribute, anticipation of next instrument selection. This involves work flow segmentation and task phase recognition.

AAK is supported by the NIHR Imperial Biomedical Research Centre (BRC).

REFERENCES

1. Velasquez, C.A., Mazhar, R., Chaikhouni, A., Zhou, T., Wachs, J.P.: Taxonomy of communications in the operating room. In: Advances in Intelligent Systems and Computing. (2018).
2. Jacob, M., Li, Y.T., Akingba, G., Wachs, J.P.: Gestonurse: A robotic surgical nurse for handling surgical instruments in the operating room. J. Robot. Surg. (2012).
3. Kogkas, A.A., Darzi, A., Mylonas, G.P.: Gaze-contingent perceptually enabled interactions in the operating theatre. Int. J. Comput. Assist. Radiol. Surg. 1–10 (2017).

Towards Semi-Automated Mechanical Thrombectomy: Path Planning Considerations for a Double Articulated Microcatheter

Colette Abah[1], Giuseppe Del Giudice[1],
Neel Shihora[1], Rohan Chitale[2], Nabil Simaan[1]

[1]*Department of Mechanical Engineering, Vanderbilt University, Nashville TN, USA*

[2]*Department of Neurological Surgery, Vanderbilt University Medical Center*
c.abah@vanderbilt.edu (DOI10.31256/HSMR2019.34)

INTRODUCTION

Intravenous thrombolysis with r-tPA has been the standard of care to treat ischemic stroke, the third most common cause of death in the world. However, the efficacy of r-tPA in treating strokes due to large vessel occlusions (LVO) is limited. In 2015, a series of multicenter randomized clinical trials demonstrated that in patients with strokes from LVO in the anterior circulation, endovascular mechanical thrombectomy is both safe and effective in improving functional outcomes [1]. The recent awareness to the importance of early revascularization via mechanical thrombectomy stands in contrast to the current availability of this intervention. Widespread adoption is partly hindered by its technical complexity. Due to the lack of distal control in existing catheters, neurointerventionalists rely on the use of a passive guidewire and a complex combination of stacked catheters to navigate to the occlusion site.

While steerable cannulas have been previously researched (e.g. [2]), there is a need for microcatheters capable of selecting branches and navigating the tortuous geometry of the internal carotid artery (ICA), in order to add maneuverability to mechanical thrombectomy. To address this need, the goal of this research is to create dexterous steerable catheters that eliminate the need for use of a guidewire and facilitate future robot-assisted thrombectomy.

This paper investigates the feasibility of navigating the ICA with a steerable robotic microcatheter. We propose the use of pre-operative CT scan for trajectory planning, and a least squares algorithm to minimize the shape error between the catheter and the vasculature. Finally, we evaluate the feasibility of using intraoperative imaging to update the pre-operative plan and track the pose of the microcatheter.

MATERIALS AND METHODS

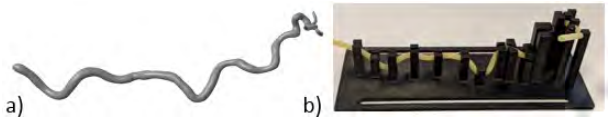

Fig. 1. Phantom vasculature model: a) Virtual b) Physical

A 3D model of the ICA was obtained by segmenting a head CT in 3DSlicer. Fig. 1a shows the virtual phantom model used for preoperative path planning. The ICA curve was parametrized as a set of arc-length equidistant vertices. For any given insertion arc length $s_i \in [0, L_{vasc}]$, the optimal attainable shape of the catheter was determined by finding the joint values $\boldsymbol{q} = [q_1, q_2]^T$ that minimize the shape deviation:

$$min\left(\sum_{i=1}^{n}\left(\left(\boldsymbol{p}(s_i,q)-\boldsymbol{c}(s_i)\right)^T\boldsymbol{W}_1\left(\boldsymbol{p}(s_i)-\boldsymbol{c}(s_i)\right)\right)+\right.$$
$$\left.\sum_{i=1}^{n}\left(\left(\hat{\boldsymbol{t}}(s_i,\boldsymbol{q})-\hat{\boldsymbol{t}}_{\boldsymbol{c}}(s_i)\right)^T\boldsymbol{W}_2\left(\hat{\boldsymbol{t}}(s_i,\boldsymbol{q})-\hat{\boldsymbol{t}}_{\boldsymbol{c}}(s_i)\right)\right)\right) \quad (1)$$

Where $\boldsymbol{p}(s_i,\boldsymbol{q})$ and $\hat{\boldsymbol{t}}$ designate the point location and local tangent according to direct kinematics of the SRMC at arc length s_i. The corresponding entities on the segmented vasculature are $\boldsymbol{c}(s_i)$ and $\hat{\boldsymbol{t}}_{\boldsymbol{c}}(s_i)$. Equation (1) was solved using the Levenberg-Marquardt nonlinear least squares formulation.

The proposed path following algorithm was validated in simulation using segmented vasculature path and a kinematic model of the Steerable Robotic Microcatheter (SRMC) shown in Fig. 2. This SRMC has flexure-based continuum segments with antagonistic actuation (e.g. [3]), bends in two planes separated by $43°$, and is mounted on a stage with insertion and roll degrees of freedom. The distal segment of the SRMC has a 0.88 mm outer diameter, which matches the size range of current (passive) thrombectomy microcatheters used for Stentriever deployment (Marksman, 0.96 mm, Rebar, 0.94 mm), and is smaller than the size range of current (passive) aspiration catheters (Sophia 6 Plus, 1.77 mm; ACE 068, 2 mm).

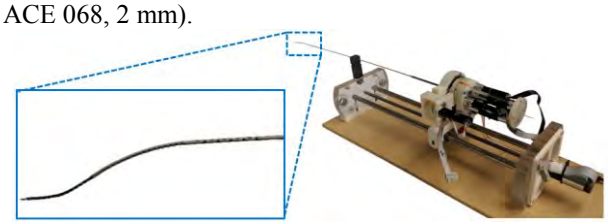

Fig. 2 Steerable robotic microcatheter (SRMC)

The kinematic model of the SRMC was determined via image-based calibration. For each segment, the associated actuation line was displaced in increments of $dq = 0.1$ mm until reaching a maximum bending range of $80°$. A picture of the bent segment was recorded for each $\boldsymbol{q}$ value. Figure 3a shows the achievable range of motion of the distal segment. Using image thresholding and cubic smoothing spline fitting, the shape of the flexible link was determined from the image, and parametrized as series of discrete equidistant points.

For each continuum segment, the local tangent along the arc length was calculated at each vertex using a forward finite difference approximation, Fig. 3b. The approach is hereby illustrated for a planar case for simplicity of notation.

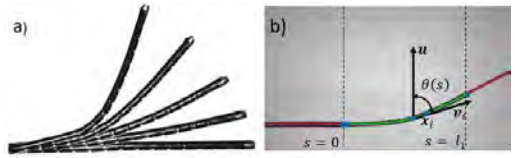

Fig. 3 a) Configurations of the distal SRMC segment $\boldsymbol{q}$ values. b) Parametrization of continuum segment shape.

Following the method of [4], the interpolation map $\boldsymbol{\theta}(s, q_i) = \boldsymbol{\psi}(s)^T \boldsymbol{A}\boldsymbol{\eta}(q_i)$, i=1,2, was obtained where $\boldsymbol{A}$ designates a shape characteristic matrix obtained by experimental calibration, $\boldsymbol{\psi}(s) = [1, s, s^2, s^3]^T$ and $\boldsymbol{\eta}(q_i) = [1, q_i]^T$. The degree of these modal vectors was determined to ensure the calibrated model fits the experimental data with an RMS error $\Delta\theta$ below 5°.

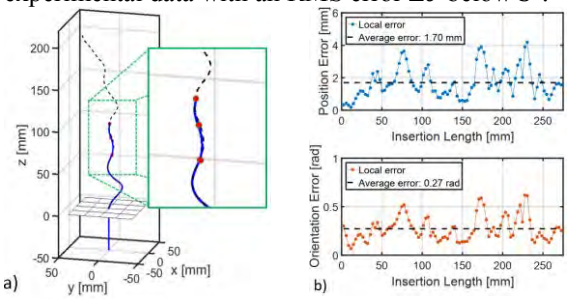

Fig. 4 a) SRMC following the trajectory of the ICA in simulation. b) RMS error as a function of insertion length.

For future image-guided SRMC steering, it is essential to track the catheter intraoperatively. We propose the use of image segmentation to update the pre-operative plan and obtain intra-operative information about the state of steerable catheter. To test this hypothesis, we conducted an experiment in an operating room equipped with a Phillips bi-plane fluoroscopy machine. A contrast agent (Omni 300) was injected into the vasculature to obtain an angiogram of the phantom vasculature. A SmartMask filter was applied to the angiogram to obtain a static roadmap of the vasculature. The SRMC was inserted into the vasculature against this static roadmap, and fluoroscopy images were saved at each step of the process. The images were segmented offline: the vasculature outline was obtained using image thresholding, and the catheter was segmented by subtracting the static background and using Canny filtering for edge detection.

RESULTS

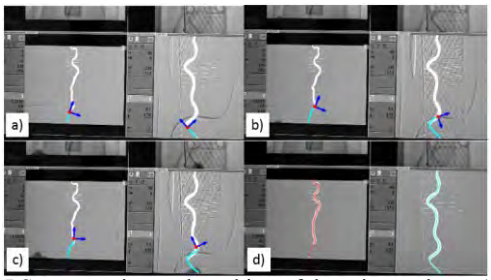

Fig. 5 Segmentation and tracking of the microcatheter (a – c) and the vasculature phantom centerline (d).

Figure 4 shows a simulation of the SRMC following the ICA path (Fig. 4a) and the RMS error as a function of the insertion depth s_i (Fig. 4b). The average position error along the full length of the vasculature was 1.7 mm.

Figure 5 shows the segmentation and tracking results superimposed on the original fluoroscopy images. Figures 5a-c show the pose of the tracked SRMC at different insertion depth. Figure 5d shows the segmented outline of the vasculature. The segmentation and tracking frequencies were 20 Hz for the vasculature, and 10 Hz for catheter.

Finally, a preliminary experiment with a planar 60^o bifurcation is shown in Fig. 6. The SRMC was controlled in joint level and it was able to select a branch within a 3.5 mm ID Polyurethane tube.

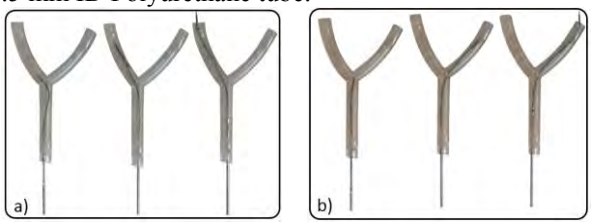

Fig. 6 Insertion and branch selection (a) left branch and b) right branch) inside a planar bifurcation using the SRMC.

DISCUSSION

This paper reported a pre-operative path planning strategy for steering a double articulated SRMC along the geometry of the ICA using pre-operative CT scans. A 0.88 mm SRMC was fabricated and an approach for calibrating its kinematics for kinematics-based steering was derived based on least-squares formulation using an artery model segmented from 3D CT imaging. Since this pre-operative plan must be updated intraoperatively for image-guided control, an approach for tracking the SRMC tip was devised based on use of bi-plane fluoroscopy image. This pipeline was evaluated in a simulation study and on a planar bifurcation model.

Future work will include the use of Gaussian filtering to reduce noise in catheter tracking and enable online segmentation. We also plan to create a simulation-based design parameter optimization using our path planner on the target anatomy from CT data. Such parameters include length of the continuum segments and bending plane offset to minimize path following error.

ACKNOWLEDGEMENT

C. Abah was supported by National Institutes of Health (NIH) award T32-EB02193 of the NIBIB.

REFERENCES

[1] M. Goyal et al., "Endovascular thrombectomy after large-vessel ischaemic stroke: a meta-analysis of individual patient data from five randomised trials," Lancet, vol. 387, no. 10029, pp. 1723–1731, Apr. 2016.

[2] Y. Chitalia, X. Wang, and J. P. Desai, "Design, Modeling and Control of a 2-DoF Robotic Guidewire," in 2018 IEEE International Conference on Robotics and Automation (ICRA), 2018, pp. 32–37.

[3] K. Oliver-Butler, Z. H. Epps, and D. C. Rucker, "Concentric agonist-antagonist robots for minimally invasive surgeries," 2017, vol. 10135, p. 1013511.

[4] J. Zhang, K. Xu, N. Simaan, and S. Manolidis, "A pilot study of robot-assisted cochlear implant surgery using steerable electrode arrays," Med. Image Comput. Comput. Assist. Interv., vol. 9, no. Pt 1, pp. 33–40, Jan. 2006.

A Low-Cost Draw-Wire Sensor for Kinematic Sensing in Wearable Assistive Robots

R. J. Varghese, R. K. Singh, J. Liu, G-Z. Yang

The Hamlyn Centre, Institute for Global Health Innovation, Imperial College London
r. varghese15@imperial.ac.uk (DOI10.31256/HSMR2019.35)

INTRODUCTION

For wearable assistive robots (exosuits), kinematic sensing networks are extremely important to get an understanding of the state of the human-exosuit system and are crucial for intuitive and synergistic human-robot control. Research and commercial projects have used different sensing modalities like IMUs, flex/bend sensors, micro-fluidics, dielectric elastomers, liquid metal alloys, *etc*. for kinematic sensing [1]. Many of these systems suffer from hysteresis, limited range, and other non-linearities. In our previous work [2], we developed a kinematic sensing framework to identify the joint angles of 2 degrees of freedom (DoFs) of the shoulder simultaneously using an arrangement of 4 draw-wire sensors (also known as string encoders/string potentiometers) in a proprioception-inspired setting.

Apart from the cost of the off-the-shelf sensor (GBP 160-260/unit), a second drawback was identified. As the sensor uses a potentiometer, the signal is sensitive to the stability of the on-board battery voltage, which also changes as the battery drains affecting signal quality. To overcome these limitations, we decided to develop a low-footprint sensor that uses a digital incremental encoder in its design to overcome this problem. The developed sensor also costs much lesser than the cheapest commercial sensor. The design and characterization of this sensor are presented here.

SENSOR DESIGN

The developed sensing module is a spring-tendon-encoder based sensor developed for tracking joint positions/angles by measuring the shortening/elongation of a tendon moving across a joint along a specific path. The CAD rendering and prototype of the SSM is shown in Fig.1(a) and (b) respectively. As the sensing unit is tendon-driven it gives the flexibility of placing the unit either proximally or distally (through a Bowden-cable arrangement).

The sensor comprises of an off-the-shelf soft clock-type spiral spring attached to a tendon-spool that moves through a pair of rollers, of which one is free to rotate and the other is attached to a rotary encoder (Bourns Inc., CA, USA). The force at the tendon (spring force+friction in rollers) was measured to be approximately constant of $\sim 2.2N$ throughout the tendon displacement. The encoder has a resolution of 512 pulses per revolution (ppr). The spacing between the rollers is adjusted by a set of adjustment screws to generate enough friction to maximize rolling/minimize slipping. The spring keeps the tendon in tension and the pulling/ releasing of the tendon is recorded by the encoder. The rollers and the base were printed using the Objet500 Connex 3D printer (Stratasys Ltd., MN, USA) using a combination of VeroBlack (high Shore hardness material) and TangoBlack (low Shore hardness) PolyJet materials. The roller-encoder combination gives the SSM a resolution of $\approx 0.07mm$. The encoder is interfaced through an Arduino Mega2560 (Arduino, Italy) micro-controller board, and streams data at 250Hz. The entire unit has dimensions: $58.9mm$ x $38.7mm$ x $27mm$ and weighs $\approx 73g$ making the system compact, low-profile and wearable (see Fig.3). A single unit costs GBP 35-40/unit.

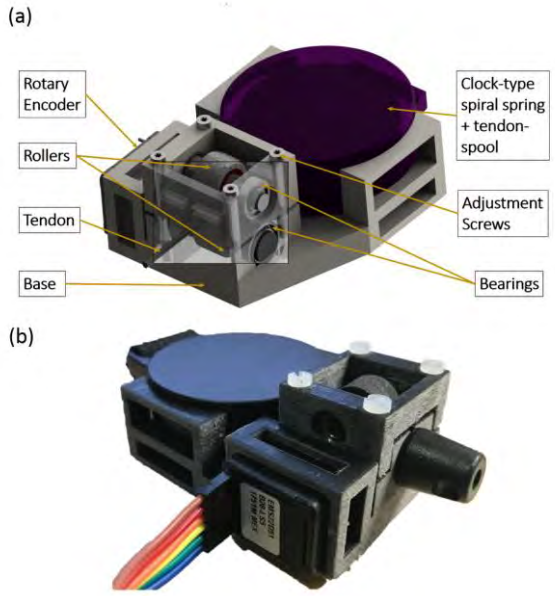

Fig. 1 The developed draw-wire sensor: a). A CAD rendering of the sensor illustrating the different components b). The current prototype of the sensor.

SENSOR CHARACTERIZATION

A characterization test rig (see Fig.2(a)) was set up to characterize the sensors. The sensor was firmly fixed to a drylin-T linear guide rail (IGUS, UK). This rail was motorized with a Faulhaber MDCDC 3006S DC motor (Faulhaber Gmbh & Co., Germany). The tendon from the sensor was fixed to a force-gauge that was mounted on the carriage of the guide rail. The experiment involved moving the carriage a distance of $200mm$ and back to its original position multiple times at a constant speed of 25 RPM. The results of three cycles of the experiment are shown in Fig.2(b).

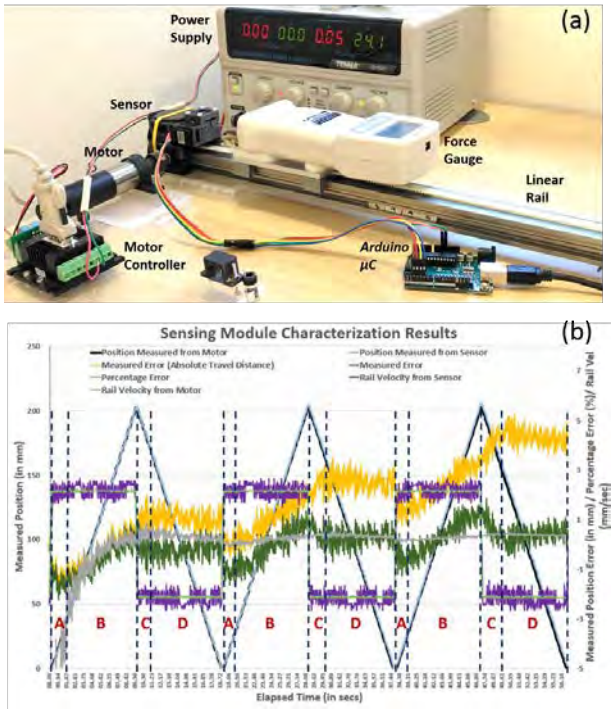

Fig. 2 Characterization of the sensor. a). Characterization Test Rig b). Sensor Characterization Results. The thick black and light blue lines correspond to the position measured by the motor and sensor (primary axis). The light green and purple data correspond to the rail velocity measured by the motor and sensor (secondary axis). The dark green, grey and light orange lines correspond to the measured error, percentage error and measured absolute error (secondary axis).

From the sensor and motor readings in Fig.2(b), it can be seen that the sensor follows the motor reasonably well. The velocity readings obtained from the motor and the sensor show that the velocity is also tracked accurately. Currently, no noise filtering has been incorporated. The derivation of position data to obtain velocity data results in a noisier signal. From the error data, the sensor's behaviour can be separated into 4 zones labelled *A, B, C,* and *D* (see Fig.2(b)). Behaviours in zones A & C is a result of slipping which occurs when the rollers experience an acceleration (static state to moving state) when the carriage changes directions. The slip (error) induced in zones A & C will be proportional to the magnitude of velocity (v). Errors in zones B & D results from slipping (between the tendons and the rollers) while the carriage is in motion. This could be because the friction between the roller and tendon is not generating enough torque to maintain rolling motion. It is clear from the measured error (dark green line) that the error generated in zone B is ≈1%, while the error generated in zone D is ≈ 0%, resulting in an average error of ≈ 0.5−0.6% (validated by the % error graph (grey line)). This bias between errors in the forward and reverse motions is the reason for the small but upward trend of the measured error (dark green line) and measured absolute error (light orange line). From the above discussion, the error multiplier (e) model for this sensor has been expressed in the following equation and is to be multiplied to the measured displacement value

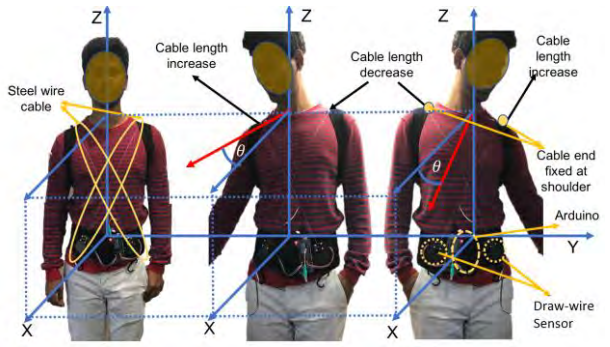

Fig. 3 Depiction of an application of the draw-wire sensors. In this application, two sensors are placed across the torso and are used to sense the user's intention to turn (by measuring change in torsal angle) before actually making the turn physically.

between two time instants to get the corrected displacement. This multiplier (see eq. below) will be used in future work for processing the sensor data in the kinematic sensing framework.

$$e = (noise) * \begin{cases} -\alpha v, & \text{if in zone } A \text{ or } C. \\ 0.01, & \text{if in zone } B \\ 0, & \text{if in zone } D. \end{cases}$$

CONCLUSION

We presented a custom-built low-cost digital alternative to an off-the-shelf analog string encoder sensor for use in a kinematic sensing in an exosuit [2]. The sensor has also been characterized and its error model has been presented as a multiplier that can be used programmatically to compensate for intrinsic bias in the sensor. We intend to improve the design by changing the internal spring to make it softer, and also intend to change the soft material on the rollers to improve contact friction. We also intend to perform another characterization test with a high-resolution displacement sensor rather than using the motor as the standard.

The sensor is currently being used in the lab for multiple kinematic sensing projects like measuring ankle dorsi-/plantarflexion angles for an exo-shoe, detecting the user's intention to turn before making a turn physically (see Fig. 3), and is primarily being investigated for future versions of the shoulder exosuit [2].

REFERENCES

[1] R. J. Varghese, X. Guo, D. Freer, J. Liu, and G.-Z. Yang, "A simulation-based feasibility study of a proprioception-inspired sensing framework for a multi-dof shoulder exosuit," in *2019 IEEE 16th International Conference on Wearable and Implantable Body Sensor Networks (BSN)*. IEEE, forthcoming.

[2] R. J. Varghese, and G.-Z. Yang, "A Proprioception-inspired Sensing Framework for a Bio-inspired Multi-DoF Shoulder Exosuit: A Preliminary Study," in *2019 IEEE/RSJ 32nd International Conference on Intelligent Robots and Systems (IROS)*. IEEE, submitted.

A Novel Hybrid Master-Slave Control Interface for Surgical Robot Remote Control

Junhong Chen[1*], Dan-Dan Zhang[1*], Wuzhou Hong[2], Jindong Liu[1], Guang-Zhong Yang[1]

[1]Hamlyn Centre for Robotic Surgery, [2] Shanghai Jiao Tong University,
d.zhang17@imperial.ac.uk (DOI10.31256/HSMR2019.36)

INTRODUCTION

Master-slave control has been implemented in most of the current surgical robotic platforms for Minimally Invasive Surgery (MIS). The master-slave control interface is used to ensure efficiency and safety during teleoperation [1]. Generally, the poses of the master manipulator end-effector are tracked online and used as input to control the poses of the slave robot's end-effector based on a predefined mapping relationship. Most of the master and slave robots are heterogeneous, due to the fact that slave robots are normally designed based on the specific requirement of the targeted surgery while master robots may need to take ergonomics into consideration. The joint-to-joint intuitive mapping cannot be utilized in this situation, where a mapping strategy should be designed for the master-slave control interface for remote control.

Most of the existing platforms utilize end-effector position mapping. However, because of the mismatch between the master and slave robot's workspace, a clutching mechanism is required to reposition the master manipulator when it reaches the workspace boundary during teleoperation, which influences the consistency of surgical procedures. A more versatile interface is worth developing to reduce the operators' workload and guarantee operation efficiency [2].

Position mapping mode is the most common mapping strategy while velocity mapping mode can be implemented to enhance the operation efficiency by eliminating the clutching number. The definition and comparisons can be viewed in [3]. In order to combine the advantages of both mapping mode, a novel hybrid interface is proposed in this paper. User studies were conducted utilizing a Phantom Omni [4] as the master manipulator and an in-house parallel robot as the slave robot to validate the effectiveness of the hybrid master-slave control interface. The user study results indicated that the proposed hybrid method is superior to using a single mapping mode.

MATERIALS AND METHODS

An anisometric interface is often used in existing surgical robot control, which employs displacement as control input [5]. The isometric interface utilizes the force or torque as the control input, which does not allow large movements from the operator. The anisometric interface can ensure high precision for control while the isometric interface can reduce the number of clutching. Therefore, the proposed hybrid control interface is realized by integrating the velocity mode and the position mode by switching between the anisometric interface for position control and the isometric interface for velocity control.

Fig. 1 shows the overview of the proposed hybrid control interface.

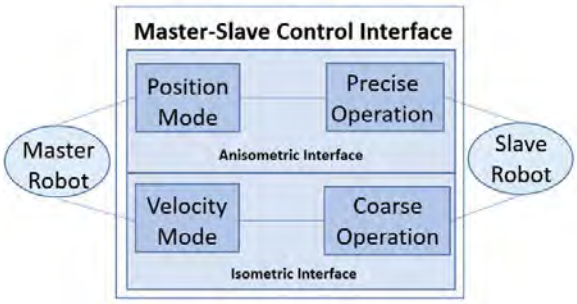

Fig. 1 Overview of the proposed master-slave control interface.

When operators are using a master side manipulator to finish given tasks, two modes of control methods can be chosen: 1) Position mapping mode, mapping the position change of master to the slave position with a given ratio, which represents an accurate way to control the end-effector for fine movements; 2) Velocity mapping mode, mapping the displacement and direction from operation center of master device to the magnitude and direction of velocity of slave side robot, which offers a non-clutching mapping for coarse movements, such as moving the microsurgical tool to the next target. By pressing the button on the Phantom Omni, the position mapping mode and the velocity mapping mode can be switched between each other. The initial velocity is set at zero at the mapping mode switching point, a virtual spring is used as feedback, so the user can feel how velocity is commanded. The velocity control vector is proportional to the master position increment generated by the operator.

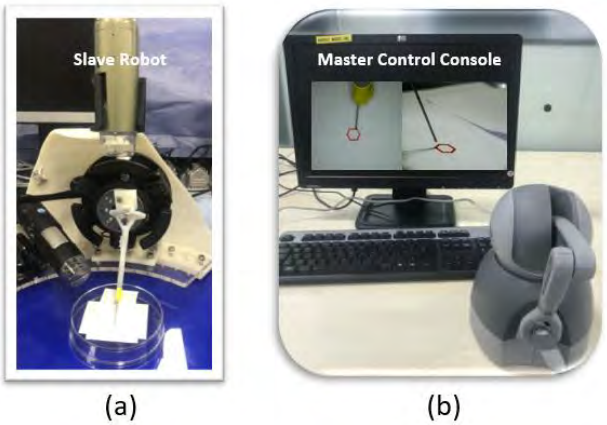

Fig. 2 Overview of the master-slave robotic system.

The hybrid control method is developed by leveraging the advantages of both mapping method. When the operator is moving towards a distant target, the motion can be

* These authors contributed equally to this paper.

regarded as coarse motion. Therefore, the velocity mapping mode can be conducted to accelerate the speed of maneuvoure. For local operation such as positioning the targeted point, the control interface can be switched towards a position mapping mode to ensure the accuracy, which is regarded as the precise motion.

In order to verify the effectiveness of the interface, two user studies were designed. The user studies were conducted using a Phantom Omni as the master controller, while a 6 Degrees-of-Freedom (DoFs) parallel robot with a micro-needle is utilized as the slave robot. The parallel robot is developed from a compact hexapod-like commercial platform, i.e. SmarPod (SmarAct, Germany). The overview of the experimental platform of the master-slave system is shown in Fig.2. Two digital cameras provide two views of the experimental scenes, which are used as visual feedback for teleoperation.

The user study includes a path following task and a positioning task. Fig.3 illustrates the scenario for user studies. The descriptions of the user studies are shown as follows.

1) Path Following Task
Subjects were required to follow a red hexagon path. The subjects were required to place their tooltip as close to the reference trajectory as possible. In this way, the position-changing maneuvers can be tested. The trajectory for tracking is viewed in Fig.3 (a).
2) Positioning Task
Pointing task requires the subjects to point the micro-needle tooltip to the targeted point precise within a short tolerant distance based on a pre-defined protocol. Six points were selected as shown in Fig.3 (b).

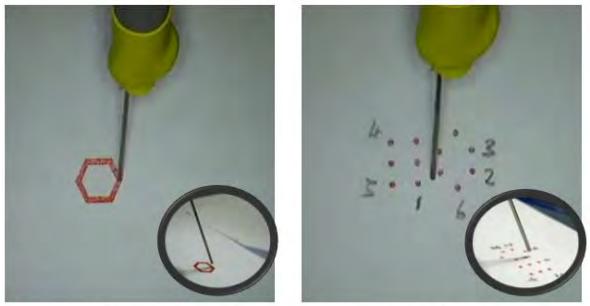

Fig.3 The scenario for user studies. (a) Path following task. (b) Positioning task.

Eight subjects were invited to join in the user study. The test began after all the subjects finished the practice section. Both kinematic data and video data were collected for results analysis. Each subject contributed three trials for two modes respectively, i.e. i) position mode; ii) hybrid mode. Since the velocity mode has been proved to be imprecision [3] based on the user study results, the comparison of this mode is not included in this paper.

RESULTS AND DISCUSSIONS

Four evaluation metrics are used to evaluate the performance of the subjects during the user studies, including the total time for fulfilling a single trial (**t**), the average speed of the slave robot for finishing each trial (**v**), the number of clutching (**C**), and the path length of the master controller end-effector ($\mathbf{P}_m$).

Table I. Results for User Studies

Path Following Task		
	Position Mode	**Hybrid Mode**
t(s)	42.2 ± 17.3	39.6 ± 15.4
v(cm/s)	0.043 ± 0.018	0.046 ± 0.018
C	17 ± 7	9 ± 6
$\mathbf{P}_m$**(m)**	2.004 ± 0.295	1.484 ± 0.500
Positioning Task		
	Position Mode	**Hybrid Mode**
t(s)	39.6 ± 14.2	39.6 ± 11.3
v(cm/s)	0.072 ± 0.027	0.073 ± 0.016
C	24 ± 10	12 ± 7
$\mathbf{P}_m$**(m)**	3.333 ± 0.341	1.984 ± 0.739

Based on the results (see Table I), we can clearly see that the hybrid mode has better performance in terms of all the evaluation metrics for the trajectory following task. As for the positioning task, except that the task completion time is similar for both modes, the hybrid mode has a higher average speed for task completion with significantly reduced number of clutching and shorter master robot path trajectory. Therefore, the teleoperation efficiency is enhanced by using the proposed method.

DISCUSSION AND CONCLUSIONS

In this paper, we present a hybrid control method by switching between isometric interface and anisometric interface. We conducted user studies on a parallel robot. The results of user studies verified that the proposed control interface has advantages in terms of task completion time and average control speed, thus improving the teleoperation efficiency.

ACKNOWLEDGEMENT

The authors would like to thank all the subjects who join in the user studies and would like to thank Dr Yang Hu for facility support.

REFERENCES

[1] Vitiello, Valentina, et al. "Emerging robotic platforms for minimally invasive surgery." IEEE reviews in biomedical engineering 6 (2013): 111-126.
[2] Pan B , Qu X , Ai Y , et al. Master–slave real-time control strategy in Cartesian space for a novel surgical robot for minimally invasive surgery[J]. Computer Assisted Surgery, 2016, 21(sup1):69-77.
[3] Jeongdo Ahn, Minho Hwang, Donghoon Baek, Hansoul Kim, Dong-Soo Kwon. Comparison of Master-Slave Mapping Strategies for Efficient Robotic Endoscopy. 2018 Hamlyn Symposium Proceeding.
[4] Silva, Alejandro Jarillo, et al. "Phantom omni haptic device: Kinematic and manipulability." 2009 Electronics, Robotics and Automotive Mechanics Conference (CERMA). IEEE, 2009.
[5] Kim, In, et al. "Research on a master manipulator using an isometric interface for translation in robotic surgery." International Journal of Advanced Robotic Systems 12.9 (2015): 128.

Design of Master Device Featured Redundant Joint for 4-DOFs Slave of Flexible Surgery Robot

Jeongdo Ahn[1], Dong-Soo Kwon[1]

[1]Department of Mechanical Engineering, Korea Advanced Institute of Science and Technology (KAIST)

wjdehwwkd@kaist.ac.kr (DOI10.31256/HSMR2019.37)

INTRODUCTION

In robot surgery, the surgeon manipulates the master device and performs the operation by remotely manipulating the surgical instruments or the slave equipped with the endoscope. The master device should be ergonomically designed for the convenience of the surgeons in consideration of intuitiveness and operability. In general, the degree of freedoms of the master device corresponds to the freedom of the slave. This is because the master device having redendant degrees of freedom has large control burden and is not intuitive. A slave master device with six degrees of freedom that can move freely in space has the same degree of freedom as a slave, and the surgeon is freely remotely controlled.

But what about masters of surgical robots with lower than six degrees of freedom? Our research team has studied 4-DOF flexible endoscopic surgery robot, K-FLEX. K-FLEX is inserted through a natural orifice like a mouth or anus using a flexible overtube, and access the lesion from a curved organ such as the pharynx, esophagus, or colon, which is difficult to access using rigid body robot. After approaching the lesion, a flexible surgical instrument of 4 degrees of freedom protrudes and performs intralumenal or translumenal surgery. In order to teleoperation this K-FLEX, a 4-DOF master device with the same degree of freedom as the slave has been developed. 4-degrees of freedom correspond to translation, yaw, pitch, and roll, respectively. It has the same structure as the slave's kinematic structure for intuitive control. However, a master device with a degree of freedom less than 6 degrees of freedom, compared to a master that can be freely manipulated in space with the hand of surgeon, feels as if the surgeon's hand is restrained by the master device. In particular, the lack of freedom to create the desired position and orientation in the spatial space and the poor operability result in a negative impact on surgical performance. To overcome this limitation, we proposed a master device with a redundant joint.

MATERIALS AND METHODS

At first, the ergonomics of the wrist were considered to determine the type of added redundant joint. When the surgeon grips the master device in a relaxed posture and assumes the neutral position, the translation degree of freedom, which is the prismatic joint of the four degrees of freedom of the wrist, is sufficient to define the position in the Z direction, It is not related to defining the position, which is the end-effector of. The yaw and pitch degrees of freedom, on the other hand, are used to define the position. The joint movements of the surgeon wrists used to move the yaw and pitch joints are wrist flexion-extension and wrist abduction-adduction, respectively. The joint range of the wrist flexion-extension (-27˚ ~ 47˚) is almost 1.5 times larger than that of the wrist abduction-adduction (-90˚ ~ 99˚) [1]. Therefore, yaw joint was added to improve the operability of yaw motion.

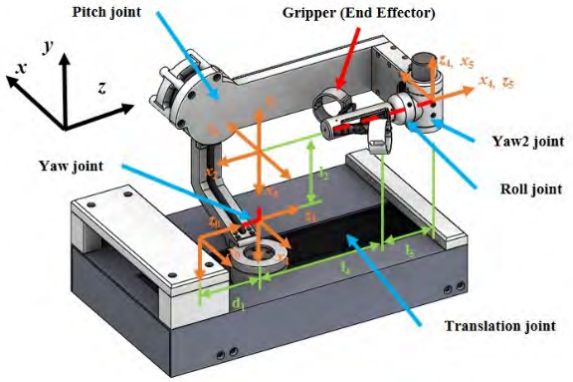

Fig. 1. Proposed master device featured redundant joint. This master device has 5 degrees of freedom including yaw2 joint. Reference frame for D-H parameters are presented.

To determine the configuration of the added yaw joint, we considered mapping between the slave and the master device. The K-FLEX instruments corresponding to the slave are designed for stitching. To perform the stitching motion, the instrument holds the needle and then maintains the rotation axis of the tip of the instrument. In other words, the roll joint should be located at the last gripper of the master device. Therefore, the added yaw joint is positioned before the roll joint. The 3D CAD model of the proposed master device is shown in Fig. 1.

RESULTS

We analyzed workspace and manipulability for dexterity analysis of master device featured redundant joint.

- Workspace analysis

Figure 2 shows the workspace analysis. The previously developed master device has a workspace volume of

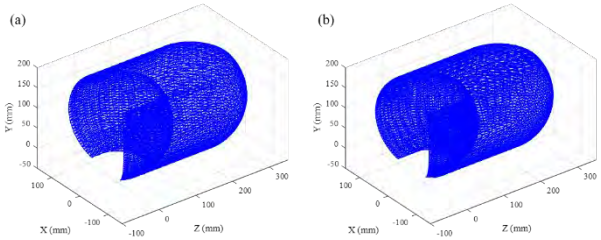

Fig. 2. Workspace analysis of previously developed 4-DOFs master device (a) and proposed master device featured redundant joint (b).

8.1578e6 mm^3 and proposed master device has a volume of 8.3481e6 mm^3. Because each master devices were designed considering average size of wrist and forearm, the volumes of each master devices have similar values.

- Manipulability analysis

However, the manipulability of each master devices were significantly different. The inverse condition number is a measure of the manipulability of the manipulator at a certain position. The value is between 0 and 1, and the closer to 1, the closer the ellipsoid is to the sphere. At this time, the joint limit of the master device should be considered for more accurate manipulability analysis and we apply the penalty function to Jacobian to obtain the inverse condition number [2]. In Fig. 3, the red-color means that the manipulability is small, and the yellow-color means that the manipulability is high. As can be seen in Fig. 3, the manipulability becomes larger toward the inside of the workspace that the master device can generate, and the smaller the manipulability becomes toward the boundary of the workspace by the limit of joint. To verify this more precisely, a global condition index (GCI) was calculated for each master device and compared. GCI is a global behavior of condition number. The larger the value, the greater the manipulability of the master device in the overall workspace. This means that the gripper, the master device's end-effector, can move dexterously within the workspace. As a result of manipulability analysis, it was found that the GCI of the proposed master device was 0.1472 and the GCI of previously developed master device was 0.111. The GCI

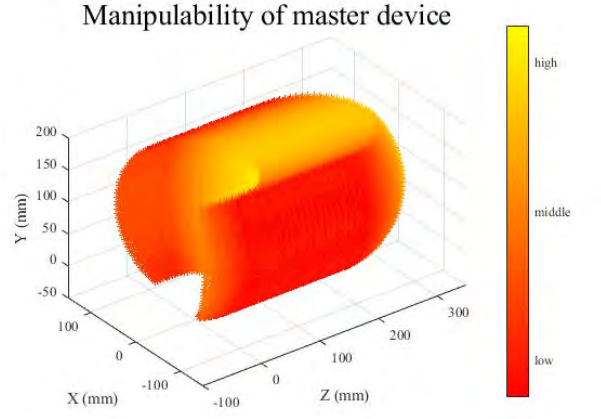

Fig. 3. Local manipulability distribution of master device at the workspace. Red-color represents low manipulability while yellow represents high manipulability.

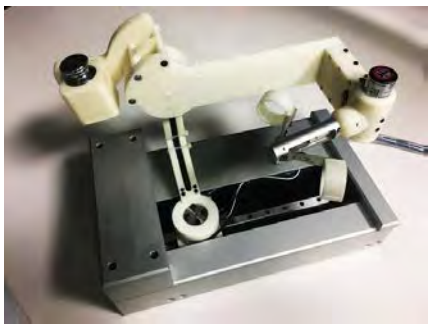

Fig. 4. Assembly of proposed master device featured redundant joint for 4-DOFs slave of flexible surgery robot.

of proposed master device was almost 8.6% larger than GCI of the previously developed master device. In other words, surgeon can more easily manipulate the proposed master device than the previously developed master device. A developed master device featured redundant joint for 4-DOFs flexible surgery robot is shown in Fig. 4.

CONCLUSION

In this paper, a master device for controlling a surgical robot with four degrees of freedom is proposed, in which a redundant joint is added to enhance operability. The proposed master device determines the yaw joint by considering the ergonomics of the wrist, and places the yaw joint in front of the roll joint in order to realize the stitching motion of the slave surgical instrument. By analyzing the workspace and manipulability of the designed master device, we verified that the operability is superior to that of the master device of 4 degrees of freedom. As a further works, the proposed master device for quantitative analysis and the existing slave robot is controlled by the master device and the peg transfer task and ESD marking simulation are performed to compare the surgical performance. We will also run NASA-TLX to verify operability and intuitiveness.

ACKNOWLEDGMENT

This work also was supported by the KAIST GCORE(Global Center for Open Research with Enterprise) grant funded by the Ministry of Science and ICT (Grant #: N11190045), and International Joint Technology Development Project funded by the Korean Ministry of Trade, Industry and Energy (Grant #: P0006718)

REFERENCES

[1] Pheasant, S. (2014). Bodyspace: anthropometry, ergonomics and the design of work: anthropometry, ergonomics and the design of work. CRC Press.

[2] Wisanuvej, P., Gras, G., Leibrandt, K., Giataganas, P., Seneci, C. A., Liu, J., & Yang, G. Z. (2017, September). Master manipulator designed for highly articulated robotic instruments in single access surgery. In 2017 IEEE/RSJ International Conference on Intelligent Robots and Systems (IROS) (pp. 209-214). IEEE.

Robot-assisted spine surgery guided by conductivity sensing: first preclinical experiments demonstrate X-ray free breach detection

Jimmy Da Silva[1,2], Thibault Chandanson[1], Guillaume Morel [2]

[1]SpineGuard,Vincennes

[2]Sorbonne Université, CNRS, INSERM, ISIR - Paris,

jimmy.dasilva@spineguard.com (DOI10.31256/HSMR2019.38)

INTRODUCTION

Inserting screws in vertebral pedicles is a major issue in spinal fusion surgery. Due to their proximity to critical anatomical regions (spinal cord, aorta), misplaced screws can induce complications [1]. Free-handed positioning results in high inaccuracy. To try to improve precision of this surgery, new medical robots and tools emerged from the research community and arrived in the market in the last few years [2], such as SpineAssist [3] from Mazor, ROSA [4] from Zimmer Biomet, iSYS 1 [5] from Interventional Systems.

Available systems rely on fluoroscopy or CT scans taken during the procedure for position checking. Notably, there is no real-time control of the gesture.

The current paper discloses a concept involving a robotic arm that holds a drill equipped with an electrical conductivity sensor. A control law couples the sensor to the robot control in such a way that vertebral breach can be avoided during vertebrae drilling. First *in vivo* experiments are shown.

MATERIALS AND METHODS

The experimental setup is a combination of the DSG technology developed by SpineGuard, a 7 DOFs robot arm WAM sold by Barrett Technology, and a motor. See Fig. 1.

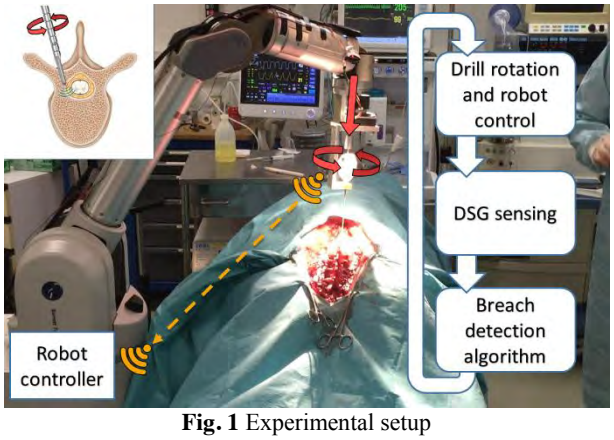

Fig. 1 Experimental setup

DSG technology [6,7,8] is a bipolar, local electrical conductivity sensor that pulses current flow at the tip of its probe. The current clinical setup is as follows: when manipulating a pedicle preparation tool equipped with DSG, a surgeon can distinguish between tissues and be alerted prior to an imminent cortical breach: this is achieved by changes in the pitch and cadence of an audio signal and a flashing LED light.

In this work, the DSG signal $s(t)$ is used to detect a breach as follows (see Fig. 2). It is assumed that the tool has initially been inserted in cancellous bone. The system then waits for the detection of an event: cortical bone penetration is detected when $s(t)$ gets below a threshold s_1. A breach alert is then produced when $s(t) > s_2$ with $s_2 = s_{min} + \delta s$, where $s_{min} = \min_{0 \le \tau \le t} s(\tau)$ and δs is a given differential threshold.

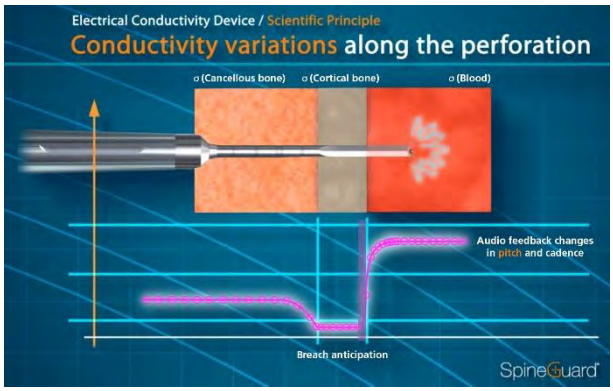

Fig. 2 DSG technology principle.

As for the robot control (see Fig. 3), at the beginning of the procedure, a transparent mode is provided to position the drill tip by comanipulation. A semi-transparent mode is then proposed allowing for orienting the drill around its tip. A simple click on a GUI starts the drilling algorithm at a constant speed v_{des}.

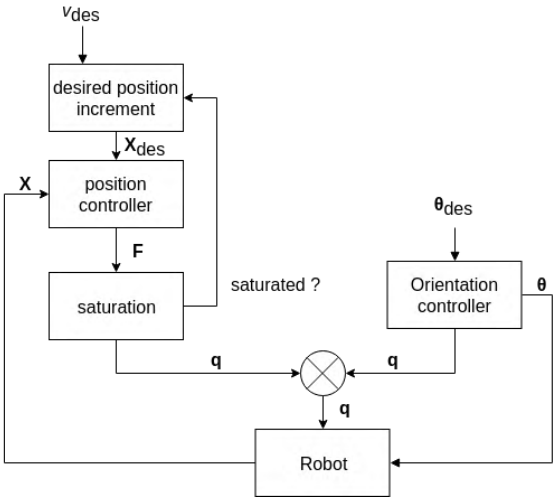

Fig. 3 Control scheme.

When the drilling starts, an operational space orientation and position controller starts running. The desired orientation θ_{des} is servoed to its initial value θ_{ini}. The desired position X_{des} is computed by:

$$X_{des}(t + dt) = X_{des}(t) + v_{des} dt\, z_{ini}, \quad (1)$$

where dt is the control period, z_{ini} is the drill axis direction and v_{des} is an adjustable penetration speed. As a security, when the resulting control force $\|F_p\|$ reaches a given value $F_{p_{max}}$, then the position increment is nulled.

RESULTS

In vivo experiments have been performed on pigs, under the control of veterinary surgeons and after approbation of an ethics comity.

Parameters of the experiments were as follows:

- Drilling motor rotation = 300 rpm,
- $s_1 = 150mV$, $\delta s = 300mV$
- $dt = 2ms$
- $F_{p_{max}} = 10N$

The surgeon was asked to manipulate the robot arm in a transparent mode so that the drill bit could perforate the spinous process of the vertebra, then click on the GUI to start the drilling.

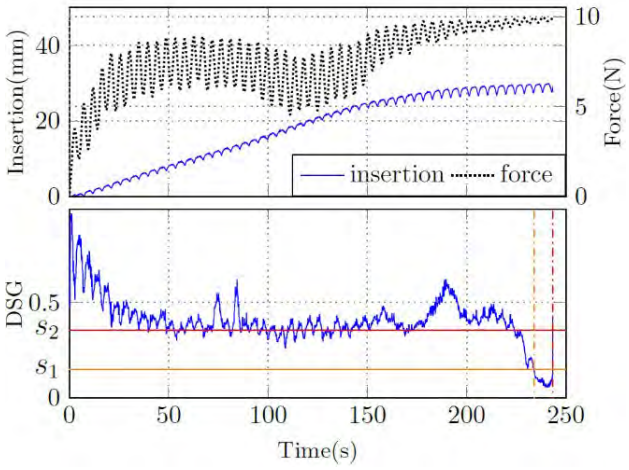

Fig. 4 Robot and DSG signals during an experiment

The curve of the DSG signal (Fig. 4) shows the expected signature: high signal at the entrance, then stabilization in the spongious phase, decrease in the cortical bone around s_1, followed by a fast rise stopped to s_2.

The force and position curves exhibit oscillations. These correspond to the breathing of the animal. Notice that the position controller involves a simple PD compensator without integral action, leading to compliance observable through the oscillations of the insertion (or penetration depth) signal.

Further, due to the force limitation, the velocity decreases when the resistance is getting higher, offering an extra layer of safety.

DISCUSSION

The current setup allows to stop the drilling right before breaching out.

An innovative system for radiation-free breach anticipation during spine surgery has been presented. It uses a measurement of the local conductivity to determine if a breach out of the bone is imminent.

The *in vivo* experiments were successfully performed but further improvements can be considered to increase robustness and accuracy.

For instance, the values of variables s_1 and δs have been manually set. Further experiments have shown that these values need to be adjusted depending on the patient's anatomy and bone state. A more sophisticated signal-processing algorithm needs to be defined in order to eliminate the tuning of these parameters and allow the recognition of a conductivity change pattern.

Further, the DSG technology could be used in many bone surgeries as a safety sensor to reduce the use of x-rays.

REFERENCES

[1] J. E. Lonstein, F. Denis, J. H. Perra, M. R. Pinto, M. D. Smith, and R. B. Winter, "Complications associated with pedicle screws", *JBJS*, vol. 81, no. 11, pp. 1519-1528, 1999.

[2] F. Shweikeh, J. P. Amadio, M. Arnell, Z. R. Barnard, T. T. Kim, J. P. Johnson, and D. Drazin, "Robotics and the spine: a review of current and ongoing applications", *Neurosurgical focus*, vol. 36, no. 3, p. E10, 2014.

[3] A. Bertelsen, J. Melo, E. S_anchez, and D. Borro, "A review of surgical robots for spinal interventions", *The International Journal of Medical Robotics and Computer Assisted Surgery*, vol. 9, no. 4, pp. 407-422, 2013.

[4] M. Lefranc and J. Peltier, "Evaluation of the rosaTM spine robot for minimally invasive surgical procedures", *Expert review of medical devices*, vol. 13, no. 10, pp. 899-906, 2016.

[5] J. Kettenbach, L. Kara, G. Toporek, M. Fuerst, and G. Kronreif, "A robotic needle-positioning and guidance system for ct-guided puncture: Ex vivo results", *Minimally invasive therapy & allied technologies*, vol. 3, no. 5, pp. 271-278, 2014.

[6] C. Bolger, M. O. Kelleher, L. McEvoy, M. Brayda-Bruno, A. Kaelin, J.-Y. Lazennec, J.-C. Le Huec, C. Logroscino, P. Mata, P. Moreta, *et al.*, "Electrical conductivity measurement: a new technique to detect iatrogenic initial pedicle perforation", *European Spine Journal*, vol. 16, no. 11, pp. 1919-1924, 2007.

[7] O. Suess and M. Schomacher, "Control of Pedicle Screw Placement with an Electrical Conductivity Measurement Device: Initial Evaluation in the Thoracic and Lumbar Spine", *Advances in Medicine*, 2016.

[8] C. Bolger and M. Bourlion, "Pedicle navigation in spondylolisthesis" in *Spondylolysis, Spondylolisthesis, and Degenerative Spondylolisthesis*, ch. 28, pp. 227-236, Lippincott Williams & Willkins, 2006.

Intraoperative Robotics for Patient Specific Instrument Manufacture: A Cadaver Trial

A. Darwood[1], S. Hurst[1], G. Villatte[2], R. Fenton[3], F. Tatti[1], H. El-Daou[1], P. Reily[1], R. Emery[1], F. Rodriguez y Baena[1]

[1]Imperial College, London
[2]Centre Hospitalier Universitaire de Clermont-Ferrand, France
[3]Desoutter Medical Ltd.
alastairdarwood@hotmail.com (DOI10.31256/HSMR2019.39)

INTRODUCTION

The accurate placement of orthopaedic implants according to a biomechanically derived preoperative plan is an important consideration in the long-term success of these interventions[1]. Guidance technologies are widely described and comprise active or passive intra-operative robotics platforms, and three dimensional (3D) printed patient specific jigs[2]. Despite improvements in placement accuracy, high cost, complex theatre integration, intraoperative inefficiency and functional limitations have prevented the widespread adoption of these technologies[3].

The authors have designed and constructed a novel intraoperative robotics platform capable of the intraoperative manufacture of bespoke patient specific guides[4,5]. The device consists of a tableside robot (Fig. 1, A) with sterile drapes (Fig. 1, B) and some low cost, sterile disposable components. The robot is placed next to the operating table and is configured for intraoperative use. It comprises a 3D optical scanner (Fig. 1, C), a three-axis sterile computer numerical control (CNC) drill (Fig. 1, D) and a two-axis receptacle into which the disposable consumables may be inserted (Fig. 2, A). The sterile consumable comprises a region of rapidly setting mouldable material (Fig. 1, E) and a clip (Fig. 1, F) allowing it to be reversibly attached to the tableside robot.

In use, patient computed tomography (CT) imaging is obtained at any point prior to surgery and a surgical plan is created in associated software (Fig. 2, B). This plan describes the axis and positioning of one or more guidewires which may, in turn, locate the prosthesis into position. Intraoperatively, osseous anatomy is exposed, and the sterile disposable is used to create a mould of the joint surface (Fig. 1, G). Once set, the mould is inserted into the robot and an optical scan of the surface is taken, followed by automatic surface registration, bringing the optical scan into the same coordinate frame of reference as the CT data and plan (Fig. 2, C). The CNC drill is then oriented such that the drill axis and position matches the planned pose with respect to the moulded surface. A guide hole is then automatically drilled into the mould blank (Fig. 2, D), which is then removed from the robot and placed back into the patient with the moulded surface ensuring precise replacement. A wire is subsequently driven through the guide hole into the osseous anatomy in accordance with the preoperative plan (Fig. 2, E). The guide blank may be slid off the wire and discarded, allowing the procedure to continue in the normal manner. In this paper, we asses this novel robot's performance *ex vivo*, in terms of its kinematics and the ability to guide planned wires into a glenoid cavity during a simulated total shoulder arthroplasty procedure.

MATERIALS AND METHODS

A prototype device was constructed along with planning software and sterile consumables (Fig. 2, A). A kinematic calibration and assessment of the device was carried out to identify the mechanical accuracy of the system. 12 cadaveric shoulder specimen (sex, age and side randomized) were obtained after application for access to human tissue samples was approved by the Imperial College tissue bank, then a preoperative CT scan performed on each specimen. A senior orthopaedic surgeon planned the ideal wire placement in each specimen and exposed the glenoid cavity via a conventional glenohumeral approach. The device and sterile disposables were used to guide the placement of guide wires into the glenoid cavity. Following wire insertion, a postoperative CT scan was obtained for each specimen. The pre- and postoperative scans were then segmented and coregistered to allow the planned vs achieved wire position to be computed. At the time of abstract submission, results for one specimen were available, with the analysis of the complete 12-samples study due for completion before the conference.

RESULTS

The overall kinematic accuracy of the prototype was 0.50 ± 0.26 mm in terms of translational positioning and $0.59 \pm 0.30°$ angular accuracy. The initial cadaveric results show overall end to end placement accuracy of 0.5mm with respect to planned vs achieved glenoid point of entry and 3.0° with respect to planned vs achieved wire angle. Data capture is currently ongoing in the remainder of the specimens.

DISCUSSION

This novel intraoperative robot demonstrates the ability to rapidly produce functional guides in accordance with a pre-operative plan. Guide wires were accurately and rapidly inserted, whilst the consumables and the compact, intraoperative platform may result in possible cost reductions and efficiency improvements. The novel registration method making use of patient anatomy found at the time of surgery may provide additional accuracy improvements and added functionality in cases that are traditionally challenging to conventional 3D printed orthopaedic guides. Additionally, registration of the moulded surface with the CT data could leverage optimizations in the algorithm's design, such as filtering, weighing and local minima suppression, to ensure a reliable and repeatable replacement fit into the surgical site. Glenoid component malpositioning has been shown to be a major contributing factor to early failure and poor prosthesis function, thus guidance technologies may play an important role in improving patient outcomes[6]. This cadaveric trial demonstrates that the intraoperative manufacture of patient-specific guides is viable and can yield results which are comparable and could even surpass traditional PSIs[7]. Further work is planned on other joint areas such as the hip and knee with a first-in-man trial scheduled for 2020.

REFERENCES:

1. Hopkins, A. R., Hansen, U. N., Amis, A. A. & Emery, R. The effects of glenoid component alignment variations on cement mantle stresses in total shoulder arthroplasty. *J. Shoulder Elbow Surg.* **13,** 668–75 (2004).
2. Malik, H. H. *et al.* Three-dimensional printing in surgery: a review of current surgical applications. *J. Surg. Res.* **199,** 512–522 (2015).
3. Beringer, D. C., Patel, J. J. & Bozic, K. J. An overview of economic issues in computer-assisted total joint arthroplasty. *Clin. Orthop. Relat. Res.* **463,** 26–30 (2007).
4. Darwood, A. Method and Apparatus for Use in the Production of a Surgical Guide. (2013). at <https://worldwide.espacenet.com/publicationDetails/biblio?II=0&ND=3&adjacent=true&locale=en_EP&FT=D&date=20161124&CC=US&NR=2016342766A1&KC=A1>
5. Darwood, A. *et al.* Intraoperative Manufacturing of Patient-Specific Instrumentation for Shoulder Arthroplasty: A Novel Mechatronic Approach. *J. Med. Robot. Res.* **01,** 1650005 (2016).
6. Gregory, T. M. *et al.* Accuracy of Glenoid Component Placement in Total Shoulder Arthroplasty and Its Effect on Clinical and Radiological Outcome in a Retrospective, Longitudinal, Monocentric Open Study. *PLoS One* **8,** e75791 (2013).
7. Villatte, G. *et al.* Use of Patient-Specific Instrumentation (PSI) for glenoid component positioning in shoulder arthroplasty. A systematic review and meta-analysis. *PLoS One* **13,** e0201759 (2018).

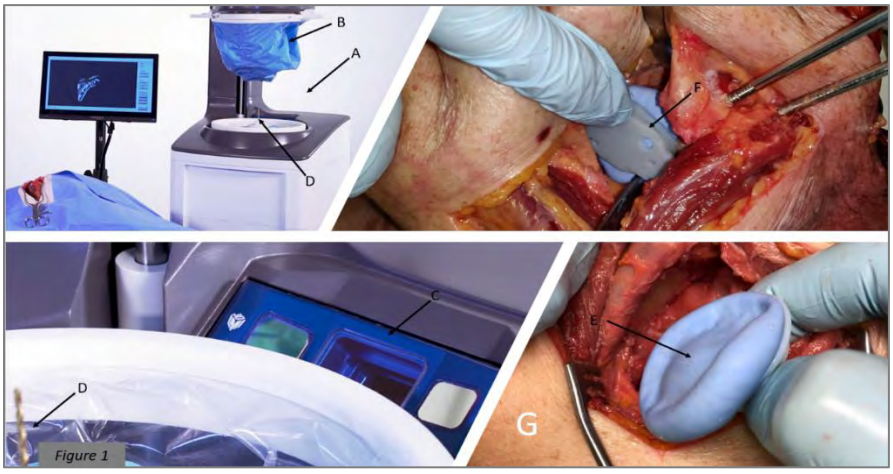

Fig. 1 *- A to G: An overview of the robot design and the surgical site moulding procedure*

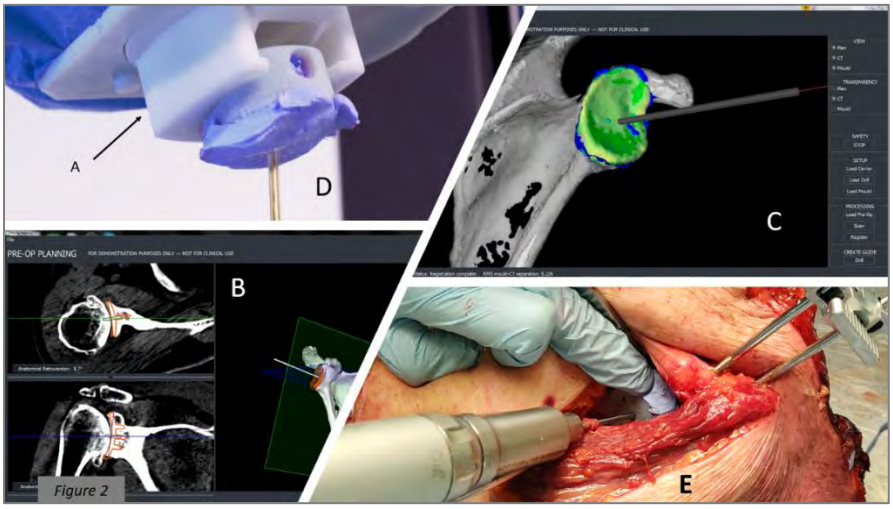

Fig. 2 *- A to E: An overview of guide production, software planning and intraoperative guide usage*

Simulation-based Adaptive Training for Robot-Assisted Surgery: a Feasibility Study on Medical Residents

A. Mariani[1,2], E. Pellegrini[1], A. Menciassi[2], and E. De Momi[1]

[1] *Department of Electronics, Information and Bioengineering, Politecnico di Milano, Italy*

[2] *The BioRobotics Institute, Sant'Anna School of Advanced Studies, Pisa, Italy*

a.mariani@santannapisa.it (DOI10.31256/HSMR2019.40)

INTRODUCTION

Virtual Reality (VR) simulators represent a remarkable educational opportunity in order to acquire and refine surgical practical skills [1]. First of all, a direct ethical advantage of simulation-based training in surgery is preventing patients from being subjected to any risk or complication during the learning phase. Secondly, simulators are characterized by a higher availability with respect to time-consuming and expensive practice in the operating room; additionally, they allow to constantly monitor the trainee's learning by quantifying metrics associated to his/her performances.

In order to maximize the learning benefit, there is a clear need for structured training curricula. Simulators have shifted the paradigm of a mentor-guided learning towards a self-directed training, with the consequent reduction of program costs [2]. Nevertheless, the success of this paradigm relies on the ability of the trainee to efficiently schedule the training session. Our study proposes an *adaptive training curriculum* that automatically schedules the training session on the basis of an objective assessment of the trainee's performances. In such a way, the trainee no longer has to choose his/her training exercises while using the simulator, but an *ad hoc* training session is online scheduled to best compensate for gaps in the surgical skills. The feasibility of such an approach is tested by analyzing medical residents' performances after adaptive or self-managed training. This work is an extension of a preliminary pilot study of ours [3], where only non-medical participants were enrolled in the experimental sessions.

MATERIALS AND METHODS

Hardware and Software

In order to carry out the experimental session, we employed the master console of a da Vinci Research Kit (dVRK, by Intuitive Surgical Inc., Sunnyvale, US). This console includes a foot-pedal tray, a stereo viewer and two master manipulators.

The VR exercises were designed using our Assisted Teleoperation with Augmented Reality (ATAR) framework [4].

Training Tasks and Performance Assessment

As initially stated, simulators are involved in technical skills learning we focused on robot-assisted surgery and we developed a curriculum composed by elementary and complex tasks. The former aims at training a single fundamental skill of robotic surgery, while the latter involves multiple skills at once. We designed two complex bimanual visuo-motor tasks that include the same elementary skills (that we derived from the analysis of a skill deconstruction list generated by robotic operations observation and interviews with experts [5]). For each elementary skill, we designed an associated elementary task to learn that specific skill. Fig. 1 shows the abovementioned VR tasks and skills.

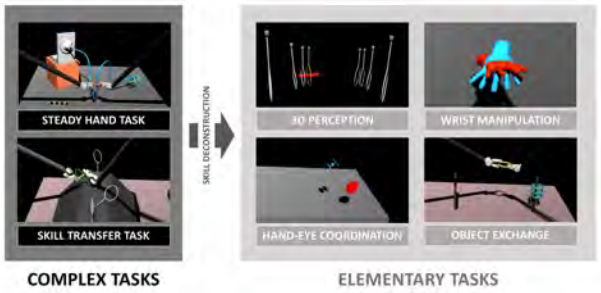

Figure 1 Vitual reality task pool: on the left, two tasks classified as complex since involving multiple fundamental skills of robotic surgery (a *steady hand task*, often included in surgical curricula, and a *skill transfer task*, resembling a rigid suturing); on the left, the associated elementary skills (*depth perception, wrist manipulation, hand-eye coordination and instrument to instrument exchange*) and respective tasks.

In order to assess the user's performances, we considered the following metrics: the *translation error* (i.e. linear distance between the actual and the ideal position of the virtual manipulator), the *orientation error* (i.e. angular difference between the actual and ideal pose of the manipulator), the *depth error* (i.e. the distance between tool and target along the perspective direction), the *exchange error* (i.e. the number of drops while performing an object instrument to instrument exchange) and the *total time* to accomplish the task. These were averaged across each task repetition and normalized in the 0-1 range by using the best and worst values of each metric from preliminary acquisitions. The final performance in each task was computed as the weighted sum of these metrics.

Experimental Protocol

12 medical residents took part to the user study. Their specifics are reported in Table I. All the subjects had none to little experience with robotic teleoperation. They were randomly divided into two groups: a *control group* (N=6), performing the self-managed training, and an *experimental group* (N=6), undergoing the adaptive training. All the users carried out an initial baseline assessment on one of the two complex tasks and a final evaluation test on both the complex tasks. In fact, the

Table I Statistics about medical residents

	CONTROL	EXPERIMENTAL
SEX	1 F, 5 M	3 F, 3 M
AGE	28.5 ± 3.9	28.2 ± 3.3
HAND	5 right-handed	6 right-handed
open*	92.7 ± 58	120.8 ± 67
laparo*	73.3 ± 37	90.4 ± 43
robot*	0	3.3 ±3

* Hours of previous experience in surgery (open, laparoscopic and robot-assisted surgery). The data refer both to first-hand experience and to assistance during the procedure.

second complex task is not part of the training curriculum, but it appears just in the final evaluation stage in order to test the transferability of the acquired skills on a task which is totally new to the trainee. The total training time (45 minutes) was selected as a constraint to have comparable protocols between the two groups. The users belonging to the *control group* directly chose their exercises and they were just provided with their percentage performance after each task repetition; the *experimental group* was provided with the task to perform according to the adaptive logic. This automatically modulated the training curriculum of the experimental group as a function of their performances in order to minimize the gaps in each elementary skill. Further details can be found in [3].

Additionally, one expert surgeon (number of robotic surgical cases > 500) took part to the experiment. His performances were used to test the *construct validity* (i.e. the ability to differentiate between groups with different levels of competence) of the designed tasks.

Statistical Analysis

Due to the small sample size, non-parametric tests (Wilcoxon rank sum test, statistically significance at $p < 0.05$) were used to compare the performances of the users before and after training.

RESULTS

The main outcomes of the study are depicted in Fig. 2 shows a comparison of the initial (before training) and final (after training) performances of the two groups. All the groups were characterized by a temporal increase in the median performances and a reduction of their variability. The initial baseline assessment proved that all the subjects belonged to the same population (no statistical significant difference). On the other hand, the expert surgeon startlingly achieved performances that were significantly higher with respect to all the other users. This qualitatively highlights the capability of the designed VR task to discriminate among different expertise levels (that means its construct validity). Moving to the final test, participants were evaluated both on the steady hand task and the skill transfer task (totally new to them): statistically significant difference between the control and experimental group was found in both the tasks (p=0.002, steady hand task; p=0.015, skill transfer task): the subjects who underwent the adaptive training achieved higher final performances compared to the ones who self-managed their training.

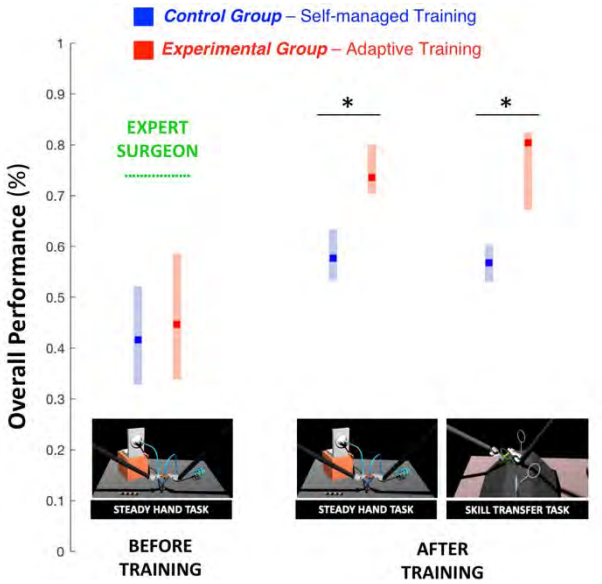

Figure 2 Overall performance of control (blue) and experimental (red) groups in the complex tasks before and after training. The marked square stands for the median across the population, while the vertical bar represents the 25th and 75th percentiles. Finally, the dotted green line shows the expert surgeon performance (without specific training on the task). Stars signal statistically significant difference.

Additionally, since they performed better in a different task involving the same skills, they probably better learned the skills instead of the task itself.

DISCUSSION

This study tested the feasibility and efficacy of a skill-oriented and adaptive curriculum for training in robotic surgery using virtual reality simulators. This novel approach was evaluated on 12 medical residents and compared to a traditional self-managed training. The proposed adaptive curriculum led to promising results, showing how a smart schedule can optimize the learning process. This automated and objective method could suggest the introduction of an artificial intelligence mentor as an integrated component of a simulation-based platform for training in robotic surgery. This way, each training session can be guided by a constant and objective performance evaluation, followed by an *ad hoc* scheduling of the intra-session curriculum. Further analysis will be carried out on a wider population and considering longer training sessions.

REFERENCES

[1] A. Aydin, *et al.*, "The role of simulation in urological training - A quantitative study of practice and opinions", Surgeon, 14: 301–7, 2016.

[2] J. MacDonald, *et al.*, "Self-assessment in simulation-based surgical skills training", *The American Journal of* Surgery, Volume 185, Issue 4, 319 – 322, 2003.

[3] A. Mariani, *et al.*, "Design and Evaluation of a Performance-based Adaptive Curriculum for Robotic Surgical Training: a Pilot Study", *EMBC 2018*: 2162-2165, 2018.

[4] N. Enayati, *et al.*, "A Framework for Assisted Tele-operation with Augmented Reality," *CRAS* 2017.

[5] G. Dulan, *et al.*, "Developing a comprehensive, proficiency based training program for robotic surgery", *Surgery*;152:477–88, 2012.

Robot-Assisted Surgical Training Over Several Days in a Virtual Surgical Environment with Divergent and Convergent Force Fields

Y. A. Oquendo[1], Z. Chua[1], M. M. Coad[1], I. Nisky[2], A. Jarc[3], S. Wren[1], T.S. Lendvay[4], A. M. Okamura[1]

[1] Stanford University, [2] Ben-Gurion University of the Negev, [3] Intuitive Surgical, [4] University of Washington
oquendoy@stanford.edu (DOI10.31256/HSMR2019.41)

INTRODUCTION

Surgical procedures require a high level of technical skill to ensure efficiency and patient safety. Due to the direct effect of surgeon skill on patient outcomes, the development of cost-effective and realistic training methods is imperative to accelerate skill acquisition [1]. Teleoperated robotic devices allow for intuitive ergonomic control, but the learning curve for these systems remains steep. Recent studies in motor learning have shown that visual or physical exaggeration of errors helps trainees to learn to perform tasks faster and more accurately [2]. In this study, we extended the work from two previous studies [3,4] to investigate the performance of subjects in different force field training conditions, including convergent (assistive), divergent (resistive), and no force field (null). We hypothesized that the group who trained in the divergent force field would show superior performance to those in the null and convergent fields.

MATERIALS AND METHODS

Experimental setup and task: We used the da Vinci Research Kit (dVRK) [5] with the Assisted Teleoperation with Augmented Reality (ATAR) framework [4] to create a virtual reality environment for a ring-on-wire manipulation task. The robotic tools were simulated as kinematic objects resembling da Vinci endoscopic mega needle drivers. Subjects in the convergent (C) field received an assistive force that pushed the participant's hand towards an ideal path, while those in the divergent (D) field received a resistive force that pushed the participant's hand away from the ideal path. In both groups, the force applied had a magnitude proportional to their distance away from the path. Force feedback was only applied when the gripper was closed on the ring that was being manipulated. Given the current pose ($P_C = [T_C, Q_C]$) and the desired pose ($P_D = [T_D, Q_D]$), where T_X is a 3-DOF position vector and Q_X is a 4-DOF unit quaternion, the force ($\mathbf{F}$) and torque ($\boldsymbol{\tau}$) produced on the tip of each instrument were:

$$\mathbf{F} = -\mathbf{k}_T*(\mathbf{T}_C - \mathbf{T}_D) - \mathbf{d}_T*\dot{\mathbf{T}}_C$$

$$\boldsymbol{\tau} = -\mathbf{k}_R*\mathrm{rpy}(\mathbf{Q}_D*\mathbf{Q}_C^{-1}) - \mathbf{d}_R*\boldsymbol{\omega}_C,$$

where $\dot{\mathbf{T}}_C$ and $\boldsymbol{\omega}_C$ are the current translational and angular rate, respectively, k_T and k_R are the translational and rotational proportional coefficients, d_T and d_R are the translational and rotational damping coefficients, and rpy() represents a transformation from quaternion to roll-pitch-yaw. k_T, k_R were positive in the convergent field and negative in the divergent field. d_T and d_R were positive in both force fields.

The visuomotor task adapted from [4] was an adaptation of the '*steady-hand'* game often included in surgical training curricula [6]. The user moves a ring along a curved wire which spans along all three Cartesian dimensions and requires up to 90° wrist rotations from each hand for completion. Users received visual feedback on their position such that the ring's color shifted gradually from red (less accurate) to yellow (more accurate) as the ring approached the wire.

Procedure: 40 surgical novices gave informed consent for the IRB-approved study, and were pseudo-randomized to one of three groups: convergent force field (n=13), divergent force field (n=15), or null field (n=12). Two divergent field subjects dropped out of the study due to physical limitations preventing task completion, and their data was not included in the analysis. Subjects were required to participate over five consecutive days, and were given a $75 Amazon gift card as compensation. On the day 1, subjects were consented, shown a video demo of the steady-hand task, and directed on how to use the dVRK system. They were instructed to perform the task as accurately and quickly as possible, with more emphasis being placed on accuracy. Subjects then completed 5 baseline trials in the null field followed by 15 trials in their assigned force field. On days 2, 3, and 4, subjects completed 20 trials per day in their assigned force field. On day 5, subjects completed 20 trials in the null field to evaluate changes in performance from baseline. A total of 20 trials per day was chosen to minimize the effect of fatigue from confounding results, and a total of five days was chosen to correspond with a work week for ease of scheduling.

Data Analysis: Data was recorded at 30 Hz. Four performance metrics were calculated for each trial: trial time (Time [s]), translational path error (TPE [mm^2]) and rotational path error (RPE [Rad·mm]) were calculated as in [3], and combined error-time (CET [Rad·mm·s]) was calculated as follows:

$$\mathrm{CET} = \mathrm{Time} \cdot (\mathrm{RPE} + \mathrm{cf}\cdot\mathrm{TPE})$$

Where cf is a constant factor of 17 rad/mm derived from the ratio of the average rotational path error and the average translational path error across all subjects and all trials. Improvement was calculated for each metric as the difference between the mean on the final day and the mean at baseline. Metrics were non-normally distributed

between groups, thus we used non-parametric statistical tests to evaluate differences in performance. Kruskal-Wallis (KW) tests were performed with the different metrics as dependent variables and the training group as independent factor. Post-hoc testing was done using the Dunn Test (DT) to determine significant differences between pairs of groups. Pairwise Wilcoxon signed-rank tests (WSR) were used to determine significance of within-subjects improvement.

RESULTS

Figure 1 presents the 25th, 50th, and 75th percentiles of performance of each group at baseline and on the final day of evaluation. At baseline, the groups significantly differed in time to completion (KW; χ^2=7.038, df=2, p=0.030). The null group had significantly lower time to completion (DT; Z=2.51, p=0.036). There was no significant difference in TPE, RPE, or CET at baseline.

The groups significantly differed in CET on the final day (KW; χ^2=6.8501, df=2, p=0.032). Further analysis revealed a significant difference between convergent and null groups (DT; Z=2.57, p=0.030). Divergent field subjects had the lowest final day median combined error-time, though this was not statistically significant. There were no significant differences between groups in any other metric.

Combined performance variability (CPV), measured as the standard deviation of CET across all trials, significantly decreased from baseline in all groups (WSR; C: p=0.017, D: p<0.01, N: p<0.01). The groups differed significantly in their CPV on the final day (KW; χ^2=7.8415, df=2, p-value=0.020), and a Dunn test for that day showed that convergent subjects had significantly higher variability than null subjects (DT; Z=2.77,p=0.016).

Figure 2 shows that all groups significantly improved their performance from baseline. Compared to the null and convergent groups, divergent subjects experienced the most improvement in time (KW; χ^2=3.18, df=2, p=0.20), TPE (KW; χ^2=1.80, df=2, p=0.41), RPE (KW; χ^2=2.37, df=2, p=0.30), and CET (KW; χ^2=3.37, df=2, p=0.18).

DISCUSSION

Divergent field subjects improved the most from baseline in all metrics. The difference between groups was not statistically significant, possibly due to outliers in the convergent field and null field groups. Even though the divergent group was significantly slower to complete the task than the null group at baseline, there was no significant difference on final evaluation.

The most significant difference between groups on the final day was in CET, which takes into account the speed-accuracy tradeoff. In surgery, the balance between speed and accuracy is especially important; it is appropriate to move quickly when the stakes of a surgical step are low, and slowly and accurately during the steps where an error could be catastrophic.

Surprisingly, even after four days of training, participants did not reach a plateau in their performance (learning curves not shown). We hypothesize that with more days to train or more trials per day, these differences may become more apparent.

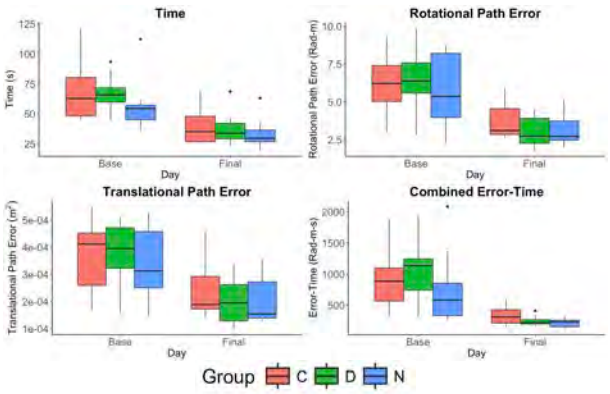

Figure. 1 The 25th, 50th (black line), and 75th percentile of each metric for each group at baseline and final evaluation. Black dots represent outliers.

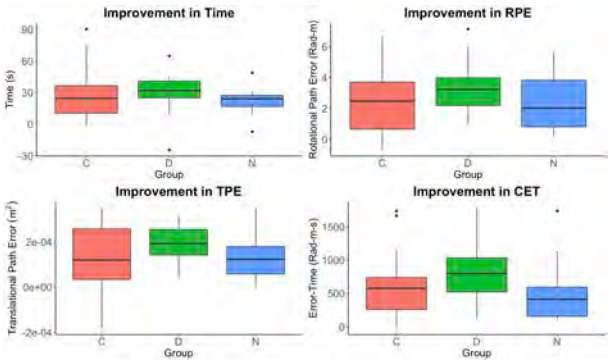

Figure. 2 Improvements from Baseline (25th, 50th, and 75th percentiles). Black dots represent outliers. All values had p < 0.01 for intragroup difference using a two-sided, paired analysis with Wilcoxon signed-rank test.

REFERENCES

[1] Birkmeyer JD, Finks JF, O'Reilly A, Oerline M, Carlin AM, Nunn AR, Dimick J, Banerjee M, Birkmeyer NJO (2013). Surgical skill and complication rates after bariatric surgery. N Engl J Med. 369(15):1434-1442.

[2] Patton JL, Huang FC (2016). Sensory-Motor Interactions and Error Augmentation In Neurorehabilitation Technology. Springer. pp. 79-95.

[3] Coad MM, Okamura AM, Wren S, Mintz Y, Lendvay TS, Jarc AM, Nisky I (2017). Training in divergent and convergent force fields during 6-DOF teleoperation with a robot-assisted surgical system. World Haptics Conference. pp. 195-200.

[4] Enayati N, Okamura AM, Mariani A, Pellegrini E, Coad MM, Ferrigno G, De Momi E (2018). Robotic assistance-as-needed for enhanced visuomotor learning in surgical robotics training: an experimental study. IEEE Int'l. Conf. Robotics and Automation. pp. 6631-6636.

[5] Kazanzides Chen PZ, Deguet A, Fischer GS, Taylor RH, DiMaio SP (2014). An open-source research kit for the da Vinci Surgical System. In IEEE International Conference on Robotics and Automation, pp. 6434-6439.

[6] Smith R, Patel V, and Satava R (2014). Fundamentals of robotic surgery: A course of basic robotic surgery skills based upon a 14-society consensus template of outcomes measures and curriculum development. Int. J. Med. Robot. Comput. Assist. Surg. 10(3):379-384.

A Musculoskeletal Modelling-based Prototyping Platform for a Tremor Suppression Exo-Glove

X. Chen*, R. J. Varghese*, A. Barbot, S. Anastasova, G-Z. Yang

The Hamlyn Centre, Institute for Global Health Innovation, Imperial College London

r.varghese15@imperial.ac.uk (DOI10.31256/HSMR2019.42)

INTRODUCTION

More than 65% of our tremor-affected population (e.g. essential tremor, Parkinson's disease) face severe restrictions in performing activities of daily living [1]. Current treatments involve therapy, pharmacotherapy and neurosurgical procedures but have shown limited efficacy and introduce additional risk and side-effects [1,2]. Wearable exoskeletons could be an ideal alternative to generate mechanical interference to cancel the manifestations. Wearable tremor suppression exoskeletons include the 'Viscous Beam orthosis' of Kotovsky & Rosen [2] and 'WOTAS' by Rocon *et al.*[1] but are bulky, and are not adaptable. Soft robotic exoskeletons with smart material-based actuators and sensors could be a potential alternative.

We are currently working towards developing a smart material-based tremor suppression exo-glove. During the initial stages of design and prototyping of an exo-glove, access to patients with tremor is limited. This work introduces a musculoskeletal (MS) modelling-based platform for virtual prototyping of tremor suppression exo-gloves based on OpenSim [3].

This work is a preliminary assessment of the developed platform and aims to compare the results obtained from simulations and theory. To this effect, we first briefly present generation of tremor in a 1-DoF wrist MS model, then add masses, springs and dampers to the wrist model to analyse their impact on the original tremor manifestation. This platform would form the basis for our evaluation of different tremor suppression solutions.

VIRTUAL PROTOTYPING METHODS

For the assessment of our virtual prototyping platform in OpenSim, a 1-degree-of-freedom (DoF) tremor model based on the generic upper-limb model developed by Saul *et al.*[4] described in [5] is used. Eq.1 describes the approximate linear 2nd order dynamics:

$$\mathbf{I}\ddot{\boldsymbol{q}} + \boldsymbol{D}\dot{\boldsymbol{q}} + \boldsymbol{K}\boldsymbol{q} = \boldsymbol{\tau} + \boldsymbol{\tau_{ext}} \qquad (1)$$

,where eq.1 contains internal torque and gravity ($\boldsymbol{\tau}$), joint displacement ($\boldsymbol{q}$), velocity($\dot{\boldsymbol{q}}$), acceleration ($\ddot{\boldsymbol{q}}$), and external torques ($\boldsymbol{\tau_{ext}}$) to cancel involuntary oscillation. $\boldsymbol{I}, \boldsymbol{D}, \&\ \boldsymbol{K}$ represent joint inertia, damping, and stiffness of the system. In the present analysis, a signal with a primary and multiple secondary frequencies are combined together and applied as activation to the muscles responsible for flexion-extension (F-E) movements. This signal generates a tremor in the wrist with a primary frequency of ~5Hz which is in the range

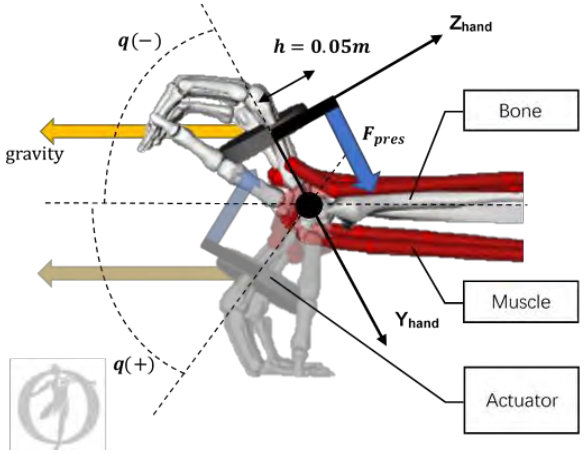

Fig.1: Tremor suppression virtual prototyping schematic showing MS model and actuator/forces

of representative tremor frequencies of 4-12Hz [1]. The hand is in a neutral position by the side of the subject making a voluntary flexion (0^0-25^0) movement.

An actuator was introduced to the tremor model developed in [5]. The actuator introduces a mass and force to simulate an external torque generated by mass, spring and damper-based actuators (see Fig.1). Eq.2 expresses the torque generated by the actuator. It is always parallel to the $\mathbf{Y}_{\mathbf{hand}}$-axis of the hand local coordinate system (see Fig.1).

$$\boldsymbol{\tau_{ext}} = -\boldsymbol{h}\boldsymbol{F_{pres}} = -\boldsymbol{h}(\boldsymbol{k_I}\boldsymbol{q} + \boldsymbol{k_P}\dot{\boldsymbol{q}}) - \boldsymbol{k_D}\boldsymbol{m}\ddot{\boldsymbol{q}} \qquad (2)$$

Substituting eq.(2) into eq. (1), we get:

$$(\boldsymbol{I} + \boldsymbol{k_D}\boldsymbol{m})\ddot{\boldsymbol{q}} + (\boldsymbol{D} + \boldsymbol{h}\boldsymbol{k_P})\dot{\boldsymbol{q}} + (\boldsymbol{K} + \boldsymbol{h}\boldsymbol{k_I})\boldsymbol{q} = \boldsymbol{\tau} \qquad (3)$$

, where $\boldsymbol{I}, \boldsymbol{D}, \boldsymbol{K}$ follow from eq.1 and $\boldsymbol{h}(m)$ is the offset between force application point and center of mass (hand) in the $\mathbf{Z}_{\mathbf{hand}}$ direction, $\boldsymbol{k_D}(m^2)$ is a measure of the radius of gyration of the actuator around the F-E joint axis, and $\boldsymbol{k_P}(Ns)$, $\boldsymbol{k_I}(N)$ and $\boldsymbol{m}(kg)$ are damper coefficient, spring coefficient and mass respectively.

After adding the external torque (according to eq.2) to the system, the hand+actuator system becomes tunable because of the changeable actuator coefficients. For the validation of this virtual prototype, the complete MS model has been restricted to a 1-DoF F-E joint. A controller class developed using the OpenSim API uses the real-time kinematics data ($q, \dot{q}, \ddot{q}$) generated by the OpenSim multi-body dynamics engine. $\boldsymbol{k_P}$, $\boldsymbol{k_I}$ and $\boldsymbol{m}$ for the actuator are the input variables for the simulations. The above mentioned inputs are varied separately, forward dynamics simulations are performed, and the resultant F-E joint angle kinematics is analyzed.

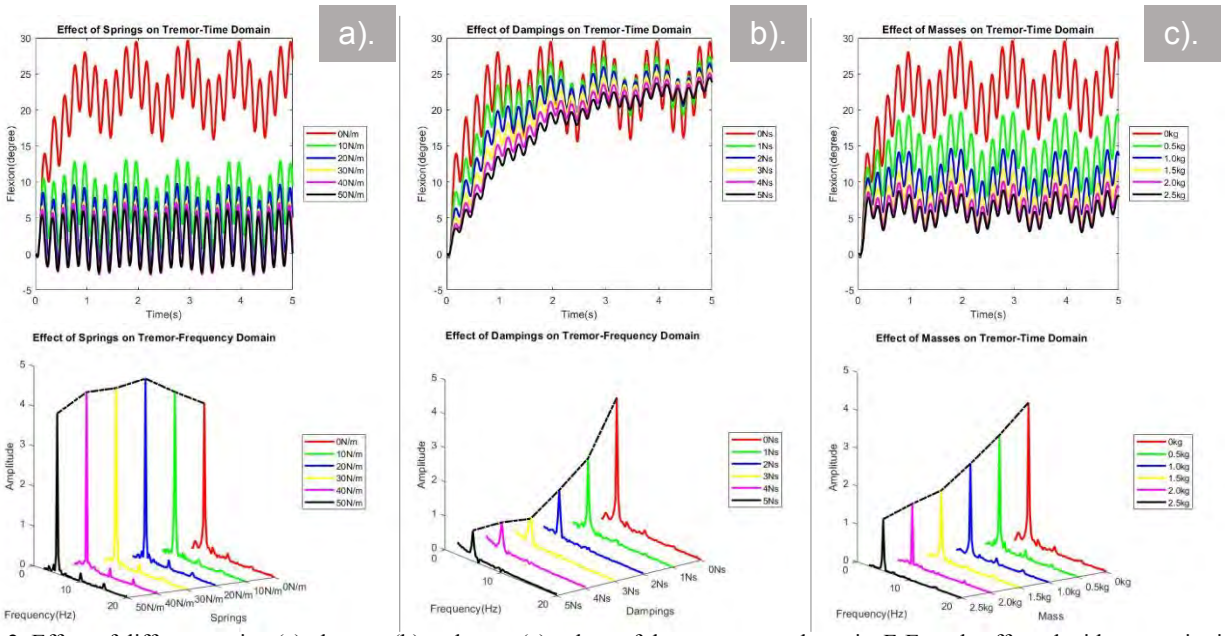

Fig.2: Effect of different spring (a), damper (b) and mass (c) values of the actuator on the wrist F-E angle affected with tremor in time and frequency domain. In the frequency domain, the voluntary movement frequencies (0-1.5Hz) is not considered.

RESULTS AND DISCUSSION

According to the steady-state esponse of a second-order system and its Fourier expansion, the frequency distribution of the steady-state response remains the same as the input. However, the amplitude of the output signal changes according to eq.4:

$$\boldsymbol{g(\omega)} = \frac{\mathbf{1}}{\sqrt{((\boldsymbol{K}+\boldsymbol{hk_I})-((\boldsymbol{I}+\boldsymbol{k_D m})\boldsymbol{\omega}^2)^2+(\boldsymbol{D}+\boldsymbol{h}\,\boldsymbol{k_p})^2\boldsymbol{\omega}^2}} \qquad \textbf{(4)}$$

Our platform is validated by comparing amplitude-response behaviour (see Fig.2) in time- and frequency-domain against expected theoretical behaviour on changing the mass, spring and damping individually with other values set to zero (from eq.4). This evaluation is evolved analytically and hence is performed in OpenSim.

From the frequency domain graphs, we can see that the output frequency of tremor doesn't change in all three cases. On comparing the frequency domain data to the theoretical output (from eq.4), we can see that on increasing the mass (Fig.2(c)) and damping coefficient (Fig.2(b)), the damped amplitude decreases monotonously. In the case of changing the spring constants (Fig.2(a)), as expected, first there is an increase and then a subsequent decrease. This is due to the non-monotonous behaviour introduced by the term: $((\boldsymbol{K}+\boldsymbol{hk_I})-((\boldsymbol{I}+\boldsymbol{k_D m})\boldsymbol{\omega}^2)^2$. In Fig. 2(a), we can see that increasing the spring constant further will result in decreased amplitude.

Additionally, from the time-domain data, it can be seen that increasing the mass and spring constants negatively affects the low frequency voluntary movement. In the case of the spring this happens because the spring tries to restore the hand to the neutral position, whereas in the case of increasing the mass, gravity inhibits voluntary F-E movement. The damper exhibits the best characteristics for reducing tremor amplitude while not affecting voluntary low-frequency movements.

CONCLUSION

In this work, we present a virtual prototyping platform for developing soft wearable tremor suppression exoskeletons. The platform is validated by using a mass-spring-damper system and the simulation results are consistent with epected theoretical behaviour. We are currently working to extend the model to all 3 DoFs of the wrist, and are also working on generating tremor using actual patient-based motion-capture and EMG data. For the next step, we intend to implement the resulting platform into Simulink® environment to test and optimize the actuation and sensing framework for our prototype.

REFERENCES

[1] E. Rocon, J. M. Belda-Lois, A. F. Ruiz, M. Manto, J. C. Moreno and J. L. Pons, "Design and Validation of a Rehabilitation Robotic Exoskeleton for Tremor Assessment and Suppression," *IEEE Transactions on Neural Systems and Rehabilitation Engineering*, vol. 15, no. 3, pp. 367-378, 2007.

[2] J. Kotovsky and M. J. Rosen, "Wearable Tremor-suppression Orthosis," *Journal of Rehabilitation Research and Development*, vol. 35, no. 4, pp. 373-387, 1998.

[3] S. L. Delp, F. C. Anderson, A. S. Arnold, P. Loan, A. Habib, C. T. John, E. Guendelman and D. G. Thelen, "OpenSim: open-source software to create and analyze dynamic simulations of movement," IEEE transactions on bio-medical engineering, vol. 54, no. 11, pp. 1940-1950, 2007.

[4] K. R. Saul, X. Hu, C. M. Goehler, M. E. Vidt, Daly, Melissa, A. Velisar and W. M. Murray, "Benchmarking of dynamic simulation predictions in two software platforms using an upper limb musculoskeletal model," Computer Methods in Biomechanics and Biomedical Engineering, vol. 18, no. 13, pp. 1445-1458, 2015.

[5] R. J. Varghese, C. Romanczyk, J. Liu, G-Z. Yang, "Modelling Tremor for Virtual Prototyping of Exo-Glove", in BioMedEng18 Conference, 2018.

Assisting Hand Movement of TBI Patients Through Robotic Orthoses

T. Meier[1], P. A. Carvalho[1], K. Y. Gandomi[1], G. S. Fischer[1], and C. J. Nycz[1*] [1]*Automation and Interventional Medicine Lab, WPI, Worcester, MA, USA*
[*]*cjnycz@wpi.edu* (DOI10.31256/HSMR2019.43)

INTRODUCTION

A large number of individuals suffer from impairments of the upper limbs due to neurological traumas and diseases such as stroke [1], cerebral palsy [2], and traumatic brain injury (TBI) [3]. These impairments often manifest as overactive reflexes and irregular muscle tone. In the hand, this causes difficulty in extending the impaired fingers. A review of hand exoskeletons shows many concepts have been explored to assist finger motion, but they have rarely been evaluated on impaired subjects [4]. Hand orthoses designed to assist individuals with the aforementioned flexed postures may require different designs from those created to assist weakness alone. For example, in [5] it was found that when testing on a subject with high spasticity, a rigid hand exoskeleton increased performance mostly during the grasping phase of a task. When unaided, the subject did not struggle to hold and manipulate objects, but rather struggled to extend their fingers around the objects.

Here, we describe the preliminary design and clinical testing of a Hand Orthosis with Powered Extension, the HOPE Hand. The HOPE hand was designed to provide individuated finger motion enabling multiple grasp patterns in the presence of high resting muscle tone or spasticity. The device was constructed using measurements we've previously collected related to the forces required to extend the fingers of individuals presenting with irregular muscle tone [6].

MATERIAL AND METHODS

An exoskeleton was designed based on the concept shown in Fig. 1. Cable guides attached to the dorsal surface of the hand create an offset d to the joint centers of the metacarpophalangeal (MCP) and proximal interphalangeal (PIP) joints, reducing the cable tension needed to oppose the resisting torque at each of these joints. The distal interphalangeal (DIP) joint was splinted in a straight or semi-flexed position as coordination of the PIP and DIP in the presence of spasticity is difficult with non-rigid mechanisms.

The exoskeleton provides two degrees of motion for the thumb. A channel across the back of the hand guides a cable to the thumb's metacarpal where it is fixed. Flexion and Abduction of the thumb into opposition is accomplish by manually pushing the cable. To maintain thumb opposition, a screw is used to lock the cable position. Furthermore, flexion/extension of the thumb's MCP can be achieved actively by pushing or pulling a second cable running along the dorsal surface. The exoskeleon is 3D printed from a photopolymer material (Durable Resin, Formlabs) and weighs 240g with Bowden cables, not including actuation unit.

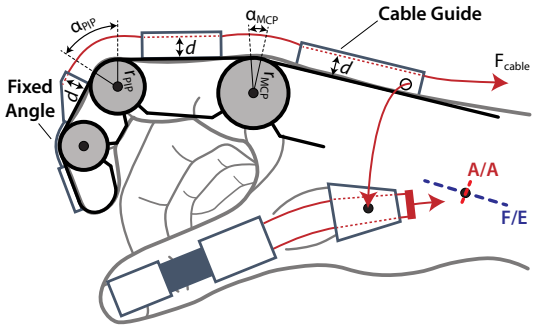

Figure 1. Flexion/Extension (FE) of the fingers provided by pushing and pulling cables running along their dorsal surface. FE and abduction/adduction (AA) of the thumb's CMC joint provided by manually pushing and pulling a cable along the dorsal surface of the hand terminating at the first metacarpal.

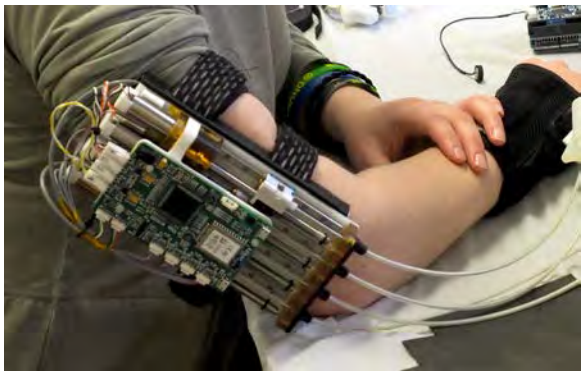

Figure 2. Four motor actuation unit worn by subject.

Force was applied to the extending cables using DC motor driven linear actuators. Based on the peak torque measured in [6], a desired 1 second response from full flexion to full extension, and an assumed quintic joint velocity profile, a peak power of 3-5W delivered to each finger was determined necessary to extend the joints against chronic spasticity. A ballscrew with 90% efficiency (MTF-0601, THK) was used to generate the cable pull through a 60-70% efficient Bowden cable. Based on these parameters, a 3W continuous power (DCX14L EB SL 6V, Maxon, inc.) brushed DC motor was chosen under the provision that over-driving by 2-3 times the continuous power rating is permissible for several sec-

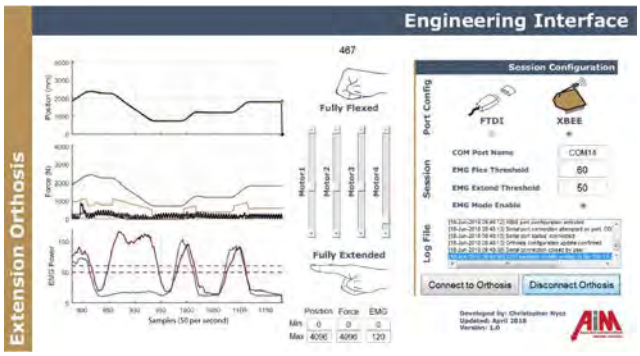

Figure 3. User interface created in MATLAB for testing.

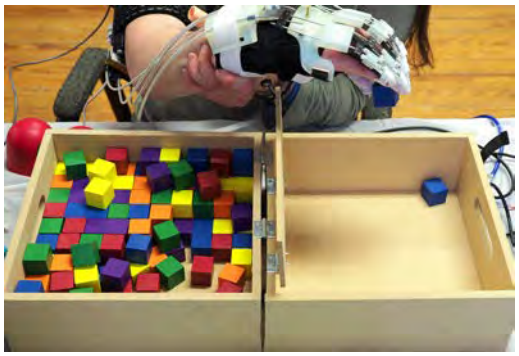

Figure 4. Subject moving blocks in a Box and Blocks test.

onds as per manufacturer guidelines. Four of these motor and ballscrew actuators were integrated into a remote actuation unit mounted to the upper arm as seen in Fig. 2. A SAM3X8E ARM Microcontroller (ATMEL, USA), on the remote actuation unit, processes signals received from up to two electromyogram sensors and can connect to a host controller via USB or XBee (S2C DigiMesh Mesh 2.4, Digi International). The microcontroller runs position control loops for each of the linear actuators with the orthosis's compliance regulating the force applied to the user. The actuation unit weighs 768g with battery capacity of 12.2Wh.

A MATLAB (2018A, MathWorks) based graphical user interface was created for device setup, monitoring, and manual position control. Device setup includes setting thresholds for EMG sensors (not used for this experiment) and customizing grasp positions to the user. The interface is shown in Fig. 3. While used for monitoring and testing, the user interface is not needed for device operation.

RESULTS

Upon approval of our study protocol from Worcester Polytechnic Institute's IRB, we conducted preliminary testing of the orthosis on a subject with unilateral high tone and spasticity (Modified Ashworth score of 3 in joints of the affected arm) in their right hand due to a TBI. Testing consisted of having the subject perform a box and blocks test, both with and without the assistance of the HOPE hand providing an assessment of the device's benefits. The Box and Blocks test is commonly used to evaluate manual dexterity [7]. Without the assistance of the HOPE hand, the subject was unable to transfer any blocks. With the use of the orthosis, the subject was able to transfer up to 2 blocks within the 60 second testing window. For the purpose of this study, the device was controlled to toggle between an open position and a three-jaw-chuck grasp via a foot-pedal. The full device with actuation unit was worn by the test subject for the duration of testing and did not further hinder their ability to position their impaired arm.

DISCUSSION

Preliminary results from testing on a single impaired subject indicate that the HOPE hand restores partial range of motion in the fingers enabling grasping of basic objects. The device was focused on providing assistance in extension, overcoming increased flexor muscle tone, with a small assistance in flexion to accomplish functional grasping. The device is able to be worn for many hours without deleterious effects on the subject's hand. The foot-pedal is not an optimal mechanism for the user to control the device during daily use, and different forms of control such as voice or EMG control should be explored. Integration with an elbow and shoulder mechanism may provide a more complete solution.

REFERENCES

[1] Bonita, R. & Beaglehole, R. Recovery of motor function after stroke. *Stroke* **19**, 1497–1500 (1988).

[2] Arner, M. *et al.* Hand function in cerebral palsy. report of 367 children in a population-based longitudinal health care program. .

[3] Walker, W. C. & Pickett, T. C. Motor impairment after severe traumatic brain injury: a longitudinal multicenter study. *J. Rehabil. Res. Dev.* **44**, 975 (2007).

[4] Chu, C.-Y. & Patterson, R. M. Soft robotic devices for hand rehabilitation and assistance: a narrative review. *J. NeuroEngineering Rehabil.* **15**, 9 (2018).

[5] Gasser, B. W. *et al.* Design and preliminary assessment of vanderbilt hand exoskeleton. In *2017 International Conference on Rehabilitation Robotics (ICORR)*, 1537–1542 (2017).

[6] Nycz, C. J. *et al.* Design criteria for hand exoskeletons: Measurement of forces needed to assist finger extension in traumatic brain injury patients. *IEEE Robotics Autom. Lett.* **3**, 3285–3292 (2018).

[7] Mathiowetz, V. *et al.* Adult norms for the box and block test of manual dexterity. *The Am. J. Occup. Ther.* **39**, 386–391 (1985).

Reciprocal Kinematic Control: using human-robot dual adaptation to control upper limb assistive devices

M. Legrand[1], E. de Montalivet[1], F. Richer[1], N. Jarrassé[1], G. Morel[1]

[1]Sorbonne University, CNRS, UMR7222 / INSERM, ISIR- Agathe, Paris, France

{mathilde.legrand,nathanael.jarrasse,guillaume.morel}@sorbonne-universite.fr (DOI10.31256/HSMR2019.44)

INTRODUCTION

Upper limb (UL) assistive robots, such as exoskeletons, prostheses or supernumerary limbs, can rarely be fully autonomous devices. Indeed, it is generally not possible to use pre-defined patterns of motions because of the great diversity of tasks and the variety of UL movement strategies to achieve any of them. Control has to be provided to the users. For that purpose, the most widespread solutions to obtain user's motor intention use physiological signals (electromyograms or electroencephalograms e.g.)[1,2], distal functional joints (for instance, head or foot motions control the end-effector position and/or orientation)[3,4] or inter-joint synergies models[5]. Despite interesting results, they all still have important limitations: the first two are neither natural nor intuitive and suffer from robustness issues, the third one does not allow very versatile devices.

To tackle these issues, we propose a new control approach, together with a new paradigm, that uses the motion strategies naturally developed by the Central Nervous System (CNS). When a limb mobility is reduced, or when an assistive device does not work properly, CNS compensates and takes advantage of motor redundancy of the body: it calls other joints to still perform the desired gesture. Typical compensatory joints for UL movements are the trunk and the scapula[6]. Our concept is to servo the robot to these body compensations. The only task of the latter is to make its user come back to a comfortable posture, and this indirectly leads to the realisation of the intended motion. The reciprocal adaptation between human and robot allows both to reduce the body compensations and perform UL movements with the assistive device. We validated a proof of concept of this paradigm on ten healthy subjects who executed a path-tracking task with an elbow exoskeleton.

MATERIALS AND METHODS

Control law

The control law is built in such a way that the user only has to focus on the end-effector (EE) position, as he/she would have done with a healthy arm. The aim is that the EE position, first reached with body compensations, remains constant, while the device moves and makes the user's compensatory joints go back to a reference position. An integration step is then added to prevent any rigid position-position coupling that does not enhance the mobility.

The approach has been first applied to control an elbow joint with the following law (see Fig.1(a) for the definition of the anatomical parameters):

1. Compute δ the distance between the EE position and the reference position of the acromion (chosen to define a non-compensatory posture, as it reflects both trunk and scapula, the main joints involved in upper body compensations),
2. Compute β_n the angle the elbow should have to allow the EE to be in its current position without any compensation, according to

$$\beta_n = \Pi - acos(\frac{L_{fa}^2 + L_{ua}^2 - \delta^2}{2L_{ua}L_{fa}}) \quad \text{(Eq.1)}$$

with L_{ua} and L_{fa} the lengths of the upper arm and the forearm respectively.

3. Compute the angular velocity command to be sent to the robotic elbow:

$$\dot{\beta} = \lambda\Delta\beta = \lambda(\beta_n - \beta) \quad \text{(Eq.2)}$$

with β the current elbow angle and λ the gain of the integrator set to 2. An activation threshold (Δβ>5 degrees) was set to avoid instabilities.

Validation

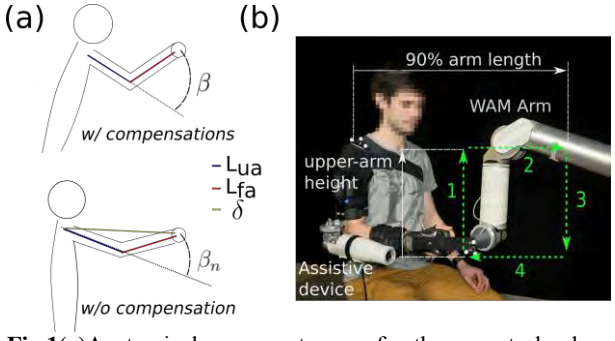

Fig.1(a) Anatomical parameters of the control law. **(b)**Experimental set-up. A WAM®Arm draws a rectangle in the sagittal plane of the subject; it pauses briefly at each corner. Numbers 1 to 4 indicate the movements steps. The dimensions are adapted to the subject's morphology. The subject is wearing a robotic joint acting like an elbow exoskeleton and a wrist splint with a rod attached to it.

Ten healthy subjects, aged 20-23, who all gave their written consent, wore an elbow exoskeleton prototype that guided their motions. The task consisted in following a moving target, carried by a WAM®Arm (Barrett Technology), that drew a rectangle in the sagittal plane of the subject. The dimensions of the rectangle were adapted to the subject's morphology (see Fig.1(b)). There were five repetitions. The task was performed in three different ways (later called modes):

1. Natural (N): the subject did not wear the exoskeleton but moved freely, without any specific instructions nor constrains. This is to be used as the reference.
2. Elbow fixed (F): the robotic joint was locked at 90 degrees, it prevented any elbow motions. This worst-case scenario showed the body compensations that can be exhibited when the mobility is reduced.
3. Reciprocal Kinematic (RK) control: the subject wore the device which, commanded with the proposed control scheme, guided the movements of his/her elbow. The end-effector and the acromion positions were tracked in real time (f=100Hz) with the motion capture system Optitrack (NaturalPoint Inc.). The reference position was defined as the initial position of the subject. The subjects received no instructions nor explanation; they were only told to perform the task and that the assistive device would help them. A training on ten repetitions was allowed before recording five.

RESULTS

The first thing to notice is that the task was correctly performed with the three modes (no statistical difference between the precision errors). To evaluate the performance of RK control, several metrics were analysed; two are presented here: the range of motion (ROM) of the acromion, which represents the compensatory displacements, and the ROM of the elbow (see Fig. 2). Statistical analysis was performed: Lilliefors test was used to assess the normality of the data, then general linear models for normally distributed data and nonparametric Friedman test for the others.

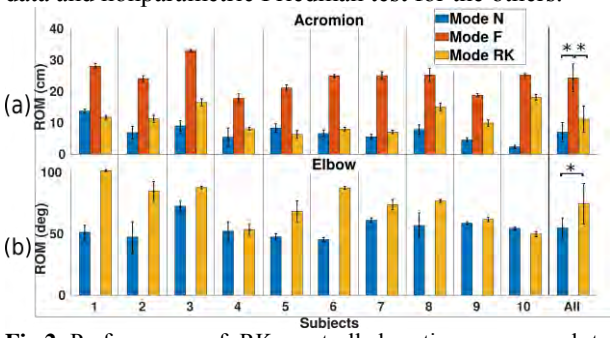

Fig.2 Performance of RK controlled-motions compared to natural and fixed-elbow ones. (a) ROM of the acromion. (b) ROM of the elbow. Metrics are averaged over the five trials and last columns is the mean over the ten subjects.

The ROM of the acromion is significantly higher for the F-mode than for N and RK ones ($p<0.05$) while no statistical difference exists between N- and RK-mode. This confirms that, due to reciprocal adaptation, RK control indeed reduces the user body compensations.

Concerning the elbow ROM, F-mode is absent as there is no movement of the joint. With RK-mode, we see an over-extension compared to the natural ROM. More detailed analysis shows that this over-extension appeared in the third stage of the movement, when the target is the furthest.

DISCUSSION

To build a natural and intuitive control for UL assistive devices, we propose to servo the robot to the body compensations of its user. This new paradigm, in which the device only focuses on correcting its user's posture, was tested with an elbow exoskeleton. It makes it possible to perform a path-tracking task, while requiring only minimal compensatory movements to work. Without any explanation provided, the users mastered the use of the device with RK in few trials, which highlights the intuitiveness of the control.

Some points of our experiment yet deserved more detailed comments. First, the motions performed with RK tend to show an over-extended elbow in the third stage of the task. This could be because the subjects leaned on one side to see better their end-effector, which led to unwanted elbow activations. This points out that the trunk is not always compensatory but can be functional (i.e. essential to do the task). We are working to detect the utilisation of the trunk (compensation or function) and adapt the answer of the device to avoid undesirable activations. Second, we worked with a motion capture system, which cannot be used in everyday life. However, the information it gave (positions of EE and acromion) can be obtained with other techniques, more suitable for home-use. For instance, it shall be possible to do the same with a simple set of two IMUs, one on the trunk and one on the arm, along with few anatomical data of the subject.

The preliminary results we obtained attest the usability and the intuitiveness of RK control. They support future tests on disabled subjects (amputees or post-stroke patients e.g.) as well as further developments for several degrees of freedom assistive devices. Moreover, RK control is task-independent, as the error vector used in the control law depends only on the reference posture (neither tasks nor compensations are explicitly defined). The experimental test of this versatility with different tasks is scheduled in the very near future. The reference posture was fixed for this experiment but further studies will make possible to have an automatically adjusted one. RK control is thus promising for a natural and versatile control of UL assistive devices, from prostheses to exoskeletons or even supernumerary arms.

REFERENCES

[1] Oskoei M, Huosheng H. Myoelectric control systems – A survey. Biomed Signal Proces 2007 July;2: 275-294.
[2] Velliste M, Perel S, Spalding M, Whitford A, Schwartz A. Cortical control of a prosthetic arm for self-feeding, Nature 2008; 453(7198):1098-1101.
[3] Resnik L, Klinger Sh, Etter K, Fantini C. Controlling a multi-degree of freedom upper limb prosthesis using foot controls: User experience. Disabil Rehabil Assist Technol 2014; 9(4):318-329.
[4] Jackowski A, Gebhard M, Thietje R. Head motion and head gesture based robot control: a usability study. IEEE TNSRE 2017 Oct;26(1): 161-170.
[5] Merad M, de Montalivet E, Roby-Brami A, Jarrassé N. Intuitive prosthetic control using upper limb inter-joint coordinations and IMU-based shoulder angles measurement: a pilot study, IROS 2016.
[6] Cirstea M, Levin M. Compensatory strategies for reaching in stroke. Brain 2000; 123;940-953.

Virtual Reality Training in Robot-Assisted Surgery: a Novel Experimental Setup for Skill Transfer Evaluation

Guido Caccianiga[1,2], Andrea Mariani[2], Elena De Momi[2], Jeremy D. Brown[1]

[1]*Johns Hopkins University, Baltimore, Maryland, USA*

[2]*Politecnico di Milano, Milano, Italy*

gcaccia1@jhu.edu, jdelainebrown@jhu.edu (DOI10.31256/HSMR2019.45)

INTRODUCTION

Currently, the use of Virtual Reality (VR) for training in Robot-Assisted Minimally Invasive Surgery (RAMIS) is widely diffuse; the daVinci Skills Simulator (dVSS) [1], dV-Trainer [2], RobotiX Mentor [3], and the Robotic Surgical Simulator [4] are all commercially available as RAMIS training platforms. While these systems are not yet capable of reproducing in VR a fully interactive operating room training environment, they still offer a useful method for extracting real-time, quantitative measurements of performance in clinically relevant surgical tasks. These measures, however, are generally used to compute manufacturer-defined scoring metrics that are often seen as subjective [5]. Various studies [6-8] have tried to investigate the utility of these systems in teaching and assessing basic and advanced robotic skills, including the predictive validity of these systems to forecast performance in the actual OR [9].

Evaluating the concurrent validity of these systems, will involve comparing them to the "gold standard," inanimate, and in-vivo training performance on the real physical da Vinci Surgical System. Both approaches to physical robotic training however, rely exclusively on structured human grading in which an expert surgeon rates a live or recorded training task using an objective assessment tool like the Global Evaluative Assessment of Robotic Skills (GEARS). While GEARS uses overall technical proficiency measures like bimanual dexterity, depth perception and efficiency of movement, it can be time-consuming, subjective, and tedious to perform. In addition, the metrics from assessments such as GEARS do not readily translate to the metrics available from the VR simulators. Further complicating this is the fact that the VR and inanimate/in-vivo task are not always identical. Vargas [10] for example evaluated the skill transfer from training on the dVSS to sutures on a porcine model, but it was difficult to draw a direct comparison between training and validation test; the skill transfer was not verified.

To easily compare VR performance with training performance on the real da Vinci, a direct relationship between the two approaches needs be established; the tasks should be identical analogs, both in terms of their physical form factor, and the measures used to evaluate skill. The Fundamentals of Robotic Surgery (FRS) training curriculum [11] attempted to solve the first challenge through the use of a skill training platform that was identical in its VR and inanimate variants. Skill assessment for the inanimate variant, however, lacked sensor-based skill measures the way the VR variant did.

Our work represents the first step towards a sensorized approach to investigate the effects of skill transfer from VR to inanimate environments for RAMIS training. Given the importance of visuo-motor skill development for RAMIS, we have designed our initial task in the framework of needle driving which requires accuracy, precision, and overall hand-eye coordination.

MATERIALS AND METHODS

In designing our needle driving training task, we wanted to build a measuring system that was capable of taking into account the needle-tissue interactions encountered during in-vivo needle driving. Of ultimate consideration was the fact that every time a needle deviates from its optimal, purely rotational, trajectory the tissue is stretched or damaged. To measure these deviations in an inanimate training task without kinematic information from the robot or external optical tracking systems, our sensorized inanimate platform utilizes three opto-mechanical measuring units featuring small rigidly attached rings resembling the entry, pass-through, and exit points of a needle-driving trajectory in-vivo (Fig1).

The base of each opto-mechanical measurement unit consists of two optical-based sensing elements (6-DoF) derived from a SpaceNavigator mouse (3Dconnexion Inc.) connected through a 45mm diameter spring. The spring is compliant enough to allow rotational and translational displacement of the ring in space while also being stiff enough to bring the ring back to the equilibrium point when the displacing force is removed. The two sensing plates can measure their relative rotational and translational displacements with a resolution of 170 increments per angular degree and 250 increments per mm, respectively. The output of each sensor is published on a ROS topic, recorded, and mapped onto a circular RGB LED ring (Worldsemi Co., Limited) to provide realtime multidirectional visual feed-back to the user. All the mechanical parts are 3D printed for the real setup (PLA springs, ABS structure). To create the virtual rendering of the inanimate task, the relative CAD models were imported into the ATAR VR simulation framework [12] and dynamically characterized with mass and friction to resemble realistic behavior. Each spring is modeled in VR as a 6 DoF visco-elastic constraint with stiffness and damping.

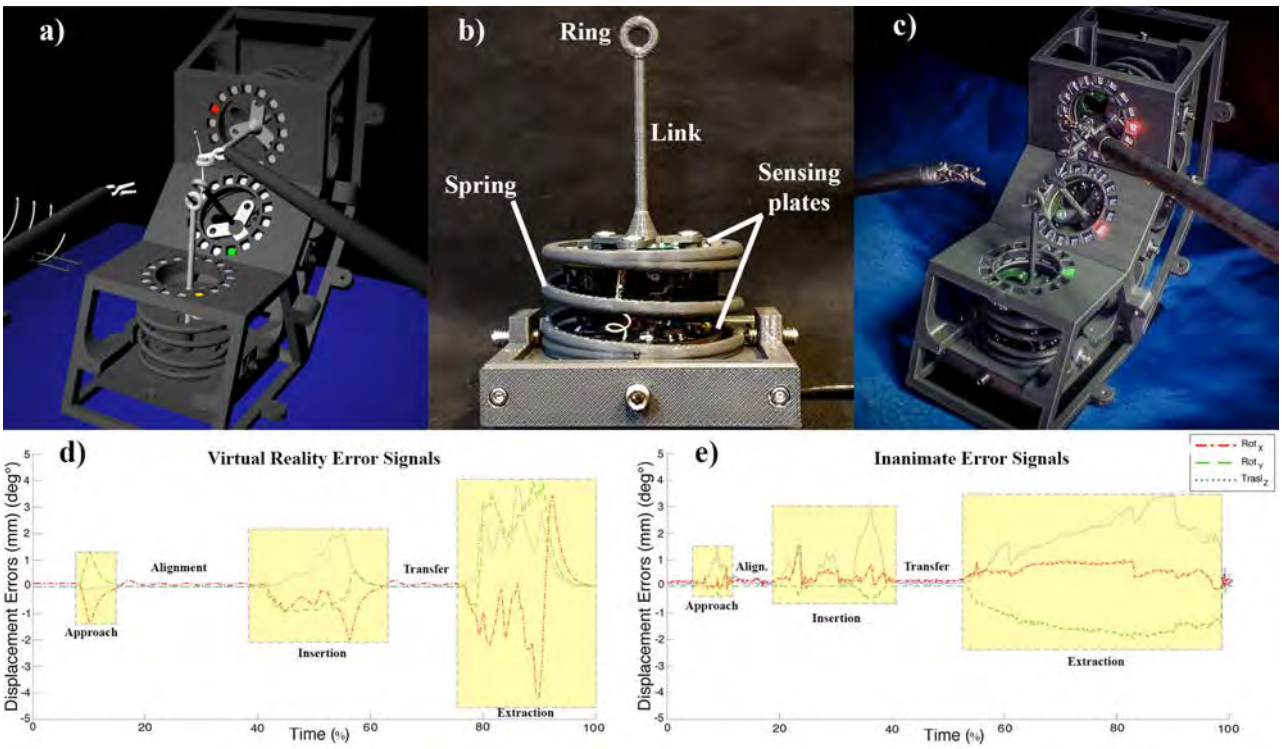

Figure 1. (a) Virtual Reality simulation. (b) Opto-mechanical measurement unit. (c) Inanimate task. (d) Raw output signals from the simulator. (e) Raw output signals from the inanimate task.

The displacement of the ring in VR is calculated at each time instant by comparing the actual kinematic pose of the virtual rings with the pose at equilibrium. A simulated LED ring is used to provide real-time feedback to the user. A daVinci S surgical system with EndoWrist Large Needle Driver instruments was used for the inanimate training platform. A daVinci Research Kit (dVRK) running the ATAR environment was used for the VR training platform. Two virtual robotic arms resembling the Large Needle Driver instruments were used to interact with virtual objects. The suture used for the task is a standard (20mm radius) GS-26 ½ round taper.

VALIDATION & DISCUSSION

We recorded the data from an experienced user (>20 hours of training in VR) performing the VR needle driving task with the dVRK (Fig. 1d) and the inanimate needle driving task with the daVinci S (Fig. 1e). Data shown highlights the three error displacement metrics (two rotational, one translation) for a single ring in both scenarios. The shaded yellow boxes highlight distinct phases of the suturing task (approach, insertion, extraction). The error profile is close to zero during alignment (pre rotation) and transfer (right hand steady holding the needle), maximum during extraction (non-dominant hand). Both the VR simulator and the inanimate platform demonstrate their capability of capturing skill-related metrics for the same needle-driving task. The modular structure of the platform can easily be scaled or rearranged to modify the complexity or the objectives of the task .

Future experiments with both novice and expert robotic surgeons will be conducted to investigate differences in training between VR and inanimate training environments, while also providing precious information about the potential for skill transfer.

REFERENCES

[1] Intuitive Surgical Inc., Sunnyvale, CA, USA
[2] Mimic Technologies Inc., Seattle, WA, USA
[3] 3D Systems Corporation, Littleton, CO, USA
[4] Simulated Surgical Systems, San Jose, CA, USA
[5] K. Dubin A., et al. A Comparison of Robotic Simulation Performance on Basic Virtual Reality Skills: Simulator Subjective Vs. Objective Assessment Tools. 2017; Journal of Minimally Invasive Gynecology. 24.10.1016
[6] Hertz A.M., et al. Head-to-Head Comparison of Three Virtual-Reality Robotic Surgery Simulators. 2018; JSLS.22(1):e2017.00081.
[7] Bric J., et al. Current state of virtual reality simulation in robotic surgery training: a review. 2015; Surgical Endoscopy. 30.10.1007/s00464-015-4517-y.
[8] Moglia A., et al. A Systematic Review of Virtual Reality Simulators for Robot-assisted Surgery. 2015; European urology. 69.10.1016
[9] Hoogenes J., et al. A Randomized Comparison of Two Robotic Virtual Reality Simulators and Evaluation of Trainees' Skills Transfer to a Simulated Robotic Urethrovesical Anastomosis Task. 2017; Urology.111. 10.1016/j.urology. 2017.09.023.
[10] Vargas M.V., et al. The transferability of virtual reality simulation-based robotic suturing skills to a live porcine model in novice surgeons: a single blind randomized controlled trial. 2016; Jour Minim Inv Gynec. 24.10.1016
[11] Visit: http://frsurgery.org
[12] Enayati N., et al. An augmented reality framework for surgical teleoperation performance enhancement and training. 2017; CRAS 2017

SlicerVR for image-guided therapy planning in immersive virtual reality

Csaba Pinter[1], Andras Lasso[1], Mark Asselin[1], Jean-Christophe Fillion-Robin[2], Jean-Baptiste Vimort[2], Ken Martin[2], Gabor Fichtinger[1]

[1] *Laboratory for Percutaneous Surgery, Queen's University, Kingston, Canada*

[2] *Kitware Incorporated, Carrboro, North Carolina, USA*

csaba.pinter@queensu.ca, gabor@cs.queensu.ca (DOI10.31256/HSMR2019.46)

INTRODUCTION

Virtual reality (VR) allows experiencing 3D-rendered scenes in a fully immersive virtual environment that has proved to be useful in variety of medical applications. There is, however, a lack of free open source software to enable immersive virtual reality experience during image-guided therapy planning. 3D Slicer [1] is a widely-used free open source medical data visualization platform, on which image-guided therapy applications can be created with minimal development overhead [2]. In an early prototype, we demonstrated the concept of VR-based image-guided therapy planning in 3D Slicer that showed improvement in the efficiency and ease of scene navigation compared to conventional display and mouse based navigation [3]. In this paper, we report the development of a comprehensive open source platform SlicerVR (www.SlicerVR.org) that provides immersive virtual reality exploration and navigation during image-guided therapy planning while taking advantage of the full functionality of 3D Slicer. Significant novelties since the early prototype include enhanced controller interactions, multiple collaborative features and more extensive support for a variety of VR hardware devices.

MATERIALS AND METHODS

System Design: SlicerVR is designed as an extension module in 3D Slicer that connects to the VR hardware seamlessly with the 3D Slicer features (Fig 1).

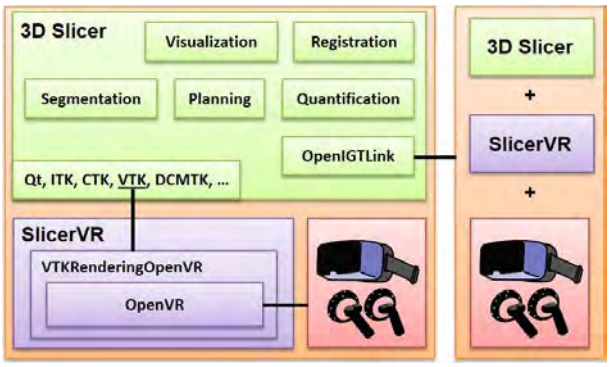

Fig. 1 SlicerVR architecture overview. Left side shows a detailed SlicerVR system with 3D Slicer and the VR hardware. The right side is a similar system connecting to the other via OpenIGTLink.

SlicerVR is designed to provide one-button integration: any scene visualized in 3D Slicer is seamlessly passed to be viewed in the VR headset and manipulated using the VR controllers. No programming or setup from the user is required. Upon installing SlicerVR as a regular 3D Slicer extension, the user connects the headset, populates the 3D Slicer scene, and then launches VR rendering by a single button press. By using the same rendering scene, SlicerVR simultaneously manipulates the immersive virtual scene and the conventional monitor-mouse based therapy planning scene. Thus, unlike conventional "virtual exploration" environments, all changes and manipulations made in the virtual scene are automatically propagated back to the therapy plan.

Controller Interaction Features: Users can choose to perform visualization tasks with moving their head (look around or into objects), using the controllers (fly, rotate, magnify, etc.), or using the mouse to set a desired view then propagate camera to VR with a button press. SlicerVR allows for prolonged convenient stay in the virtual environment by automatically harmonizing rendering parameters with user motions and actions (*i.e.* progressive rendering), thereby preventing motion sickness. Manipulating objects, such as moving and rotating using the controllers intuitively, is also possible. Moving 2D slice views is achieved by attaching "handle" objects to the slices via the volume reslice and transform functions of 3D Slicer. Surgical tools can be simulated by showing arbitrary tool models in place of the controllers. In addition, any function in the 3D Slicer ecosystem can be made accessible in the virtual environment via simplified VR-accessible user interface widgets, including therapy planning tasks, such as registration or changing therapy parameters.

Collaborative Features: Multiple users can share and manipulate the same scene. The state of the 3D Slicer instance of each VR user is synchronized via an OpenIGTLink [4] connection. Headsets and controllers of the other users can be broadcasted and displayed as well. This scene sharing enables the creation of novel cooperative experiences, such as collaborative planning or telemedicine. In a 1 to N scenario, where multiple trainees observe an instructor explaining anatomy or an intervention, the trainees can watch the VR scene from arbitrary distance, angle and magnification.

Hardware Support: We accommodate a wide range of users by supporting a variety of popular VR hardware through using the OpenVR software development kit providing hardware abstraction. SlicerVR supports all OpenVR-compatible headsets, such as the HTC Vive, all Windows Mixed Reality headsets (by Acer, Lenovo, HP, etc.), and Oculus Rift.

RESULTS

Some of the image-guided therapy planning scenarios enabled by SlicerVR include the following.

Pedicle screw placement planning. The scene contains volume rendering of the spine CT or surface rendering of segmented vertebrae (set to be static), and a number of screws (set to be movable). The user naturally picks up and places the screws in the optimal position, which can be verified by "looking into" the anatomy along the screw (see Fig. 2).

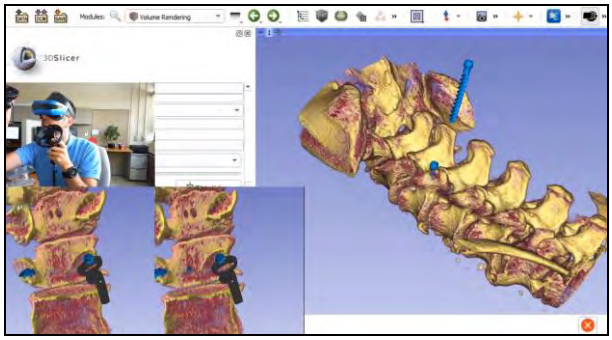

Fig. 2 Using SlicerVR for pedicle screw insertion planning. The background shows 3D Slicer with a single 3D view displaying the spine CT in volume rendering and the screws. The bottom left shows the VR mirror – what the user sees with each eye. The middle left shows the user with the headset and controllers, placing the current screw. Introduction video: https://youtu.be/F_UBoE4FaoY

Visualization of cardiac tomographic and echo images: Cinematic image series in standard DICOM 3DE format can be viewed in motion, allowing for full immersive visualization of the beating heart.

Ultrasound-guided needle insertion training: These skills are difficult to acquire due to simultaneous manipulation of the ultrasound device and needle. VR helps in training by improving hand-eye coordination and spatial awareness. The trainees can re-watch their insertions in VR to better understand the spatial relationships involved.

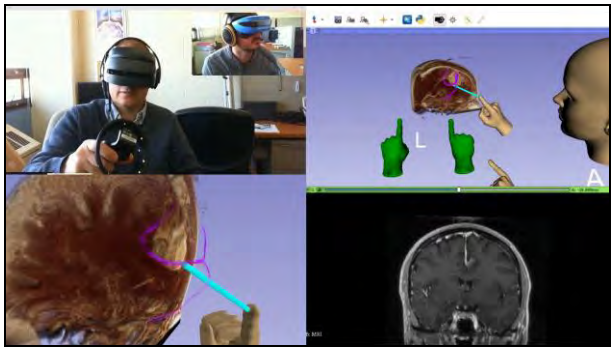

Fig. 3 Remote VR collaboration for brain surgery planning using real-time tractography. Top left: Participants local (blue headset) and remote (black headset). Bottom left: VR mirror image (local). Top right: 3D view of the SlicerVR instance (local). Bottom right: coronal slice in the position of the tractography seed (local). Introduction video: https://youtu.be/rG9ST6xv6vg

Brachytherapy catheter identification: Paths of brachytherapy catheters are challenging to follow due to their diverging and often crisscrossing pattern. VR enables better visualization of the catheters through stereoscopic vision and intuitive navigation (*i.e.* head movements), thus affording faster and more reliable identification of the catheters.

Collaborative surgery planning: Brain tumour surgery planning can be performed in remote VR collaboration using SlicerVR (see Fig. 3). The MRI image is shown in volume rendering with diffusion tractography calculated real-time with the tip of a needle used as seed point that can be moved using the VR controllers by either participant. The head and hands of each participant can be seen in the scene as virtual avatars.

DISCUSSION

Ongoing work includes the development of in-VR user interfaces. This will allow displaying arbitrary user interface widgets available in 3D Slicer or built specifically for VR. A laser pointer originating from the controller will interact with the panel similarly to conventional mouse interactions. This framework will make possible advanced use cases such as segmentation, which is crucial in planning (*e.g.* defining the target) or can be used in training (*e.g.* anatomy education or annotations).

An increasing number of VR hardware (such as HTC Vive Pro) are equipped with video cameras. By showing the real-time stereo camera image in the background, VR turns into augmented reality, which opens the way for a wide range of novel applications of SlicerVR in interventional navigation. For example, by using real position-tracked surgical tools instead of VR controllers we can render highly realistic and sophisticated image-guided therapy planning and training scenarios.

The SlicerVR extension is freely available for download in the 3D Slicer extension manager for versions 4.10 and later. To date, SlicerVR (www.SlicerVR.org) has been downloaded over 1,000 times.

REFERENCES

[1] Fedorov, A., Beichel, R., Kalpathy-Cramer, J., Finet, J., … Kikinis, R. (2012). 3D Slicer as an image computing platform for the Quantitative Imaging Network. Magnetic Resonance Imaging, 30(9), 1323–1341.

[2] Ungi, T., Lasso, A., Fichtinger, G. Open-source platforms for navigated image-guided interventions. Medical Image Analysis, 2016 Oct;33:181-186.

[3] Choueib, S., Pinter, C., Lasso, A., … & Fichtinger, G. (2019, March). Evaluation of 3D slicer as a medical virtual reality visualization platform. In Medical Imaging 2019: Image-Guided Procedures, Robotic Interventions, and Modeling (Vol. 10951, p. 1095113). International Society for Optics and Photonics.

[4] Tokuda, J., Fischer, G. S., Papademetris, X., Yaniv, Z., Ibanez, L., ... & Kapur, T. (2009). OpenIGTLink: an open network protocol for image-guided therapy environment. The International Journal of Medical Robotics and Computer Assisted Surgery, 5(4), 423-434.

dVRK-XR: Mixed Reality Extension for da Vinci Research Kit

Long Qian, Anton Deguet, Peter Kazanzides

Laboratory for Computational Sensing and Robotics, Johns Hopkins University
{long.qian, anton.deguet, pkaz}@jhu.edu (DOI10.31256/HSMR2019.47)

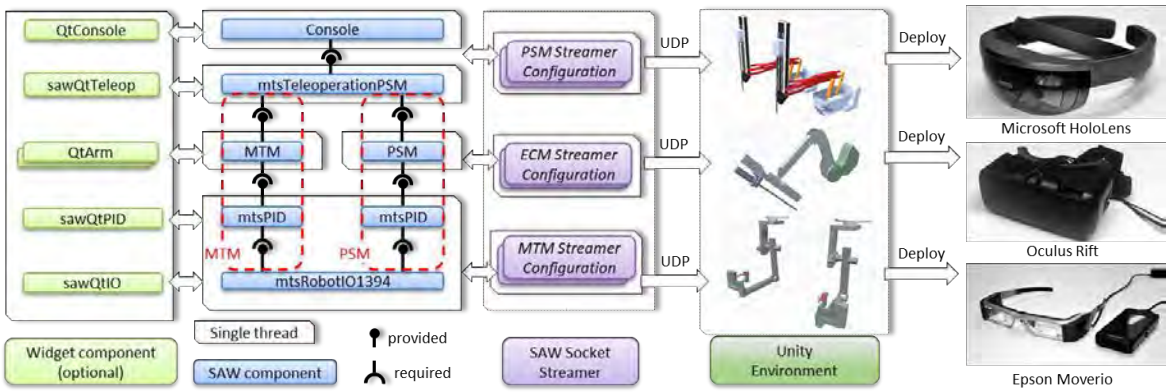

Fig.1 Overview of dVRK-XR open source package and integation with existing dVRK software stack

INTRODUCTION

The da Vinci Research Kit (dVRK) has become a widely adopted research platform for surgical robotics research since its initial public release in 2012. To date, it has been installed at 35 institutes worldwide. In the past decade, research interest in mixed reality (including augmented reality and virtual reality) has increased among both the robotics and medical communities [1], due to the improved usability of mixed reality headsets and the much reduced hardware cost. In this paper, we describe dVRK-XR (https://github.com/jhu-dvrk/dvrk-xr), an extension to the dVRK open source package that facilitates the integration of mixed reality in surgical robotics research.

MATERIALS AND METHODS

Software Architecture

The system architecture of dVRK-XR is shown in Fig. 1. The dVRK employs a component-based software architecture [3], in which different modules can be dynamically loaded with a JSON-based configuration. In fact, this feature enables us to extend the dVRK software stack in a clean and reliable way. We implement a new component: *sawSocketStreamer*, which can be connected to the existing dVRK program and send JSON-serialized messages at a fixed framerate over UDP. The message to send, the destination IP address, port number, and framerate can be dynamically configured using a JSON file. For example, with a Patient-Side Manipulator (PSM), we can inform *sawSocketStreamer* to retrieve the results of a function named "*GetStateJoint*" at 100Hz from the dVRK, then serialize the returned results and send to a specified destination.

Robot Representation in Unity

The application is built with Unity (https://unity.com), a popular development tool for mixed reality applications.

Fig. 2 An example application using dVRK-XR [2]

The Unity program can receive and deserialize the incoming messages. Therefore, the result of "*GetStateJoint*" of the PSM is available to the Unity environment. We use the DH parameters of the manipulator to build a tree of GameObjects in Unity that corresponds to its kinematics tree. The relative transformation of a parent node and child node can either be fixed, controlled by a specific field of an incoming message, or associated with another joint to reflect a passive mechanical linkage. The convention is similar to Unified Robot Description Format (URDF). We construct the PSM, ECM and MTM for Unity. With real-time messages containing joint state, the visualization of the manipulators can be synchronized with the real robot.

Target Mixed Reality Platforms

A major advantage of using Unity as a framework is its compatibility with multiple mixed reality platforms, e.g. VR platforms like Oculus (Desktop) and Google Cardboard (Android), AR platforms like Microsoft HoloLens (Windows UWP). Although Unity takes care of the graphics API of multiple platforms, the socket API and threading API does not cover Windows UWP, which is not a POSIX-compatible platform. Therefore, we explicitly implement an asynchronous UDP client using Windows UWP APIs. Currently, dVRK-XR supports Windows, Linux, Windows UWP and Android.

Multi-Threading and Rendering Performance

For a mixed reality application, it is critical to keep the rendering framerate as high as possible in order to provide a smooth user experience. We implement dVRK-XR with such concern in mind. On the server side, *sawSocketStreamer* is asynchronous with respect to the dVRK control and on the client side, the socket handling and rendering are done in different threads. When the rendering of a new frame is triggered, the latest message is pulled from the socket client, then deserialized and visualized.

RESULTS

End-to-End Latency

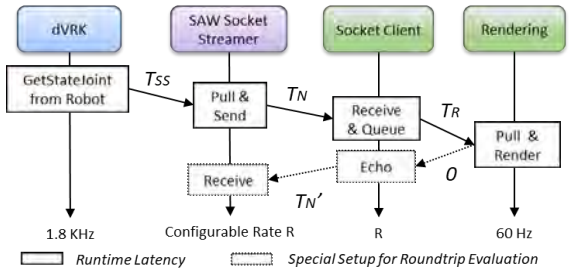

Fig. 3 The evaluation of end-to-end latency

We evaluate the end-to-end latency (T) between a real da Vinci robot and its virtual representation in dVRK-XR, as shown in Fig. 3. The runtime latency is:

$$T = T_{SS} + T_N + T_R \quad (1)$$

where, i) T_{SS}: the latency between *sawSocketStreamer* and the joint state generated from the robot, ii) T_N: the networking time for sending the UDP packet, iii) T_R: the time between arrival and rendering. We assume that the latency introduced by the receiving mechanism of *sawSocketStreamer* and rendering is half of the average frame time, therefore: $T_{SS} = 0.000278\ ms$, $T_R = 0.5 / R$. We add a timestamp to the data packet, recording the time that a specific joint state is generated from the robot. The evaluation of T_N is not trivial because the time on the device and robot is not synchronized accurately. Therefore, we configure the socket client to echo the exact same message back, and we assume that $T_N' = T_N$. We measure the round-trip time T_{RD}, w.r.t. different frame rate of socket streamer. So,

$$T_{RD} = T_{SS} + T_N + T_R + T_N' \quad (2)$$

Combining (1), (2), the overall latency is:

$$T = (T_{RD} + T_{SS} + T_R) / 2 \quad (3)$$

We configured the framerate of *sawSocketStreamer* to be *50 Hz*, *100 Hz*, *150 Hz*, *200 Hz* and *250 Hz*, and used Windows Desktop (tethered device, e.g., Oculus Rift or HTC Vive) and HoloLens as mixed reality platforms.

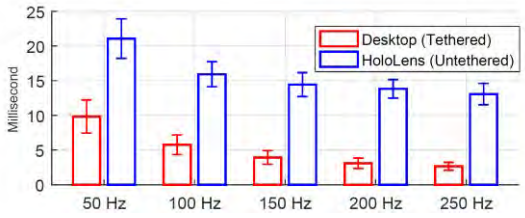

Fig. 4 Mean and standard deviation of end-to-end latency

The resulting end-to-end latency is shown in Fig. 4. The latency for a tethered device is less than *10 ms*, and for an untethered device, it is also smaller than a single frame if the *sawSocketStreamer* runs at *100 Hz* or higher. The visualization is real-time and low-latency.

DISCUSSION

dVRK-XR can enable many research opportunities that integrate surgical robotics and mixed reality. As an example, we developed an augmented reality application for the patient-side assistant in da Vinci surgery [2]. The assistant may need to insert a robotic instrument without knowing the position of the tip before it enters the field-of-view of the endoscope. Moreover, he or she may navigate a laparoscopic instrument with bad hand-eye coordination, due to the mis-orientation of the endoscopic view. With dVRK-XR and fiducial tracking, we can provide real-time visualization of the robotic instruments, endoscope and its field-of-view indicator, via the optics of HoloLens. The virtual rendering appears overlaid on top of the actual instrument (Fig. 2). A comparative study between ARssist and traditional visualization for the first assistant shows that the hand-eye coordination was much improved and the time to complete tool manipulation was significantly reduced [4].

Apart from benefiting the patient-side assistant, there are many other application scenarios with dVRK-XR:

- Teleoperation of virtual PSM or ECM
- Port/Trocar planning in robotic surgery
- Collaboration and interaction with remote experts
- Immersive visualization for training and education.

CONCLUSION

We developed dVRK-XR, an open source extension that enables mixed reality research with surgical robotics. The design considered compatibility, modularity, and user comfort. Our evaluation shows that dVRK-XR achieves real-time low-latency visualization on both tethered and untethered mixed reality platforms. We believe dVRK-XR will benefit the open source surgical robotics research community by easing the implementation of XR applications and extending the current research spectrum.

REFERENCES

[1] Barsom EZ, Graafland M, Schijven MP. Systematic review on the effectiveness of augmented reality applications in medical training. Surgical Endoscopy. 2016 Oct; 30 (10): 4174-4183.

[2] Qian L, Deguet A, Kazanzides P. ARssist: augmented reality on a head-mounted display for the first assistant in robotic surgery. Healthcare Technology Letters. 2018 Jan; 5(5): 194-200.

[3] Kazanzides P, Chen Z, Deguet A, Fischer GS, Taylor R H, DiMaio SP. An open-source research kit for the da Vinci® Surgical System. In IEEE Intl. Conf. on Robotics and Automation (ICRA) 2014 May (pp. 6434- 6439).

[4] Qian L, Deguet A, Wang Z, Liu YH, Kazanzides P. Augmented reality assisted instrument insertion and tool manipulation for the first assistant in robotic surgery. In IEEE Intl. Conf. on Robotics and Automation (ICRA) May 2019.

Feasibility of Volumetric OCT Imaging using Continuum Robots with Equilibrium Modulation

Giuseppe Del Giudice[1], Jin-Hui Shen[2], Karen Joos[2], Nabil Simaan[1]

[1]*Department of Mechanical Engineering, Vanderbilt University, Nashville TN, USA*

[2]*Vanderbilt Eye Institute, Vanderbilt University Medical Center, Nashville TN, USA*

giuseppe.del.giudice@vanderbilt.edu (DOI10.31256/HSMR2019.48)

INTRODUCTION

Continuum Robots (CR) have enabled dexterous access for surgical interventions for tasks requiring dexterity at a macro-scale resolution, with the finest resolution in sub-millimetric motion, for example as demonstrated in [1]. However, there are a host of tasks requiring micro-scale motion such as micro-vascular reconstruction and image-based biopsy (e.g. [2], [3] [4]) or confocal endo-microscopic imaging (e.g. [5]). Recently, a new concept of micro/macro motion generation using CR with equilibrium modulation (CREM) was presented in [6]. According to this design concept (Fig.1a) macro-motion is achieved by pushing and pulling on tubular backbones as in [7]. Micro-motion is achieved by sliding equilibrium modulation wires inside the backbones, thereby, shifting the static equilibrium pose of the robot (equilibrium modulation).

In [6] we integrated a custom B-mode optical coherence tomography (OCT) probe modified from [8] and demonstrated the ability of CREM to achieve micro-motion. The integrated probe still requires significant work on image dewarping as was demonstrated in [9]. Since the goal of this work is to discern feasibility of 3D OCT using CREM and to determine the attainable 3D scan resolutions, we present a proof-of-concept system using an external OCT probe.

MATERIALS AND METHODS

To obtain 3D OCT using a B-mode probe, micro-motion was used to move a sample perpendicular to the imaging plane of the probe (this motion direction will be referred to as normal motion direction (NMD)). Fig. 1(B) depicts this process. To achieve this goal, the setup shown in Fig. 2 was used. A CR segment was bent 30° relative to its straight configuration. This pose was designated as a sample configuration within the macro motion workspace and macro motion joints were held fixed. The end effector (EE) was monitored from opposing sides using a microscope camera for visual tracking using the method in [6] and a Thorlabs OCT probe (Thorlabs Telesto-II-1325LR-5P6 – 3.5 to 7 mm imaging depth with 5.5 to 12.0 µm Axial Resolution in Air) for OCT imaging of samples attached to the EE.

For each experiment, different sample materials were attached to the EE and micro-motion was achieved by inserting three equilibrium modulation wires within the tubular macro-motion backbones. At every 0.5 mm of insertion a B-mode OCT scan was acquired while pausing the insertion. OCT images were segmented using Matlab image processing toolbox and processed in order to create a 3D OCT model.

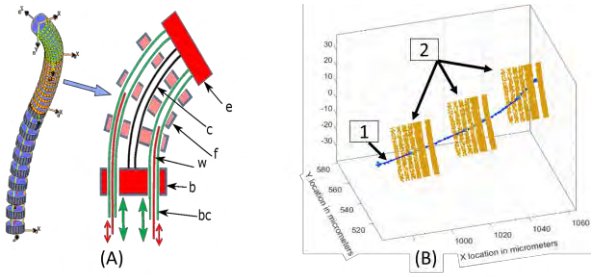

Fig. 1 (A) CREM Concept: ***b***-base disk, ***c***-central backbone, ***bc*** - secondary backbone, **e** - end disk, ***w*** - equilibrium modulation wire, ***f***-spacer disk. **(B)** an example of OCT image acquisition along the robot's EE micro-motion path in the normal motion direction (NMD): ***1***- Robot EE path, ***2*** – three sample images of a multilayer cellophane tape along the path.

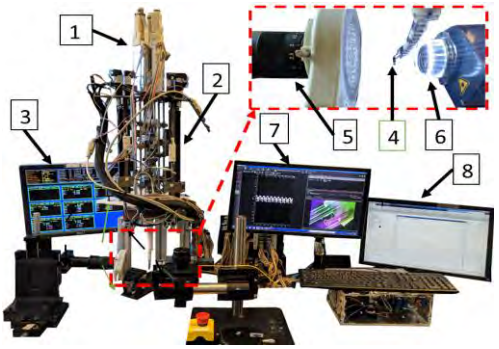

Fig. 2 Experimental setup: ***1***-micromotion AU, ***2***-CR AU, ***3***-XPC Target, ***4***-EE, ***5***-Microscope camera, ***6***-OCT probe, ***7***-Thorlab OCT machine, ***8***- Matlab Host Computer.

RESULTS

Three samples were used in three experiments in order to test the feasibility of our method with different materials and different shapes. First, a metric brass screw (0.8 mm diameter, 0.2 mm pitch) was scanned, Fig. 3. A profile image of the screw was taken to compare to the known screw pitch geometry (Figs. 3 A-B). Micro motion was initiated to generate a 3D scan which was reconstructed in Figs. 3 C-E. The pitch based on the profile image (Fig. 3A-B) was 209.8±5 µm while based on the 3D scan it was 210.7±5 µm based on analysis of Fig. 3D. This designates an average error is

0.5%. The micro motion seen in Fig 3E corresponded with 92µm motion in NMD and it corresponds to 89 scans. Therefore the NMD resolution was 1.03 µm.

In the second experiment, a multilayer cellophane tape with an additional layer of double-sided tape on top was enclosed in Agar, Figs 4 A-C. The double-sided tape was added to simulate a thicker layer at the top of the sample. This experiment was motivated by a future application of 3D retinal layer reconstruction.

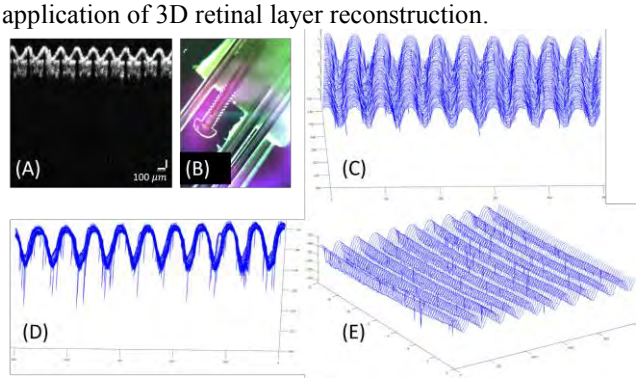

Fig. 3 Screw pitch reconstruction: ***A***-OCT Image, ***B***-Screw sample image (OCT camera view), ***C-D-E***-3 different views of the reconstracted profile.

Results of the 3D reconstruction are shown in Figs. 4 D-F. The thickness of the layers measured based on a single OCT image had an average of 71.7 µm while the thickness measured from the reconstructed model had an average of 67.4 µm. The average error is circa 6%. According to the regular tape supplier, the tape layer has an average thickness of 70 µm, including the glue layer. To simulate the reconstruction of a capillary blood vessel we used an artificial channel generated in agar, Fig. 5. The channel was made by placing a 220 µm NiTi wire in liquid agar. After solidification, the wire was removed, and the sample scanned. The average area measured using three B-mode OCT images as in Fig. 5A was 2.4746e+04 µm^2. The cross-sectional area average for the 3D reconstructed model was 2.6329e+04 µm^2. This represents an average deviation of 6%.

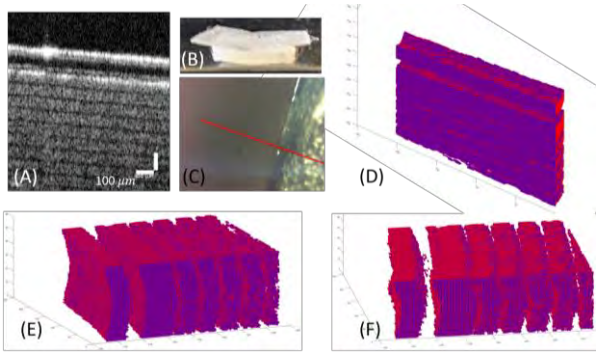

Fig. 4 Multilayer cellophane tape reconstruction: ***A***-OCT Image, ***B***-Side view of the multilayer cellophane tape with the double-sided tape added on top, ***C***- Multilayer tape Sample image (OCT camera view), ***D-E-F***- 3 different views of the reconstracted profile.

DISCUSSION

Micro motion generated using CREM has been demonstrated and shown to achieve NMD motion resolutions close to 1 µm. This suggests that the 3D reconstructed models can have a resolution of adjacent B-mode images that exceeds the OCT probe's image scan resolution. In this work, we have used optical tracking of the EE position for reconstruction. Future work will use modeling of micro-motion kinematics to achieve such reconstruction. Recent results we obtained using calibration of micro-motion demonstrated that such a model can be within 5 µm from the ground truth tracking data. Future work will include integrating a custom-built B-mode OCT probe into the CR and performing real-time 3D OCT reconstruction using micro-motion kinematics.

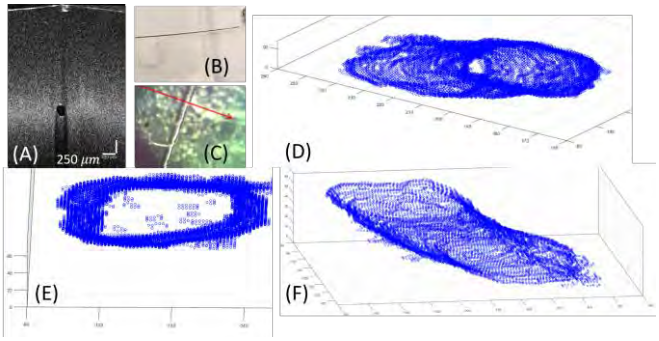

Fig. 5 Micro Channel reconstruction: ***A***-OCT Image, ***B***-NiTi wire used to create the channle still in the agar sample, ***C***-Channel sample image (OCT camera view), ***D-E-F***-3 different views of the reconstracted profile.

REFERENCES

[1] N. Simaan, A. Bajo, A. Reiter, L. Wang, P. Allen, and D. Fowler, "Lessons learned using the insertable robotic effector platform (IREP) for single port access surgery," *J. Robot. Surg.*, vol. 7, no. 3, pp. 235–240, 2013.

[2] W. Luo, F. T. Nguyen, A. M. Zysk, T. S. Ralston, J. Brockenbrough, D. L. Marks, A. L. Oldenburg, and S. A. Boppart, "Optical biopsy of lymph node morphology using optical coherence tomography," *Technol. Cancer Res. Treat.*, vol. 4, no. 5, pp. 539–547, 2005.

[3] J. G. Fujimoto, "Optical coherence tomography for ultrahigh resolution in vivo imaging," *Nat. Biotechnol.*, vol. 21, no. 11, pp. 1361–1367, 2003.

[4] E. Ayvali, C. P. Liang, M. Ho, Y. Chen, and J. P. Desai, "Towards a discretely actuated steerable cannula for diagnostic and therapeutic procedures," in *IJRR*, 2012.

[5] P. Giataganas, M. Hughes, C. J. Payne, P. Wisanuvej, B. Temelkuran, and G.-Z. Yang, "Intraoperative Robotic-Assisted Large-Area High-Speed Microscopic Imaging and Intervention," *IEEE Trans. Biomed. Eng.*, vol. 66, no. 1, pp. 208–216, Jan. 2019.

[6] G. Del Giudice, L. Wang, J.-H. Shen, K. Joos, and N. Simaan, "Continuum robots for multi-scale motion: Micro-scale motion through equilibrium modulation," in *2017 IEEE/RSJ IROS*, 2017, pp. 2537–2542.

[7] N. Simaan, R. Taylor, and P. Flint, "A dexterous system for laryngeal surgery," in *IEEE ICRA*, 2004, vol. 1, pp. 351–357.

[8] K. M. Joos and J.-H. Shen, "Miniature real-time intraoperative forward-imaging optical coherence tomography probe," *Biomed. Opt. Express*, 2013.

[9] H. Yu, J. H. Shen, K. M. Joos, and N. Simaan, "Calibration and Integration of B-Mode Optical Coherence Tomography for Assistive Control in Robotic Microsurgery," *IEEE/ASME Trans. Mechatronics*, 2016.

A Flexible Endoscopic Robotic Suturing System for Gastrointestinal Perforations: Animal Study

L. Cao[1], X. Li[1], P. T. Phan[1], A. M. H. Tiong[1], H. L. Kaan[2]
K. Y. Ho[3], P. W. Y. Chiu[4], S. J. Phee[1]

[1]*Robotics Research Center, Nanyang Technological University, Singapore.*

[2] *Department of Surgery, National University Hospital, Singapore.*

[3] *Yong Loo Lin School of Medicine, National University of Singapore, Singapore.*

[4]*Department of Surgery, Chinese University of Hong Kong, Hong Kong.*

lin.cao@ntu.edu.sg (DOI10.31256/HSMR2019.49)

INTRODUCTION

Gastrointestinal perforations may be caused due to complicated flexible endoscopic procedures such as Endoscopic Submucosal Dissection (ESD), Endoscopic Full-Thickness Resection (EFTR), and Natural Orifice Transluminal Endoscopic Surgery (NOTES). The most reliable approach of closing gastrointestinal perforations is by suturing which, however, is usually done through open or laparoscopic surgery. Suturing through flexible endoscopic procedures is highly desirable but challenging due to the confined space of the lumen and target area, high dexterity and force demands of suturing tasks, and critical size and strength requirements of the closure. Although two endoscopic defect closure devices exist on the market, i.e., Over-The-Scope Clip (OTSC, Ovesco Endoscopy Inc., Germany)[1] and OverStitich (Apollo Endosurgery Inc., US)[2], both devices are not for standard suturing due to the use of clips or fastening elements, and they are limited with large sizes and the lack of dexterity or tool triangulation.

We developed a flexible endoscopic robotic suturing system [3] which can endoscopically close gastrointestinal wounds with standard stitches and knots using a robotic suturing arm (Ø4.4 mm) and a grasping arm (Ø4.2 mm). Both arms are flexible, through-the-scope, and have five Degrees Of Freedom (DOFs). This paper presents an in-vivo test of this system suturing an incision on the rectum wall of a live pig.

MATERIALS AND METHODS

The two robotic arms, remotely controlled by a surgeon via a master console, can be inserted through the two tool channels of a customized endoscope which is controlled by an endoscopist. This through-the-scope feature enables tool exchange without withdrawing the endoscope during surgery. As shown in Fig. 1a, the suturing arm is a five-DOF grasper (gripping, yaw, pitch, roll, and translation) with two jaws. The double-point lancet needle (gauge 21, 10 mm long) can be inserted into the needle receiving holes on the two jaws. The needle can be switched between the jaws by a pair of tendon-sheath-driven locking blades (Fig. 1 b and c) which can be translated to engage or disengage with the notched slots (Fig. 1 b) on the needle tips. During suturing, the 10-mm-long needle is locked to one of the

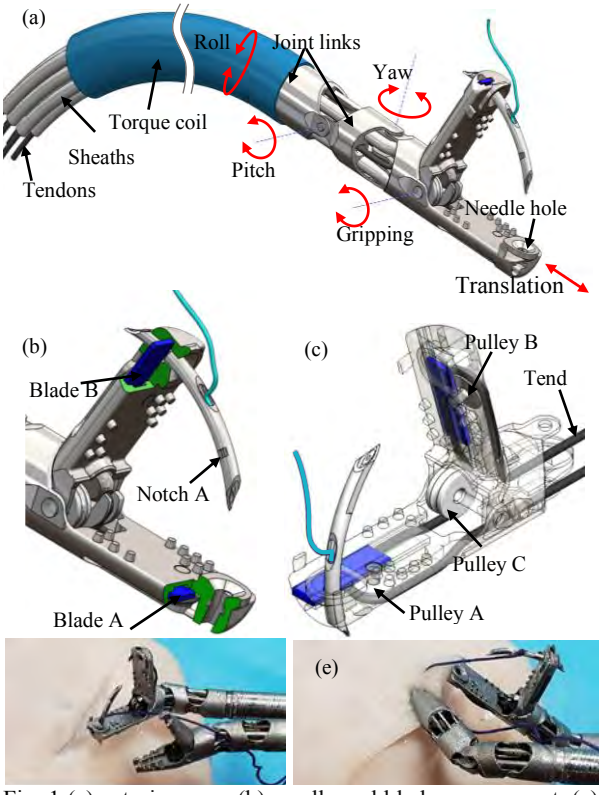

Fig. 1 (a) suturing arm; (b) needle and blade engagement, (c) tendon-controlled blades, (d)-(e) working prototype.

two jaws, resulting in a profile of the suturing device much larger than the endoscope tool channel(Figure 1a~c); thus, a nitinol guidewire was proposed to deploy the needle so that the suturing arm can be delivered through the endoscope channel [3]. The grasper arm is a simplified version of the suturing arm without the needle manipulation mechanism. The prototypes of the two arms are shown in Fig.1d-e.

This suturing system was tested via an in-vivo study on a live pig (about 70 kg) with ethical approval (NO.: INH2018/017). The setup of the animal study is shown in Fig. 2. A colonoscope was inserted into the rectum of the pig under general anesthesia. A 10 mm submucosal incision was cut in advance. Then, the robotic arms were inserted to the incision site through the two working channels of the colonoscope. The needle was deployed

Fig. 2 Setup of the in-vivo animal study

through a nitinol guidewire. Four running stitches were made for the incision, followed by a Surgeon's Knot by passing the needle through suture loops. Stitching and knot-tying were intuitively teleoperated by the operator via the robotic system through the master console. The suture was then cut; the needle and the instruments were withdrawn through the endoscope channels. The pig was euthanized after the procedure.

RESULTS

It took around 3 minutes to deploy the needle and withdraw the guidewire. Fig. 3 shows the suturing process. The suturing arm on the right pointed the needle tip to the desired stitching point (Fig. 3b) and to the suture loop (Fig. 3d). Meanwhile, the grasper on the left helped lift and feed the tissue to the suturing arm as well as handling the suture thread. By translating the two arms into opposite directions, the knot was securely tightened (Fig. 3e). After the closure, the suture was cut, and the needle was completely released from the suturing device and subsequently taken out by the grasper. The times spent on stitches and knot (three throws) were 11 mins and 4 mins, respectively.

DISCUSSION

The needle locking mechanism was reliable and ensured successful needle switching during the trial. When the needle penetrated through tissue, the rotating jaw always had a snapping motion and the needle tip became visible, both of which indicated that the needle was ready to be switched. The needle could then be easily switched by pressing the associated button on the handle of the right haptic device. This approach made needle manipulation easy. In this trial, the robotic grasper played an important role in lifting and feeding the tissue to the suturing arm as well as handling the suture thread. The cooperation between the two arms made suturing more natural and intuitive. The five DOFs of the two arms were vital for tool triangulation which naturally suits suturing tasks while other existing devices [1-2] have only one arm without triangulation. In particular, the rolling DOF ensured that the grasper/needle could grasp/puncture tissue edges at any desired orientations, which is necessary for incisions with random orientations. Moving the tip of the endoscope was occasionally needed to help the arms reach the suture or tissue in difficult scenarios. The through-the-scope feature is particularly useful when a new needle needs to be used for additional stitches. The feasibility of deploying the needle using a nitinol guidewire was also confirmed robust. Suturing in this trial took much longer time than previous ex-vivo trials [3] because of the limitation of

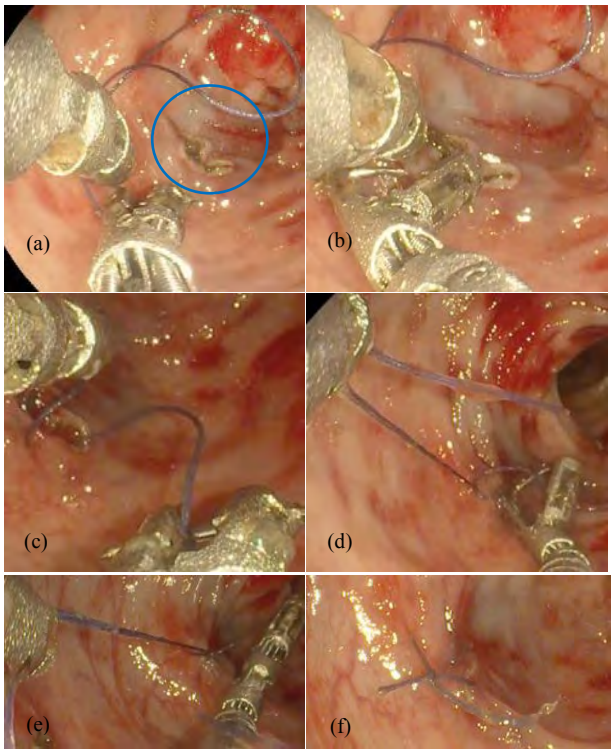

Fig. 3 Suturing process and result. (a) robotic arms deployed at the incision site (the blue circle); (b) driving the needle through the tissue; (c) four stitches made; (d) creating knots by passing the needle through suture loops; (e) securing the knots by translating the robotic arms into opposite directions; (f) suture was cut, and incision was closed.

the system in sealing insufflation gas. The time can be significantly shortened with proper insufflation. The jaws, with unilateral opening, can be opened with 78 degrees and thus the suturing device can maximally bite tissue with 3.4mm thickness while the thickness of stomach and colon tissue is normally within 3mm. Further development with bilateral opening jaws can enhance the reach of the instruments, and thicker tissue would be handled easier.

This in-vivo trial confirms that the system can be used to endoscopically make standard stitches and knots (not possible with existing devices) in a realistic surgical scenario. It is expected that this system be used to close defects or perforations in ESD, EFTR, and NOTES, etc.

ACKNOWLEDGEMENTS

Research supported by National Research Foundation (NRF) Singapore (NRFI2016-07).

REFERENCES

[1] G. Iabichino, L. H. Eusebi, M. A. Palamara, *et al.*, "Performance of the over-the-Scope Clip System in the Endoscopic Closure of Iatrogenic Gastrointestinal Perforations and Post-Surgical Leaks and Fistulas," *Minerva Gastroenterologica e Dietologica,* vol. 64, pp. 75-83, 2018.

[2] S. H. Chon, U. Toex, P. S. Plum, *et al.*, "Successful Closure of a Gastropulmonary Fistula after Esophagectomy Using the Apollo Overstitch and Endoscopic Vacuum Therapy," *Endoscopy,* vol. 50, pp. E149-E150, 2018.

[3] L. Cao, X. G. Li, P. T. Phan, *et al.*, "A Novel Robotic Suturing System for Flexible Endoscopic Surgery," the International Conference on Robotics and Automation, Montreal, Canada, 2019.

Development of a Robotic Endoscope Automated via Laryngeal Imaging for Tracheal Intubation (REALITI)

Q. Boehler[1], P. Hofmann, D. Gage[2], A. Gehring, C. Chautems[1], P. Biro[3], B.J. Nelson[1]

[1]*Multi-Scale Robotics Lab, ETH Zurich*

[2] *University of Zurich*

[3] *Institute of Anesthesiology, University Hospital Zurich*

qboehler@ethz.ch, peter.biro@usz.ch (DOI 10.31256/HSMR2019.50)

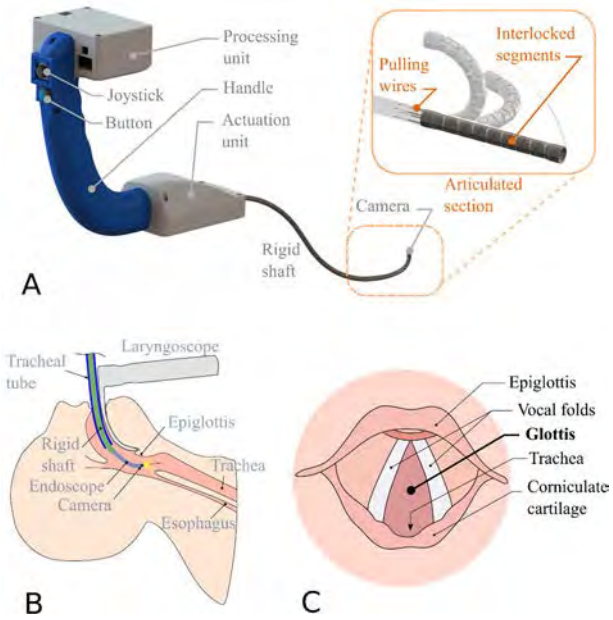

Fig. 1 Tracheal intubation with robotic assistance. A: REALITI device, B: Assisted tracheal intubation, C: Anatomy of the larynx from the endoscopic camera view.

INTRODUCTION

From general anesthesia to emergency medical services (EMS), tracheal intubation (TI) is considered to be the worldwide gold standard to secure the airway of a patient in need of respiratory assistance [1]. State-of-the-art TI consists of placing a tracheal tube (TT) into the trachea of the patient while lifting their jaw with a laryngoscope. This approach is called "direct-laryngoscopy" as it provides a direct view on the glottis, which is the entrance of the trachea. Inability to perform TI in time or TT misplacement can result in severe morbidity and mortality caused by asphyxia, hypoxemia, and pulmonary aspiration [2]. These casualties occur more frequently in EMS situations where TI is performed under difficult and stressful circumstances [3]. Moreover, anatomical factors or systemic conditions can make TI more difficult even for an experienced anesthesiologist in a hospital setting [4]. Alternatives to alleviate difficulties of direct-laryngoscopic TI have been established and include video-laryngoscopes or flexible endoscopes used to guide the TT [5]. However, when performed manually, a successful TI still relies solely on the dexterity and experience of the physician to first recognize key anatomical features such as the glottis, and then to steer the TT into the trachea. Our aim is to develop a robotic assistance for TI for these two critical aspects of the procedure using a Robotic Endoscope Automated via Laryngeal Imaging for Tracheal Intubation (REALITI). This work is focused on the development of a first prototype of the REALITI device, and its use in performing an assisted TI on a standard intubation-training manikin.

MATERIALS AND METHODS

The REALITI is a handheld device comprised of a motorized 2-degrees-of-freedom endoscope, a handle, and a processing unit, as depicted in Fig. 1A. The articulated section located at the distal end of a rigid shaft acts as a guide for the TT. An endoscopic camera placed at its tip provides a constant video feedback of the distal end of the endoscope to an external monitor wired to the device.

To perform a TI with the device, the endoscope is inserted into the patient's mouth and moved forward manually towards the trachea (see Fig. 1B and C). The TT is then fed over the endoscope, and the device is removed from the patient's mouth while the TT is held in place. The device is intended to operate in two modes when being inserted into the trachea; (1) a manual mode where the bending motion of the endoscope is manually controlled by the user via a joystick, (2) an autonomous mode where the endoscope is automatically steered toward the glottis. Switching between the modes is triggered by the user via a button. Both the joystick and the button are located on the front of the handle and can be operated by the user with the thumb while moving the whole device. This design ensures that the user is kept in charge of the procedure by having the possibility to manually control the tip motion at any moment.

The prototype of the device developed within the scope of this work integrates a customized, innovative design for the articulated section. This section consists of 24 interlocked segments cut from a 5.5 mm stainless steel rod using a micro-waterjet fabrication process. The outer diameter of the endoscope shaft is suitable for the positioning of standard TTs (6.5 to 9.0 mm inner diameter). The endoscope is steered by two pairs of

antagonistic pulling wires attached to an actuation unit comprised of two DC-motors (1000:1 HPCB 6V dual-shaft, Pololu Co.). A processing unit (Odroid-XU4, Hardkernel Ltd.) with a Linux OS (Ubuntu 18.04) generates the control signals for the motors in both modes, and detects the anatomical features within the camera image (MD-VBS20904L-120-01, Misumi Electronics Co.). The user inputs coming from the joystick are used as the reference signals for a PID velocity controller for the two bending directions of the endoscope. A visual servo-control approach [6] is implemented to minimize the distance between the image center and the centroid of the detected glottis, when the autonomous mode is triggered by the user. Both controllers are tuned to ensure a smooth and stable motion of the endoscope within the two operating modes. The maximum speed of the distal orientation is limited to 60 deg/s in order to provide ergonomic handling of the device.

The detection of the anatomical features is performed using Haar Featured-based Cascade Classifiers [7] implemented in Python using the OpenCV library [8]. Four key features depicted in Fig. 2 are detected, and the recognition training is performed using 500 to 700 positive images and 500 to 900 negative images for each feature.

A dedicated user interface depicted in Fig. 3 is displayed on an external monitor and is comprised of the tip camera image, the detected anatomical features, the state of the tracking, the configuration of the endoscope, and the activated mode. Two crosshairs are reported on the video feedback and represent the center of the glottis, and the center of the image. This latter is the target position of the glottis center in the autonomous mode. Depending on the detected anatomical features and the recorded history, general instructions are also given, e.g. “Move the device to the left”, “Go forward”.

RESULTS

The initial testing of the endoscope manual control was first performed in an open environment. The endoscope could be controlled in a stable manner without overshoot for orientations of up to 60° around its central axis and in all directions, which would be sufficient to perform a standard TI on a human patient.

When using the device to perform the TI on a manikin, the trachea was successfully entered using both operating modes and without prior training of the user in standard TI procedures. The autonomous mode could be used in the first stage of the procedure, i.e. right after the initial detection of the glottis, or when closer to the trachea, without further need to adapt the visual controller parameters. The anatomical features were detected at 200 Hz with the tip camera running at 30 fps, which is compatible with the required dynamic of the procedure.

When first inserting the device into the oral cavity, the corniculate cartilage and/or the posterior commissure of the larynx are encountered (Fig. 2A). When moving toward the larynx, the glottis should be detected (Fig. 2B). Successful intubation occurs when the tip of the device has entered the subglottic trachea after passing the vocal folds (Fig. 2C).

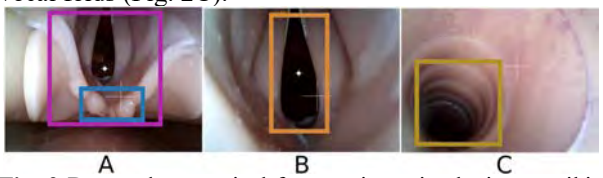

Fig. 2 Detected anatomical features in an intubation manikin along a TI with the REALITI device. A: Larynx (purple) and corniculate cartilage (blue), B: glottis, C: trachea.

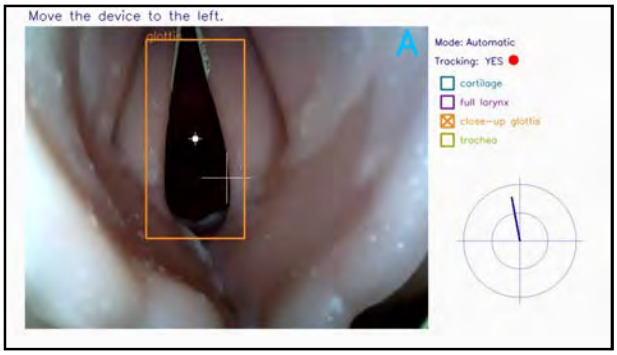

Fig. 3 User interface of the REALITI device. The state of the endoscope is represented as a line within a circular target indicating the azimuthal direction (angle of the line) and the amplitude of the direction (length of the line).

DISCUSSION

Our device is the first robotic endoscope dedicated to TI, which can assist the procedure by detecting features within the endoscopic image and by automated steering of the device toward the trachea. In this work, a prototype was developed to perform both manual and automated intubation on a training manikin. Results showed a distinct detection of the glottis and a stable motion in both modes. The relative performance of both modes, and the impact on the user of the general instructions displayed on the interface are to be investigated within proper study settings involving several users on pre-defined tasks.

The next steps will also include the development of a preclinical prototype for *ex vivo* testing and the implementation of the glottis detection on *in vivo* endoscopic images.

REFERENCES

[1] Thomas EBM, Moss S. Tracheal intubation. Anaesth Intensive Care Med 2017; 15: 5-7

[2] Apfelbaum JL et al. Practice guidelines for management of the difficult airway. Anesthesiology. Feb 2013;118(2):251-70.

[3] Pepe PE, Roppolo LP, Fowler RL. Prehospital endotracheal intubation: elemental or detrimental? Crit Care, 2015. 19: p. 121.

[4] Glick DB, Cooper R, Ovassapian A. (Eds.). (2012). The difficult airway: An atlas of tools and techniques for clinical management. Springer Science & Business Media.

[5] McCluskey K, Stephens M. Alternative techniques for tracheal intubation. Anaesth Intensive Care Med 2017; 18: 163-167

[6] Chaumette F, Hutchinson S. Visual servo control. II. Advanced approaches [Tutorial]. IEEE Robot Autom Mag, 2007 Mar;14(1):109-118.

[7] Viola P, Jones M. (2001). Rapid object detection using a boosted cascade of simple features. CVPR (1), 1, 511-518.

[8] OpenCV: Cascade Classifier Training. Retrieved from https://docs.opencv.org/3.4.3/dc/d88/tutorial_traincascade.html

Towards Robotic Cleft Palate Repair: Teleoperated Suturing with a 3mm Pin-Jointed Wrist on the da Vinci Research Kit

G.Wu[1,2], D.Podolsky[2], N.Hussein[1], M.Mikic[1,2], T.Looi[1], C.R.Forrest[2], J.M.Drake[1,2]

[1]*Center for Image Guided Innovation and Therapeutic Intervention, Sick Kids Hospital*

[2]*Institute of Biomaterials and Biomedical Engineering or Department of Surgery, University of Toronto james.drake@sickkids.ca* (DOI10.31256/HSMR2019.51)

INTRODUCTION

Cleft palate is a congenital anomaly that requires surgical repair. The procedure is technically challenging due to the small confines of the infant oral cavity and the reduced visualization and access. Surgical robotics offers a promising approach that improves visualization and provides increased dexterity in challenging small workspaces such as the infant oral cavity. The da Vinci Surgical System (dVSS) is the most widely adopted robotic surgical platform, yet the instruments are too large for the infant oral cavity [1]. A novel, miniaturizable, pin-jointed wrist mechanism that has a more compact articulation was proposed by Podolsky et al. in 2018 [2]. Here the mechanism has been further reduced in size to a functional 3mm diameter wrist as a more suitable instrument for infant trans-oral robotic surgery. The mechanism was evaluated in several teleoperation tasks to demonstrate the efficacy of the instrument.

MATERIALS AND METHODS

1. Design Updates, Fabrication and Set-up

A guide curve was incorporated in the centre of link-1 to balance the moments about the centre pin of link-1 (see Figure 1). Additionally, a backend mechanism was designed to mitigate cable slack caused by link-2 rotation (see Figure 2b). As link-2 pivots about joint-1, the path lengths of the link-3 cables changes since the cables are not passing through the centre of link-1. A mechanism utilizing specifically shaped cams was designed to compensate for the changing cable path lengths. The cams were coupled to link-2 and rotate as link-2 rotates, pushing on sliders to increase the backend cable pathlength by a distance equal to the change in the pathlength of the wrist (see Figure 2b and c).

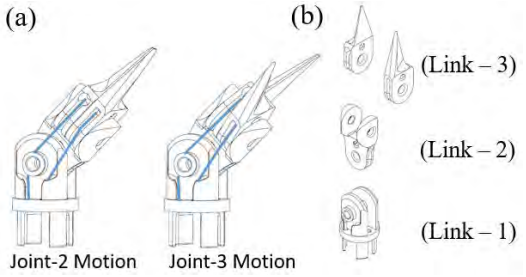

Figure 1. (a) CAD of new wrist with centre pivot (joint-1 motion is the rolling of the shaft, (b) exploded view of links.

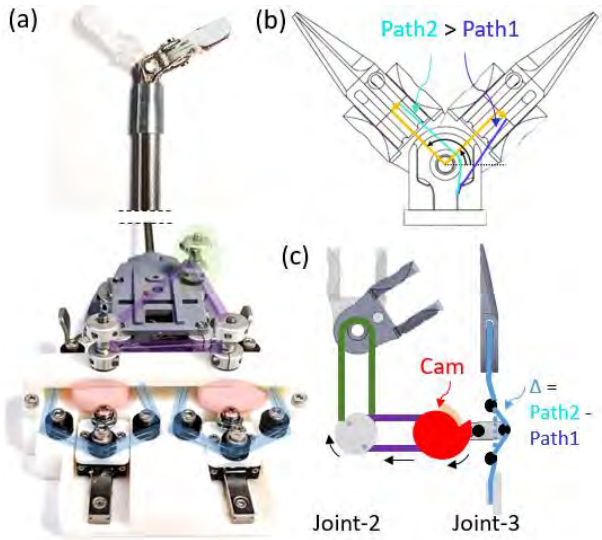

Figure 2. (a) Image of overall wrist and backend mechanism, (b) path change of drive cables (purple to aqua line) as the wrist pivots (yellow to yellow line), (c) concept diagram of backend cam mechanism

Links 1 and 2 were fabricated from stainless steel using direct metal laser sintering (DMLS). The link-3 gripper tips were 3D printed with SLA using Verowhite.

The da Vinci Research Kit (dVRK), an open-source customizable dVSS, was used to perform all teleoperated tasks [3]. The Deviant-Hartberg (DH) parameters were adjusted to match the wrist dimensions in the dVRK configuration files.

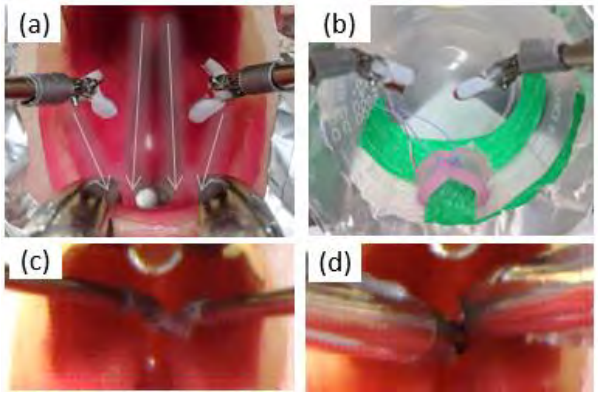

Figure 3. (a) Tracing task paths in cleft palate phantom, (b) completed suturing task, (c-d) sample images taken for pixel count at four key positions in the cleft palate (c) 3mm tools (d) 8mm tools

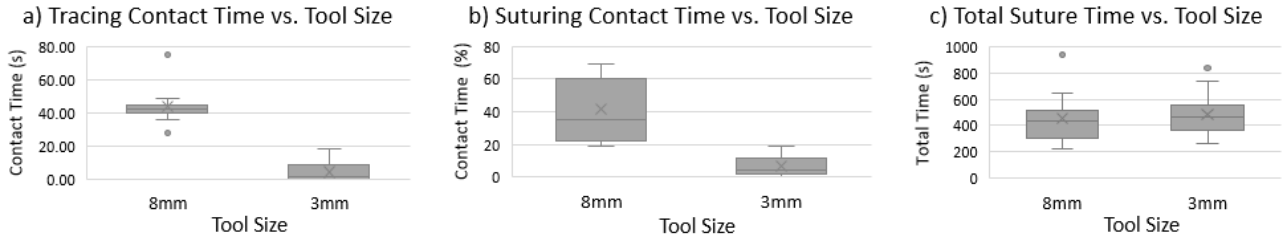

Figure 4. (a) Box plot of contact time during tracing cuts into cleft palate anatomy, (b) box plot of contact time percentage during suturing task, (c) box plot of overall time taken to suture.

2. Contact Time during Teleoperated Tasks

Collisions between the instruments and oral aperture can be dangerous, resulting in tissue trauma. During the two teleoperated tasks, the time that the tools were in contact with the oral aperture was measured. The oral aperture and the tools were lined with foil so that contact between the tools would result in a short circuit that could be measured with an Arduino.

2a. Tracing Task

Critical positions of the cleft palate were traced in a validated phantom [4] using the 3mm and 8mm instruments (see Figure a). The trace simulates incisions made on the hard and soft palate of the cleft.

2b. Suturing Task

The 3mm and 8mm instruments were used to suture a rectangular piece of silicone (30x7x1mm, Ecoflex 20 – the same material utilized in the cleft palate phantom) to form a loop (see completed suture in Figure b) all within a 30mL medicine cup. 4-0 polyglactin suture of length 50mm was used and two knots were tied. The cup, which is smaller than the cleft palate workspace, was used to simulate working within a confined area. This simulation mirrored the closure of the palatal mucosa and the difficulties of working near the edges of the workspace. The task was completed five times for each of the 8mm and 3mm instruments by both a cardiac and plastic resident who are trained surgeons.

3. Pixel Count

ImageJ (NIH) was used to trace and count the pixels of the obstructed portion of the field of view (area occupied by the instruments) to assess the difference in visualization when using 8mm versus 3mm instruments. To obtain the images, the instruments were placed at four key positions within a cleft palate phantom and a screenshot of the camera view was taken (see Figure 3c and d for sample images).

RESULTS

The contact times for the 8mm versus 3mm instruments for the tracing task (2a) and suturing task (2b) are shown in figure 4a and 4b, while 4c shows the overall time taken to suture. No statistical analysis was performed due to the low trial count (n = 10) for this pilot data. From a qualitative assessment of the boxplots, the 3mm instruments had less contact time than the 8mm instruments for the both the tracing and suturing tasks (Fig 4a and 4b), but it took approximately the same time to complete the suturing task with the 3mm instruments. Furthermore, it is clear from figure 5 that the view is less obstructed with the 3mm tools.

DISCUSSION

The ability of this 3mm wrist mechanism to compactly articulate and perform a complex surgical task such as suturing is demonstrated by the reduced collision time within a small workspace. Furthermore, the smaller instruments provided a less obstructed view that improves visualization.

Using the 3mm instruments increased the time taken to perform the suturing task due to several manufacturing and set-up issues listed below.

1. Unnecessarily large gripper size due to brittle 3D printed material that would otherwise easily break.
2. Pins that protrude from the wrist catching on the suture.
3. Instruments colliding with the camera system as it is much wider than a true dVSS endoscope.

Future work would address these limitations and also include the development of various end effectors (i.e. blunt dissector, suction, scissors/scalpel), to evaluate the instruments in a full cleft palate repair. Overall, the wrist mechanism proposed allows further miniaturization and more compact articulation that results in improved visualization and reduced collisions within small workspaces and is a more suitable design for infant oral cavity surgery compared to existing instruments.

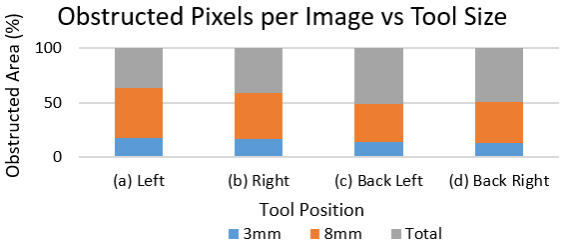

Figure 5. Stacked bar graph showing obstructed area

REFERENCES

[1] N. Nadjmi, "Transoral robotic cleft palate surgery," *Cleft Palate-Craniofacial J.*, vol. 53, no. 3, pp. 326–331, 2016.

[2] D. Podolsky *et al.*, "A Dexterous 3-DOF Surgical Wrist for Compact Articulation Using Cable Guide Channels," *J. Med. Device.*, no. c, pp. 1–43, 2018.

[3] P. Kazanzidesf, Z. Chen, A. Deguet, G. S. Fischer, R. H. Taylor, and S. P. Dimaio, "An open-source research kit for the da Vinci Surgical System," *Proc. - IEEE Int. Conf. Robot. Autom.*, pp. 6434–6439, 2014.

[4] D. Podolsky, D. M. Fisher, K. W. Wong, T. Looi, J. M. Drake, and C. R. Forrest, "Evaluation and Implementation of a High-Fidelity Cleft Palate Simulator," *Pediatric/craniofacial*, vol. 139, no. 1, pp. 85–96, 2016.

Prototype Designs of a Cable-driven Parallel Robot for Transoral Laser Surgery

M. Zhao, T.J.C. Oude Vrielink, A.A. Kogkas, D.S. Elson, G.P. Mylonas
Department of Surgery and Cancer, Imperial College London
m.zhao15@imperial.ac.uk (DOI10.31256/HSMR2019.52)

INTRODUCTION

Transoral laser surgery is a commonly used method in which a laser beam is used to perform vaporization, incision, ablation, or photocoagulation of the hypopharynx and larynx tissues, for example, the vocal cords tissue. Two techniques are commonly practised; *free beam* and *fibre* delivery. Free beam delivery uses an articulated suspension arm to transmit the laser to a laser micro-manipulator, which reflects the beam to the target tissue via optical lenses and mirrors. The distance between the laser aperture and the target tissue is about 400 mm. In contrast, the fibre delivery technique uses a flexible optical fibre to transmit the laser beam, and the maximum distance of the end tip of the fibre to the tissue is only a few millimetres.

In the free beam delivery technique, a galvanic mirror-based laser beam scanner is integrated on the laser micromanipulator. The laser scanner allows patterns such as straight lines, arcs and circles to be projected on the target tissue. Accurate laser scanning improves surgical outcome by removing diseased tissue while preserving non-targeted areas. Additionally, operation times are reduced, and thermal damage is limited. However, the scanning laser beam can only be used under direct line of sight, and a rigid straight suspension laryngoscope is needed during surgery to create a direct working channel for the laser beam. This can be uncomfortable for the surgeon during prolonged operations, the manipulability is poor and extensive training is required. Furthermore, suspension laryngoscopy may lead to surgical cervical vertebrae and dental arch lesions and postoperative pain.

In contrast, fibre delivery transoral laser surgery overcomes the limitation of the direct line of sight, and a suspension laryngoscope is not necessary. The laser fibre tip can be controlled by a hand-held surgical instrument or teleoperated surgical robot arm. This can only achieve manual level accuracy, repeatability and velocity and does not allow for automated laser scanning. Recently, a robotic-assisted transoral laser surgery system, μRALP, was developed [1], which incorporates a micro-fabricated laser deflecting mechanism on the distal tip of a semi-flexible endoscope robotic system. Another system relies on a magnetic laser scanner [2]. Both systems are currently at the pre-clinical stage.

ESD CYCLOPS [3, 4] is a cable-driven parallel surgical robot currently undergoing pre-clinical validation in advanced GI techniques. Here, a transoral robotic surgery (TORS) system based on the same concept of the CYCLOPS is presented. This is based on a cable-driven parallel mechanism (CDPM) used to manipulate the tip of a flexible laser fibre. This is achieved by thin cables connected to a fibre-accommodating over-tube, which like string puppets achieves movement of the laser fibre in space. Unlike serial mechanisms, parallel approaches do not suffer from errors accumulating through the kinematic chain and are expected to allow accurate laser scanning. The CDPM can be attached at the end of a flexible endoscope or a curved laryngeal blade, obviating the need for a suspension laryngoscope. Therefore, this approach has the promise to overcome the limitations related to the line of sight and perform pattern or free scan paths. In this paper two prototype designs are introduced for TORS: an endoscope-based system (endoTORS) and a laryngoscope-based (laryngoTORS).

MATERIALS AND METHODS

A robot mechanism for transoral surgery was designed and fabricated, composed of two parts: the cable-driven parallel manipulator and the control system. The CDPM includes a scaffold, cables inserted through small openings positioned around the scaffold, and two instrument-accommodating over-tubes. The shape of the scaffold is a hollow cylinder (20 mm diam., by 20 mm long). Size and shape can be changed based on patient-specific data and operational needs. Two over-tubes are used, one for controlling the position of the laser fibre and the other for a surgical instrument, such as forceps. Each over-tube is driven by 6 cables and each of the cables is connected to a remote servomotor. This allows the over-tube assemblies to be controlled in five degrees of freedom (DoF); three translations, yaw and pitch.

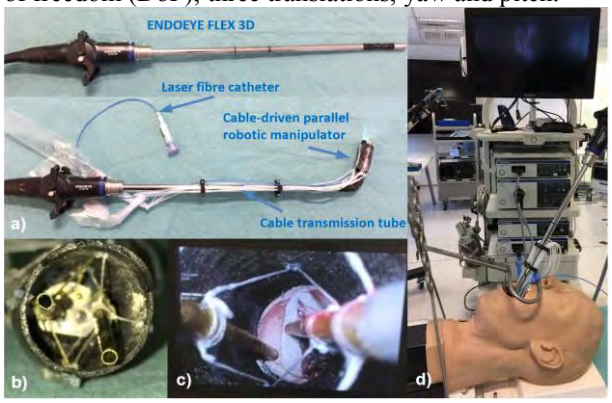

Fig. 1 Early prototype of the endoTORS. a) The robot mechanism assembled on a tip-articulating endoscope. b) Front view of the robot showing the scaffold, cables and over-tubes. c) Endoscopic view of the robot scaffold. d) The setup of the endoTORS robot on a head and neck phantom. A mouth gag is used to keep the mouth open.

The laser fibre (FiberLase CO_2, Lumenis Ltd., Israel), being cylindrical, does not require a 6th (roll) DoF. If required by the surgical instrument, the roll can be achieved by an external motor to rotate a torsionally stiff flexible instrument. Opening and closing of the grasper are also achieved by retrofitting an external motor with its handle. Twelve brushless DC motors (1226S012B, Faulhaber, Germany) and an EtherCAT controller (MC 5004 P, Faulhaber, Germany) are used to control the bimanual system. Motor control could be achieved in teleoperation mode using a pair of haptic manipulators (Geomagic Touch, 3D Systems, USA), or programmatically from a connected computer.

Fig. 1 shows an early prototype of the endoTORS system. The CDPM is attached to the articulated tip of an endoscope. The distal diameter outer end of the endoscope is 10 mm and the angulation range is 100 degree in four directions (ENDOEYE FLEX 3D, LTF-190-10-3D, Olympus, Japan). This allows the robotic end-effector to move with the endoscope.

Fig. 2 shows the prototype of the laryngoTORS system. Like commercial video laryngoscopes (Fig. 2a), the CDPM was built on a curved laryngeal blade (Fig. 2c-d). The curve angle can be defined based on patient-specific data. The robot position can be fixed by means of an adjustable and locking supporting arm after the desired positioning has been achieved (Fig. 2e-f). A miniature camera is used for visualisation.

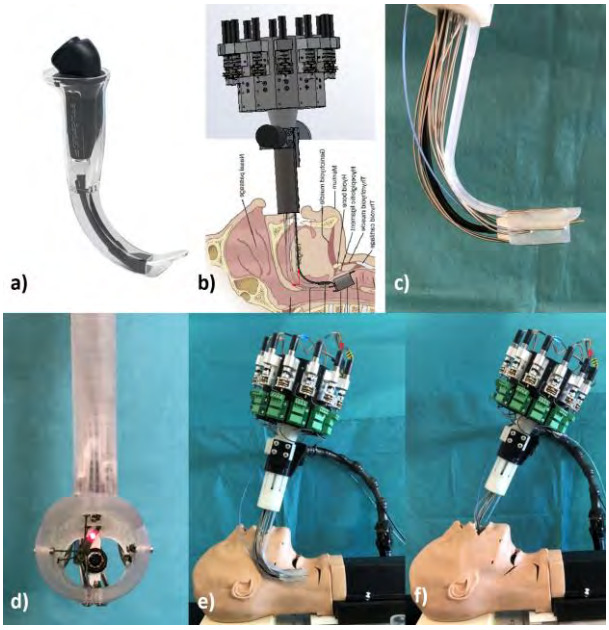

Fig. 2 a) An example of a video laryngoscope (GlideScope Video laryngoscope, Verathon, Inc., USA). b-d) The design and prototype of the laryngoTORS system. e-f) Demonstration of the operational position of the robot, based on a head and neck phantom.

RESULTS

Testing using a silicone head and neck phantom showed that both systems – endoscope-based and laryngoscope-based – were able to access and expose the epiglottis, glottis and vocal folds. For the preliminary validation of the two designs, a simulated incision path –shown in Fig. 3a as a red arc line with dimensions 8x2 mm– was manually traced via a master manipulator. The root mean square error (RMSE) and the maximum absolute error (MAE) are 0.11 ± 0.08 mm and 0.20 mm respectively.

Computer generated and automatic straight and arc line pattern scans were performed by the laryngoTORS system. The fibre projects a red aiming beam. Using MATLAB, the trajectory of the aiming spot centroid was tracked and compared with the predefined scan patterns. The experimental results are shown in Table 1

Table 1: Experimental results of pattern scans performed by the laryngoTORS.

Experiments	RMSE (mm)	MAE (mm)
Straight line (6 mm), 6 times	0.12± 0.07	0.40
Arc line (6x1.5 mm), 6 times	0.10± 0.06	0.49

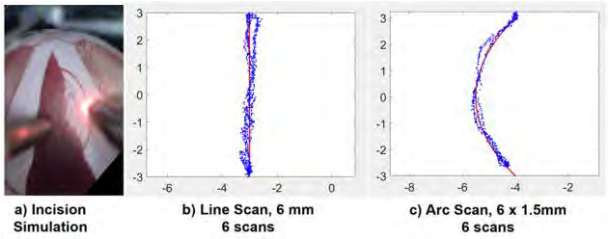

Fig. 3 a) An example of the incision path tracing test performed here with the endoTORS system. b-c) The experimental results of the automatic pattern scan performed by the laryngoTORS robot.

DISCUSSION

Both systems can overcome the limitations of the line of sight. The endoTORS system is currently based on the size specifications of the directional tip of ENDOEYE FLEX 3D endoscope, where bending point and tip length are fixed. This can introduce certain restrictions but does not invalidate the ability of the robot to be customised on patient-specific data. In contrast, the laryngoTORS is fully customisable. Visual servoing control and semi-autonomous task performance are under development.

REFERENCES

[1] Lescano S, Zlatanov D, Rakotondrabe M, Andreff N. Kinematic analysis of a meso-scale parallel robot for laser phonomicrosurgery. In Interdisciplinary Applications of Kinematics 2015 (pp. 127-135). Springer, Cham.

[2] Acemoglu A, Mattos LS. Magnetic laser scanner for endoscopic microsurgery. In2017 IEEE International Conference on Robotics and Automation (ICRA) 2017 May 29 (pp. 4215-4220). IEEE.

[3] Mylonas GP, Vitiello V, Cundy TP, Darzi A, Yang GZ. CYCLOPS: A versatile robotic tool for bimanual single-access and natural-orifice endoscopic surgery. In2014 IEEE International Conference on Robotics and Automation (ICRA) 2014 May 31 (pp. 2436-2442). IEEE.

[4] Vrielink TJ, Zhao M, Darzi A, Mylonas GP. ESD CYCLOPS: A new robotic surgical system for GI surgery. In 2018 IEEE International Conference on Robotics and Automation (ICRA) 2018 May 21 (pp. 150-157). IEEE.

Challenges of Autonomous Robotic Surgery

P. Fiorini, D. Dall'Alba, M. Ginesi, B. Maris, D. Meli, H. Nakawala, A. Roberti, E. Tagliabue

Department of Computer Science, University of Verona (Italy)
paolo.fiorini@univr.it (DOI10.31256/HSMR2019.53)

INTRODUCTION

The possible addition of autonomous functions to robotic devices is fueling an intense debate on their impact on work and daily activities. Two classifications of autonomy have been proposed for the fields of self driving cars [1] and surgical robots [2] with six levels:

0	No Autonomy/Automation during the task
1	Assistance to the operator during the task
2	Partial automation on executing single acts
3	Supervised plan/execution of act sequences
4	Unsupervised plan/execution of a full task
5	Plan/execution of full task

However, the discussion is mostly focusing on aspects that are far in the future, neglecting to address the specific difficulties and benefits of reaching the lower levels of autonomy. In fact, reaching autonomy level 1 would already imply that the system has enough perception and reasoning to understand the situation and give useful advice to the operator. In level 2, the system will be capable of task-level autonomy, thus the initial two levels set the foundations that will support the full autonomy stack. In this paper we present our efforts to associate robot motions to their semantic meanings by developing a hybrid cognitive framework to support task understanding, i.e. learn a specific motion, provide its semantic interpretation and execute it within a task.

MATERIALS AND METHODS

The quest of a cognitive architecture for robots goes back to the early days of robotics [3] and still produces new results, e.g. the I-SUR (Intelligent Surgical Robot) framework [4]. However, the integration of *a priori* knowledge with experimental data is still an open question. Here, we represent *a-priori* knowledge with an ontology and robot motions with a *Finite State Machine* (*FSM)* in the context of a peg-and-ring task [5]. We chose this task because is a standard training exercise for robotic surgery and could be used as an early benchmark for autonomous surgical robots.

Figure 1 shows the framework four main components as green rounded rectangles. The *FSM* represents the model of the peg-and-ring task learned from experimental data. *Ontology* represents the a-priori knowledge, used for high-level task planning and reasoning. *Vision* performs segmentation and tracking of objects, i.e. pegs, rings and the table. *Dynamic Motion Primitive (DMP)* describes the end-effector trajectory within each state of the *FSM*. The overall framework is implemented in Robot Operating System

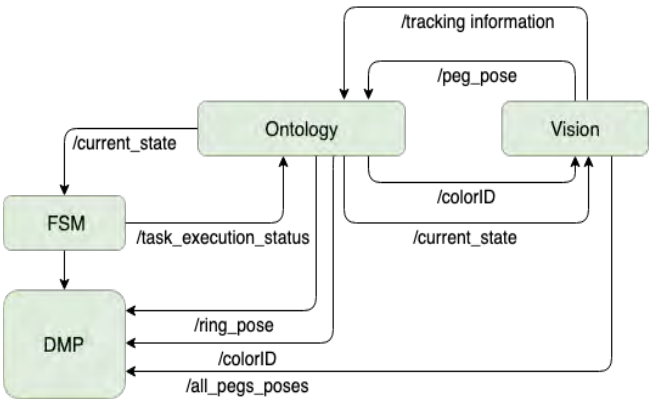

Fig. 1: A knowledge-based architecture for task execution.

(ROS). The labels on the directed arrows show ROS topics and data flow between the framework components: *colorID* represents the element ID's; *peg pose* and *ring pose* represent their poses; *all pegs poses* contains all poses; *current state* shows the state inferred by ontology; *task execution status* contains the status of the action; *tracking information* contains status of ring tracking. The ontology encodes the semantic knowledge about the task and the *FSM* represents the different motion controllers.

Motion controllers are learned using the Dynamic Movement Primitives (*DMPs*) approach [6] that generates a point-to-point trajectory by solving the following second order Ordinary Differential Equation (ODE) of spring-mass-damp type:

$$\tau \dot{v} = K(g - x) - Dv - K(g - x_0)\, s + Kf(s)$$

$$\tau \dot{x} = v$$

where: x and v are the trajectory and its velocity, respectively, x_0 and g are the starting and goal position, $\mathbf{K}$ and $\mathbf{D}$ are the elastic and damping matrix, and f is a forcing term, which depends on a re-parametrization of the time governed by the so-called canonical system:

$$\tau \dot{s} = -\alpha s; \quad \alpha > 0$$

The matrices $\mathbf{K}$ and $\mathbf{D}$ are chosen to be diagonal, in order to separate the evolution of the solution along each dimension, and such that the system is critically damped $(K_{i,i} > 0\,,\, D_{i,i} = 2\sqrt{K_{i,i}})$.

We employ this method because the trajectory can be learned from a single instance of a motion and can be generalized to multiple instances. Furthermore *DMP* trajectories adapt to new starting and goal positions and to changes in the environment at execution time.

Clearly, this task is very different from an anatomical environment and to address realistic surgical tasks we are developing new computational models and

localization methods for the instruments.
Since living tissues are highly deformable, it is necessary to model their response to the mechanical interaction with the robot. Realistic models of soft tissues are usually developed with the finite element method (*FEM*) [7]. *FEM* describes the tissues as continuum media and determines their future positions by solving physical balance laws, trading high accuracy for high computation cost. Since this makes them non real-time compatible, we use geometry-based approaches, e.g position-based dynamics (*PBD*), to model objects as an ensemble of particles whose positions are updated, as a solution of a quasi-static problem subject to geometrical constraints [8].
Because of the deformable environment, standard localization methods, e.g. Simultaneous Localization and Mapping (SLAM) cannot be applied directly to command instrument motions, landmark tracking must replace identification to localize the instruments [9]
A-priori knowledge is not sufficient to capture all the aspect of an intervention, and data collected with da Vinci Research Kit (dVRK) are not very representative of surgical tasks. Thus we are starting to analyze real clinical data to extract task structure, by integrating Deep Learning techniques [10] with a-priori knowledge, e.g. ontologies, to reduce training time and dependency on data set annotation.

RESULTS

Figure 2, shows an example of the peg-and-ring task using the proposed cognitive architecture. The actions of peg reaching, grasping and moving to destination are learned by generalizing the *DMP* execution of three separate actions, one per color. The position of the rings on the table are randomly set and the *DMP* module adapt the trajectory parameters to the current ring and peg locations. The pre- and post-conditions of each action are verified by the ontology module, that also checks the validity of the sensory data. The nominal motion was learned without obstacles, while the executed trajectories accounts for the presence of obstacles, without explicit programming. Learning requires only a few task repetitions and is very fast. Because of this method generality we ported the peg-and-ring task to the dVRK without major efforts.

DISCUSSION

The main goal of this research is to make the robot understand, i.e. be aware of, its own actions and, in our approach, we define "task understanding" as task explanation by ontology rules identification. We define a hybrid cognitive architecture where rules represent the discrete (or logical) state of the task while motion control, i.e. the continuous, time-driven, part of the task, are implemented using the *DMP* paradigm. Motions can be abstracted and adapted to different anatomical situation, without changing the logical task structure. Each motion is described by a *DMP* with a specific set of parameters that can represent its semantic meaning. Thus the robot can learn a motion, represent it with an abstract concept, e.g. a suture, and adapt it to a specific

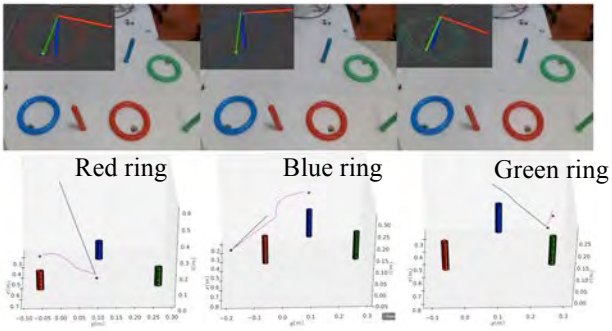

Fig. 2: End effector trajectories grasp and obstacle avoidance in different settings.

case, all within the ontology and DMP hybrid anatomy. In the future, the robot will learn the environment model, use it to localize its instruments in the anatomy and learn from the data how to interact with the tissues. These elements will help us map a generic surgical task to a specific patient situation.

ACKNOWLEDGMENT

This research is funded by the European Union's Horizon 2020 research and innovation programme (grant agreement No 742671 "ARS" and No 688188 "MURAB").

REFERENCES

[1] https://web.archive.org/web/20170903105244/https://www.sae.org/misc/pdfs/automated_driving.pdf
[2] G.-Z. Yang, J. Cambias, K. Cleary, et al., Medical robotics—Regulatory, ethical, and legal considerations for increasing levels of autonomy. Sci. Robot. 2, eaam8638 (2017).
[3] P. Fiorini and J. Chang, Autonomous Organization of Grasping Tasks , SPIE Symposia on Aerospace Sensing, Artificial Intelligence VII, Orlando, FL, March 27- 31 1989, pp. 591-602.
[4] R. Muradore, P. Fiorini, et al., Development of a Cognitive Robotic System for Simple Surgical Tasks , Int J Adv Robot Syst, 2015, 12:37, doi: 10.5772/60137.
[5] M. Ginesi, D. Meli, H. Nakawala, A. Roberti, P. Fiorini, A knowledge-based framework for task automation in surgery, IEEE RA Letters (under review)
[6] H. Hoffmann, P. Pastor, D.-H. Park, and S. Schaal, Biologically inspired dynamical systems for movement generation: automatic realtime goal adaptation and obstacle avoidance, IEEE Int. Conf. 2009 on Robotics and Automation, pp. 2587–2592.
[7] Zhang J, Zhong Y, Gu C (2018) Deformable models for surgical simulation: A survey. IEEE reviews in biomedical engineering 11:143–164
[8] E. Tagliabue, D. Dall'Alba, E. Magnabosco, C. Tenga, I. Peterlik, P. Fiorini, Position-based modeling of lesion displacement in Ultrasound-guided breast biopsy CARS 2019 (under review)
[9] M. Carletti, M. Cristani, D. Dall'Alba, and P. Fiorini, A Robust Particle Filtering Approach with Spatially-Dependent Template Selection for Medical Ultrasound Tracking Applications, VISAPP 2016.
[10] Nakawala, H., Bianchi R., Pescatori L.E., et al. "Deep-Onto" network for surgical workflow and context recognition, Int J. CARS (2019) 14:685-495.

Hand-held stiffness measurement device for tissue analysis

*T. A. Zodage[1], A. N. Chaudhury[2], R. A. Srivatsan[2], N. Zevallos[2] , H. Choset[2]

[1] Mechanical Engineering, BITS Pilani,

[2] Robotics Institute, Carnegie Mellon University

*tzodge@gmail.com (DOI10.31256/HSMR2019.54)

INTRODUCTION

We develop a novel means of detecting tumors to better assist in early detection of cancer. Several conventional methods such as MRI or CT scans detect tumors, but these methods are time consuming -- taking around 20-90 minutes, need expertise to handle the machines and are less affordable in lower income settings [3]. Due to the cost and time involved in these methods, surgeons use palpation techniques for preliminary tests on superficial tumors on the breast, tongue or the prostate. Physicians typically palpate the tissue manually to get a qualitative estimate of stiffness [4]. As these palpation techniques are qualitative, the diagnosis depend on the expertise of the doctors investigating a particular case. The qualitative nature of the estimation makes it difficult to keep records of the tissue stiffness and analyze it over time.

To quantitatively interpret palpation, researchers have worked towards developing devices for tissue stiffness measurement. Fischer [4] was one of the first to devise tissue compliance meter to quantitatively investigate soft tissue consistency. Arokoski et al. [5] and Oflaz [6] measured the tissue's resistance to a deforming force as a measure of stiffness for a constant, preset indentation depth. The use of a constant length probe in [5] and [6] limits the range of stiffness which can be measured. Jalkanen et al. [7] suggested measurement of resonance frequency piezo crystal in contact with the tissue to estimate the stiffness of the underlying tissue. However, this only gives information about the local stiffness, but not the location of the point of investigation. Nguyen et al. [3] suggested the use of tactile photoelastic films to quantify the location and shape of the tumours. These techniques involve complex setup and specialized hardware.

Taking these issues into account, this work presents a stiffness measuring device which uses a simple setup using a monocular camera [9] along with a commercial force sensor. In addition to measuring the stiffness at a point, our device also generates a map of the stiffness distribution over the surface of the tissue. This makes it easier to visualize the shape and size of the tumor (refer to Fig. 1) compared to [4], [5], [6]. Since we do not need to use a constant length indenter as [5] our device gives a wider range of operation. In order to test our device, we perform experiments on silicone tissue phantoms embedded with stiff inclusions.

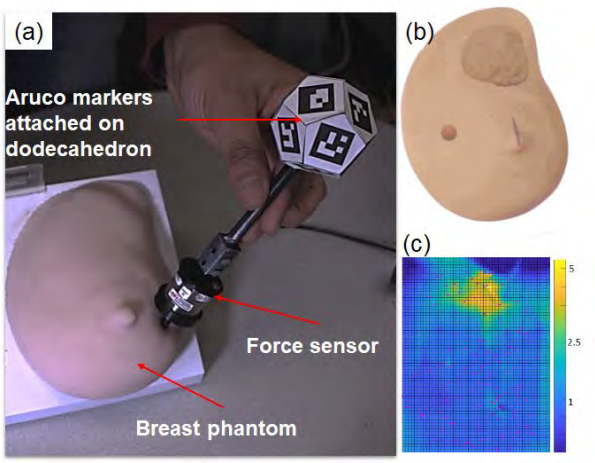

Fig. 1 (a) Our device with position sensing at the top and a force sensor at the tip. (b) Approximate location and shape of the tumors in breast phantom (c) Stiffness map generated using our device shows a stuff region in the top of the breast.

We also provide qualitative (stiffness map images) and quantitative (RMS error in stiffness) comparison results of our method to a ground truth generated using an industrial robotic arm.

MATERIALS AND METHODS

The position sensor is inspired from a recent work by Wu et al. [9] on a 6 degrees of freedom (DoF) tracking pipeline for a passive stylus for mixed reality applications. The method uses a 3D printed fiducial of known geometry (a dodecahedron of 2 cm side length in this case) with binary square markers (we used ArUCo markers [9]) glued to the faces, as shown in Fig. 1(a). The 6 DoF pose of the stylus is inferred by imaging the fiducial with a monocular machine vision camera (we used a Point Grey Chameleon3 camera with a Fujinon 2.8mm-8mm/f1.3" lens) and refining the pose estimate by performing two unconstrained minimization steps. The first step minimizes the reprojection error of the marker corners for the pose estimate and the second step minimizes the appearance distance (difference between observed and expected image intensities) to further refine the estimate on the pose. In our experiments, we achieved a worst case position error of 0.4 mm.

For the force sensor, we use a commercial 6 DoF force torque sensor (ATI nano 25E). We fabricated a tissue phantom by embedding a hard plastic of unknown shape in a silicone specimen (Smooth-on EcoFLEX-20) of dimensions 10cm x 10cm x 2cm.

EXPERIMENTS AND RESULTS

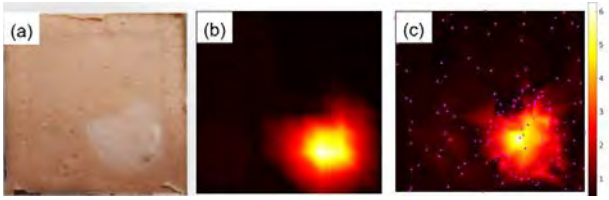

Fig. 2 (a) Flat tissue phantom with embedded plastic tumor. (b) Ground truth stiffness map generated using industrial robot arm (c) Stiffness map generated using our device. (Pink points shows probing locations)

The tissue phantom was manually palpated at 150 points at approximately uniform intervals and the visual and the force data were logged in real time. A threshold force was estimated by placing the probe in contact with the organ. The readings of position and force sensor were recorded. The stiffness at a point was calculated when the force measured by the force sensor was above the threshold force. For each indentation, we calculated the slope of force vs displacement of the indentation point, to obtain the local stiffness. This data was used to interpolate the stiffness information of the surface in between two indentation points [8].

To generate the ground truth stiffness map, we repeated the probing experiment using an industrial robot arm attached with the same force sensor. The tissue sample was probed at 100 points in a raster scan pattern. The stiffness map generated using our device was found to be similar to that of the ground truth (see Fig. 2 (b) , (c)).

In order to calculate the error in the stiffness, We selected a grid of 20x20 points at approximately same position on the ground truth and the stiffness map generated using our device. The root mean square error in stiffness was 0.86 N/mm. Work is currently underway to improve the bounds on the measurement errors.

As an edge usage, we demonstrate our device to obtain surface geometry of organs. Since generating point clouds for tissues is challenging using vision-based sensors, we use our probe to perform contact based geometry estimation. We show a 3D surface map of a kidney phantom, generated using our device in Fig. 3.

DISCUSSION

This work demonstrates the development of a hand held device for quantitative and qualitative estimation of stiffness over the surface of a tissue sample. In addition to finding the stiffness map, we also demonstrate the use of this device to find the geometry of an organ surface. Since our device uses a combination of position and force sensing, it does not require prior knowledge of stiffness range of the

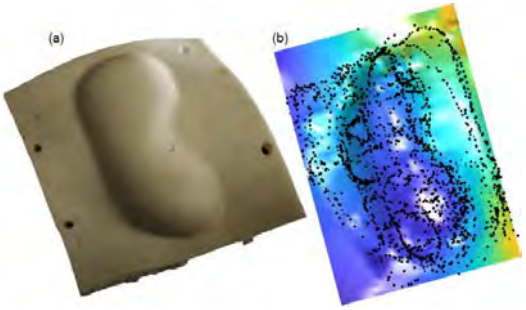

Fig. 3 (a) Kidney phantom. (b) 3D map of kidney phantom generated using our device. (Black points show tip contact locations)

organ, unlike most prior devices. As a result, our device can be used for soft organs such as the breast as well as stiffer organs such as the kidney (Fig. 1, Fig. 3).

An important benefit of our device is the low cost. However, the use of an industrial force sensor slightly offsets this benefit. As future work, we plan to integrate an inexpensive and light-weight, miniature force sensor developed in our previous work [10]. We also plan to perform tests on ex-vivo and live tissues to obtain better understanding of the problems that might arise in real world situations. Currently we process the data offline, however, future work will address this by using a C++ implementation of the pipeline for realtime tip tracking.

REFERENCES

[1] "What You Need to Know About Brain Tumors", NIH Publication No.09-1558, 2009.

[2] H. C. McLane, A. L. Berkowitz, B. N. Patenaude, E. D. McKenzie, E. Wolper, S. Wahlster, G. Fink, and F. J. Mateen, "Availability, accessibility, and affordability of neurodiagnostic tests in 37 countries"

[3] C. V. Nguyen, and R. F. Saraf. "Tactile Imaging of an Imbedded Palpable Structure for Breast Cancer Screening." ACS Applied Materials & Interfaces 6.18 (2014): 16368–16374. PMC. Web. 1 Aug. 2017.

[4] A. A. Fischer,"Tissue compliance meter for objective documentation of soft tissue consistency and pathology" Arch. Phys. Med. Rehabil., 1987, 68, 122-5.

[5] J. P. A. Arokoski, J. Surakka, T. Ojala, P.i Kolari and J. S. Jurvelin "Feasibility of the use of a novel soft tissue stiffness meter", 2005 Physiol. Meas. 26 215

[6] H. Oflaz, "A new medical device to measure a stiffness of soft materials" Acta of bioengineering and biomechanics" Wroclaw University of Technology 16(1):125-31 · April 2014

[7] V .Jalkanen, B.M.Andersson and O.A.Lindahl "Stiffness of a small tissue phantom measured by a tactile resonance sensor" IFMBE Proceedings, 2010.

[8] N. Zevallos, R. A. Srivatsan, H. Salman, L. Li, J. Qian, S. Saxena, M. Xu, K. Patath, H. Choset," A real-time augmented reality system for overlaying stiffness information", RSS 2018

[9] Po-Chen Wu *et.al.*, "DodecaPen: Accurate 6DoF Tracking of a Passive Stylus" ,UIST 2017,October 22–25, 2017, Quebec City, QC, Canada.

[10] L. Li, B. Yu, C. Yang, P. Vagdargi, R. A. Srivatsan and H. Choset, "Development of an inexpensive tri-axial force sensor for minimally invasive surgery", IROS proceedings, 2017

Admittance control of a handheld microsurgical instrument

G. Russo[1], S. Moccia[2,3], J. N. Martel[4], A. Perin[5], R. F. Sekula[6], L. Bascetta[1], E. De Momi[1], C. N. Riviere[7]

[1]*Dept. of Electronics, Information and Bioengineering, Politecnico di Milano, Milan, Italy*
[2]*Department of Advanced Robotics, Istituto Italiano di Tecnologia, Genoa, Italy*
[3]*Department of Information Engineering, Università Politecnica delle Marche, Ancona, Italy*
[4]*Department of Ophthalmology, University of Pittsburgh, Pittsburgh, USA*
[5]*Besta NeuroSim Center, IRCCS Istituto Neurologico C. Besta, Milan, Italy*
[6]*Department of Neurological Surgery, University of Pittsburgh, Pittsburgh, USA*
[7]*The Robotics Institute, Carnegie Mellon University, Pittsburgh, USA*
camr@ri.cmu.edu (DOI10.31256/HSMR2019.55)

INTRODUCTION

The current state of the art in neurosurgery for deep-seated brain tumors and cerebrovascular lesions still yields high postoperative rates of cerebral infarction and cranial nerve deficits. In particular, petroclival meningioma resection is one of the most challenging and risky procedures: reported rates of permanent cranial nerve deficits range from 20% to 76%, while the rate of gross total resection ranges from 20% to 85% [1]. Robotics has potential to reduce morbidity and mortality by performing assistive functions such as reduction of unwanted motion and minimization of force applied to nerves and vascular structures.

Handheld robotic instruments for neurosurgery may offer advantages in terms of cost and ease of use compared to other approaches such as teleoperated or shared-control robots [2]. This paper describes a method for minimization of force applied by an active handheld robotic micromanipulator known as Micron [3]. Wells et al. [4] previously presented a method for parallel position/force control of Micron. As an alternative approach with a clearer physical interpretation, this paper presents an admittance control approach [5] that modifies the setpoint of the position control to minimize applied force, and demonstrates the approach in an artificial simulation of neurosurgical blunt dissection.

MATERIALS AND METHODS

Robotic Instrument

Micron is an actively handheld surgical tool composed by a miniature Gough-Stewart platform attached between the end-effector and a cylindrical handle (Fig. 1). The position control, which considers the human presence in the loop, actuates the end effector to provide functions such as physiological tremor compensation, virtual fixtures, or force control.

A Fiber Bragg Grating force sensor with two degrees of freedom [6] was embedded in the end-effector of Micron. To emulate a force sensor with three degrees of freedom, the sensor was augmented with a load cell mounted underneath the workpiece; load cell data were fused with the onboard sensing to obtain the force parallel to the long axis of the instrument.

Fig. 1 Micron, an active handheld microsurgical instrument.

Admittance Control

The inputs to the admittance control are the set-point of the position loop and the force measurements. Then the control provides an updated set-point for the position loop (Fig. 2). The main goal is to modify the set-point of the position control with the aim of reducing the applied force: when no force is acting on the manipulator, there is no force feedback and the position control should fit the desired trajectory. When an external force is present, the controller changes the position in accord with the selected mass-damper-spring dynamics.

Since microneurosurgical tasks generally involve small velocities and very small accelerations, the virtual mass coefficient is set to zero. The environment has low stiffness, so contact stability can be easily achieved [5]. Hence, decoupling the admittance control for each direction, we get the following dynamics (Figs. 2, 3):

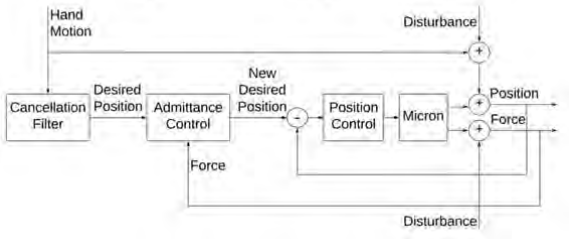

Fig. 2 Complete position and admittance control block diagram of Micron.

$$d\,(\dot{x}_d - \dot{x}_a) + k\,(x_d - x_a) = f \qquad (1)$$

where d and k are the virtual damping and virtual stiffness coefficients, f is the external applied force and $(x_d - x_a)$ is the desired position change. The parameter values, selected by manual tuning, are:

$$m = 0 \quad mN/(m/s^2)$$
$$d = 10 \quad mN/(m/s)$$
$$k = 0.02 \quad mN/m$$

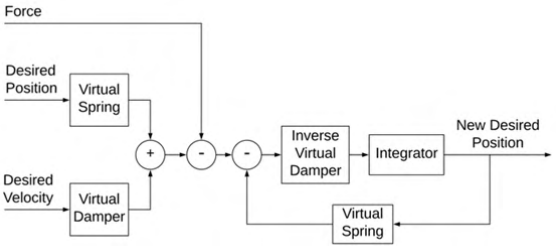

Fig. 3 Admittance control block diagram with one degree of freedom.

Experiment

The method has been tested under a board-approved protocol in a blunt dissection experiment with a human in the loop. Sorbothane® rubber was chosen as an underlying substrate due to its tissue-like properties [7]. On each rubber workpiece, to enable a simulation of blunt dissection, 10 circles of polyethylene film (12.7 μm thick, 3.6 mm in diameter) were placed (Fig. 4).

The task involved peeling of the polyethylene from the Sorbothane. The experimental subject, not a surgeon, had considerable experience with Micron. The procedure was performed under 16x magnification using a Zeiss OPMI® 1 stereo operating microscope. The subject was instructed to apply the least possible force during the task. The subject peeled 32 circles under each of two test conditions: with tremor compensation only, and with tremor compensation plus admittance control. Force was measured in three dimensions throughout each task.

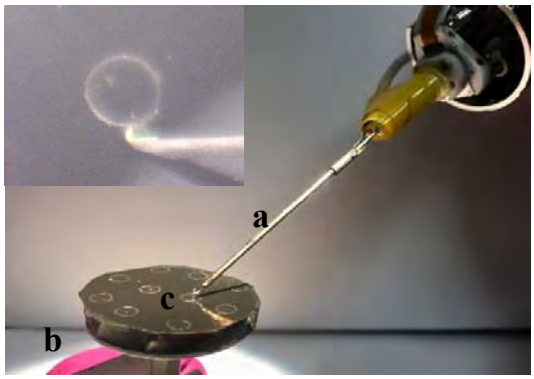

Fig. 4 Representation of a peeling test in progress. (a) FBG sensor embedded in Micron end effector; (b) Sorbothane® as artificial tissue model; (c) circular layers of polyethylene film. Inset: view through microscope.

RESULTS

Averages of the maximum applied force in the three directions are reported in Fig. 5, together with the standard deviation. Forces are reported in body coordinates (where z is the long axis of the instrument).

Table 1 Comparison between applied forces [mN] under position control and applied forces under admittance/position control.

		Maximum applied force (confidence interval 90%)	Average applied force (confidence interval 90%)
Position Control	X	18.30 ± 0.92	3.38 ± 0.16
	Y	8.90 ± 0.71	2.48 ± 0.44
	Z	12.53 ± 0.96	4.84 ± 0.01
Position Control and Admittance Control	X	13.26 ± 0.81	2.62 ± 0.14
	Y	6.17 ± 0.49	1.65 ± 0.15
	Z	8.09 ± 0.38	3.38 ± 0.01

DISCUSSION

This paper reported on the implementation of admittance control to minimize force applied during blunt dissection with an active handheld microsurgical instrument. Preliminary results showed a decrease in the exerted force by 27% and 30% in the transverse coordinates, and 35% along the long axis of the instrument. Future work will deal with optimization of the control system tuning, and testing under more realistic conditions.

ACKNOWLEDGEMENT

Partially funded by U.S. National Institutes of Health (grant no. R01EB000526).

REFERENCES

[1] Xu F et al. Petroclival meningiomas: an update on surgical approaches, decision making, and treatment results. Neurosurgical Focus. 2013; 35(6): E11.
[2] Bagga V and Bhattacharyya D. Robotics in neurosurgery. Ann R Coll Surg Engl. 2018;100(6_sup):19-22
[3] Yang S et al. Manipulator design and operation of a six-degree-of-freedom handheld tremor-canceling microsurgical instrument. IEEE/ASME Trans Mechatron. 2015;20(2):761-72.
[4] Wells TS et al. Hybrid position/force control of an active handheld micromanipulator for membrane peeling. Int J Med Robot. 2016;12(1):85-95.
[5] Keemink AQ et al. Admittance control for physical human–robot interaction. Int J Robot Res. 2018; 37(11), 1421–44.
[6] Iordachita I et al. A sub-millimetric, 0.25 mN resolution fully integrated fiber-optic force-sensing tool for retinal microsurgery. Int J Comput Assist Radiol Surg. 2009; 4:383–90.
[7] VanIngen-Dunn C et al. Development of a humanlike flesh material for prosthetic limbs. Proc Int Conf IEEE Eng Med Biol Soc 1993; 1313–4.

Tremor Reduction using Time Delay Estimation on Handheld Microsurgical Device

Jintaek Im, Sukho Park, Cheol Song

Department of Robotics Engineering, DGIST, Daegu, Korea shpark12@dgist.ac.kr, csong@dgist.ac.kr (DOI10.31256/HSMR2019.56)

INTRODUCTION

Performance of microsurgery has been mainly limited by physiological limitations of humans. For instance, humans have physiological hand tremor which has amplitude around hundreds of micrometers and 6-12 Hz frequencies [1]. During the microsurgery, it prevents surgeons from maneuvering surgical tool precisely, usually resulting in unintended motions which might damage to a surgical lesion.

To overcome this issue, several types of handheld microsurgical manipulators such as Micron and SMART have been developed to assist precise and safe surgical operation [2, 3]. Both of them have more than one PZT motor as an actuator, and measure the distance between the end-effector and surgical target by an optical tracking system and common-path optical coherence tomography (OCT), respectively. They demonstrated the reduction of hand tremor by utilizing feedback loops such as P and PID control for regulation control.

Furthermore, feed-forward tremor suppression using a Kalman filter and tremor prediction algorithm have also been suggested for better tremor cancellation [4, 5]. Kalman filter estimates an end-effector's velocity and converted it to a feed-forward input by considering a time latency of a plant. However, Kalman filter consists of dynamic mathematical model and requires tuning of its coefficient for performances on both small and large scale of hand tremors.

In this study, time delay estimation (TDE)-based tremor estimator is added to the regulation control loop which works as a P-control. Because its sampling rate is 40 times faster than physiological hand tremor, TDE-based estimator can be worked. The performances in both time domain and Fourier domain are compared with P-control without TDE estimator by calculating root mean square error (RMSE) after achieving Fourier transformed results, respectively.

MATERIALS AND METHODS

A. System Configuration

Figure 1 shows the system configuration of the SMART manipulator. This system has one PZT motor, so that it has one degree-of-freedom.

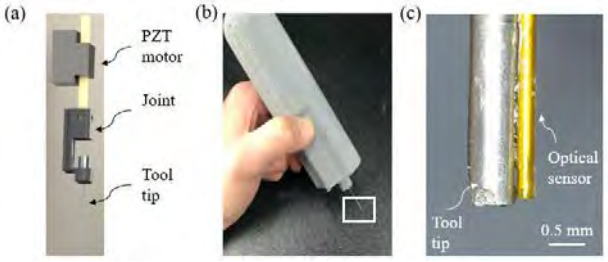

Fig. 1 System configuration of the SMART manipulator (a) an internal structure of motor configuration, (b) an implemened image with a housing, (c) a magnified image of its tool tip including an optical sensor.

The tool tip is connected to the PZT motor through a rigid joint as shown in Fig.1 (a) and the PZT motor is fixed to the housing in Fig.1 (b). An fiber-optic OCT distance sensor is attached to the tool tip to get real-time positions from the sample (Fig.1 (c)).

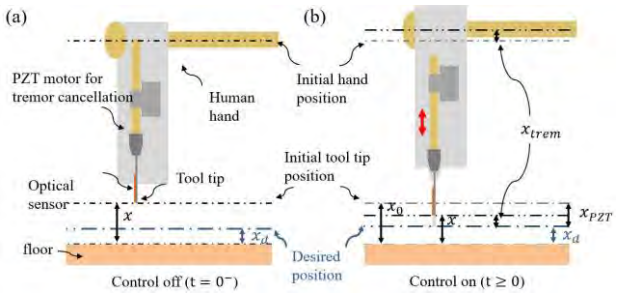

Fig. 2 Control procedure and parameter setting in the SMART manipulator (a) right before control is initiated, (b) after control activated.

In Fig. 2, the control procedure and parameters are described. Before the control is initiated, the distance, x from the tool tip and static floor only depends on the human hand's motion. As described in Fig.2 (b), once the control is activated, all the parameters: x_0, x_{PZT} and x_{Trem} can be measured with respect to initial positions in Fig.2 (a). From these parameters, Eq. (1) can be derived as follows.

$$x(t) = x_{PZT}(t) + x_0 + x_{Trem}(t) \quad (1)$$

where t is the time variable and x_0 is the tool tip's position measured right before the control is initiated. x_{PZT} is the displacement of the tool tip by the PZT motor, and it can keep the tool tip at the desired position, x_d. Among the parameters in Eq. (1), x_{Trem} is a noise which needs to be cancelled. It encompasses the uncertainties which are hard to predict; however, once the sampling interval, L, is small enough compared to tremor, next

tremor can be estimated by its previous value. In that sense, the Eq. (2) can be derived.

$$x_{Trem}(t) \approx x_{Trem}(t\text{-}L) = x(t\text{-}L)\text{-}x_{PZT}(t\text{-}L)\text{-}x_0 \quad (2)$$

By the time delay estimation, it is possible to approximate x_{Trem} to previous known value.

B. Block Diagram

The control loop using the time-delay-based estimator is described in Fig.2, and it is to keep current position at the desired position by compensating tremor.

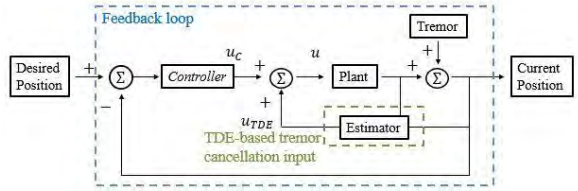

Fig. 3 Block diagram for TDE-based tremor reduction system.

The control input, u is achieved by adding the outputs from the controller and the term of TDE, as in Eq. (3).

$$u(t) = u_C(t) + u_{TDE}(t) \quad (3)$$

In this study, the P controller is adopted and the total feedback loop is repeated so that the error (e) between the desired position (x_d) and current position (x) converges to zero.

$$x_d = e(t) + \mathcal{L}^{-1}\{G(s)U(s)\} + x_{Trem}(t) \quad (4)$$

where $\mathcal{L}^{-1}\{\cdot\}$ means inverse Laplacian and $G(s)$ and $U(s)$ denote the plant transfer function and the plant input, respectively. Especially, $G(s)$ is modeled as f_{PZT}/s and $U(s)$ can be regarded as $U_C(s) + U_{TDE}(s)$, as shown in Eq. (3). By taking time derivative on both sides, Eq. (4) can be written as

$$\dot{e}(t) + f_{PZT}u_c(t) + f_{PZT}u_{TDE}(t) + \dot{x}_{Trem}(t) = 0 \quad (5)$$

In Eq. (5), $\dot{x}_{Trem}(t)$ can be approximated to $\dot{x}(t\text{-}L)\text{-}\dot{x}_{PZT}(t\text{-}L)$ by using Eq. (2).

$$u_{TDE}(t) = -1/f_{PZT}\{\dot{x}(t\text{-}L)\text{-}\dot{x}_{PZT}(t\text{-}L)\} \quad (6)$$

When we applied the P controller ($u_C=K_P e(t)$) and the TDE in Eq. (6), the final error dynamics can be derived as

$$\dot{e}(t) + f_{PZT}K_P e(t) = 0 \quad (7)$$

As shown in Eq. (7), the error dynamics can be an asymptotically stable and the error can converge to zero.

RESULTS

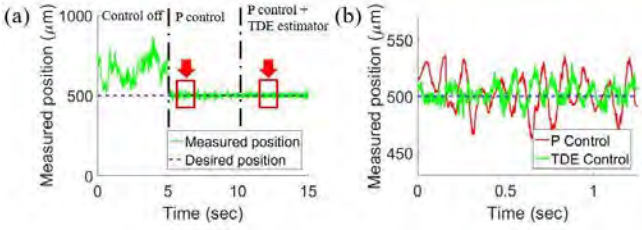

Fig. 4 Regulation control result (a) measured probe position during control off, P control with and without TDE estimator, (b) zoomed result of two cases.

Figure 4 shows the results of the regulation control where x_d is *500 μm*. From the result, the tremor can be effectively reduced by the proposed control algorithm. In detail, the P controller with TDE can show lower peak-to-peak fluctuations compared to the P controller. The performance of the controllers (P controller without or with TDE) are quantitatively compared in the time domain and the frequency domain, as shown in Fig. 5. We found that the proposed algorithm shows the decreased RMSE value by 26.92% during five trials and the reduced tremor amplitude in the interest frequency domain (6 to 12 Hz).

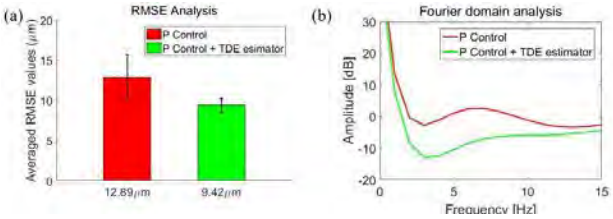

Fig. 5 Evaluations on two control performances (n=5) (a) RMSE comparison, (b) Fourier domain comparison.

DISCUSSION

In this study, we introduced TDE to estimate the hand tremor in the SMART and demonstrated the performance of regulation control algorithm using a conventional P control and TDE. From the experiment, it secures that the proposed algorithm could successfully reduce tremor amplitude in both time domain and frequency domain.

ACKNOWLEDGEMENT

This work was supported by the DGIST R&D Program of the Ministry of Science and ICT (19-RT-01) and National Research Foundation of Korea (NRF) (2015R1C1A 1A01052915).

REFERENCES

[1] Payne, C. J., and G.-Z. Yang., Hand-held medical robots. Ann. Biomed. Eng. 42:1594–1605, 2014.

[2] Yang, S., MacLachlan R. A., and Riviere C. N., Manipulator design and operation of a six-degree-of-freedom handheld tremor-canceling microsurgical instrument. IEEE/ASME Trans. Mechatron., 20(2): 1–12, 2015.

[3] Song, C., Park D. Y., Gehlbach P. L., Park S. J., and Kang J. U., Fiber-optic OCT sensor guided "SMART" micro-forceps for microsurgery. Biomed. Optics. Exp. 4:1045–1050, 2013.

[4] Becker, B. C., MacLachlan, R. A., Lobes, L. A., Hager, G. D., & Riviere, C. N., Vision-based control of a handheld surgical micromanipulator with virtual fixtures. IEEE Transactions on Robotics, 29(3): 674-683, 2013.

[5] Cheon, G. W., Gonenc, B., Taylor, R. H., Gehlbach, P. L., & Kang, J. U., Motorized Microforceps With Active Motion Guidance Based on Common-Path SSOCT for Epiretinal Membranectomy. IEEE/ASME Transactions on Mechatronics, 22(6): 2440-2448, 2017.

Development of 5-DOFs Master-Slave system with intentional adjustment of hysteresis based on antagonistic tendon control

Hansoul Kim[1], Joonhwan Kim[2], Minho Hwang[2], Dong-Soo Kwon[2*]

[1]Robotics Program, KAIST, Daejeon, 305-701, Korea

[2]Department of Mechanical Engineering, KAIST, Daejeon, 305-701, Korea

robotgksthf@kaist.ac.kr (DOI10.31256/HSMR2019.57)

INTRODUCTION

Flexible endoscopic robots are expected to be a next-generation surgical robot platform overcoming the barriers of single-port surgery and Natural Orifice Transluminal Endoscopic Surgery (NOTES) with their high lesion accessibility and versatility. Unlike the laparoscopic robots which consist of rigid links, flexible robot platforms mainly use tendon-sheath mechanisms, to maintain flexibility. However, tendon-sheath mechanisms cause hysteresis problems, degradeing robot performance. Therefore, various hysteresis reduction and compensation methods have been proposed in previous study to overcome this problem. A feedback method using image information from an endoscopic camera has been proposed, as well as a hysteresis model based feedforward method [1-2]. These previous studies have focused on hysteresis reduction, but did not extend to verifying whether the proposed methods were effective in improving robot performance during surgery. It is desirable to establish criteria for the amount of hysteresis reduction needed for high performance from a flexible endoscopic surgical robot.

To determine these criteria, endoscopic tasks should be performed under various hysteresis conditions. For this purpose, a master-slave system that can intentionally adjust hysteresis and perform endoscopic tasks has been developed in this paper.

MATERIALS AND METHODS

A master-slave system capable of hysteresis adjustment and performing endoscopic tasks was developed in this study as shown in Fig. 1. The slave robot consists of 5 DOFs (roll, pitch, yaw, translation, and grasping) surgical tool, seven motors (XM-430, ROBOTIS, Korea), four load cells (333FDX, KTOYO, Korea), and two encoders (7S-400-2MC-50-00E, NEMICON, Japan). The master device was developed with the same degree-of-freedoms (DOFs) and kinematic configuration as the surgical tool.

It was assumed in this study that hysteresis occurs only in two wire-driven bending joints. Therefore, the hysteresis was adjusted only for those two bending joints. To intentionally adjust the hysteresis, the surgical tool should have sufficient accuracy. Analysis of the developed surgical tool showed inherent hysteresis problem due to wire slack. In order to overcome the hysteresis problem caused by wire slack, an antagonistic tendon control scheme for controlling both position of

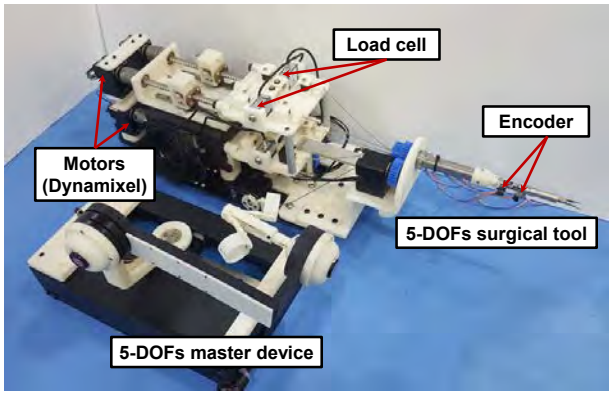

Fig. 1 Hysteresis adjustable 5-DOFs Master-Slave system

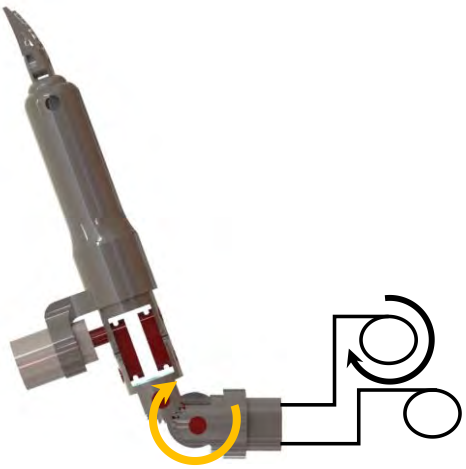

Fig. 2 Concept and notation of proposed control scheme

joint and wire tension was used. This control scheme has mainly been used in wire-driven system such as robotic hands.

Previous antagonistic tendon control schemes input torque directly to the motor based on the equations of the robot dynamics. In this paper, the control scheme was implemented by using the compensated rotation value of the motor to simultaneously control the position of joints and tension of the wires. Since the actual state of the robot was used in the proposed control scheme, an encoder was used to provide feedback of the actual position of the joint, and a load cell was used to provide feedback of the actual tension of the driving wire. The concept of the proposed control scheme and the notation used in the equation are shown in Fig. 2.

The position of the bending joint and the tension of the driving wire were controlled using a PID controller. The

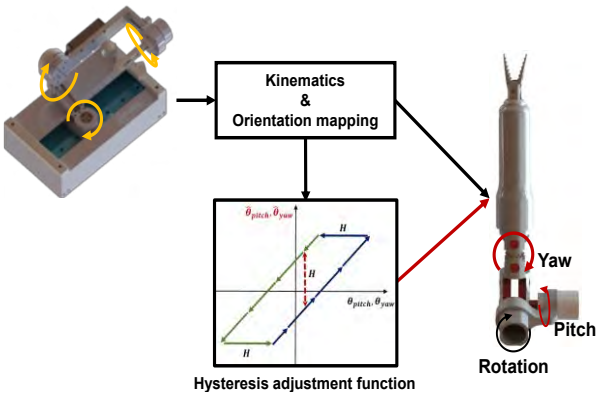

Fig. 3 The concept of hysteresis adjustment function

required torque for the bending joint to rotate from the actual angle θ to desired angle θ_d can be expressed as τ.

$$\tau = K_p e + K_d \dot{e} + K_i \int e$$

Where e is the position error of the joint. The required torque for the driving wire to maintain the desired tension T_{1d} can be expressed as τ_{shift1}.

$$\tau_{shift1} = K_{pt1} e_{t1} + K_{dt1} \dot{e}_{t1} + K_{it1} \int e_{t1}$$

Where e_{t1} is the tension error of the driving wire. The rotation value to be compensated for motor M_1 that satisfies both the desired joint angle θ_d and desired tension value T_{1d} can be expressed as e_1.

$$e_1 = \frac{1}{K}\left(\frac{1}{2}\tau + \tau_{shift1}\right)$$

e_1 is updated for each control cycle and compensated for actual rotation value of the motor M_1. The compensated rotation value can be expressed as $\hat{\theta}_1$.

$$\hat{\theta}_1 = \theta_1 + e_1$$

The motor M_2 is also compensated using the same equation. Here K_p, K_d, K_i, K_{pt1}, K_{dt1}, K_{di1}, and K are hyperparameters of the controller, and were tuned by trial and error.

After implementing the proposed control scheme, the hysteresis adjustement function was designed to intentionally adjust the hysteresis of the two bending joints as shown in Fig . 3. Using the values of θ_{m1}, θ_{m2}, and θ_{m3} obtained from the master device, a transformation matrix, and orientation mapping strategy to calculate θ_{pitch}, θ_{yaw}, and $\theta_{rotation}$, maintaining the same orientation for the master device and surgical tool is achieved. After that, θ_{pitch} and θ_{yaw} are input to the hysteresis adjustment function to obtain the intentionally adjusted angles $\hat{\theta}_{pitch}$ and $\hat{\theta}_{yaw}$. Finally, the value of angles $\hat{\theta}_{pitch}$, $\hat{\theta}_{yaw}$, and $\theta_{rotation}$ are input to surgical tool. The amount of hysteresis is adjusted by changing the value of H.

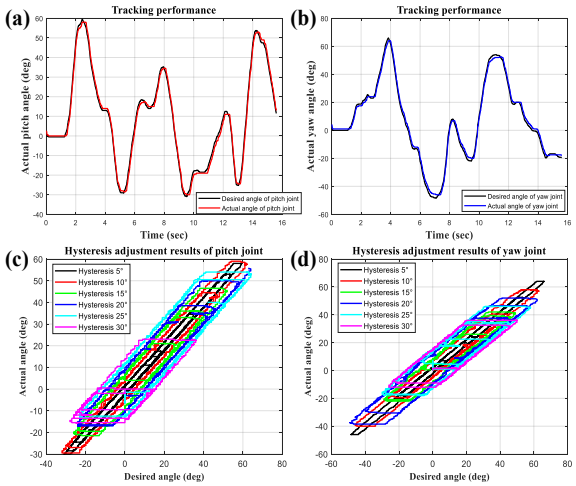

Fig. 4 (a) Tracking performance of pitch joint, (b) Tracking performnace of yaw joint, (c) Hysteresis adjustment of pitch joint, and (d) Hysteresis adjustmnet of yaw joint

RESULTS

To confirm the performance of the proposed control scheme, and the effectiveness of the hysteresis adjustment, a non-periodic trajectory was input to the surgical tool using the master device. The maximum position error of two bending joint was approximately 3.43° and 3.25° respectively. The hysteresis was adjusted to between 5 to 30°, with intervals of 5°, as shown in Fig . 4.

DISCUSSION

In this study, a 5-DOFs hysteresis adjustable master-slave system was developed. An antagonistic tendon control scheme was used because the surgical tool should have enough accuracy to intentionally adjust hysteresis, and the hysteresis adjustment function was designed to adjust the hysteresis of bending joints from 5 to 30° with intervals of 5°.

As a future work, by performing endoscopic tasks under various intentionally-adjusted hysteresis conditions using this system, we will identify the effect of surgical tool hysteresis on performance of tele-operated endoscopic tasks.

ACKNOWLEDGEMENT

This research was supported by a grant of the Korea Health Technology R&D Project through the Korea Health Industry Development Institute(KHIDI), funded by the Ministry of Health & Welfare, Republic of Korea(grant # : HI17C2012)

REFERENCES

[1] Reilink, R., Stramigioli, S., & Misra, S. (2013). Image-based hysteresis reduction for the control of flexible endoscopic instruments. *Mechatronics*, *23*(6), 652-658.

[2] Do, T. N., Tjahjowidodo, T., Lau, M. W. S., Yamamoto, T., & Phee, S. J. (2014). Hysteresis modeling and position control of tendon-sheath mechanism in flexible endoscopic systems. *Mechatronics*, *24*(1), 12-22.

Quantifying the Benefits of Robotic Assistance in Various Microsurgical Procedures

Olivia Puleo[1], Yunus Sevimli[1], David Levi[1], Ashwin Bhat[1], David Saunders[1], Russell H. Taylor[2]

[1]*Galen Robotics, Inc.*

[2]*Laboratory for Computational Sensing and Robotics, Johns Hopkins University*

[olivia.puleo, yunus.sevimli, david.levi, ashwin.bhat, dave.saunders]@galenrobotics.com, rht@jhu.edu (DOI10.31256/HSMR2019.58)

INTRODUCTION

While advances in surgical and optical technologies have led to the advent of microsurgical procedures, it is now the limitation of human dexterity that limits the use and extent of these procedures. Robotic systems that offer finer motor control and improved precision may allow a larger number of patients to benefit from these interventions that are currently constrained by human ability [1]. The Galen robot is a next generation research system of the original Robotic ENT Microsurgical System (REMS), a 5 degree of freedom robotic platform designed primarily for microsurgical applications. It works cooperatively with the surgeons, can hold adapted standard surgical instruments with its universal surgical tool exchanger and identification system, and helps mitigate hand tremor, which may offer advantages over conventional interventions in the form of reduced damage to the surrounding tissues and time savings in the operating room [1-2]. This paper summarizes the methods and findings of three studies conducted to quantify the benefits of using the robot over freehanded approaches. Specifically, the authors have studied the use of the platform in simulated microlaryngeal phonosurgery, microvascular anastomosis, and stapedotomy tasks.

Disclaimer: *The Galen System is under development by Galen Robotics, Inc. and is not for commercial sale.*

MATERIALS AND METHODS

1 – Microlaryngeal Surgery Study

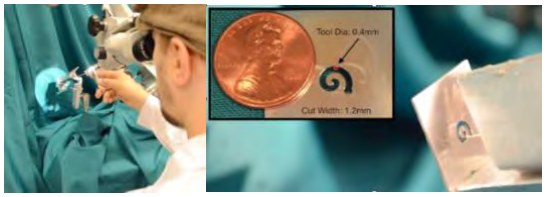

Fig. 1 Left: Microlaryngeal study setup. Right: Close up of the smallest spiral and the tool tip inserted into it.

The setup for the microlaryngeal surgery study was devised to simulate phonosurgery by traversing a spiral channel using a mock laryngoscope under microscopic vision [3]. Nine participants of varying experience levels were tasked with guiding a 0.4 mm diameter microlaryngeal needle through spirals of three different channel widths both with and without the REMS while avoiding contact with the sides of the slot. Data was collected in the forms of contact time – time the needle spent touching the edges of the spiral – and a survey to elicit feedback from the participants.

2 – Microvascular Surgery Study

Six naïve participants and one expert were recruited for this study. To simulate microvascular anastomosis, a chicken thigh model was used [4]. Participants were seated at a surgical microscope and tasked with performing three front wall sutures with three knots tied per suture on an artery of 2.4-3.0 mm inner diameter, with and without REMS assistance for their dominant hand. Along with measuring time to completion (TTC), a new microvascular tremor scale (MTS) was used to score the performance, and the interrater reliability of the scale was determined.

Fig. 2 Left: Microvascular study setup. Right: close up of REMS-assisted trial.

3 – Stapedotomy Study

A middle ear phantom modeling the view of the incus a surgeon would have after removing a calcified portion of the stapes was created using 3D printed parts and a force/torque sensor (ATI Nano 17, Apex, North Carolina) [5]. Six participants were asked to place and crimp a piston prosthesis onto the model both freehanded and with robotic assistance, three times each. The means of both the maximum force applied to the model incus and the change of force over time (dF) were recorded for prosthesis placement and for crimping.

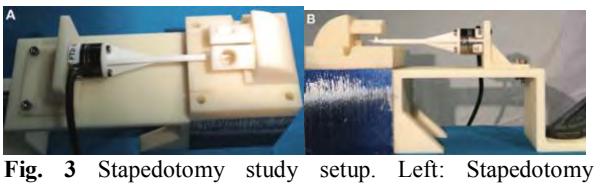

Fig. 3 Stapedotomy study setup. Left: Stapedotomy visualization. Right: 3D-printed incus.

RESULTS

1 – Microlaryngeal Surgery Study

Nine participants completing three different spiral widths led to 27 sets of data to compare [3]. Of those, 24

show reduced contact time in the REMS group compared to the manual group. Additionally, five test conditions yielded no contact time at all, all of which were achieved with robotic assistance. The overall contact time was significantly decreased when using the REMS over freehand, as well as with the larger two spirals. When subgroup analysis was performed of the smallest spiral width, the group more familiar with microlaryngeal surgery demonstrated improved performance with the robot whereas those without did not.

Evaluation of the exit surveys indicated that all participants determined that they thought the task was a good representation of laryngoscopy, rated their surgical skill more highly with the robot than without, and indicated a desire to use the robot once clinically available.

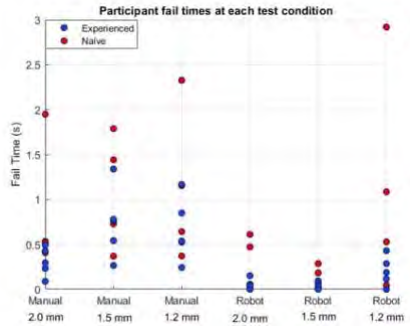

Fig. 4 Results of the spiral experiment

2 – Microvascular Surgery Study

The microvascular naïve participants received a mean MTS score of 2.40 freehand and 0.72 with REMS-assistance, more than a three-fold reduction [4]. While the score was also reduced for the microvascular expert, the difference was not significant. The time to completion did not have a significant difference between free-hand and REMS-assisted trials for either the naïve or the expert participant(s); however, there was a meaningful reduction in TTC between the first and second trial, regardless of the set of conditions they started with which they started.

To determine the inter-rater reliability of the MTS, the Intraclass Correlation Coefficient (ICC) was calculated. Between seven expert microvascular raters, the ICC for consistency was 0.914.

A qualitative self-assessment was performed through an exit survey. All six naïve participants found the REMS more accurate and thought it improved instrument handling and stability compared to freehand. Five out of six also preferred using the REMS over the freehand procedure.

3 – Stapedotomy Study

Across all participants, the mean maximum force exerted while crimping the prosthesis around the simulated incus freehanded was 469.3 mN, which was significantly more than the robot-assisted value of 272.7 mN; the placement force and there was no significant difference in *d*F value between freehand and robot-assisted crimping [5]. Comparison of the freehand performance of the expert participant versus the non-expert participants revealed that the expert surgeon applied significantly less force during placement ($p = 0.002$) and crimping ($p = 0.004$), along with significantly less *d*F during crimping ($p < 0.0001$). Evaluating the expert participant's freehand performance against the nonexpert robot-assisted performance reveals no significant difference between the two groups.

CONCLUSION

The studies discussed above examine the use of a cooperatively controlled robot in three different microsurgical applications – microlaryngology, micro-anastomosis, and stapedotomies. In simulated phonosurgery, the system offered objective improvement in precision over the participants' manual performance [3]. Subjectively, the participants felt that the REMS aided their performance and expressed an interest in using the REMS in their clinical practice [3]. The second study demonstrated that it is feasible to use the REMS in microvascular anastomosis for microvascular naïve subjects, as well as showed that the MTS was a reliable grading system for assessing microvascular tremor [4]. Finally, the stapedotomy study showed that the robot was able to help reduce the maximum force exerted while crimping a stapes prosthesis around a simulated incus [5]. Along with that, the nonexpert surgeons went from applying significantly more force during placement and crimping as compared to the expert to having no significant difference between them [5].

These studies represent the beginning of an effort to quantify the benefits of using a cooperatively controlled robot in microsurgical procedures. Further testing can be done in order to include more middle strata in terms of participant expertise to better define the robot's role in teaching and clinical settings. Furthermore, additional studies mimicking different surgical procedures can elucidate the robot's potential contributions to those types of operations.

REFERENCES

[1] Olds, K. (2015). Robotic Assistant Systems for Otolaryngology-Head and Neck Surgery (Doctoral dissertation).

[2] Sevimli, Y., Wilkening, P., Feng, L., Balicki, M., Olds, K., Keady, T., Taylor, R. (2016, June). Surgical Workflow Integration of the Robotic ENT Microsurgical System. Paper presented at the Hamlyn Symposium in Medical Robotics, London, UK.

[3] Akst, L. M., Olds, K. C., Balicki, M., Chalasani, P., & Taylor, R. H. (2018). Robotic microlaryngeal phonosurgery: Testing of a "steady-hand" microsurgery platform. *The Laryngoscope*, *128*(1), 126-132.

[4] Feng, A. L., Razavi, C. R., Lakshminarayanan, P., Ashai, Z., Olds, K., Balicki, M., ... & Richmon, J. D. (2017). The robotic ENT microsurgery system: A novel robotic platform for microvascular surgery. *The Laryngoscope*, *127*(11), 2495-2500.

[5] Razavi, C. R., Wilkening, P. R., Yin, R., Lamaison, N., Taylor, R. H., Carey, J. P., & Creighton, F. X. (2019). Applied Force during Piston Prosthesis Placement in a 3D-Printed Model: Freehand vs Robot-Assisted Techniques. *Otolaryngology–Head and Neck Surgery*, *160*(2), 320-325.

Index of Authors